

DISSERTATION

ENVIRONMENTAL AND ECONOMIC EVALUATION OF ALGAL-BASED BIOFUELS
THROUGH GEOGRAPHICALLY RESOLVED PROCESS AND SUSTAINABILITY
MODELING

Submitted by

David Quiroz

Department of Mechanical Engineering

In partial fulfillment of the requirements

For the Degree of Doctor of Philosophy

Colorado State University

Fort Collins, Colorado

Summer 2023

Doctoral Committee:

Advisor: Jason C. Quinn

Bret Windom

Bryan Willson

Kenneth Reardon

Copyright by David Quiroz 2023

All Rights Reserved

ABSTRACT

ENVIRONMENTAL AND ECONOMIC EVALUATION OF ALGAL-BASED BIOFUELS THROUGH GEOGRAPHICALLY RESOLVED PROCESS AND SUSTAINABILITY MODELING

Advanced algal renewable fuels have been the subject of extensive research during the last decades. Their advantages over conventional biofuel feedstocks position algal biomass as a promising feedstock for the development of a sustainable and circular bioeconomy. Despite recent technological improvements, techno-economic analyses (TEAs) show that algae-derived fuels fail to be cost-competitive with petroleum fuels. Moreover, results from life-cycle assessments (LCAs) indicate declining greenhouse gas emissions when compared to petroleum fuels, but their water, health and air pollution impacts are still uncertain. This is explained by the fact that most published TEAs and LCAs of algal systems are not supported by high-resolution models and can only provide average sustainability metrics based on results from restricted data sources. These assessments often lack the resolution to correctly analyze the temporal and regional variations of biomass yields which have a direct impact on TEA and LCA metrics. Based on the current state of the field, there is a critical need to develop dynamic models that can inform sustainability assessments and consequently assist decision-making and technology development.

This first part of this research work focuses on establishing the foundations for spatially explicit and temporally resolved LCA and TEA by developing and validating models that

capture the thermal and biological dynamics of open algal cultivation systems. The modeling work is heavily focused on providing accurate predictions of evaporation losses in open algae raceway ponds and investigating the effects of evaporation rates on pond temperatures and growth rates. To date, this is the first modeling effort focused on predicting the evaporation losses of open algal ponds at the commercial scale. The outputs from the thermal model are then used to inform a biological algae growth model that is validated with experimental data representing the current biomass productivity potential. When integrated with hourly historical weather data, the modeling tools provide spatiotemporal mass and energy balances of the algal cultivation, dewatering, and conversion to fuel processes. These results are then leveraged with sustainability tools such as LCA and TEA to provide sustainability metrics at a high temporal and spatial scale.

After developing a robust modeling framework, the modeling tool is leveraged with two distinct water LCA methods to provide a comprehensive assessment of the water impacts of algae-derived renewable diesel production across the United States. First, a water footprint analysis is conducted to understand the direct freshwater and rainwater consumption of algal cultivation and provide a framework for comparison to traditional biofuel feedstocks. The second method provides a county-level water scarcity footprint by analyzing the impact of algal systems on local water demand and availability. This assessment allows for the proper identification of potential algal sites for algal cultivation and locations where the deployment of algal systems will exacerbate local water stress. Ultimately, this research chapter provides the first holistic investigation of the water consumption and environmental water impacts of algal systems across the U.S. and establishes benchmarks for comparison to other fuels.

Finally, the work comprising the third research chapter includes a novel global sustainability assessment that integrates the developed process modeling framework with regional-specific TEA and LCA. The spatially explicit TEA considers regional labor costs, construction factors, and tax rates to assess the economic viability of algal biofuels across 6,685 global locations. Similarly, a well-to-wheels LCA was performed by accounting for the regional life cycle impacts associated with electricity generation, hydrogen, and nutrient production across ten different environmental categories including health, air pollution, and climate impacts. This framework enables the identification of algal sites with optimal productivity potential, environmental impacts, and economic viability. Discussion focuses on the challenges and opportunities to reduce costs and environmental impacts of algal biofuels in various global regions.

ACKNOWLEDGEMENTS

I would like to acknowledge Dr. Kenneth Reardon, Dr. Bret Windom, and Dr. Bryan Willson for generously providing their knowledge and expertise. I am also sincerely grateful to my advisor, Dr. Jason Quinn, for his patience, mentorship, and constant support through my graduate school. I would also like to thank all the amazing colleagues in the Sustainability Research Laboratory. Most importantly, I would like to express deepest gratitude to friends and family, Adriana Varela, and Cecilia, Armando, Enrique, and Gabriel Quiroz for their patience and encouragement.

TABLE OF CONTENTS

ABSTRACT.....	ii
ACKNOWLEDGEMENTS.....	v
CHAPTER 1: INTRODUCTION.....	1
CHAPTER 2: DEVELOPMENT OF A DYNAMIC OPEN POND THERMAL MODEL FOR COMMERCIAL-SCALE ALGAL PONDS ¹	6
2.1 Introduction.....	6
2.2 Materials and methods	9
2.2.1 Thermal model.....	9
2.2.2 Biological model.....	14
2.2.3 Thermal and biological model validation	16
2.2.4 Simulation framework	18
2.3 Results and discussion	20
2.3.1 Thermal model validation.....	20
2.3.2 Biological model validation.....	21
2.3.3 Model extrapolation.....	23
2.4 Conclusions.....	33
CHAPTER 3: LIFE-CYCLE WATER ASSESSMENT OF MICROALGAL-BASED BIOFUELS IN THE UNITED STATES.....	35
3.1 Introduction.....	35
3.2 Materials and methods	37
3.2.1 Cultivation model.....	38

3.2.2 Conversion Model.....	40
2.3 Water LCA Methods.....	41
3.3 Results and discussion	44
3.3.1 National water footprint mapping.....	44
3.3.2 Water footprint breakdown.....	49
3.3.3 Water scarcity implications.....	55
3.4 Conclusions.....	59
CHAPTER 4: A GLOBAL LIFE EVALUATION OF THE SUSTAINABILITY OF ALGAL-	
BASED BIOFUELS	60
4.1 Introduction.....	60
4.2 Materials and methods	62
4.2.1 Biological growth model.....	62
4.2.2 Open-raceway pond thermal model.....	63
4.2.3 Biomass dewatering, storage, conversion, and upgrading.....	63
4.2.4 Meteorological data	64
4.2.5 Life cycle assessment.....	64
4.2.6 Techno-economic analysis.....	66
4.3 Results.....	67
4.3.1 Global productivity potential	67
4.3.2 Global warming potential	69
4.3.3 Additional environmental impacts.....	72
4.3.3 Techno-economic analysis.....	74
4.4 Discussion.....	76

CHAPTER 5: CONCLUSIONS AND RECOMMENDATIONS	80
5.1 Overall conclusions.....	80
5.2 Future directions of thermal and growth modeling	80
5.3 Future directions of algal water life cycle assessment.....	81
5.4 Future directions of global sustainability assessment.....	82
REFERENCES	84
Appendix A.....	110
Appendix B	132
Appendix C.....	157

CHAPTER 1: INTRODUCTION

Due to climate instability and rising temperatures, nations around the world have pledged to reach net carbon neutrality by 2050 [1]. Achieving these climate goals will require the rapid reduction of greenhouse gas emissions (GHG) from high-emitting sectors (e.g., energy, agriculture, and transportation), for which in many cases, there are not definite decarbonization pathways yet [2]. For example, decarbonizing the energy sector requires the retirement of current fossil-fueled power plants and the scale-up of solar photovoltaics and onshore wind [3], [4]. On the other hand, decarbonizing transportation represents a more complex challenge [3], [4]. Given the high-reliance on fossil fuels across all modes of transport, reducing global transportation emissions involves the combined design of more efficient transportation systems with the development and deployment of low-carbon technologies [4].

Although the expansion of renewable electricity capacity facilitates the electrification and emissions reductions of light-duty vehicle fleets, the combined emissions from heavy-duty trucking, buses, rail, and maritime shipping represent a considerable share of the total GHG emissions of this sector (43%) [5]. As these fleets primarily rely on high energy density fuels [4], the adoption of drop-in sustainable fuels such as renewable diesel (RD) is a more feasible and meaningful strategy to immediately abate the GHG emissions of these fleets while leveraging existing fuel infrastructure. This is reflected in the recent biofuel market (2021), in which global RD demand increased by 65% relative to 2019 [6]. While low-carbon liquid fuels are an attractive solution to reduce emissions from hard-to-electrify fleets, commercial biofuel

production is still constrained by the limited availability of waste and edible oil-based feedstocks [6].

Microalgae are a lipid-rich source of biomass that exhibits rapid growth and the ability to be cultivated on marginal lands [7]–[9]. Moreover, microalgae offer the advantage of bio-assimilating nutrients and carbon from wastewater and industrial carbon streams [10]–[12]. This contributes to a complex biochemical composition that can be converted into a variety of bioproducts. Due to its potential for dramatically higher productivity compared to alternative oil-based feedstocks, microalgae are a promising bioresource to establish a sustainable renewable fuel supply chain at the scale required to decarbonize transportation. Consequently, algal biofuels have been a topic of ongoing research in the bioenergy field. Over the last decades, experimental and modeling efforts have resulted in an enhanced understanding of algal biomass cultivation [13]–[18] and the development of noble conversion to fuel pathways [19]–[21]. Despite recent technical advances, the costs of algal biofuels remain below commercially viable levels [22].

The techno-economic viability and environmental sustainability of algal systems are often analyzed using sustainability modeling tools such as techno-economic analysis (TEA) and life cycle assessment (LCA), respectively. Both TEA and LCA require a rigorous quantification of the mass and energy flows of the system through detailed process modeling, therefore, the validity of sustainability modeling outputs is highly dependent on process model fidelity [22]. Additionally, capturing the impacts of weather variability on algal growth rates is of particular importance as biomass productivity is directly correlated to the economic and environmental metrics of the system. Dynamic biological models with the ability to quantify the impacts of

changing culture temperatures and light intensity at fine time scales are required for proper representation of outdoor algal productivity [23]–[26].

Moreover, biological modeling must be informed by accurate pond temperatures, which fluctuate with changing weather conditions [25], [27], [28]. As detailed by existent studies [25], [26], [29], [30], highly resolved models (with sub-daily time scales) are critical for representing the impacts of weather dynamics on the evaporation rates and temperatures of open-raceway ponds (ORP) systems accurately. To date, thermal models for algal cultivation systems cannot estimate evaporation rates and temperatures of commercial-scale ORPs as pilot-scale data is often used for model validation [27], [28], [31]. This has contributed to the large variability of water consumption metrics and the lack of a holistic understanding of the life cycle water implications of commercial-scale algal biofuels.

Beyond modeling assumptions, water LCAs of algal biofuels do not usually follow a standard life-cycle framework. studies often employed a water footprint (WF) accounting method [23], [32]–[35] or water scarcity footprint (WSF) methods [36], [37], and fail to provide an objective framework for comparison to conventional biofuel systems or regional comparison. In addition, multiple studies fail to quantify the indirect water consumption of upstream operations such as water consumed during electricity generation [23], [32], [36], which potentially underestimates the total water consumption of the algae to fuels process [34], [38]. More importantly, previous studies do not account for the contribution of rainwater to the WF of algal systems, which is particularly relevant when comparing total water consumption to conventional (terrestrial) biofuel systems. In summary, there is a need for a comprehensive microalga water LCA that establishes a proper comparison to other biofuels and identifies locations in which commercial algal biofuel production will exacerbate local water stress.

Furthermore, TEAs and LCAs of algal biofuels often focus on locations in suboptimal latitudes for algal cultivation, which can underrepresent the sustainability potential of the technology. Although existing studies in the literature have used high-resolution models to understand the productivity potential, resource requirements, techno-economics, or environmental impacts of microalgae-based fuels, these assessments are often limited to a small number of case study locations [39]–[41] or regions with suboptimal climatic conditions for microalgae cultivation such as the United States [23], [42]–[45]. To date, there is only one study that provides a global assessment of the productivity potential of algal fuels [29]. However, this analysis focused on cultivation in closed photobioreactors, which has been proven to be economically unviable for a low-value product such as fuels; but more importantly, this past assessment lacks sustainability modeling. The lack of sustainability data for underexplored potential locations for algal cultivation is a major research gap in the algal biofuel literature.

The work outlined here intends to advance the state of algal research by integrating dynamic growth modeling with sustainability tools for temporally and spatially resolved TEA and LCA. The first part of this work focuses on the development and validation of a highly resolved thermal model for commercial-scale ORPs. The model will leverage experimental temperature data from lab-scale systems for validation and use heat transfer principles to extrapolate results for larger-scale systems. Secondly, the validated model will be used to perform a water LCA that considers freshwater and rainwater consumption, as well as regional water scarcity impacts. By integrating modeling results with two different water LCA methodologies, a complete assessment of the water impacts of algal biofuel production will be provided. Finally, optimal global productivity potential, environmental impacts, and economic viability of algal biofuels are identified by using validated biophysical and sustainability

modeling. Region-specific labor costs, construction factors, and tax rates enable for spatially resolved TEA while the LCA includes regional impacts of electricity, hydrogen, and nutrient markets across ten environmental categories. This work is intended to allow researchers and decision-makers to better understand the advantages and challenges of algal biofuels over conventional fuels from a global environmental and techno-economic perspective.

CHAPTER 2: DEVELOPMENT OF A DYNAMIC OPEN POND THERMAL MODEL FOR COMMERCIAL-SCALE ALGAL PONDS¹

2.1 Introduction

Despite the many advantages of algal biomass, multiple economic and environmental hurdles must be surpassed to achieve large-scale adoption of algal biofuels [46], [47]. A leading environmental challenge is the effect that industrial cultivation of algae will have on water resources. Specifically, the water that must be supplied to make up for evaporation losses in open raceway pond (ORP) systems must be accurately quantified with results used to make informed decisions regarding water scarcity and depletion of freshwater sources. Multiple studies have quantified evaporation losses from ORPs with results ranging from 0.5 to 22.3 m³ m⁻² yr⁻¹ [32], [48], [49]. This variability is primarily attributed to the ¹range of methodologies and assumptions used to estimate evaporation losses [50]. Previous studies often simplify the analysis by using evaporation models that neglect pond temperatures or assume that evaporative behavior in algae ponds follows that of pan or lake evaporation [48], [49], [51]. Other studies provide evaporation estimates through the coupling of evaporation models to dynamic thermal models with high temporal resolution [25], [27], [52]. This methodology is the most appropriate since it captures important geographical and temporal differences in evaporation rates from algae ponds, but an

¹This chapter was published as a peer-reviewed journal article: Quiroz, D., Greene, J. M., McGowen, J., & Quinn, J. C. (2021). Geographical assessment of open pond algal productivity and evaporation losses across the United States. *Algal Research*, 60, 102483. <https://doi.org/10.1016/J.ALGAL.2021.102483>

appropriate selection of the evaporation model and validation data is fundamental to reduce the uncertainty of these assessments [53]. Ultimately, previous studies have not had sufficient data to validate modeling work.

Evaporation from free water surfaces is a function of the water surface temperature and meteorological conditions such as relative humidity, vapor pressure, wind speed, and ambient temperature. Methods for modeling evaporation rates from free water surfaces range in complexity and accuracy [54]. The most simple and inaccurate is the pan evaporation method, but more physically sound models that capture meteorological-based effects have been used in studies focusing on evaporation from algal ponds [50], [52], [53], [55]. These models often rely on empirical equations correlating wind speed to evaporation and are designed to estimate evaporation rates from lakes or cooling ponds [56]–[58]. Béchet et al. [53] reviewed and tested several evaporation models against experimental data measured in a pilot-scale pond and concluded that purely empirical evaporation models fail to accurately predict evaporation rates from algal systems since they were originally validated for water bodies with different spectral characteristics (algae cultures are more opaque), depths, and surface area [53], [59]. However, the model proposed by the Béchet et al. [53] was limited to a range of pond sizes, since the effects of natural convection were not considered. The need to account for both mass transfer modes (natural and forced convection) is crucial when modeling systems with a larger surface area, such as commercial algae ponds, as the evaporation rate is inversely related to the characteristic length of the system [53], [59], [60].

Equally critical is the need to validate thermal models with experimental data relevant to the system properties and scale. Studies in the literature often use observations from elevated experimental algae raceways to validate thermal models, which may provide inaccuracies when

extrapolating results for commercial algae ponds [25], [28]. Khawam et al. [61] demonstrated that the temperature profiles from elevated raceways differ from those in commercial ponds. These variances are fundamentally linked to evaporation effects amplified by the paddlewheel. The additional turbulence and increase of pond surface area caused by the paddlewheel have a direct impact on the evaporation rates of experimental ponds. Therefore, to reduce the uncertainty in the computation of evaporation rates from commercial ponds, evaporation models must be validated at a pond scale where paddlewheel effects are minimal. Wigmosta et al. [52] validated an empirical evaporation model using corrected pan or lake evaporation measurements, however, the water used in pan evaporation has different spectral properties than algae cultures and wind effects are not completely captured due to the small surface area of evaporation pans [50], [53], [62]. In addition, when compared to annual net lake evaporation rates, White and Ryan [15] measured higher evaporation rates from a commercial algae farm located in New Mexico, providing evidence that evaporation rates from algal ponds differ from those of lake systems.

Clearly, there exists a need for a robust temporal and geographical assessment of the evaporation losses from large-scale production of algal biomass. Although Wigmosta et al. [52] provided a novel and thorough outlook on the land and water consumption for large-scale algae farms, the assumptions used result in high uncertainty when estimating evaporation rates at larger scales. This research chapter focused on estimating the evaporation losses of commercial scale cultivation of microalgae through dynamic thermal and biological modeling. The models were developed and validated to predict evaporation rates, temperature profiles, and areal productivity of large-scale systems. The work additionally includes a novel analysis of geographical and seasonal temperature sensitivity which can inform strain optimization studies

and provide insights on productivity maximization methods for open algae cultivation systems. Two different farm scales (400 and 4000 hectares) are modeled with evaporation losses and temperatures for 198 locations across the US over 21 years evaluated. The uncertainties in predicting evaporation losses and pond temperatures using typical meteorological year (TMY) data [63] and actual weather data sets are also analyzed. The discussion focuses on the co-dependence of evaporation, temperature, and growth in algae systems and highlights the importance of accurate co-modeling of these parameters.

2.2 Materials and methods

This study is built upon accurate computations of evaporation losses and biomass production at high temporal and spatial resolutions. Evaporation losses were determined using an energy balance approach through dynamic thermal modeling, while biomass productivity yields were estimated using a coupled thermal and biological growth model [24]. Although both models function as an integrated unit, validation of the thermal and biological model was performed independently using experimental observations for pond temperature, depth, and algal concentration. When coupled with historical meteorological data, model capabilities allow for a geographical and temporally resolved assessment of the evaporation losses associated with commercial-scale algal cultivation in ORPs. The following sections provide detailed descriptions of the thermal model, biological model, validation data, and the simulation approach used in this work.

2.2.1 Thermal model

Thermal modeling is the foundation of this analysis, thus, a high-fidelity thermal model capable of providing accurate simulations of temperature and evaporation rates is essential to

reduce error propagation in subsequent computations. The thermal model used in this study is a modification of the model developed by Greene et al. [25]. The model performs a transient energy balance for an isothermally spatial system to calculate time-resolved thermal outputs based on the algae culture's thermal properties and various heat fluxes driving the thermal behavior of the pond [25]:

$$\rho c_p V \frac{dT_p}{dt} = \sum Q_n \quad (1)$$

where ρ denotes the culture density [kg m^{-3}], c_p is the specific heat of the culture [$\text{J kg}^{-1} \text{K}^{-1}$], V is the pond's volume [m^3], T_p is the temperature of the culture [K], t is the independent time coordinate [s], and $\sum Q_n$ is the sum of the heat fluxes [W]. Heat fluxes include direct and diffuse solar radiation, water inflow, pond radiation, atmospheric radiation, ground conduction, convection, and evaporation. The governing equation was integrated in time using a fourth-order Runge-Kutta method with a fixed time-step of one hour [25].

Primary model inputs include parameters describing the geometry of the pond such as the length, width, and operating depth, and meteorological conditions: global horizontal irradiance (GHI), ambient temperature, relative humidity, and wind speed. To predict accurate evaporation rates and pond temperatures, the following heat transfer models were modified from Greene et al. [25]: atmospheric radiation, ground conduction, convection, and evaporation. The methods selected to model these heat transfer mechanisms are explained in detail in the following sections. Heat transfer models that were not modified are included in Appendix A.

2.2.1.1 Atmospheric radiation

The atmospheric radiation heat flux was found to be a highly sensitive forcing term dependent on the ambient temperature (T_{amb}) and sky emissivity (ϵ_{sky}). The method to

calculate the radiation emitted by the atmosphere to the pond is defined by the Stefan-Boltzmann law:

$$Q_{atmo} = \varepsilon_{sky} \cdot \sigma \cdot A_s \cdot T_{amb}^4 \quad (2)$$

where σ is the Stefan-Boltzmann constant, A_s represents the surface temperature, and T_{amb} is the ambient air temperature [K] [64]. The sky emissivity was calculated using the Brunt equation, previously used for algae pond models by Khawam et al. [65]:

$$\varepsilon_{sky} = a + b \cdot \sqrt{p_a} \quad (3)$$

where a and b are empirical coefficients set to 0.6 and 0.031 [mm Hg^{-0.5}], and p_a is the saturated vapor pressure at the ambient temperature in mm Hg [66].

2.2.1.2 Ground conduction

The conductive heat transfer between the pond and ground plays an important role in lowering pond temperatures during periods of intense solar radiation. Ground conduction is a function of the thermal properties of the soil beneath the pond which include thermal conductivity (k_g), and the thermal diffusivity (α_g). The heat transfer interactions between the pond and ground are calculated using the solution for the heat diffusion equation. This solution assumes a constant pond temperature during the duration of the time-step and takes the form:

$$Q_{ground} = \frac{k_g \cdot A_s \cdot (T_P - T_g)}{\sqrt{\pi \cdot \alpha_g \cdot h}} \quad (4)$$

where T_g is the ground temperature assumed to equal the annual average ambient temperature or the average for the period of the analysis [67]–[69], and h is the time-step of the analysis [69], [70]. The thermal conductivity was empirically calibrated to 1.7 [W m⁻¹ K⁻¹] and the thermal diffusivity was set to 7.9×10^{-6} [m² s⁻¹], in accordance with values in the literature [70].

2.2.1.3 Convection

Convective effects at the pond surface deserve special attention, specifically when modeling ponds with large surface areas. This study uses a semi-empirical flat plate model to calculate heat transfer via convection. Different from other studies, this model accounts for convective effects from both natural and forced convection, which are calculated using correlations that relate the size of the system to the wind speed (forced convection) and density gradient (natural convection). To simplify model operations, the effects of wind direction were not considered by defining the characteristic length of the system to be the ratio of surface area to perimeter of the pond. The forced convection model is taken directly from Greene et al. [25], while natural convection effects are calculated using the following Nusselt number correlations for the laminar and turbulent regime, respectively:

$$Nu_L = x \cdot Ra_L^{1/4} \text{ for } (10^4 \leq Ra_L \leq 10^7, Pr \geq 0.7) \quad (5)$$

$$Nu_L = y \cdot Ra_L^{1/3} \text{ for } (10^4 \leq Ra_L \leq 10^{11}, Pr \geq 0.7) \quad (6)$$

where x and y are empirical coefficients set to 0.54 and 0.15, and Ra_L is the dimensionless Rayleigh number [69]. In the case where mixed natural and forced convection effects are present, the following correlation was used:

$$Nu_L = (Nu_{L,f}^n + Nu_{L,n}^n)^{1/n} \quad (7)$$

where $Nu_{L,f}$ and $Nu_{L,n}$ are the Nusselt numbers obtained from the forced and natural convection correlations, and n is an empirical coefficient set to 3 [69]. Forced convection correlations and convective heat flux equations are further described in Appendix A.

2.2.1.4 Evaporation

As previously mentioned, the selection of an appropriate evaporation model is paramount to produce robust evaporation estimates. The mass transfer correlations used to model evaporation are analogous to the convection correlations presented in the previous section. Similarly, both mass transfer from forced and natural convection were considered. The main advantage of this evaporation approach over others in the literature is the use of nondimensional parameters which provide a method to scale up results from pilot-scale ponds to commercial ponds. Additionally, by separating the forced and natural convection components, the appropriate accounting of both transport phenomena is ensured. Methods to model evaporation from forced convection effects followed the ones used in Greene et al. [25]:

$$Sh_L = c \cdot (Re_L)^{0.5} (Sch_L)^{\frac{1}{3}} \quad \text{for } Re_L < (3 \times 10^5) \quad (8)$$

$$Sh_L = d \cdot (Re_L)^{0.8} (Sch_L)^{\frac{1}{3}} \quad \text{for } Re_L > (5 \times 10^5) \quad (9)$$

The empirical coefficients c and d were calibrated to 0.65 and 0.045, respectively. The natural convection correlations for mass transfer have the form of Eqs. (5,6), previously defined by Lloyd et al [71]:

$$Sh_L = x \cdot Ra_L^{\frac{1}{4}} \quad \text{for } (2.2 \times 10^4 \leq Ra_L \leq 8 \times 10^6) \quad (10)$$

$$Sh_L = y \cdot Ra_L^{\frac{1}{3}} \quad \text{for } (Ra_L > 8 \times 10^6) \quad (11)$$

where Sh_L is the dimensionless Sherwood number [72]. The approach for mixed mass transfer follows that of Eq. (7), substituting the Nusselt number for its mass transfer counterpart, the Sherwood number. Once the Sherwood number is defined, the evaporation rate m_e [kg m⁻² s⁻¹] can be determined:

$$m_e = \frac{Sh_L \cdot D_{w,a}}{L_c} \cdot \left[\frac{p_w}{T_p} - \frac{RH \cdot p_a}{T_{amb}} \right] \cdot \frac{M_w}{R} \quad (12)$$

where $D_{w,a} = 2.4 \times 10^5$ [m² s⁻¹] denotes the mass diffusion coefficient of water vapor in the air, L_c is the characteristic length [m], RH is the relative humidity of the ambient air, $R = 8.314$ [Pa m³ mol⁻¹ K⁻¹] is the ideal gas constant, and p_a and p_w [Pa] are saturated vapor pressures at T_{amb} and T_p , respectively [25], [31], [50]. The heat transfer is then calculated using the following equation:

$$Q_{evap} = -m_e \cdot L_w \cdot A_s \quad (13)$$

where $L_w = 2.45 \times 10^6$ [J kg⁻¹] is the latent heat of the water.

2.2.2 Biological model

To determine microalgal biomass yields, this study adopted the biological modeling methodology developed by Greene et al. [25]. This model calculates algae growth based on the primary physical processes affecting growth: culture temperature, respiration losses, and light availability impacted by culture concentration and incoming solar radiation [25]. The model correlates a carbon fixation rate to multiple efficiency factors which serve to account for conditions deviating from optimal. The rate of bulk algal concentration is calculated using the following equation:

$$\frac{dC_x}{dt} = \frac{C_1 \cdot 0.458 \cdot GHI \cdot \varphi_L(t) \cdot \varphi_T(t) \cdot \Phi_{photon} \cdot A}{V} + \frac{D(t)}{V} \quad (14)$$

where $C_1 \cdot 0.458 \cdot GHI$ represents the conversion from GHI to photosynthetically active radiation (PAR) in the 400-700 nm range, Φ_{photon} is the photon efficiency in terms of grams of biomass per mol photon, A is the surface area of the pond, V is the volume of the pond, $D(t)$ is

the decay rate quantifying biomass losses from dark respiration, φ_L and φ_T are the light and temperature efficiencies, respectively [25].

The calculation of algal growth begins by defining a carbon to photon conversion factor, which has a value of 1.5 [g biomass per mol photon] [25]. The model proceeds to quantify temperature effects on carbon fixation through a cardinal temperature model. This temperature model requires the input of four parameters describing the temperature response of the organism: minimum and maximum temperatures tolerated by the microalgae strain, the optimal temperature for growth, and the pond temperature (provided by the thermal model). The light efficiency component considers photoinhibition and concentration effects of the algae culture to provide a light efficiency ranging from zero to unity. Concentration effects are quantified using a depth-integrated Beer-Lambert's law and the assumption that the culture is well-mixed [25]. To calculate light response effects, two specific-strain parameters must be defined: the optical density coefficient (defined as the slope of the curve comparing biomass concentration [g m⁻³] and the optical density [OD₇₅₀]) and the saturation light intensity. The optical density coefficient was experimentally determined to 0.38 m⁻¹ while the saturation light intensity was calibrated to 480 μmol m⁻² s⁻¹ based on experimental data from existing studies [73]–[75]. The final foundational input of the growth model is the percent of biomass lost during dark respiration, which was estimated based on experimental data from Edmundson et al. [76], used along the temperature efficiency factor to compute the decay rate [25]. After a complete species characterization is achieved, the model proceeds to calculate the time-resolved culture concentration. Further details are presented in Greene et al. [25].

2.2.3 Thermal and biological model validation

Experimental data was leveraged to validate both the thermal and biological models. The thermal model was validated with data from the literature. Temperature and pond depth observations measured by Béchet et al. [53] in their comparison study were used to assess the model's accuracy. To the authors' knowledge, the data set used by Béchet et al. [53] is the most detailed collection of parallel temperature and pond depth measurements from a pilot-scale ORP system in the literature. Similarly, the growth model was validated with algal concentration data from the trials performed at the Arizona Center Algae Technology and Innovation (AzCATI). The growth model validation data includes on-site measurements of PAR, pond temperature, and algal concentration for an elevated experimental ORP. Both tools were verified and validated separately to provide an unbiased assessment of model quality.

Thermal validation data included all foundational inputs required to compute simultaneous pond temperatures and evaporation rates at an hourly resolution. As detailed by Béchet et al. [53], the pond used for this analysis was refilled regularly during the first half of the study and left to evaporate during the latter trials. The data set was reduced by eliminating periods where either evaporation or temperature measurements seem to vary (likely due to instrumentation issues, pond harvesting, or rainfall events) resulting in a total validation period of 314 days. Rainfall events were considered of low impact and were not included in the thermal balance calculations. Model inputs with the highest uncertainty were used to calibrate the model. Among these parameters are the soil properties, absorptivity and emissivity of the culture, and the empirical coefficients of the convection and evaporation correlations. These parameters were bounded by retrieving minimum and maximum values from the literature. The final calibrated values were chosen by simultaneously minimizing the evaporation and temperature error through

the entire validation period using a multi-objective optimization algorithm in MATLAB®. It is important to point out that due to a lack of temperature and depth data, the model was not further validated with an unbiased dataset. The temperature error was calculated by comparing the hourly modeled to the hourly measured pond temperatures. The evaporation error is reported using two different metrics. The error is first reported as the relative mean percentage error obtained from comparing the hourly modeled to the measured pond depth. In addition, as a means to compare to previous studies, the evaporation error was also calculated by comparing the total modeled evaporated depth during the validation period to the total measured evaporated depth, following the methods in Béchet et al. [53].

Similarly, the growth model was validated with experimental data collected in the summer of 2019 from growth experiments of *Acutodesmus obliquus* (UTEX 393) grown at AzCATI in Mesa, AZ (33.41° N, 111.83° W). This data set represents current experimental values of outdoor cultivation in pilot-scale systems and illustrates performance improvements over the validation data used by Greene et al. [25]. Three elevated experimental ponds, each with a surface area of 4.2 m² and a volume of 820 L, were operated semi-continuously at a depth of 20 cm. The culture was grown in BG-11 media with ammonium bicarbonate as the N-source and a 16:1 N:P ratio with 5 ppt salinity. Algal concentration was measured in triplicates during the morning and afternoon. Simultaneous measurements of pond temperature and PAR were collected on-site. The selected data were collected from June 2019 to August 2019 resulting in a total of 24 harvests, from which three were discarded based on a statistical analysis of the grams to PAR ratio for that period. Experimental pond temperature and PAR were input into the growth model along with six model inputs characterizing the strain, listed in Appendix A. The model

was calibrated with half of the data set and validated with the remaining harvests. The error was calculated by comparing the measured algal concentration to the modeled output.

2.2.4 Simulation framework

The simulation approach used in this study integrates the validated thermal and growth model with historical meteorological data and a harvesting scheme to predict pond temperatures, evaporation losses, and biomass yields. Thermal simulations were done for two different algae farm sizes with weather data from two different sources, resulting in a total of four scenarios. Results for each of the selected locations were generated in MATLAB® and spatially interpolated in R using kriging interpolation to cover the contiguous United States (CONUS) and Hawaii. Simulation outputs include heat maps illustrating regional variances in evaporation loss and maximum pond temperatures.

2.2.4.1 Meteorological data

Historical weather data comprising of hourly measurements of solar radiation, wind speed, relative humidity, and air temperature were retrieved from the National Solar Radiation Data Base (NSRDB) [77] and the typical meteorological year (TMY3) files from the National Renewable Energy Laboratory (NREL) [78]. The NSRDB files contain data from 1998 to 2018 from 198 locations across the U.S. Each of the locations was simulated by resetting the model at the start of each year. The TMY3 files are comprised of hourly data from 903 locations in the US. Results generated from the two data sets were compared to assess if the analysis could be simplified by using TMY3 data without a significant loss in accuracy.

2.2.4.2 Facility design and operation

Results for two different farm sizes were generated to gain a better understanding of the implications of facility size on evaporation losses. The baseline scenario models an algae farm with an area of 400 hectares, based on TEA and resource assessment (RA) models in literature [52], [79]–[83]. The second scenario considers a 4000-ha farm sized according to projected biomass requirements by downstream conversion processes [19], [84], [85]. To simulate real-time facility operations, the growth model was coupled with a dynamic harvesting scheme. Ponds were assumed to be operated semi-continuously with an initial concentration of 0.1 g L^{-1} . Harvesting was assumed to occur at the first of either achieving 0.45 g L^{-1} or 3 days from system inoculation.

2.2.4.3 Temperature tolerance

Pond temperatures have been shown to have an important impact on the growth rates, reliability, composition, and overall performance of algae species grown in ORPs [16], [65], [86]–[88]. Therefore, a comprehensive understanding of the temperature limits of commercial ORPs is not only critical for the appropriate siting of algae cultivation facilities but also to support strain selection decisions. This study provides temperature profiles of commercial ORPs computed with historical weather data and a validated thermal model designed to predict temperatures in commercial ORPs. The temperature profiles for the 400-ha baseline scenario were processed to determine the maximum temperatures for three different time intervals: a one-hour, two-hour, and three-hour culture exposure. Moreover, simulated pond temperatures for five distinct locations were examined to identify seasonal and geographical trends based on descriptive statistics. Results from the temperature tolerance assessment include dynamic maps illustrating maximum temperatures reached in commercial algae facilities and a geographical and

temporal comparison of pond temperatures of commercial-scale facilities. Finally, the interactive effects of temperature and exposure time to avoid temperature-related culture crashes were investigated.

2.3 Results and discussion

The results of this research chapter are presented in three different sections, 1) results obtained from the validation of the thermal model including error in the predicted temperature and evaporation rates, 2) results and errors associated with the validation of the biological model, and 3) results obtained from the simulation process including national productivity yields and temperature tolerance analysis.

2.3.1 Thermal model validation

The thermal model validation process quantifies the model's ability to simultaneously predict pond temperatures and evaporation rates accurately. The error was quantified by comparing a total of 7,525 data points. Plot regressions illustrating model accuracy are presented in Figure 1. The temperature accuracy shows an average error of -0.96 ± 2.72 °C, consistent with values reported in the literature for previous validation efforts [24], [40], [62]. The highest average temperature errors were seen in the winter and spring season, where lower temperatures were predicted. The lower modeled temperatures during these months are an effect of the overprediction of evaporative cooling. Furthermore, wind speed measurements were the highest during the spring and winter months, as seen in Figure A - 1; this likely indicates that temperature errors are directly correlated to evaporative effects.

The average annual evaporation error was calculated to be 1.46 ± 5.92 %. In terms of the total evaporated depth, the model demonstrated an overall under-prediction of 20.2 %, which is

within the range reported by B chet et al. [25]. The winter and summer seasons presented the highest evaporation errors of $5.69 \pm 3.71 \%$ and $-3.24 \pm 4.7 \%$, respectively. Wind speed data was found to be the primary driver of evaporation error. The error seen during the winter months is linked to high wind speeds and lower relative humidity conditions during these months. Similarly, the summer error was also found to be highly correlated to wind speed measurements. Pond temperatures increased over periods of low wind speeds, causing the model to underestimate evaporative cooling effects (see Figure A - 4). These thermal validation results highlight the importance of accurate wind speed measurements to reduce the uncertainty in predictions of evaporation rates. The data from the seasonal analysis of the validation effort and time-series for both temperatures and pond depths are shown in Appendix A.

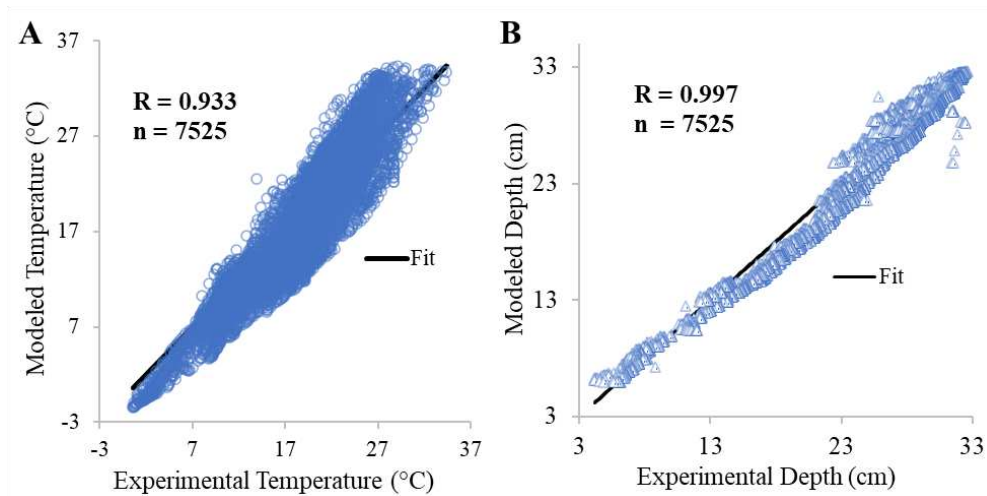


Figure 1. Modeled versus experimental pond (A) temperature and (B) depth. Average annual temperature error: $-0.96 \pm 2.72 \text{ }^\circ\text{C}$. Average annual evaporation error: $1.46 \pm 5.92 \%$. Although a high R-value was obtained from the evaporation model, a 20.2 % error was calculated when comparing the total measured and modeled evaporated depths during the validation period.

2.3.2 Biological model validation

The growth model validation in this study quantifies the predictive error and evaluates the model's performance in simulating growth rates of UTEX 393. Experimental and modeled biomass concentration (AFDW) for the validation data set is illustrated in Figure 2. The model

provided accurate predictions of concentration over the simulated period with an average relative error of $-4.59 \pm 8.13 \%$. The error from the biological model is within the range of previously reported values for this specific strain [89]. When comparing the areal productivity for the summer 2019 growth campaign, the model calculated areal productivity of 27.7 g per m²-day, which translates to an underestimating error of 1.82 %.

In addition, this predictive error was found to be highly sensitive to the strain's saturation light intensity. UTEX 393 is considered an all-season strain with peak performance occurring in the summer months. The biological model was not coupled with the thermal model for validation given that the temperature profiles of the systems used for thermal and biological validation are different due to system differences (the experimental system is an elevated small-scale pond). Growth data was obtained from experimental ponds where the paddlewheel enhances evaporative cooling. Determining temperature with the current thermal model would have introduced unnecessary error since the model was not built to capture paddlewheel effects.

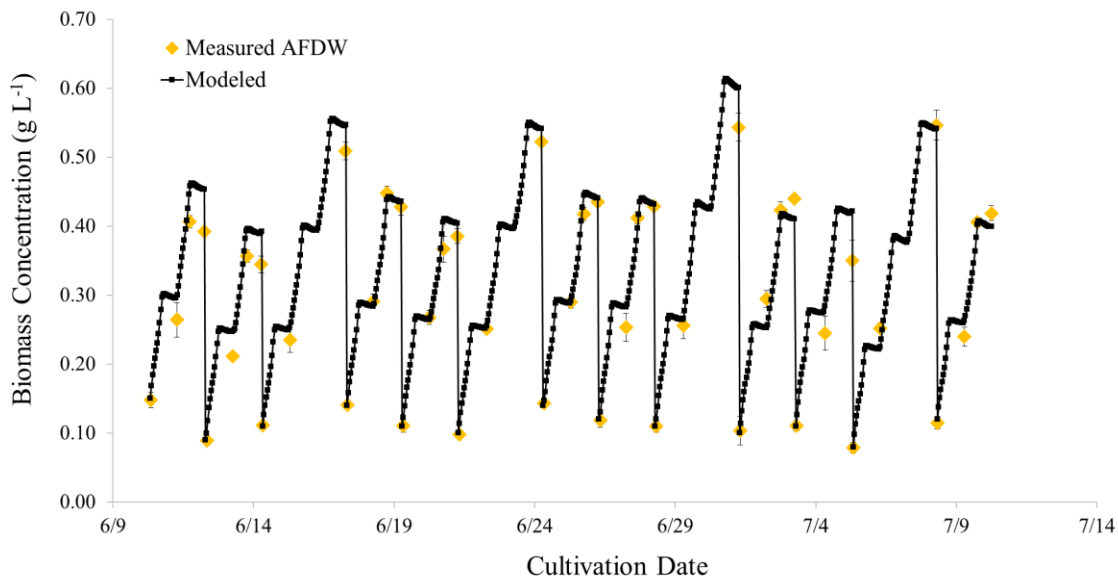


Figure 2. Biological model validation for the summer 2019 runs of *Acutodesmus obliquus* UTEX 393. A total of 12 harvests were simulated, the initial biomass concentration for each of the semi-continuous runs was set to the respective concentration in each

run. Error bars on the measured data represent the standard deviation of the algal concentration of 3 different ponds. The biological model showed an average error of -4.59 ± 8.13 %.

2.3.3 Model extrapolation

The following section presents the results generated from the simulations conducted with the coupled thermal-biological model. The results from the model extrapolation effort are divided into three sections: (i) evaporation losses, (ii) temperature tolerance, and (iii) microalgae productivity.

2.3.3.1 National evaporation losses

The evaporation losses for the different combinations of weather data sets and facility scales were determined and leveraged to identify regions with the highest evaporation rates for algae cultivation. Results for the baseline scenario of a 400-ha facility generated with weather data from the NSRDB are illustrated in the form of a dynamic map covering the CONUS and Hawaii. As depicted in Figure 3, marked regional differences exist when it comes to evaporation losses. As expected, evaporation losses are the highest in the desert south-west region, where high light intensity and dry conditions predominate. Annual evaporation losses reached a maximum of $1.68 \text{ m}^3 \text{ m}^{-2} \text{ yr}^{-1}$ in this area. The Gulf Coast region and Hawaii, where more humid conditions are present, land on the middle to lower range of the spectrum. The lowest evaporation losses are seen at the northern latitudes where lower temperatures and light intensity predominate. A national annual mean of $0.74 \text{ m}^3 \text{ m}^{-2} \text{ yr}^{-1}$ was determined.

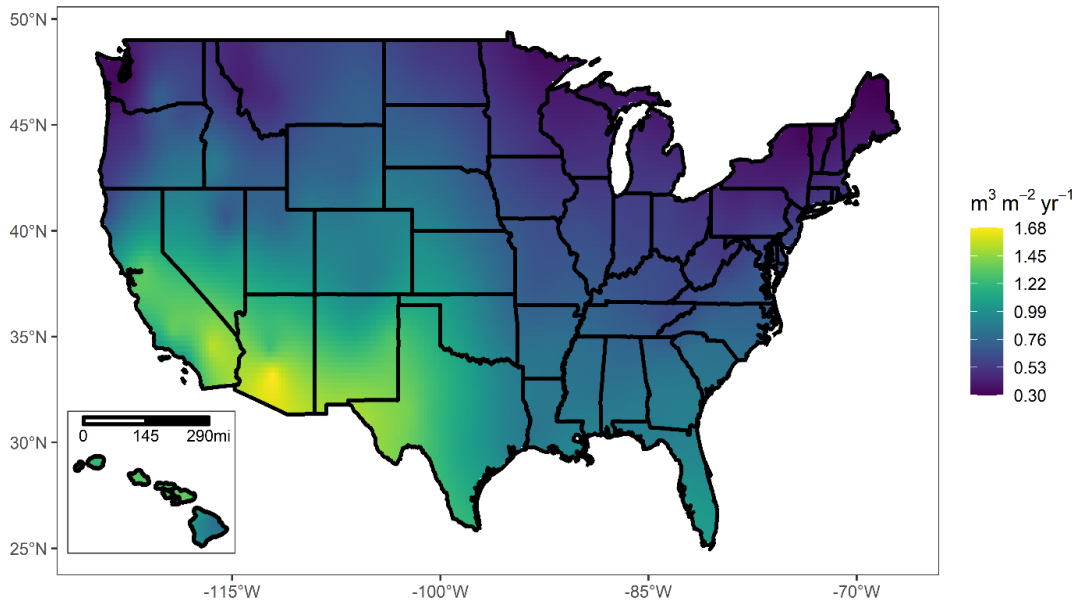


Figure 3. Mean annual evaporation losses ($\text{m}^3 \text{m}^{-2} \text{yr}^{-1}$) for a 400-ha cultivation facility calculated with weather data from the NSRDB. Results represent the annual mean of 21 years (1998-2018). A national average of $0.74 \pm 0.29 \text{ m}^3 \text{m}^{-2} \text{yr}^{-1}$ was calculated.

Compared to the literature, the evaporation losses calculated in this study follow the same geographical trends provided by Guieysse et al. [32] but with key differences in the upper and lower limits. The differences between these values are expected and can be attributed to the scale of the system that was modeled (400 ha in this study vs pilot-scale in Guieysse et al. [32]) and the accounting of natural convection mass transfer in this work. For example, when comparing evaporation losses in arid climates, this study calculated a maximum of $1.68 \text{ m}^3 \text{m}^{-2} \text{yr}^{-1}$, while Guieysse et al. [32] estimated a value of $2.27 \text{ m}^3 \text{m}^{-2} \text{yr}^{-1}$, a 35% reduction. On the other hand, accounting only for forced convection mass transfer in tropical weathers can systematically introduce error in the evaporation losses of these regions since higher humidity and lower wind speeds make natural convection the dominating mode of mass transfer. When comparing evaporation losses in Hilo, HI, results indicate evaporation losses for a 400-ha facility equal to $0.81 \text{ m}^3 \text{m}^{-2} \text{yr}^{-1}$, this represents a 69% increase from the value of $0.48 \text{ m}^3 \text{m}^{-2} \text{yr}^{-1}$ computed by Guieysse et al. [32]. Results in Merced, California follow those previously modeled in the

literature ($1.33 \text{ m}^3 \text{ m}^{-2} \text{ yr}^{-1}$ in this study vs $1.32 \text{ m}^3 \text{ m}^{-2} \text{ yr}^{-1}$ in Guieysse et al. [32]) and evaporation losses in Sebring, Florida resulted in a 10% reduction, from $1.15 \text{ m}^3 \text{ m}^{-2} \text{ yr}^{-1}$ estimated by Guieysse et al. [32] to $1.03 \text{ m}^3 \text{ m}^{-2} \text{ yr}^{-1}$ calculated in this study. This comparison indicates that differences in evaporation losses due to pond scale and natural convection effects are higher in arid and tropical climatic zones, while less significant in locations representing Mediterranean and sub-tropical climates.

Additionally, historical pan evaporation data curated by Dewes et al. [90] was used to approximate the differences in evaporation losses from commercial microalgae ponds and pan evaporation measurements. Evaporation losses results were found to be significantly lower than pan evaporation measurements with an average absolute difference of 59%. For corrected pan evaporation or lake evaporation, this average reduces to 45%. These variations decreased at locations with lower wind speeds, implying that pan evaporation methods fail to capture wind effects present at commercial-scale algae ponds. The data demonstrates that the differences in depth and surface area of these systems make pan evaporation data inadequate to model evaporation from commercial algae ponds.

The additional scenario modeled with weather data from the NSRDB provided further evidence of the interconnection between wind speed, surface area, and the magnitude of evaporation losses. When comparing evaporation losses from the 4000-ha facility scenario to the previously simulated 400-ha sized facility, the calculated annual evaporation losses decreased by an average of 4%. Considering the error associated with predictions, the results indicate that evaporation losses are not significantly impacted by scale within the range considered, however, there is a marked difference between evaporation rates of pilot-scale and commercial systems primarily attributed to the surface area of the systems. As the area of the facility increases, the

effects of wind speed are less relevant since evaporation is primarily driven either by a combination of forced and natural convection (mixed convection) or purely by buoyancy effects. Changes in evaporation losses were the lowest in locations with low wind speeds as shown in Fig. A - 13. These results show that evaporation rates at the 400-ha scale are representative of larger-scale systems.

Evaporation results were also compared to simulations with TMY3 data. Results generated with the TMY3 data set follow the same regional trends, but with a wider range for both facility sizes. The difference in evaporation losses between the 400-ha and 4000-ha for the TMY scenario is more pronounced than those computed with weather files from the NSRDB. Results generated with TMY3 data show a 14% reduction in the evaporation losses of a 4000-ha compared to a 400-ha facility, which is more than three times higher than what was found with weather data from the NSRDB (4%). This difference is higher than the results calculated with the NSRDB files due to the low accuracy of wind speed measurements in TMY3 files. TMY3 data was originally developed to mimic typical conditions for solar radiation measurements and assigns lower weights to wind speeds, which might contribute to propagating error in the evaporation calculations. This is confirmed by observing the results from the weather data comparison. The average absolute difference in evaporation losses between the results generated with TMY3 and NSRDB files for a 400-ha facility was calculated to be 16% (Fig. A - 17). For a system size of 4000-ha, the average difference in evaporation losses decreases to 8% (Fig. A - 18) attributed to the small influence of wind speeds at this scale. These results indicate that accurate evaporation modeling requires robust wind speed data.

2.3.3.2 Temperature tolerance evaluation

The performance of commercial outdoor algae cultivation is heavily influenced by the thermal conditions of the culture. Since pond temperatures are also dependent on the magnitude of evaporative effects, co-modeling of pond temperatures and evaporation at a high temporal and spatial resolution are needed to gain an accurate and in-depth understanding of temperature profiles of commercial-scale facilities. The computed pond temperatures for the entire simulation period were processed to analyze seasonal and geographical trends.

The maximum temperatures that a specific strain will tolerate to avoid culture failure for one hour are illustrated in Figure 4. As it is readily visible in Figure 4, the highest summer temperatures are observed in the southern latitudes, where temperatures exceed 40°C. The analysis was also extended to a maximum temperature exposure or tolerance of two and three hours. The average variation between the one-hour and two-hour temperature tolerance was 0.4°C. When comparing the one-hour and three-hour scenarios, a larger difference of 1.4°C was calculated. These results can support informed decisions on strain selection and potential facility sites. For example, a strain grown in Phoenix, AZ must have a one-hour temperature tolerance of 44.6 °C and tolerate temperatures above 43°C for three consecutive hours of culture exposure while a strain grown in Lexington, KY must tolerate a one-hour exposure of 38.9 °C and a three-hour temperature tolerance of 37.4 °C.

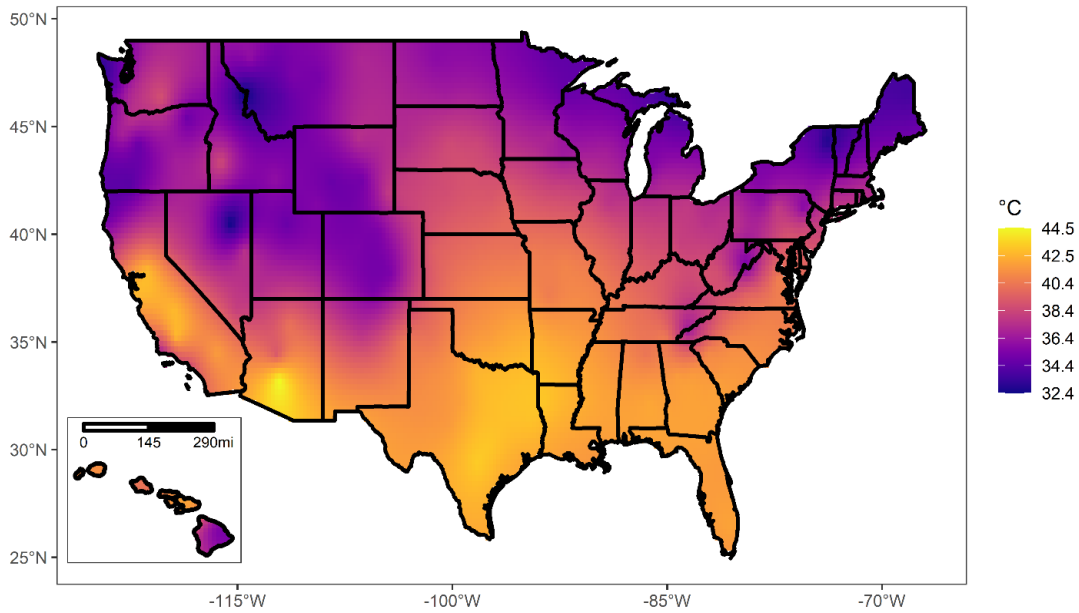


Figure 4. Mean maximum pond temperatures for the CONUS and Hawaii for a 400-ha facility. The illustrated temperatures are the one-hour temperature that must be tolerated to avoid culture crashing. Results represent the annual mean of 21 simulated years (1998-2018).

Although a marked distinction exists between the southwestern and Gulf Coast regions in terms of evaporation rates, this is not the case for their temperature profiles and a similar range of maximum temperatures was found in both regions. This difference is explained by examining the parameters with the highest impact on the heat fluxes which influence pond temperatures. Evaporation rates were highly sensitive to wind speeds and relative humidity conditions, similarly temperature profiles are also influenced by ambient temperatures and solar radiation. For instance, ambient temperature is higher in the desert southwest, but the low relative humidity enhances evaporative cooling consequently decreasing pond temperatures. On the other hand, pond temperatures in the Gulf Coast region are closer to ambient conditions due to the high humid conditions in the region.

When expanding the facility size, a relatively low increase in temperatures was observed for results generated with both weather data sets. The average temperature difference between

the 400-ha and 4000-ha using weather data from the NSRDB increased by 1% (Fig. A - 30). Similarly, the difference for the TMY3 case was calculated to increase by 3% (Fig. A - 32). Results reflect that a relatively low error is introduced when computing temperature profiles with TMY3 data as opposed to the error observed in the prediction of evaporation losses. The low variance is linked to the fact that TMY3 files do provide proper solar radiation and ambient temperature measurements, in contrast to wind speed data. The average temperature difference between the results generated with TMY3 and NSRDB weather data for a 400-ha and 4000-ha facility was calculated to be 4% and 3%, respectively (Fig. A - 33 and Fig. A - 34). Considering model uncertainty, the differences in temperature between scales at this range are not statistically significant but illustrate that temperature profiles of smaller ponds (e.g. pilot-scale) could differ to those of commercial-scale systems.

The variances in temperature profiles between system scales are likely linked to the reduction in evaporation rates as pond area increases. The calculated temperatures were found to be higher when compared to those measured in experimental raceways (summer maximum of ~35°C in Mesa, AZ) [86]. To emphasize the impact of scale, temperature profiles for the 400-ha scale were also compared to those of a 100 m² pond previously modeled in the literature [17]. The total hours per year that temperatures exceeded 35°C or the “temperature risk factor (TRF)”, a metric previously used in the literature to quantify overheating risks, was used for comparison. For instance, we estimated an average TRF of 175 hr yr⁻¹ in Tampa, FL while Béchet et al. [17] reported a value of approximately 168 hr yr⁻¹ for Sebring, FL. The variation in results was found to be higher for arid climates, where the average TRF for Phoenix, AZ was calculated to be 231 hr yr⁻¹ and Béchet et al. [17] estimated a value of 150 hr yr⁻¹ [17]. The comparison to the

literature indicates that temperatures of larger systems could potentially exceed those measured at pilot or experimental scale.

Additionally, a more in-depth seasonal and geographical assessment of pond temperatures was performed. Descriptive statistics of pond temperature data corresponding to five case studies spanning the 21-year simulated period are shown in Figure 5. The seasonal variability results demonstrate the importance of high temporal resolution in temperature modeling. Results allow the identification of subtle differences among locations and seasons. The first thing to note is the similarities in temperature ranges but differences in the spread of temperatures when comparing Baton Rouge, Phoenix, and Tampa. For example, the median temperature during spring and summer at these three locations is approximately the same, but temperatures in Baton Rouge and Tampa are much closer to the median. Selecting strains with optimal temperatures around the median will have a more advantageous effect in Baton Rouge and Tampa than in Phoenix, where temperatures are more dispersed around the median. This is demonstrated by the high productivity results from Lihue, where the range and dispersion are smaller than all the other locations for the four seasons and the seasonal variability is minimal.

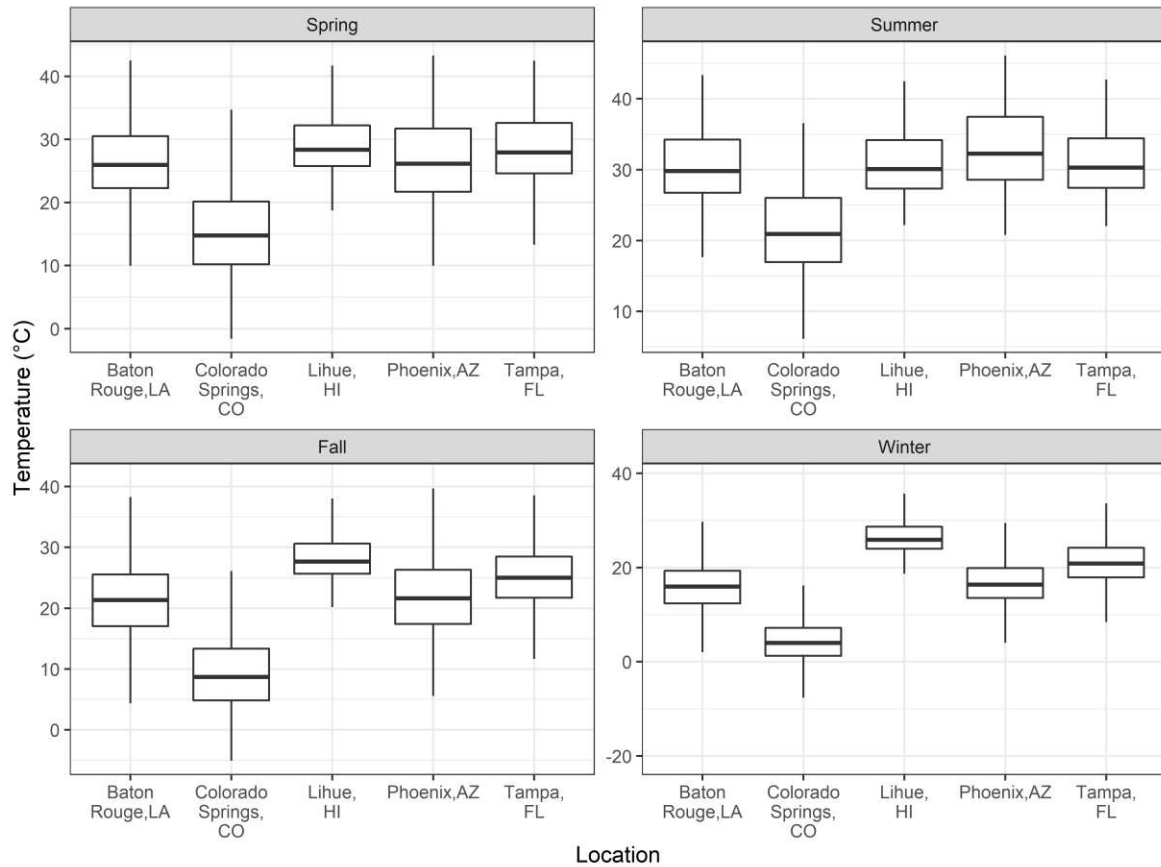


Figure 5. Mean seasonal temperature profiles for the 21-year simulation period for five distinct locations across the US. The boxes represent the interquartile range, outliers are not included.

Furthermore, when observing locations like Colorado Springs, temperatures during the spring, fall, and winter render open cultivation unproductive. Successful biomass cultivation at regions with this temperature profile will require the incorporation of temperature-regulated systems. Another alternative is varying the culture's depth as a temperature regulation strategy. This strategy is supported by temperatures in thinner cultures being significantly higher. Depth control as an optimization strategy has been previously discussed in the literature and it cannot only enhance productivity but can also impact water consumption metrics, depending on the cultivation strategy of the pond and climatic location [17], [89].

Results highlight the importance of temperature on the outdoor cultivation of biomass in ORPs. More importantly, the data indicates that the temperatures measured in elevated raceways

are not representative of commercial-scale ORPs. The temperatures calculated in this study are significantly higher than those seen in experimental trials of elevated raceways [86]. Given the importance of temperature on algal growth, it is important to establish accurate temperature profiles of commercial ponds and understand the effects on the economics and operations of algal facilities. Future research will focus on the integration of these temperature profiles with strain-specific temperature crashing models to understand geographical differences in the operational days of algae facilities.

2.3.3.3 Geographically resolved biomass productivity

Areal productivity yields from semi-continuous cultures of UTEX 393 were computed to provide a national landscape of the current productivity potential. The computed annual biomass productivity values of the simulated locations were averaged, and surface interpolated to define the optimal areas for algae cultivation based on the algae growth model. The outputs are illustrated in the dynamic map shown in Figure 6. The maximum biomass yields are located in Hawaii and Key West, FL reaching annual yields above $23 \text{ g m}^{-2} \text{ day}^{-1}$. In the case of the Southwest region, outputs show that productivities above $15.5 \text{ g m}^{-2} \text{ day}^{-1}$ can be attained with moderate seasonal variability. Seasonal variability at middle latitudes is more pronounced. For example, facilities in northern Nevada presented summer biomass yields above $14.2 \text{ g m}^{-2} \text{ day}^{-1}$, but biomass productivity during the fall and winter months was substantially lower due to temperature effects resulting in an annual average productivity of $7.5 \text{ g m}^{-2} \text{ day}^{-1}$. Results suggest that reducing seasonal variabilities in middle and northern latitudes would require temperature regulation strategies or strains with a wider temperature tolerance.

The results represent an optimistic scenario of biomass production based on model extrapolation from elevated raceways operated at Mesa, AZ and uncertainties in these

calculations are anticipated since the model was validated with data for a particular location and season. The modeled annual-average productivity of $18.1 \text{ g m}^{-2} \text{ day}^{-1}$, at this location, was calculated to be 14 % higher than the annual average of $15.9 \text{ g m}^{-2} \text{ day}^{-1}$ obtained from cultivation experiments [91]. These productivity differences are likely associated with the differences in temperature profiles of elevated raceways to commercial ORPs. The predicted open pond productivities provide a general outlook of the current biomass production potential at a national scale and illustrate the gap between the current achievable performance in pilot-scale systems (national annual average of $12.5 \text{ g m}^{-2} \text{ day}^{-1}$) and the commercial annual average target of $25 \text{ g m}^{-2} \text{ day}^{-1}$, typically modeled in sustainability assessments [22], [92], [93].

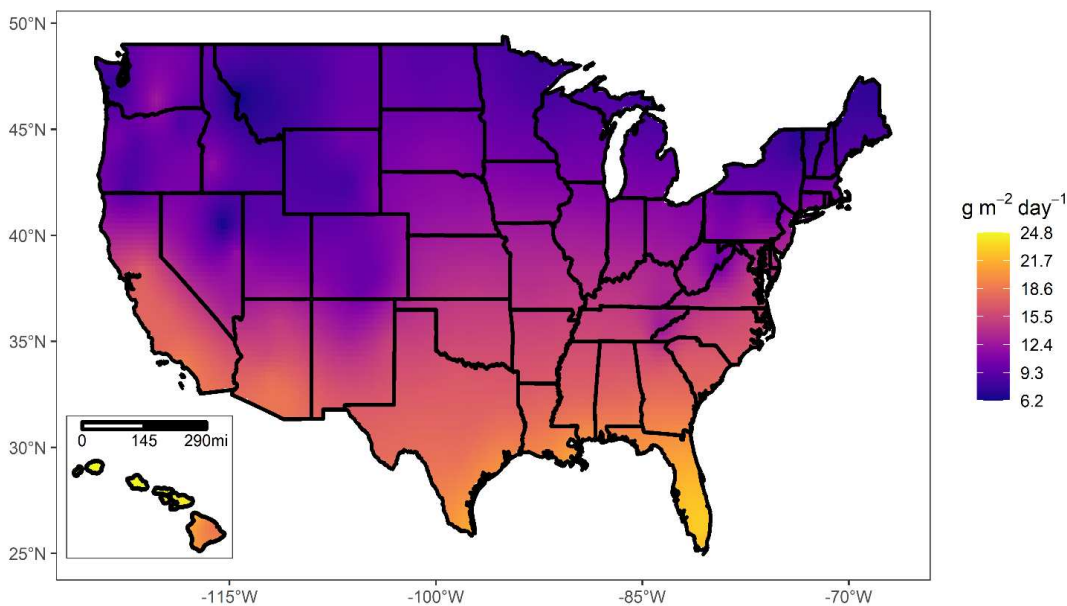


Figure 6. Mean annual biomass productivity ($\text{g m}^{-2} \text{ day}^{-1}$) yields of *Acutodesmus obliquus* (UTEX 393) for the conterminous US and Hawaii. Results represent the annual mean of 21 simulated years (1998-2018) using the computed temperature profiles of a 400-ha facility. A national annual mean of $12.1 \text{ g m}^{-2} \text{ day}^{-1}$ was calculated.

2.4 Conclusions

This study provides a robust assessment of the evaporation losses of commercial-scale algae cultivation for conventional algae systems using a validated model with an average temperature predictive error of $-0.96 \pm 2.72 \text{ }^\circ\text{C}$ and evaporation accuracy of $1.46 \pm 5.92\%$. A

validated biological model with an error of $-4.59 \pm 8.13\%$ was used to calculate areal productivities. The model was leveraged with historical weather data to provide a temporal and geographical assessment of the evaporation losses, temperature, and productivity potential. Results highlight the interactions between geographic inputs and facility sizes on temperature profiles and evaporation losses of algae farms. Accurate prediction of evaporation rates requires high-quality weather data, specifically wind speed measurements, while the temperature profiles are more sensitive to temperature and solar radiation parameters. Appropriate selection of the evaporation model is of equal importance as the evaporation model must capture the effects of pond size to reduce the uncertainty in these calculations. This study also incorporates a novel outlook on the temperature tolerances needed for cultivation in commercial-scale open systems.

CHAPTER 3: LIFE-CYCLE WATER ASSESSMENT OF MICROALGAL-BASED BIOFUELS IN THE UNITED STATES²

3.1 Introduction

While algal biofuels have the potential to reduce the national reliance on fossil fuels, high water consumption associated with algal biomass cultivation represents a major concern potentially compromising the sustainable commercialization of this technology. Although there are multiple life-cycle assessments (LCA) focused on algal biofuels in the literature, the lack of freshwater consumption impacts represents a major research gap in the field [22]. Understanding the added water demand that algal cultivation will have on local water sources is paramount to avoid future water-related risks, particularly when the cultivation of algal biomass is envisioned to be deployed in locations that are experiencing considerable water shortages such as the southwest U.S. [94]. Water consumption is often measured using a WF methodology, where the WF of a product is the sum of direct and indirect water consumption [95]. More recently, a new method to assess the WSF of a product has been proposed by the Water Use in LCA (WULCA) research group [96]. The Available Water Remaining (AWARE) is a consensus-based model

²This chapter was published as a peer-reviewed journal article: Quiroz, D., Greene, J. M., & Quinn, J. C. (2022). Regionalized Life-Cycle Water Impacts of Microalgal-Based Biofuels in the United States. *Environmental Science and Technology*, 56(22), 16400–16409. DOI: 10.1021/acs.est.2c05552

used to determine a WSF based on a characterization factor that quantifies water availability and demand in a specific region over a set timeframe [97].

In previous assessments, the water consumption of algal systems has been estimated using the discussed methods. However, studies often employed one method exclusively resulting in either a WF [23], [32]–[35], [49] or WSF accounting [36], [37] and fail to provide a complete assessment of the water impacts. Previous studies do not account for geographic considerations or are restricted to a few locations [32], [34], [49], [98]. In addition, multiple studies do not use a life-cycle assessment framework and neglect water consumption of upstream processes or the direct consumption of the conversion to fuel process [23], [32], [36], [43], which underestimates the total water consumption of the algae to fuels process [34], [38]. More importantly, quantifying the contribution of rainwater to the WF of algal systems is important to make an objective comparison to terrestrial crops. An accurate water balance requires models able to calculate evaporation rates at a high spatiotemporal scale [23] and careful tracking of algal pond depth to avoid culture dilution caused by high precipitation rates [32]. Wigmosta et al. [43] is the only study that includes rainwater in water balance calculations, however, the evaporation model used in the analysis was validated with small-scale pond data and was not designed to estimate the evaporation rates of commercial-scale systems accurately [23]. This is critical as evaporation rates not only impact water balances but also propagate to temperature and growth rate calculations [23]. The WF of algal systems has not been clearly defined in the literature due to a lack of appropriate models and incorrect modeling assumptions or methodological inconsistencies.

This research chapter focuses on estimating the WF and WSF of renewable diesel derived from algal biomass by integrating water LCA methodologies with a robust dynamic cultivation

model. This work builds upon previous modeling work [23] with novel aspects including a thorough investigation of the impacts of water recycling, rainwater, and indirect water consumption on the WF of the system. By using the high-fidelity model validated by Quiroz et al. [23], the impacts of system scale on evaporation rates and consequently on water consumption, pond temperatures, and growth rates are accurately modeled. In addition, the cultivation model was coupled with a state-of-the-art conversion model [99] to analyze the direct and indirect water consumption of the biomass-to-fuel process. The local water scarcity impacts associated with the deployment of commercial-scale algal biofuel systems across the US are also investigated. When integrated, the models provide a geospatial analysis of the life cycle WF, including blue, green, and indirect WFs, and WSF of the algae to renewable diesel process. Results identify the most water-intensive processes in the algae-to-fuel pathway, compare the magnitudes of direct and indirect water consumption, and illustrate the most suitable locations for algae fuel production based on water consumption impacts. The discussion focuses on comparing these results to the water intensity of saline algal cultivation and traditional biofuel systems. This is the first work to complete a holistic life cycle water assessment and water scarcity evaluation for the entire US of an algal-based biorefinery.

3.2 Materials and methods

This research chapter assesses the geographically resolved water consumption of algal biofuels through two different water LCA methodologies. Both are informed by mass and energy balances calculated from an engineering process model encompassing the geographically resolved biomass cultivation, dewatering, and fuel conversion stages, as shown in Figure 7. The following subsections provide detailed descriptions of the cultivation (including the growth model), conversion, and water LCA methods adopted in this analysis.

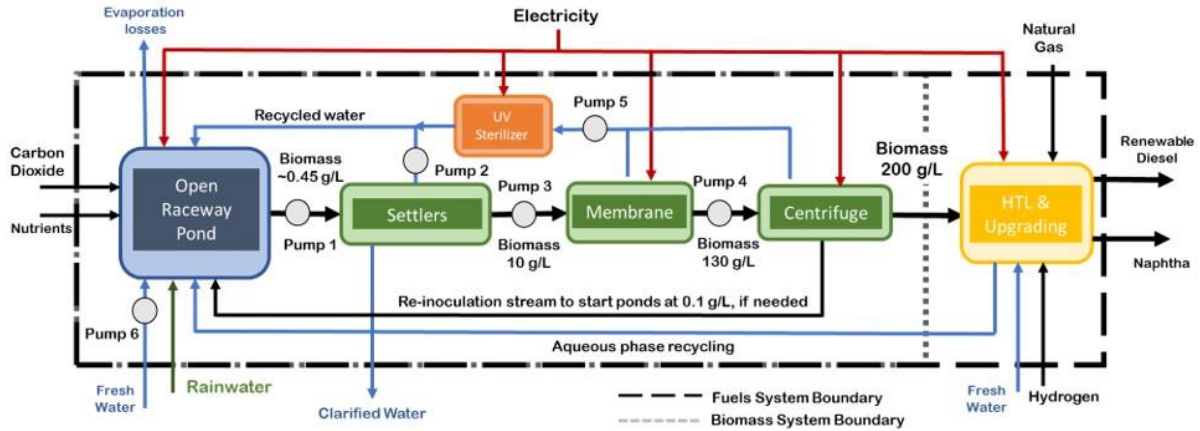


Figure 7. System diagram illustrating the microalgae cultivation process in open-raceway ponds, three-step dewatering process, and conversion and upgrading to renewable diesel through hydrothermal liquefaction (HTL) and hydrocracking.

3.2.1 Cultivation model

The cultivation model used in this analysis includes the biomass growth process in commercial-scale open-raceway pond (ORP) systems followed by a three-step dewatering process consisting of settlers, membranes, and centrifuges. Detailed descriptions of these modules are provided in the following subsections.

3.2.1.1 Open-Raceway Pond Model

ORPs have been the most studied algae growth architecture in the literature due to their low cost and simplicity. Given the open nature of these systems, ORPs are subjected to the changing conditions of the environment, therefore, models with hourly timescales are required to accurately simulate pond conditions. Thermal conditions in the ORP system were calculated using the model validated by Quiroz et al. [23], while growth rates were simulated using the dynamic growth model validated by Greene et al. [25] Temporally and spatially resolved outputs for a 400-hectare facility cultivating the strain UTEX 393 were generated following the framework in previous modeling work with results presented in Appendix B [23].

The foundational model from Quiroz et al. [23] was modified to include precipitation data to model realistic pond operations. Daily precipitation data for 21 years, retrieved from the Center for Hydrometeorology and Remote Sensing database, was disaggregated into hourly time steps and included in the water balance [100]. The depth of the ponds was kept between 15 and 25 cm by tracking hourly net evaporation rates, defined as the difference between evaporation and precipitation rates. If the pond depth exceeded the allowable maximum, the pond was harvested and reset to 15 cm and a concentration of 0.1 g L^{-1} . Similarly, potential culture dilution caused by incoming precipitation was prevented by ensuring the concentration in the ponds was maintained above 0.1 g L^{-1} . Further details on model calculations, implementation, and data curation are presented in Appendix B.

3.2.1.2 Dewatering Model

The dewatering module is composed of a three-step dewatering process to remove excess water from the biomass, 0.45 g L^{-1} to 200 g L^{-1} , based on the modeling work of Davis et al.[18]. The biomass was first routed through settlers where it exits with a concentration of 10 g L^{-1} . The water retrieved from the biomass stream is recycled back to the ponds except for when the ponds are drained due to excess precipitation. During pond drainage, the clarified water was routed back to the local water source. The clarified water stream exiting the settlers was assumed to contain a negligible concentration of nutrients and algae [18].

Subsequently, the biomass stream is routed to the remaining dewatering processes depicted in Figure 7, and recycled water is sterilized in an ultra-violet sterilizer before being returned to the ORPs. For the case when ponds do not have enough biomass to be restarted to 0.1 g L^{-1} , mainly caused by constant harvesting during intense precipitation periods, a fraction of biomass is routed from the exit stream of the centrifuge back to the ponds. This pond operating

strategy reduces freshwater consumption by storing all available rainfall and preventing culture failure induced by diluted cultures.

Energetics and recycling efficiencies of the dewatering and cultivation equipment are presented in Table 1. The recycling efficiencies used in this study are informed by previous modeling work in the literature [18] and represent a current technical hurdle that must be addressed for the optimal performance of commercial-scale systems. The impacts of these assumptions and other key model inputs were tested through a sensitivity analysis, and further methods are presented in Appendix B.

3.2.2 Conversion Model

After dewatering the biomass to 20% solids, the biomass was converted to biocrude via hydrothermal liquefaction (HTL) based on the work of Chen et al.[99] Inputs to the HTL model include biomass composition and biomass productivity yields. The ash-free lipid, protein, and carbohydrate content of the biomass were set to 22%, 25%, and 53%, respectively [13]. The ash content of the biomass was assumed to be 8% [13]. After the biomass is processed to a biocrude, upgrading to renewable diesel and naphtha is done via hydrocracking [99]. The nutrient-rich aqueous stream exiting the HTL module is recycled back to the ponds, while the gaseous stream is utilized for on-site heat and power [99].

Table 1. Primary model inputs used for the calculation of mass and energy flows in the biomass production process.

	Value	Unit
Open-Raceway Ponds		
Inoculation density [23]	100	g L ⁻¹
Harvest density [23]	450	g L ⁻¹
Harvest volume [13]	75	%, fraction of pond
CO ₂ utilization [18]	90	%
Biomass Elemental Composition		
Carbon (C) [18]	48.3	%, AFDW basis
Nitrogen (N) [18]	9.5	%, AFDW basis
Phosphorous (N) [18]	1.2	%, AFDW basis
Others (H, O, S) [18]	41.0	%, AFDW basis
Biomass Component Composition		
Lipids [18]	22.1	%, AFDW basis
Protein [18]	25.4	%, AFDW basis
Carbohydrates [18]	52.5	%, AFDW basis
Ash [18]	8.00	%, DW basis
Diammonium Phosphate Composition		
Phosphorous [25]	20	%, weight
Nitrogen [25]	18	%, weight
Ammonia Composition		
Nitrogen [25]	82	%, weight
Dewatering		
Settlers target concentration [18]	10	g L ⁻¹
Biomass blowdown loss [18]	0.1	%
Settlers separation efficiency [18]	90	%
Membrane target concentration [18]	130	g L ⁻¹
Membrane separation efficiency [18]	99.5	%
Centrifuge target concentration [18]	200	g L ⁻¹
Centrifuge separation efficiency [18]	97	%
Energy Consumption		
CO ₂ delivery power [18]	0.0439	kWh kg ⁻¹ CO ₂
Paddlewheel power [18]	55.1	kWh hectare ⁻¹ day ⁻¹
Membrane power [18]	0.04	kWh m ⁻³
Centrifuge power [18]	1.35	kWh m ⁻³
UV sterilizer power [18]	2.71e-03	kWh m ⁻³
Freshwater pump power [18]	0.257	kWh m ⁻³
Ponds to settlers pump power [18]	0.0189	kWh m ⁻³
Settlers recycling pump power [18]	0.0177	kWh m ⁻³
Settlers to membrane pump power [18]	0.129	kWh m ⁻³
Membrane to centrifuge pump power [18]	0.0194	kWh m ⁻³
Recycling stream pump power [18]	0.184	kWh m ⁻³

2.3 Water LCA Methods

The primary goal of this study is to determine the WF and WSF of microalgae biomass and biofuels. The direct and indirect water consumption of the supply chain was included to provide a final value of life cycle water consumed per functional unit. Two different system boundaries were established to facilitate comparison to other energy crops and biofuels from

previous assessments. The first system boundary includes the biomass cultivation and dewatering to 20% solids processes while the second system boundary is expanded to incorporate the fuel conversion process (Figure 7). Similarly, the functional units for each system configuration were set to one metric ton of ash-free dry weight biomass and one GJ of renewable diesel, respectively.

2.3.1 Water Footprint Methodology

The most common method used to quantify the water consumption of bioenergy systems is the WF method developed by Hoekstra et al.[95]. The total WF of a product is defined as the addition of three different WF components: blue, green, and gray WFs. Each component is further divided into a direct and indirect WF. The indirect WF measures upstream water consumption in the supply chain, while the direct WF refers to on-site water consumption. It is worth noting that this method considers water consumption only and neglects the impacts to water quality [95].

The blue WF of a product measures the amount of water consumed from surface or groundwater sources [95]. In the case of algal cultivation, freshwater consumption is equal to the difference between the volume of water withdrawn from the water source (to make up for evaporation losses and water incorporated in the biomass stream) and the volume of clarified water returned to the catchment area, due to system drainage. Accordingly, an increase in the water discharged due to inefficiencies in the dewatering equipment has no impact on the net freshwater consumption of the system. However, an increment in the volume of discharged water could have implications for the gray WF of the system, as discussed below. The water used for cooling equipment and other processes in the conversion stage was assumed to all be consumed,

making the total blue water demand equal to the sum of the water consumed in the cultivation and conversion processes.

In addition to estimating blue WFs, computing the green WF is essential in the water analysis of energy crops. The green WF measures the volume of rainfall that is not returned to groundwater sources and is either stored or consumed [95]. Green water demand was calculated by tracking the volume of rain entering the ponds. This study assumed that all rainwater is stored in the ponds and therefore all precipitation contributes to the green WF.

In contrast to the blue and green components, the gray WF measures freshwater pollution and is defined as the volume of freshwater required to dilute pollutants to meet water quality standards [95]. Different from terrestrial crops, the gray WF of algal cultivation can be minimized by proper nutrient recycling and treating waste streams before disposal [98]. For example, all disposed water from cultivation is previously clarified in the settlers to reduce the concentration of suspended solids in the clarified water stream. Based on experimental data reported in the literature [101]–[104], the algae culture was assumed to consume all available nutrients and therefore the nutrient load in the harvested and water discharged streams was assumed to be negligible. For the same means, the effluent from the conversion stage was recycled back to the ponds instead of being directly disposed. Considering the above assumptions, algal cultivation does not generate a gray WF, and the analysis focused on blue and green WFs with a sensitivity to this assumption explored.

The indirect WFs attributed to process consumables were retrieved from different LCA databases and literature. Water consumption associated with the production of diammonium-phosphate, ammonia, hydrogen, and natural gas was retrieved from the GREET 2021 model [105]. The water consumed in electricity generation was determined by expanding the methods

presented in Lee et al. [106] to an eGRID subregion level [107]. More detailed indirect WF calculations are provided in Appendix B.

2.3.2 Available Water Remaining Methodology

The Available Water Remaining in the US (AWARE-US) model [108] was used to calculate the WSF of algal biomass and biofuels based on a monthly analysis that is averaged into seasonal results. This model defines the WSF as the product of direct freshwater consumption and a characterization factor (CF). The CF is a water-stress indicator characterizing the water availability and demand of a given location relative to the water availability of a specific location [96], [97]. The AWARE-US model provides monthly characterization factors for US counties relative to the US average freshwater availability [108]. The output of the analysis is a monthly WSF at a county level. The methods used to interpolate model outputs to a county level are described in Appendix B.

3.3 Results and discussion

The WF of algae biofuels is presented and disaggregated into the direct blue, green, and indirect blue, and then summed for a total WF. The grey WF is regarded as negligible assuming optimal operation of the system. Process model outputs are then analyzed to understand the parameters that have a major impact on WF results. Results are combined with AWARE-CF to determine the WSF of algal-based biofuels with seasonal resolution. The results presented in this section are the averages of the 21-year simulation.

3.3.1 National water footprint mapping

The life cycle WF for all simulated sites were surface interpolated and results for the algal fuels system are summarized in Figure 8. The range of total life cycle WF was calculated to

be $30 \text{ m}^3 \text{ GJ}^{-1}$ with the maximum located in the northwest U.S. ($39 \text{ m}^3 \text{ GJ}^{-1}$), while Hawaii and southern California yield the smallest WFs, ranging between 9 and $10.6 \text{ m}^3 \text{ GJ}^{-1}$. The large WFs in the Pacific Coast are explained by the high precipitation rates and low biomass yields in the region. Similarly, the large WF of hydroelectricity has a modest impact on the indirect water consumption of algae farms located across the northwestern US (Figure 8C). While the larger indirect WF of sites in Florida is correlated to the energy penalty associated with elevated rainwater usage. These results show that even in scenarios with high energy consumption, the indirect WF is an order of magnitude lower than the direct blue and green components of freshwater cultivation. In conclusion, direct freshwater and rainwater consumption are the largest contributors to the total WF and the indirect WF of upstream processes was found to be strongly dependent on the WF of electricity generation.

The results from the work illustrate that the indirect WF of freshwater cultivation is low and dominated by electricity usage in the system. Contrastingly, the indirect WF is dramatically impacted in a saline cultivation scenario, where there is an increase in electricity consumption due to higher pumping and blowdown energy needed to maintain adequate salinity levels. The differences in WFs between freshwater and saline cultivation scenarios for Tampa, FL, and Corpus Christi, TX were quantified following the saline modeling assumptions provided in Appendix B. Results show that saline cultivation in Corpus Christi, TX provides a 30% reduction in the total WF by eliminating freshwater consumption to make up for evaporation which exceeds the increased indirect water consumption from pumping (Figure B - 13). In Tampa, FL saline cultivation increased the indirect WF component by an order of magnitude, which resulted in similar total WFs as the freshwater cultivation scenario. These two case studies highlight the

potential of coastal areas for reducing the WFs of algal systems through saline cultivation, but also show it is location-dependent.

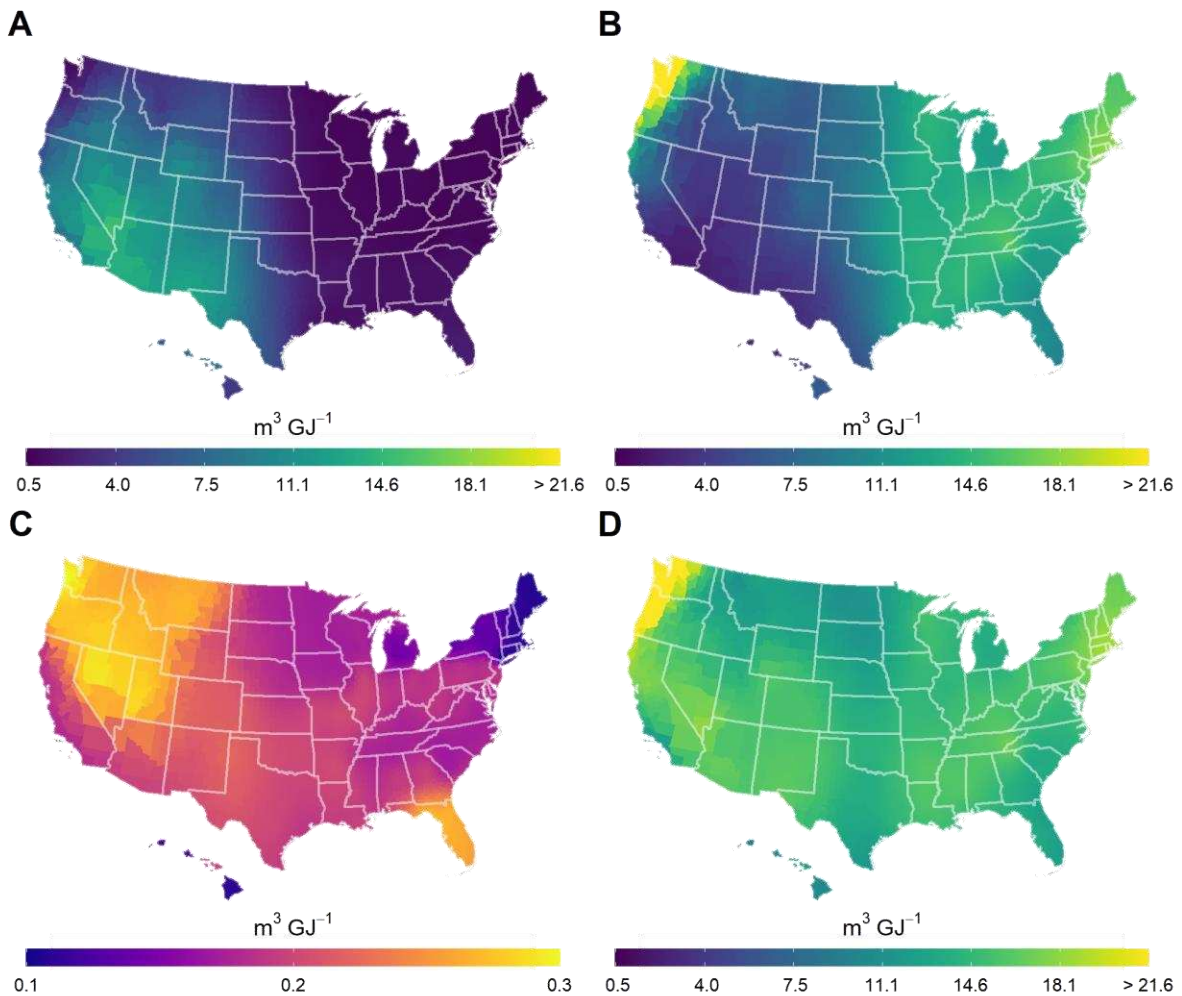


Figure 8. Life cycle water footprint breakdown of algal diesel: (A) direct blue water footprint, (B) direct green water footprint, (C) indirect blue water footprint, and (D) total water footprint.

The regional differences observed in Figure 8 emphasize the need for water LCAs with geospatial resolution. For instance, the blue WF (Figure 8A) is driven purely by evaporation rates with the highest rates located in dry climates such as the Desert Southwest. Contrastingly, the southeastern US shows the largest green WFs (Figure 8B) and the smallest blue WFs, explained by the high precipitation rates in the region. However, when comparing the total WF

of these regions, similar trends are observed in total WFs. For example, the total WF of Phoenix, AZ was found to be only 3% larger than that of Macon, GA, although freshwater consumption in Phoenix represents 85% of the total water consumption compared to 14% in Macon, GA. The freshwater consumption in a water-scarce region such as the southwestern US will potentially bring about more severe environmental impacts than the consumption of rainwater in Georgia. This comparison stresses a limitation of the WF method, as it only accounts for water consumption, but does not consider water stress impacts. This is further explored in this study through water scarcity calculations.

The results from this study were also compared to published water LCAs using identical system boundaries and metrics. Compared to the algal WFs ($\text{m}^3 \text{GJ}^{-1}$) reported by Ou et al. [41], an average difference of 14% across the eight sites used for comparison was estimated. These discrepancies were larger in sites located in the Midwest US and are attributed to differences in evaporation modeling, meteorological data, and biomass yields. At the same time, the model used in this study predicts lower freshwater consumption per area ($\text{m}^3 \text{m}^{-2} \text{yr}^{-1}$) across the eight sites used for comparison, corresponding to an average difference of 38%. Moreover, the magnitudes of other water consumption sources (i.e. conversion and indirect) agree with the results from this analysis, implying that differences between water LCAs of algae systems are mainly attributed to variations in net evaporation rates and growth rates.

Furthermore, a WF comparison to first and second-generation biofuels shows blue WFs of algal fuel systems can approximate those of conventional corn ethanol and soybean biodiesel systems, and the difference depends on the location where algal biomass is cultivated. In particular, the blue WF of algal fuels in the southwestern US is generally larger than the average blue WFs of corn ethanol and soybean biodiesel cultivated in Iowa, but comparable if algal

biomass is cultivated in the Gulf Coast region (Figure 9A). A comparison to wheat straw ethanol shows that algal production in California and Texas incurs smaller blue WFs; however, when algal biomass is cultivated in Arizona, production of first and second-generation biofuels generates a smaller blue WF. Although a larger volume of freshwater is required for algal cultivation in these locations, the higher biomass yields make the blue WF of algal biofuels comparable to those of its first and second-generation counterparts. In summary, the regional variations of freshwater consumption and biomass yields must be considered to determine the scenarios under which algal fuels present a smaller blue WF than conventional biofuel systems.

In the context of the green WF component, algal systems present some advantages over terrestrial energy crops. Notably, the impact of higher growth rates achieved by algae systems is best reflected when comparing the green WF between biofuels. The results illustrated in Figure 9A show that algal renewable diesel uses less rainwater per unit of energy than all other biofuel systems.

In terms of gray water, algal cultivation presents the advantage of generating no gray WF if pollutants loadings in waste streams are carefully tracked, ponds are properly managed, and recycling across process stages is practiced [98], [109]. It is important to note that complete nutrient assimilation in the ponds is critical for maintaining negligible gray WFs in algae systems. Negligible gray WFs in algal systems are dependent on proper pond management, and operating the ponds without carefully tracking nutrient loadings and water discharged volumes could result in considerable gray WFs (Figure B - 2). Contrastingly, the gray WF of terrestrial crops is a function of fertilizer loss and has been found to represent a large portion of the total WF [110], [111], particularly for corn ethanol (Figure 9A). Based on the modeled gray WFs,

findings of this comparison suggest that a shift to algal biofuels has the potential to lower the gray and green water consumption of bioenergy.

As shown in Figure 9A, if all components are considered, the total WF of algal biofuel systems is approximately four to six times smaller than the average WF of corn ethanol while an order of magnitude smaller than that of soybean biodiesel. If only blue and gray WFs are compared, algal systems have a larger total WF than soybean and switchgrass biofuels but a smaller total WF than corn grain and wheat straw ethanol. This comparison indicates that from an overall WF perspective, algal systems benefit from their higher growth rates and opportunity for recycling nutrients.

3.3.2 Water footprint breakdown

The results shown are all driven by the different parameters calculated by the engineering process model, thus, evaluating the mass and energy balance is critical to identifying opportunities for reducing freshwater consumption. The analysis indicates that freshwater and rainwater consumption in the biomass production process dominates the overall water consumption of algae systems. As seen in the blue WF breakdown of the six case study locations shown in Figure 9B, water consumed in the conversion process is minimal compared to the evaporation losses during the cultivation stage. Consequently, algae fuel systems benefit from the recycling of cultivation water embedded in the biomass making them less water-intensive than traditional terrestrial-based biomass systems, where the water leaving with the biomass is assumed to be consumed. The outcomes from both modeled system boundaries demonstrate that water consumed in the biomass production stage dominates the total WF and the co-location of biorefineries with farms decreases the WF of algae fuels by promoting water recycling across processes.

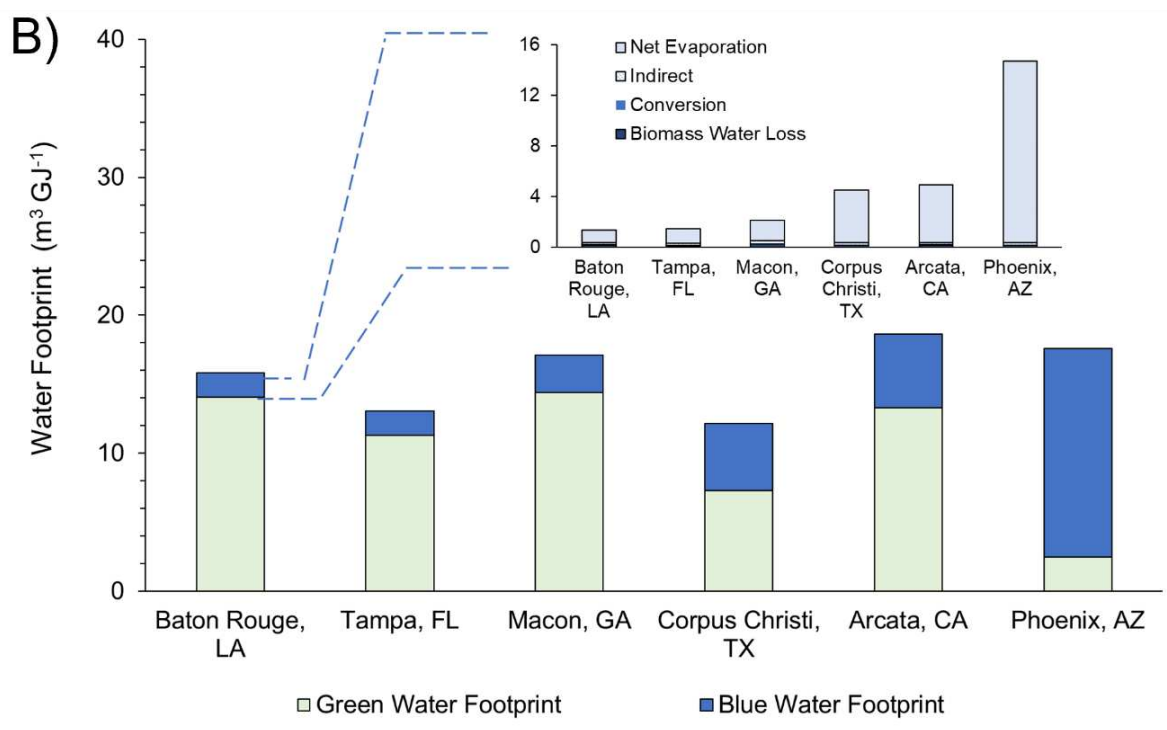
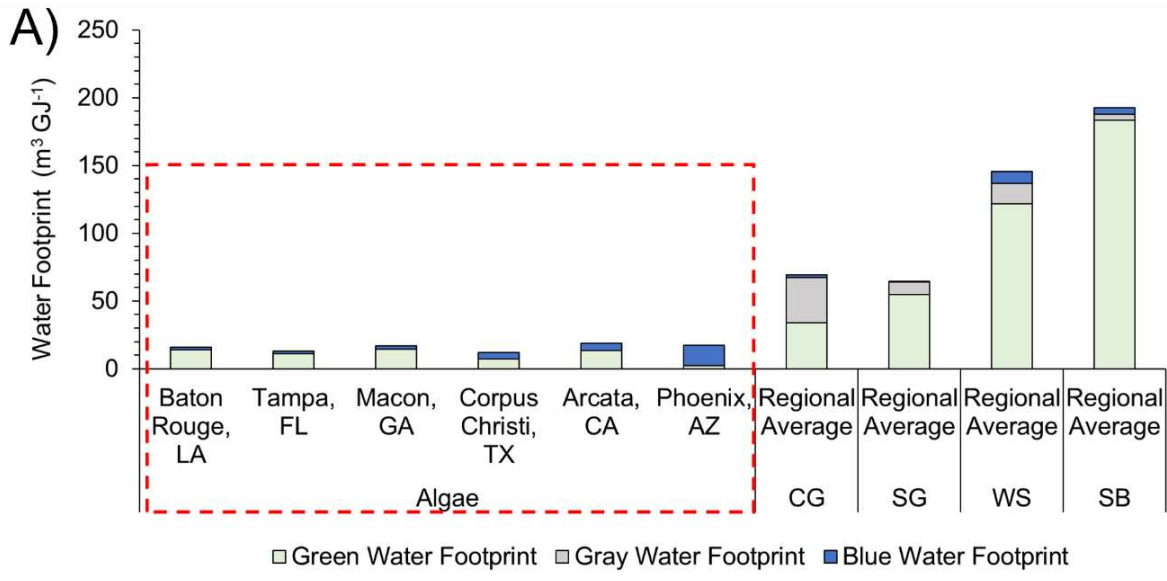


Figure 9. A) Life cycle water footprint comparison between renewable diesel from microalgal biomass for six locations in the United States and average regional life cycle water footprints for first and second-generation biofuels derived from corn grain (CG), switchgrass (SG), wheat straw (WS), and soybean (SB). The water footprints of corn grain and wheat straw ethanol, as well as those of soybean biodiesel and switchgrass biodiesel blend, were retrieved from the literature [112]–[115] and represent average values of high crop production areas: corn and soybean are assumed to be grown in the Corn Belt and the southeastern US, while switchgrass and wheat straw are mainly cultivated in the central and eastern US. B) Life cycle water footprint of algal fuel systems across six locations in the US. Inset, the blue water footprint breakdown. The water footprint values of algae sites represent the average of the 21 simulated years. Mass allocation methods were used in the computation of residue feedstocks (wheat straw) [116].

Beyond the effects of water recycling, the usage of rainwater also contributes to minimizing freshwater withdrawal and consumption. This is observed when comparing the net evaporation rates in this study, ranging from 0.05 to 1.47 m³ m⁻² yr⁻¹, with the range previously calculated by Quiroz et al.[23] (0.30-1.68 m³ m⁻² yr⁻¹). The wider range presented in Quiroz et al. [23] is expected, as rainwater was not accounted for, and instead, a “gross” evaporation rate was estimated. The southeastern US is one of the regions that benefit the most from rainfall utilization. For example, in Tampa, FL most of the water consumption can be supplied with rainwater. The model outputs demonstrate that the net water consumption of algal systems is primarily influenced by evaporation losses and rainwater contributes to increasing the water efficiency of these systems.

The evaporation losses in the cultivation stage drive the water intensity of algal systems therefore it is critical to select sound evaporation models to reduce the uncertainty in evaporation estimates. To understand the importance of evaporation modeling in water usage metrics, net evaporation rates were compared to those of Wigmosta et al. [43] In general, the results from this study were found to be 31% lower, based on the 204 sites used for comparison. This difference is anticipated as Wigmosta et al. [43] used corrected pan evaporation data for model validation [43], which has been shown to differ by 45% from commercial-scale algae systems [23]. The differences in scales of the modeled facilities are critical as the surface area has a direct influence on evaporation rates [23]. Facility sizes modeled in Wigmosta et al. [43] were selected based on land availability, while this work fixed a standard 400-ha wetted area. Although direct comparison would require harmonizing model inputs, the comparison highlights the importance of selecting appropriate evaporation models when modeling water consumption in open algae systems.

Biomass yields have a direct impact on the WF of the system, as it impacts the functional unit. The modeled productivity yields agree with experimental values for UTEX 393 [13] with annual averages reaching a maximum of $23.6 \text{ g m}^{-2} \text{ day}^{-1}$ in Hawaii and Florida (Figure B - 4A). It should be noted that these values represent optimistic yields for commercial microalgae cultivation since the impacts of culture failure are not accounted for in the analysis. The potential impacts of pond contamination on modeled areal productivity values are illustrated by reducing biomass yields by a safety factor (Figure B - 5). The results presented here represent projections based on the current biomass production potential in pilot-scale systems and should be improved by considering the impacts of culture mixing in commercial-scale systems as well as pond contamination and reliability.

Other model outputs were found to be consistent with previous modeling work [23]. Nutrient demands were found to scale directly with biomass yields, while electricity consumption is a function of operational days, growth rates, and precipitation rates (Figure B - 6). The high electricity demand in the Gulf Coast states is credited to the higher pumping and dewatering power needed to control the depth of the ponds during periods of intense rainfall. Energy balance results show that minimizing freshwater use through the effective use of rainwater in the cultivation process comes with an increase in electricity consumption caused by more frequent pond harvesting and larger processing volumes.

Moreover, the impacts of model inputs on the blue and indirect WFs for two case study locations were tested through a sensitivity analysis (details included in Appendix B). The results of the sensitivity analysis (Figure B - 16) indicate that in sites with low precipitation such as Phoenix, AZ the parameters that directly impact evaporation losses and biomass yields are the most sensitive to both the direct blue WF and indirect WF. Contrastingly, in sites with high

precipitation such as Tampa, FL, the depth limits of the ponds were found to be sensitive. These inputs have an impact on the amount of rainwater that can be stored in the ponds and consequently impact the amount of freshwater needed to refill the ponds at the minimum depth. Although a reduction in the separation efficiency reduces the amount of biomass converted into fuels, there is also a decrease in the amount of water needed to make up for losses, as more water is recycled back to the ponds. An increase in the separation efficiency increases the amount of biomass that is sent to conversion but increases the volume of water needed to make up for water losses (less water is recycled) and therefore balances the impacts of increased yields on the blue WF of the system.

Beyond the effects of water recycling, the usage of rainwater also contributes to minimizing freshwater withdrawal and consumption. This is observed when comparing the net evaporation rates in this study, ranging from 0.05 to 1.47 m³ m⁻² yr⁻¹, with the range previously calculated by Quiroz et al. [23] (0.30-1.68 m³ m⁻² yr⁻¹). The wider range presented in Quiroz et al.[23] is expected, as rainwater was not accounted for, and instead, a “gross” evaporation rate was estimated. The southeastern US is one of the regions that benefit the most from rainfall utilization. For example, in Tampa, FL most of the water consumption can be supplied with rainwater. The model outputs demonstrate that the net water consumption of algal systems is primarily influenced by evaporation losses and rainwater contributes to increasing the water efficiency of these systems.

The evaporation losses in the cultivation stage drive the water intensity of algal systems therefore it is critical to select sound evaporation models to reduce the uncertainty in evaporation estimates. To understand the importance of evaporation modeling in water usage metrics, net evaporation rates were compared to those of Wigmosta et al. [43] In general, the results from this

study were found to be 31% lower, based on the 204 sites used for comparison. This difference is anticipated as Wigmosta et al. [43] used corrected pan evaporation data for model validation [43], which has been shown to differ by 45% from commercial-scale algae systems [23]. The differences in scales of the modeled facilities are critical as the surface area has a direct influence on evaporation rates [23]. Facility sizes modeled in Wigmosta et al. [43] were selected based on land availability, while this work fixed a standard 400-ha wetted area. Although direct comparison would require harmonizing model inputs, the comparison highlights the importance of selecting appropriate evaporation models when modeling water consumption in open algae systems

Biomass yields have a direct impact on the WF of the system, as it impacts the functional unit. The modeled productivity yields agree with experimental values for UTEX 393 [13] with annual averages reaching a maximum of $23.6 \text{ g m}^{-2} \text{ day}^{-1}$ in Hawaii and Florida (Fig S4A). It should be noted that these values represent optimistic yields for commercial microalgae cultivation since the impacts of culture failure are not accounted for in the analysis. The potential impacts of pond contamination on modeled areal productivity values are illustrated by reducing biomass yields by a safety factor (Figure B - 5). The results presented here represent projections based on the current biomass production potential in pilot-scale systems and should be improved by considering the impacts of culture mixing in commercial-scale systems as well as pond contamination and reliability.

Other model outputs were found to be consistent with previous modeling work [23]. Nutrient demands were found to scale directly with biomass yields, while electricity consumption is a function of operational days, growth rates, and precipitation rates (Figure B - 6). The high electricity demand in the Gulf Coast states is credited to the higher pumping and

dewatering power needed to control the depth of the ponds during periods of intense rainfall. Energy balance results show that minimizing freshwater use through the effective use of rainwater in the cultivation process comes with an increase in electricity consumption caused by more frequent pond harvesting and larger processing volumes.

Moreover, the impacts of model inputs on the blue and indirect WFs for two case study locations were tested through a sensitivity analysis (details included in Appendix B). The results of the sensitivity analysis (Figure B - 16) indicate that in sites with low precipitation such as Phoenix, AZ the parameters that directly impact evaporation losses and biomass yields are the most sensitive to both the direct blue WF and indirect WF. Contrastingly, in sites with high precipitation such as Tampa, FL, the depth limits of the ponds were found to be sensitive. These inputs have an impact on the amount of rainwater that can be stored in the ponds and consequently impact the amount of freshwater needed to refill the ponds at the minimum depth. Although a reduction in the separation efficiency reduces the amount of biomass converted into fuels, there is also a decrease in the amount of water needed to make up for losses, as more water is recycled back to the ponds. An increase in the separation efficiency increases the amount of biomass that is sent to conversion but increases the volume of water needed to make up for water losses (less water is recycled) and therefore balances the impacts of increased yields on the blue WF of the system.

3.3.3 Water scarcity implications

Aside from quantifying life cycle water usage, the local water stress associated with the deployment of algal systems was calculated and reported as a WSF. The seasonal results shown in Fig. 4 illustrate the temporal dynamics of water consumption, availability, and biomass yields. The largest WSFs are found in the southwestern US, where water stress levels vary between

1700 and 1760 m³-U.S._{eq} per GJ during spring (Figure 10A). Similar water stress levels propagate to southern and western California during the summer (Figure 10B). While there is an increase in water consumption during summer, this is balanced by an increase in biomass yields, consequently, the magnitude of WSFs during summer is comparable to those seen in spring. Similarly, the same regions present the highest water stress levels during the fall season (Figure 10C), but there is a reduction in the WSF compared to summer levels. The winter season experiences a reduction in water stress levels in California while southwestern Texas displays a minor change compared to fall. The seasonal analysis indicates that biomass yields drive the WSF during spring and summer, while water consumption is the driving factor during the fall and winter seasons.

As discussed above, the temporal variations of the WSF are a product of the seasonal variabilities of freshwater consumption and biomass yields. Potential algae sites must support high growth and low evaporation rates, in addition, sites must be located in areas with sufficient water availability to support a low WSF (low AWARE-US CF). Based on these criteria, the southeastern and Gulf Coast U.S are characterized as the most suitable regions for microalgal fuels (Figure 10) and biomass production considering WSF (Figure B - 14). The southeastern US region achieves the maximum biomass yields with average areal productivities above 20 g m⁻² day⁻¹ and the abundant rainwater has a propitious effect on the WSF, by not only reducing the water consumption of algal systems but also increasing freshwater availability and therefore returning a low AWARE-US CF. There was found to be minimal variability among the distribution of WSF for counties in Gulf Coast states and Georgia. Even in the scenario of having below-average precipitation rates, the maximum seasonal WSF in the region remains between 5.2 and 5.8 m³-U.S._{eq} m⁻² month⁻¹, suggesting that the WSF is more strongly correlated to

biomass yields. The analysis reveals that the southeastern US is the best candidate for siting algal systems based on WSF due to the low water consumption, high growth rates, and low water stress levels.

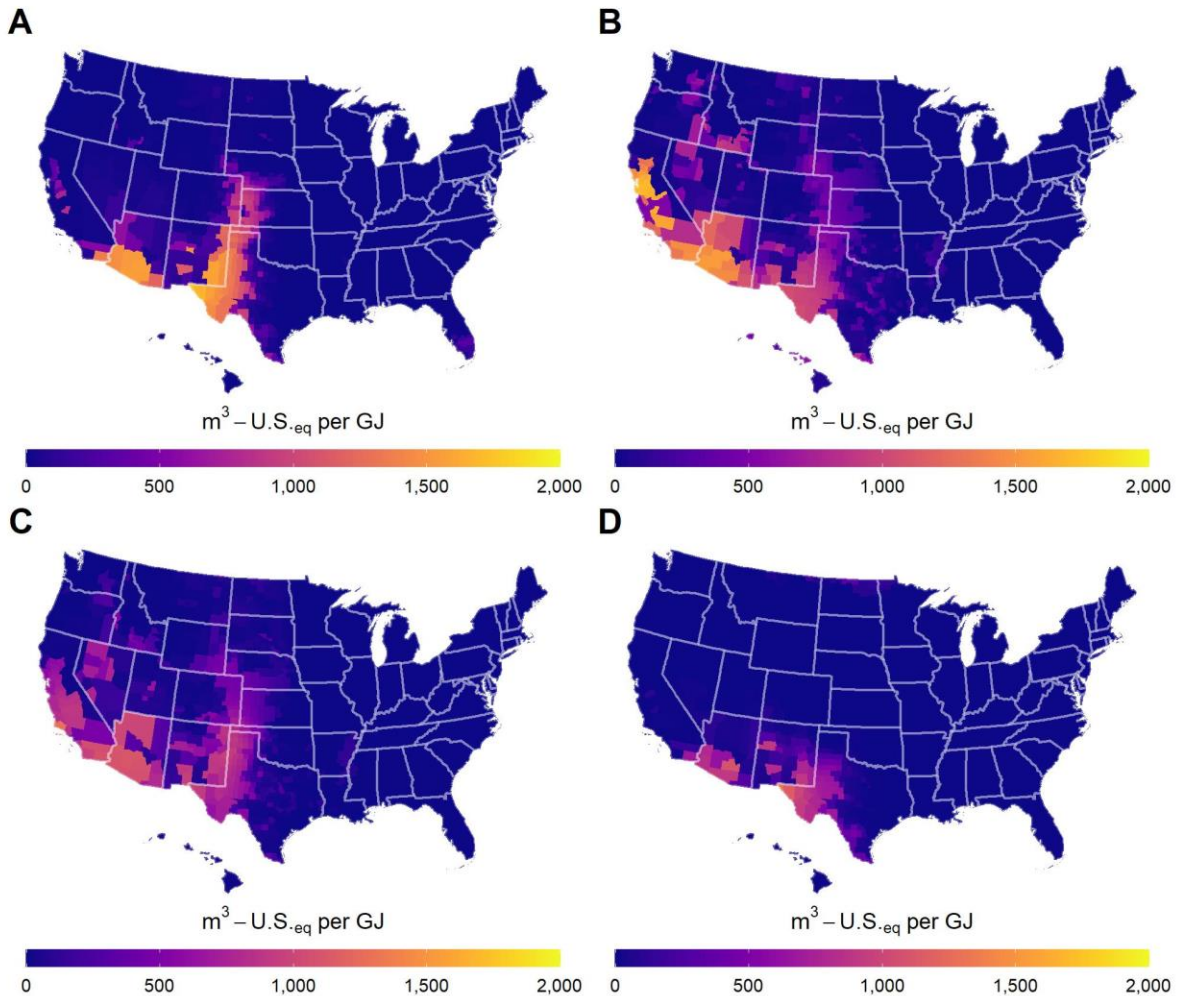


Figure 10. Seasonal water scarcity footprints of renewable diesel from algal biomass: (A) spring, (B) summer, (C) fall, and (D) winter.

Although sites in the southwestern US also present high biomass yields, low water availability in the western US risks unsustainable cultivation of algal biomass in the region. For instance, if algal farms are projected to be deployed in Arizona or southern California, these facilities will need to be supported by saline water sources to avoid any negative water stress

impacts and minimize freshwater withdrawals. Furthermore, if freshwater were available in the region, algal biomass proves to be a more efficient user of water than conventional energy crops and could potentially substitute terrestrial protein crops (e.g., soybean) in water-scarce regions such as CA and AZ.

Moreover, the results presented here suggest that the deployment of algal systems would not stress water resources in the southeastern US and thus could be developed alongside traditional agriculture. Although this study is not meant to establish the freshwater, wastewater, or saline resource availability and the implications on the scalability of these systems, the water scarcity analysis shows that freshwater consumption should not be a deterrent against the scale-up of algal facilities in certain geographical locations. However, land and CO₂ availability in the southeastern US are resources that could risk the sustainable scaling of these systems [43], [45]. Ultimately, freshwater is not a resource limiting the scale-up of algal biomass production and algal biomass can be characterized as a low water alternative to conventional terrestrial energy crops.

It is also important to note that the WSFs presented here consider only freshwater consumption impacts. As discussed, the cultivation of algal biomass in the southeastern US will require an appropriation of the available precipitation that could lead to changes in green water availability or impact the water supply of other crops in the area. Additionally, freshwater availability can also be reduced as groundwater will not be naturally recharged by rainwater [117]. Therefore, expansion of this analysis could investigate the green WSF of algal cultivation in areas where green water consumption dominates and analyze the tradeoffs between areas with large blue WSF and those with large green WSF.

3.4 Conclusions

The WF and WSF of microalgal biomass cultivation and conversion to fuel across the continental US and Hawaii are evaluated through a regionalized water LCA. The biomass cultivation stage was found to be the most water-intensive process with evaporation losses in open ponds representing the major source of freshwater consumption in the system. When all WF components are considered, the WF of algal renewable diesel was found to be smaller than that of traditional biofuels, however, algal biofuels generate larger blue WFs. The smaller WFs of algal renewable diesel are a result of both higher growth rates and the lack of a gray WF component stemming from nutrient recycling and proper waste stream management. In terms of WSF, sites in the Gulf Coast and the southeastern US were found to have the lowest water stress levels. Finally, cultivation in the southwestern US will cause substantial water stress in the region and saline algal cultivation is advised to reduce the water consumption of sites in these water-scarce regions. The potential of reducing the WF of algal systems in coastal areas by implementing saline cultivation was also explored. Although saline cultivation reduces freshwater consumption, there is an increase in indirect water consumption and future work should focus on better quantifying this component as it was shown to be equivalent to the water savings associated with evaporative makeup water. Finally, for a true understanding of the potential indirect water consumption impacts associated with cultivation in saline or brackish water, a detailed quantification of the energetics of groundwater pumping and brine disposal methods is required.

CHAPTER 4: A GLOBAL LIFE EVALUATION OF THE SUSTAINABILITY OF ALGAL-BASED BIOFUELS³

4.1 Introduction

The sustainability of algal biofuels has been extensively studied through LCA and TEA with results highlighting the technical, economic, and environmental challenges associated with biomass cultivation and conversion to biofuels [13], [21], [22], [118], [119]. As LCA and TEA are informed by process modeling, accurate prediction of the current algal productivity potential is critical for robust sustainability modeling [25], [29]. Existing studies [23], [25], [43], [89] have integrated spatiotemporal biological growth modeling with meteorological data to compute dynamic biomass productivity potentials. This modeling framework decreases the uncertainty that productivity inputs introduce to process models and subsequently propagates to LCA and TEA outputs [29]. However, spatiotemporal analyses have been often limited to regions with suboptimal weather conditions for algal cultivation such as the U.S. [23], [43], [44], [89] and to a restricted number of global case study locations [32], [39], [40]. Aside from process modeling limitations, the scarcity of life cycle data for location-specific supply chains constrains the focus of LCAs to specific regions as well as environmental impacts (e.g., global warming potential) [41], [44], [118]. Similarly, TEAs usually use regional average economic data and ignore the effects of local cost factors (e.g., labor expenses) on process economics [118]. In addition, a

³This chapter was submitted for publication as a peer-reviewed journal article: Quiroz, D. Greene, J.M., Limb, B.J., Quinn, J.C. (Manuscript in review). A global life-cycle and techno-economic assessment of algal-based biofuels.

holistic sustainability assessment requires concurrent evaluation of environmental and techno-economic aspects, but predictive spatial modeling is often only integrated into life cycle models with studies typically excluding techno-economic modeling [41], [44]. Based on the current state of the field, a global sustainability assessment considering region-specific climate conditions, supply-chain environmental impacts, and economic factors is necessary to understand the true sustainability potential of microalgae RD, particularly in regions with favorable climatic conditions for microalgae cultivation but for which limited data is available.

This research chapter integrates dynamic engineering process models with global weather datasets and spatially explicit sustainability data to investigate the environmental and economic implications of large-scale production of microalgae-derived RD around the globe. Process models tracking the hourly mass and energy flows through cultivation, dewatering, anaerobic storage, conversion via hydrothermal liquefaction (HTL) and upgrading to RD were leveraged to calculate the annual inputs and outputs of the system at 6,685 global locations. The developed well-to-wheels LCA considers the regional life cycle impacts of the different process inputs across 10 environmental impact categories. Similarly, the TEA accounts for regional-specific construction factors, labor costs, and corporate tax rates to calculate a minimum fuel selling price using a discounted cash flow analysis. Global maps were developed by surface interpolating simulation outputs to identify optimal locations for microalgae RD production in terms of environmental sustainability and economic viability. Discussion focuses on understanding the impacts of regional LCA and TEA inputs on the sustainability of an algal-based biorefinery system.

4.2 Materials and methods

The engineering process model used in this study integrates validated biophysical and thermal models developed by Greene et al. [25] and Quiroz et al. [23], respectively, with hydrothermal liquefaction (HTL) modeling from Chen and Quinn [99]. When integrated with meteorological data, the modeling framework enables temporally and spatially explicit LCA and TEA of the system. Modeling methods, meteorological data, LCA, and TEA used in the analysis are presented in this section with further data provided in Appendix C.

4.2.1 Biological growth model

Algal cultivation in open-raceway ponds was modeled by utilizing the biological growth model developed by Greene et al. [25]. The dynamic biological model simulates bulk algal growth rate by accounting for an hourly carbon fixation rate primarily impacted by light and temperature efficiencies [25]. Fundamental model inputs include parameters characterizing the response of the strain to temperature, light saturation, dark respiration losses and the time-resolved temperature of the culture. Based on previous validation work and the potential for fuels, algal cultures of the strain *Scenedesmus obliquus* (UTEX 393) were modeled. As reported by Quiroz et al. [23], the validation showed an average error of $-4.6 \pm 8.1\%$ relative to experimental growth data for 12 modeled harvests spanning a 30-day cultivation trial at the Arizona Center for Algal Innovation [7]. The model has been additionally validated across three unique strains with experimental growth observations from ponds operated at two different cultivation sites during three growing seasons [25]. In this study, ponds were assumed to be operated semi-continuously and harvested at a biomass retention time of 3 days or a concentration of 0.3 g L^{-1} . For further details on the biological model and UTEX 393 validation, readers are referred to Greene et al. [25] and Quiroz et al. [23], respectively.

4.2.2 Open-raceway pond thermal model

As culture temperature is a fundamental input to the biological growth model, hourly pond temperatures were computed by using the thermal pond model developed and validated by Quiroz et al. [23]. The thermal model performs an energy balance of the system by considering the different heat fluxes acting on the algal culture based on hourly weather conditions, depth of the culture and wetted surface area of the facility [23]. As described by Quiroz et al. [23], the thermal model predicts pond temperatures and evaporation rates at a $-0.96 \pm 2.72^\circ\text{C}$ and $1.46 \pm 5.92\%$ accuracy, respectively. Consistent with previous modeling work, pond temperatures and evaporation rates for 4-hectare (10 acre) ponds in a 2,023 wetted-hectare (5,000 acres) facility [18], [44], [118] were modeled. For further details on the development and validation of the thermal model, readers are referred to Quiroz et al. [23].

4.2.3 Biomass dewatering, storage, conversion, and upgrading

A three-step biomass dewatering process consisting of settlers, hollow fiber membranes, and centrifuges was modeled following the process efficiencies and energy inputs reported by Davis et al. [21]. In addition, the water separated from the biomass stream was assumed to be sterilized before being recycled to the pond. Process inputs to model ultraviolet sterilization were retrieved from Beckstrom et al. [120]. After biomass dewatering to 200 g L^{-1} , anaerobic storage was modeled based on the work by Wendt et al. [121] to manage variations in seasonal biomass yields. Conversion to RD via HTL and hydrocracking was then modeled using the open-source HTL model developed by Chen and Quinn [99]. A dry-weight HTL feed composition of 49% proteins, 23% carbohydrates, 20% lipids and 8% ash was assumed based on experimental strain composition data [21]. Furthermore, feed components (excluding ash and water) [99] were assumed to be converted into HTL products using biocrude, aqueous phase, gases and solid

yields of 45%, 25%, 13%, and 9%, respectively [122]. Additional dewatering and conversion inputs are provided in Appendix C.

4.2.4 Meteorological data

Historical weather data used in thermal and biological growth calculations included modeled observations of surface global horizontal irradiance, ambient temperature, wind speed and relative humidity. Hourly modeled surface global horizontal irradiance, 2m ambient temperature, 2m dew temperature and 10m wind speeds for the year 2021 were retrieved from the fifth global reanalysis (ERA5) dataset generated by the European Centre for Medium-Range Weather Forecasts [123]. Relative humidity was estimated using the ratio of vapor pressures calculated at dew and ambient temperatures. Surface global horizontal irradiance was converted into photosynthetically active radiation by following the methods in Greene et al. [25]. Data files for 6,685 locations across a 1.5° by 1.5° grid were extracted from the ERA5 dataset for global biological and thermal modeling. Modeling outputs of the simulated locations were then interpolated using kriging methods in the software ArcMap 10.8 [124].

4.2.5 Life cycle assessment

A spatially resolved LCA was performed to analyze the well-to-wheels environmental impacts of the system. The LCA examines the ten impact categories included in the Tool for Reduction and Assessment of Chemicals and Other Environmental Impacts version 2.1 [125]. Following the Sixth Assessment Report by the Intergovernmental Panel on Climate Change (IPCC) [126], GWPs for carbon dioxide, methane, and nitrous oxide of 1, 29.8, and 273 for a 100-year time horizon were used. Although HTL outputs renewable diesel and naphtha, all

emissions were allocated to a MJ of liquid fuel product based on energy densities of 42.8 MJ kg⁻¹ and 43.4 MJ kg⁻¹, respectively.

A core component of this analysis was to investigate the implications of regional supply chains on the environmental impacts of microalgae biorefineries. Therefore, the LCA leverages life-cycle data for 171 electricity, 2 hydrogen, 9 ammonia, and 4 DAP markets retrieved from the EcoInvent 3.91 database [127]. Hydrogen, nutrients, and electricity impacts varied regionally as these are major contributors to the GWP of algal biofuels [99], [128], [129]. Accordingly, life-cycle natural gas impacts from HTL have been found to have a minimal contribution to the overall GWP of the system [99] and were assumed to be globally constant. The regional boundaries of the electricity, hydrogen, ammonia, and DAP markets are illustrated in Appendix C.

A detailed carbon balance was performed by accounting for the carbon uptake by the biomass as well as direct biorefinery, fuel combustion, and land use change (LUC) emissions. The carbon uptake process during cultivation was modeled considering the carbon composition of the biomass, assumed to be 1.97 g C g⁻¹ biomass ash-free dry weight [21]. Emission factors in the Greenhouse Gases, Regulated Emissions, and Energy Use in Transportation 2021 [130] model were used to model emissions from natural gas combustion in the biorefinery and combustion of fuel products. Finally, DLUC emissions were estimated by following the 2006 IPCC Guidelines for National Greenhouse Gas Inventories [131] with further details provided in Appendix C.

4.2.6 Techno-economic analysis

A spatially explicit TEA was performed to determine the economic viability of the production of microalgae biofuel at the simulated locations. The TEA uses a discounted cash flow rate of return analysis to model the net present value of the project during a 30-year lifetime. Important cash flow inputs include land costs, operational expenses and capital costs which were estimated using data presented in previous techno-economic models in the literature [18], [99], [120], [121], [132]. Additionally, standard “Nth-of-a-kind” plant assumptions such as a fixed 10% internal rate of return, 8% loan interest and 7-year modified accelerated cost recovery system were used in the analysis [13], [18], [21].

Geographically resolved TEA inputs include labor indices, construction factors and corporate tax rates. By using a location-specific labor index and construction factor, the labor costs and capital expenses of a microalgae biorefinery at any location can be estimated [133]–[135]. The labor index represents the total hourly labor costs of a location relative to the labor costs of a reference location [134], [135]. Data from multiple sources [136]–[138] were used to calculate country-specific labor costs relative to the U.S. Similarly, the construction factor measures the costs associated with construction, equipment operation, and purchasing materials at a location relative to the U.S. [133]–[135]. Construction factors for 38 different countries were retrieved from Richardson’s [139] and corporate tax rates for 118 countries were sourced from the Organization for Economic Co-operation and Development database [140]. Regional averages of the different TEA inputs were used for locations in which data was not available.

4.3 Results

4.3.1 Global productivity potential

The spatial distribution of annual average areal productivity is illustrated in Figure 11. Lower temperatures and suboptimal light conditions in northern latitudes lead to low biomass yields ($2.7\text{-}5.7\text{ g m}^{-2}\text{ d}^{-1}$). The impacts of elevation are also displayed by the concentration of low yields in northern India, Bhutan, Nepal (Himalayas) and western North America (Rocky Mountains). As expected, biomass yields are maximized through cultivation in regions near the equator such as northern Brazil, Central Africa, Central America, and islands in Southeast Asia, where productivity values were predicted above $25\text{ g m}^{-2}\text{ d}^{-1}$. Furthermore, biomass productivity in the Middle East was found to peak in Yemen and ranged between $20\text{ and }25\text{ g m}^{-2}\text{ d}^{-1}$. Similar yields were found to be achievable in northern and southern Africa, southern Brazil, and northern Australia. Growth modeling results demonstrate that regions around the equator hold a greater productivity potential than regions with established algal research programs such as the U.S. and Europe [141]–[143]. This is primarily due to the weather being optimal for algal cultivation, specifically minimal temperature extremes and ample light.

The temporal variability in biomass yields was analyzed by comparing results presented in the seasonal areal productivity maps provided in Figure C - 9. Equatorial regions were found to present an average maximum-to-minimum seasonal productivity ratio of 1.1, as anticipated by the low variability of pond temperatures and consistent day light hours in central latitudes. Average pond temperatures in regions around the equator were calculated to vary between $29\text{ – }33\text{ °C}$ (Figure C - 10), a suitable range for the cultivation of UTEX 393 whose optimal cultivation temperature is 30.1 °C . In terms of light availability, equatorial regions presented larger solar losses due to cloud cover than northern latitudes (Figure C - 13), but low variability

in daily light hours supported consistent productivity. Biomass yields in equatorial locations were found to peak ($29 \text{ g m}^{-2} \text{ d}^{-1}$) in Kenya during the months following the winter solstice when solar irradiance is at its maximum in southern and eastern Africa (Figure C - 12). A larger seasonal variability was observed in southern Europe, Central Asia, and the eastern U.S. where peak global productivity values between the $28 - 29 \text{ g m}^{-2} \text{ d}^{-1}$ were predicted in the summer and winter productivity ranged between 3.8 and $8 \text{ g m}^{-2} \text{ d}^{-1}$. This is explained by a higher solar irradiance in the northern hemisphere and warmer temperatures compared to other seasons. The seasonal productivity results highlight the sensitivity of growth rates to temperature and light availability suggesting that solar irradiance has a greater impact on equatorial regions, as the culture is generally maintained at ideal temperature levels. The growth modeling additionally shows seasonal variability increases as simulation locations move away from the equator.

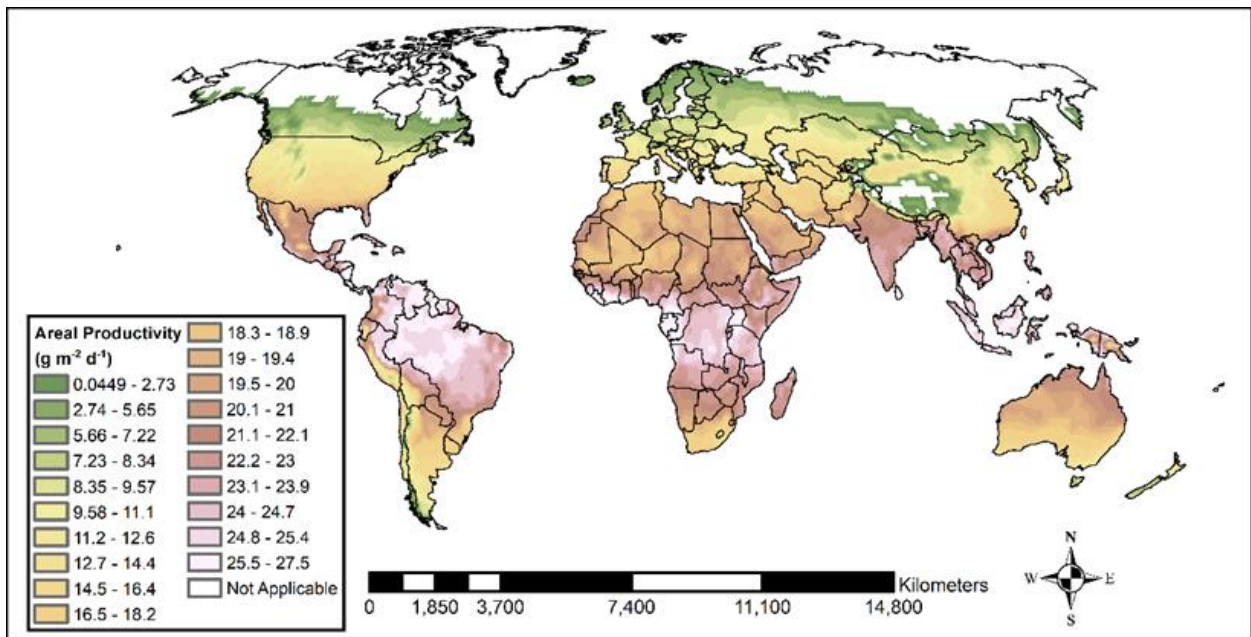


Figure 11. World map of predicted microalgae productivity potential from a validated biological growth model simulating semi-continuous cultivation of *Scenedesmus obliquus* in open-raceway ponds. Results are based on the simulation of 6,685 global locations across a 1.5° by 1.5° .

4.3.2 Global warming potential

The global warming potential (GWP) of the system was analyzed by accounting for the well-to-wheels life cycle emissions of the biofuel production process including direct land use change (DLUC) emissions with global results presented in. As illustrated in Figure 12, well-to-wheels GWP results were found to range from 21 g CO_{2eq} MJ⁻¹ to 188 g CO_{2eq} MJ⁻¹. The results show algae-based RD is superior to conventional diesel (global range of 87-97 g CO_{2eq} MJ⁻¹ [127]) in several regions, but specifically in Costa Rica, Uruguay, Brazil and central Africa where GWPs of 29-50 g CO_{2eq} MJ⁻¹ were predicted. The net GWP of the system was found to be influenced by the carbon intensity of electricity grids and affected to a minor degree by biomass yields and operational days. This is exemplified by the low GWP of France and southern Norway where cultivation is only feasible in the summer months and electricity is primarily sourced from nuclear and hydropower generators, respectively. Contrarily, warmer conditions in the northern region of India make year-round cultivation possible but GWPs were among the global highest (177-188 g CO_{2eq} MJ⁻¹) due to the large share of coal electricity in the region [127]. Similarly, the GWPs in southeastern Asian islands ranged between 114 and 177 g CO_{2eq} MJ⁻¹ due to the combined effect of carbon-intensive electrical grids and high DLUC emissions (Figure C - 14) in these countries, despite presenting optimal biomass yields. As demonstrated by these examples, the GWP of algal biofuel systems varies across geographies with the carbon intensity of regional electricity being the main contributor to these variations and DLUC representing an additional important factor.

Aside from the influence of electricity emissions, geographic variations in GWP were also driven by DLUC emissions (Figure C - 14). This is particularly the case in the Brazilian Amazon, Congo River Basin, and Southeast Asian rainforests where DLUC emissions averaged

18 g CO_{2eq} MJ⁻¹. By contrast, DLUC emissions in regions with land cover types containing low carbon stocks such as shrubland and herbaceous vegetation were found to range between 0.7-2.6 g CO_{2eq} MJ⁻¹ and be mainly located in southern Africa, central Asia, and central Australia regions. Cultivation in North Africa and the Middle East, where barren and sparse vegetation land is predominant, was predicted to generate near-neutral or minimal DLUC effects. The displacement of forests in Central America, Mexico, the eastern U.S., western Canada, and eastern Europe generated larger DLUC impacts (7 – 34 g CO_{2eq} MJ⁻¹). Finally, the cultivation of microalgae in cropland in the northern parts of France, western India, and eastern China generated negative DLUC emissions due to the avoided soil carbon emissions associated with tillage (Figure C - 14). While these areas have a negative DLUC, emissions associated with the production of RD combined with lower relative productivities result in less-than-optimal total GWP. Although biomass productivities favor equatorial locations, incorporating DLUC emissions makes these locations unsustainable from an environmental impact perspective.

The calculated GWP of five case study locations was analyzed by partitioning the total emissions into resource (Fig. 3J) and process contributions (Fig. C - 15). Results illustrate how the carbon stored in the biomass (-125 g CO_{2eq} MJ⁻¹) is distributed among HTL co-products with emissions from fuel product combustion modeled as 71 g CO_{2eq} MJ⁻¹ (Fig. 3J). Moreover, the carbon released by the gas (16 g CO_{2eq} MJ⁻¹) and aqueous phase (31 g CO_{2eq} MJ⁻¹) of HTL was equal across locations (Fig. S15), as biomass carbon composition was assumed constant. Following the carbon balance, about 6% of the carbon in the biomass stays sequestered in the biochar co-product. In New Delhi, India, and Beijing, China, where electricity is primarily sourced from coal, electricity emissions were found to represent more than 67% of the released CO_{2eq} emissions of the system. The delivery of CO₂ and the cultivation process were found to be

the most energy-intensive activities within the system boundary. Due to the availability of low-carbon electricity, upstream emissions from hydrogen and ammonia production dominate in Brasilia, Brazil and Narbonne, France (Fig. 3J). While results in Phoenix, U.S. are driven by the combined impacts of cultivation and HTL as natural gas and hydropower electricity comprise 50% of its electricity mix [127]. Upstream emissions from diammonium phosphate (DAP) production were found to have a smaller contribution (3-7%) while upstream emissions from natural gas were negligible across the five locations (Fig. 3J). Results demonstrate that the region-specific impacts of the resources driving the GWP of the system can vary across regions, and strategies to reduce the GWP of the different processes should therefore differ. For instance, using an alternative conversion pathway that eliminates hydrogen consumption could result in larger GWP reductions in Brazil than in China, but implementing a lower energy mixing regime would provide larger GWP reductions in China.

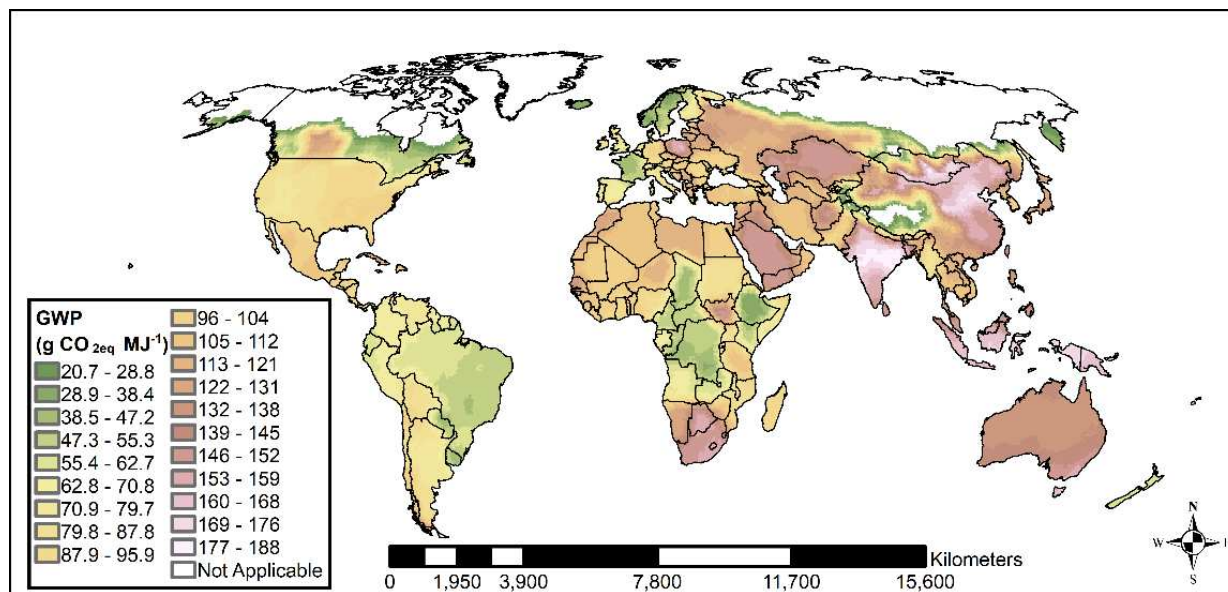


Figure 12. Net global warming potential (GWP) of microalgae-based biofuels generated by interpolating results of the simulated 6,685 global locations. Results represent well-to-wheel greenhouse gas emissions including direct land use change emissions.

4.3.3 Additional environmental impacts

The environmental impacts of electricity are not only manifested in the GWP of the system. Additional LCA results highlight the negative effects of coal electricity propagating across the environmental impact categories shown in Figure 13A-F. For example, results reveal that coal combustion causes the harmful acidification and smog impacts seen in Pretoria, South Africa, New Delhi, India and Beijing, China whereas the high eutrophication, carcinogenic, non-carcinogenic, and ecotoxicity values in these locations were associated with the impacts of coal mining and residue treatment [127]. Moreover, the treatment of wastes from nutrient production contributes to ecotoxicity and non-carcinogenic effects across all locations but has a marked influence on the acidification and eutrophication values of Narbonne, France and Brasilia, Brazil. When comparing well-to-pump acidification impacts to those of petroleum diesel production (35-96 mg SO_{2eq} MJ⁻¹ [127]), results for algal RD were found to be worse for all locations. Well-to-pump eutrophication impacts were also found to be higher than those of petroleum diesel with Narbonne, France being 1.3 times higher than the global diesel average (20 mg N_{eq} MJ⁻¹). When compared to production of RD from miscanthus in the U.S. (105 mg N_{eq} MJ⁻¹) [144], Narbonne, France and Brasilia, Brazil were found to present 40% and 55% lower eutrophication impacts, respectively; explained by the higher nutrient loss associated with conventional terrestrial crops. Based on these comparisons, the results of several environmental categories are affected by the upstream life cycle impacts of electricity, and deployment of renewables will support reducing the gap between algal RD and petroleum diesel in terms of acidification and eutrophication impacts.

The well-to-wheels life cycle fossil fuel depletion, respiratory effects, and ozone depletion impacts for the five case study locations are depicted in Figure 13G-I. As seen in

Figure 13G, energy-intensive processes such as ammonia and hydrogen production dominate fossil fuel depletion impacts as expected. Total fossil fuel depletion was found to be similar across all locations except Beijing, China, explained by most ammonia in Beijing, China is produced by gasification (less energy-intensive) instead of steam reforming [127]. Respiratory effects (Figure 13H) follow smog results (Figure 13F), however, the impacts of Phoenix, U.S. were found to be higher than those in Pretoria, South Africa. Respiratory effects are impacted by the life cycle impacts of electricity (Figure 13H) and although the share of coal electricity supplied to Phoenix, U.S., is lower than in Pretoria, South Africa, coal power plants in Phoenix, U.S. burn lignite, which generates higher PM_{2.5} emissions than combustion of hard coal [145] in Pretoria, South Africa. Lastly, ozone depletion impacts (Figure 13I) are affected by the release of chlorofluorocarbons during the extraction of petroleum and natural gas needed to produce hydrogen and ammonia [127]. Results show that hydrogen and ammonia impacts dominate fossil fuel and ozone depletion effects while respiratory effects are dominated by electricity, particularly, the type of coal used in coal power plants.

Limiting environmental impact assessment to GWP does not accurately capture all the idiosyncrasies associated with algal biofuels. Expanding the analysis to include additional environmental impact categories illustrates, on a geospatial resolution, fundamental differences in terms of unit process operations. For example, GWP results show the importance of DLUC in specific locations and electricity carbon intensity, while other environmental categories highlight the need to consider the impacts of consumables as a priority over electricity. The analysis additionally demonstrates that while algal biofuels might offer climate benefits; production in certain locations can result in more damaging air quality, eutrophication, and acidification impacts relative to petroleum diesel. Overall, the life cycle impact assessment adds to the

existing body of literature on algal biofuels by providing regionalized human health, smog formation, acidification, eutrophication, ecotoxicity, ozone depletion, and climate change impacts.

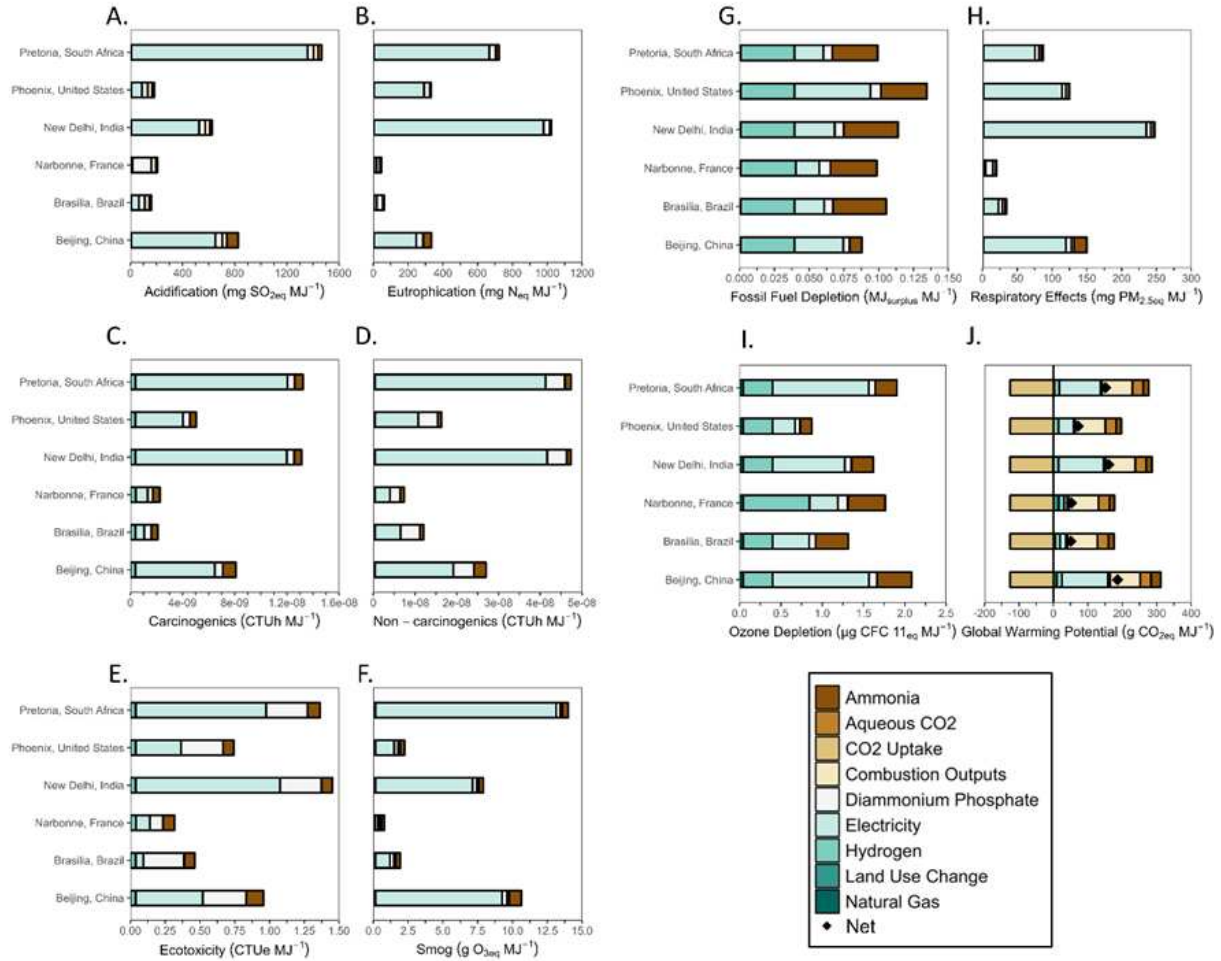


Figure 13. Life cycle assessment results of microalgae-based biofuel production at five case study locations showing results for ten environmental impact categories: A) acidification, B) eutrophication, C) carcinogenics, D) non-carcinogenics, E) ecotoxicity, F) smog, G) fossil fuel depletion, H) respiratory effects, I) ozone depletion, and J) global warming potential.

4.3.3 Techno-economic analysis

Global minimum fuel selling prices of algal RD, in 2021 U.S. dollars per liter of gasoline-equivalent (LGE), are presented in Figure 14. Minimum fuel prices are predicted to be the lowest (\$1.72 – \$2.04 LGE⁻¹) in high-productivity areas, namely, equatorial regions, Central America, and India (Figure 14). Conversely, algal RD production in northern latitudes produced

economically unviable results. Fuel prices in North Africa, central Mexico, and Australia, where productivity averaged $20 \text{ g m}^{-2} \text{ d}^{-1}$, fluctuated between $\$2.1$ and $\$2.6 \text{ LGE}^{-1}$. Regional construction factors (Figure C - 2) and labor costs (Figure C - 3) in areas with high biomass output were found to be generally lower than those of countries in the northern hemisphere, further improving the techno-economic viability in high-productivity regions. Tax rates had a minimal impact on the overall fuel prices as demonstrated by the predicted low prices in northern Brazil, despite the tax rate being among the highest globally (34%). TEA results indicate that biomass yields drive the economics of algal biofuels and regions with optimal weather conditions offer greater advantages in terms of productivity and some cases more favorable economic parameters (e.g., lower labor and construction costs) than those with suboptimal weather conditions.

In addition, TEA results for five case study locations were broken down by resource and process contributions (Figure C - 16 to Figure C - 19). Brasilia, Brazil presents the lowest minimum fuel selling price ($\$1.85 \text{ LGE}^{-1}$) and highest productivity among locations. Notably, the fuel price in Narbonne, France ($\$2.98 \text{ LGE}^{-1}$) was predicted to be higher than the results in Beijing ($\$2.85 \text{ LGE}^{-1}$) despite having higher productivity (1.3 times). The difference is derived from the fact that labor costs in Narbonne, France are twice as large as in Beijing, China (Figure C - 3). When results are fragmented into process contributions, the operational and capital expenses of biomass cultivation were determined to represent 60% of the total fuel price. This result is consistent with previous studies [22], [118], [146]. Algae require the supply of a concentrated CO_2 source to support elevated productivity. This important supply can contribute 23%-39% of the total operational costs of the system. Other required nutrients (nitrogen and phosphorous) represent 30% of the total operational costs. Consistent with previous studies [22],

[118], the open pond infrastructure represents 45% of the capital costs of cultivation (Figure C-18). Both the operational and capital costs of HTL were found to contribute to 30% of the total costs across all locations, with hydrogen accounting for 26%-44% of the variable costs of HTL. As shown by these results, the economic viability of algal RD across the case study locations is restricted by the costs of biomass production, specifically the capital costs of open pond systems and the operational costs of CO₂ delivery. It is important to note that this analysis treats CO₂ as a material expense with a constant global cost of \$45 tonne⁻¹ [18], however, the availability and processing costs of CO₂ can vary across geographies and ultimately impact fuel prices. Nonetheless, location-specific algal fuel prices enable a direct comparison to country-specific petroleum baselines for assessing the competitiveness of algal RD in local diesel markets.

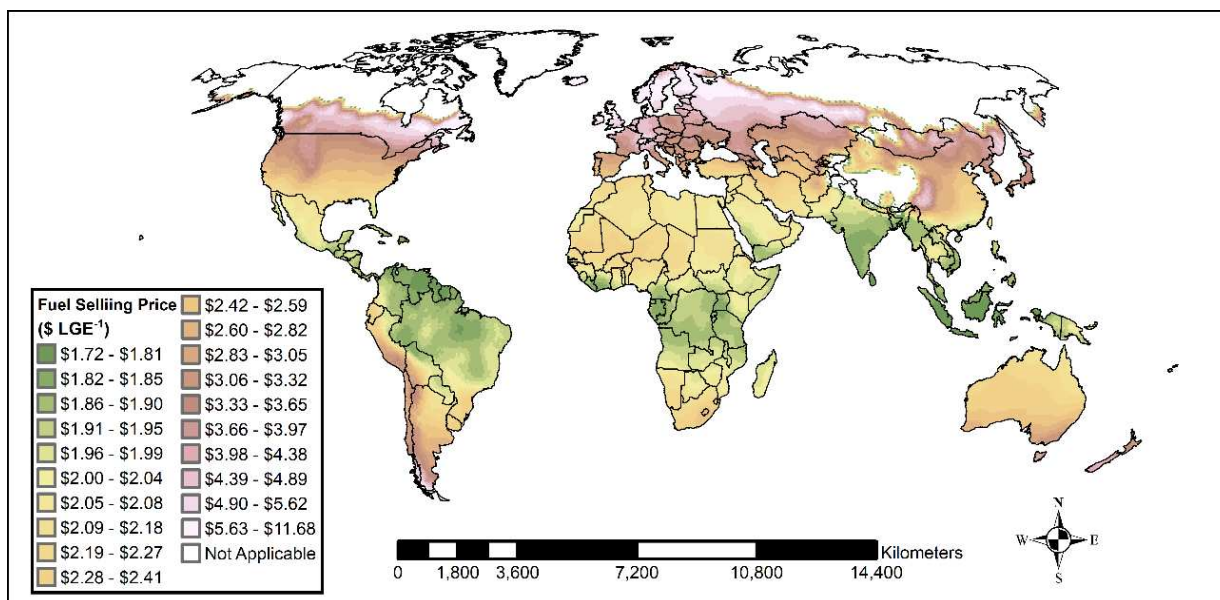


Figure 14. Global minimum fuel selling price of microalgae-based biofuels per liter of gasoline equivalent (LGE). Results represent the fuel selling price that yields a net present value of zero for the 30-year plant lifetime.

4.4 Discussion

This analysis quantifies the global economic and environmental impacts of algal RD production through geospatially and temporally resolved biophysical process modeling, LCA,

and TEA. Modeling results highlight the disparity between the underexplored productivity potential of regions with limited algal research activity and those with high algal research expenditure [147]. The estimated yields are optimistic as the effects of pond contamination were not modeled due to a lack of culture stability data and cultivation was only interrupted by freezing events. Future work will also need to focus on modeling the biochemical composition of the biomass as a function of light, nitrogen availability, and temperature [29]. Despite these limitations, the biophysical model successfully captures the effects of weather conditions on microalgal growth rates with global productivity trends agreeing with previous modeling efforts in the literature [29] but updated to reflect the current near-term potential in open raceway ponds.

Although growth modeling results identify equatorial regions as the most optimal for biomass cultivation, detrimental effects from DLUC emissions deem some of these sites unsuitable for cultivation. The LCA additionally demonstrates that production in countries with a higher share of renewable energy technologies can result in similar GWP as production of soybean RD in the U.S. ($30\text{-}33 \text{ g CO}_2\text{e MJ}^{-1}$) [148]. Nevertheless, careful consideration must be given to the interpretation of LCA results as consequential impacts were not included in the analysis. This is notably important to consider in regions lacking the electricity infrastructure for industrial-scale production of algal biofuels. For instance, Sub-Saharan Africa has among the lowest electricity access rates in the world [149] and a microalgae biorefinery would likely cause a shift in electricity demand and marginal electricity emission rates would then need to be considered. A lack of data did not enable this to be included in this analysis. However, the results presented here identify promising locations that can then be explored in more detail.

Compared to LCA, there is a larger uncertainty in TEA results as country-specific economic data was found to be scarce. For this reason, different data sources and regional

averages were used to estimate spatially resolved TEA inputs. The TEA additionally disregards variations in project interest rates across geographies and instead uses a static internal rate of return (10%) which might be more representative of high-income countries. There is a greater risk in investing in emerging economies which would translate to a higher internal rate and increase in the predicted fuel selling prices. The incorporation of local commodity prices will also reduce uncertainty in TEA results. As more data on local labor, commodity prices, construction costs and project financing become available, uncertainties in TEA results can be reduced. Beyond these limitations, outputs from this analysis help decision-makers identify potential areas for algal biofuel investment in terms of labor costs, capital expenses, and productivity potential.

Results presented here identify promising sites for algal RD production based on optimal climatic conditions and sustainability metrics. However, the availability of land, CO₂ and water must also be considered. For instance, process economics restrict algal cultivation to land with a natural 1% slope [18] and DLUC effects to shrubland and barren land. Despite not competing with cropland, algae farms must have access to a high-purity CO₂ source (e.g., hydrogen or ethanol plants) to reduce CO₂ transportation costs. More recently, research on alkaliphilic strains has been found to enable direct capture of CO₂ from ambient air [150], [151]. This not only eliminates co-location requirements but also reduces the economic and environmental penalty of concentrating and compressing CO₂ [146], [150], [151]. Aside from land and CO₂, a freshwater supply is required to make up for evaporation losses in open ponds. Although algal biofuels generate lower WFs than biofuels from terrestrial crops [44], algal cultivation can exacerbate water stress in arid regions. Cultivation of marine strains would expand potential locations to areas with available saline and brackish water resources. Based on this discussion, the results

presented here should be treated as preliminary, and concurrent sustainability and resource assessment is needed for a complete understanding of the economic viability, environmental impact, and resource requirements of algal biofuels.

The analysis highlights current techno-economic and environmental challenges associated with algal RD. As results indicate, optimal biomass yields are not enough to offset the costs of open pond cultivation and the lack of co-products from HTL makes the technology incompatible with such a capital-intensive cultivation platform. However, conversion pathways that offer revenues from high-value non-fuel products could justify the investment in open ponds [21], [22]. Valorizing algal proteins and carbohydrates through their conversion to chemicals and bioplastics represents a potential path toward economic viability for open algal cultivation. Environmental metrics could also benefit from the displacement credits derived from non-fuel co-products. In parallel, algal HTL could benefit from the integration of low-cost cultivation architectures such as attached growth systems. Attached systems eliminate the expenses of nutrients, CO₂, and biomass drying by utilizing substrates to grow algal polycultures while treating nutrient-rich water [152], [153]. Given its lower costs compared to open pond cultivation and the opportunity for water-remediation credits, attached algae cultivation could improve the economics and environmental impacts of algal fuels from HTL. While the analysis presented global locations with higher fuel prices and unfavorable environmental impacts relative to conventional diesel, some locations show promising results. Algal systems still need continued research in alternative cultivation platforms and conversion pathways that can reduce energy and material demands to support commercially viable and sustainable biofuels.

CHAPTER 5: CONCLUSIONS AND RECOMMENDATIONS

5.1 Overall conclusions

As shown by this study, robust sustainability modeling of algal biofuels requires high-fidelity spatiotemporal process models to accurately capture the impacts of fluctuating light intensity and temperatures, system scale, and ORP operations on algal growth rates. To date, the lack of detailed spatiotemporal models in the literature has limited the accurate modeling of life cycle algal water consumption metrics. This is the first modeling effort to evaluate the economic viability and environmental impacts of algal-based biofuels at a high spatiotemporal resolution with results highlighting the opportunities and challenges associated with algal biofuels. In particular, this work demonstrates that expanding sustainability assessment to regions with optimal weather conditions for algal biomass cultivation captures the true sustainability potential of algal-based biofuel. In addition, modeling outputs show that despite several regions showing lower environmental impact metrics relative to conventional petroleum fuels and biofuels, the economics of algal-based biofuels are still constrained by the high capital and operational costs of growing algal biomass. Reducing the costs of algal biomass will require minimizing material inputs (e.g., CO₂ and nutrients) as well as the development of conversion pathways that can offer revenues from high-value co-products.

5.2 Future directions of thermal and growth modeling

The thermal model built as part of this research work is the first model to account for the impacts of natural convection mass transfer in algal ponds. Although the model uses physical principles to model heat transfer effects, the semi-empirical evaporation model requires

experimental temperature and evaporation data for calibration. Due to limited experimental data from commercial ORPs, the model was only validated for a single location. Future improvements must be focused on comparing model performance relative to experimental measurements across different locations and seasons.

Additionally, future growth model refinement should focus on stochastically modeling culture failure and biomass composition, as these are important aspects of outdoor cultivation that have direct effects on process economics. As part of modeling biomass composition, the dependence of growth rates on nitrogen availability must also be captured. In parallel, stochastically modeling weather parameters to assess how interannual weather variability impacts productivity variability can provide insights on the risks of outdoor algal biomass cultivation. Finally, a better understanding of the temperature limits and exposure period of algal cultures is also necessary to correlate thermal stress with culture failure. These model improvements will translate to more accurate and robust TEA and LCA.

5.3 Future directions of algal water life cycle assessment

As evaporation losses are the primary source of water consumption, uncertainty in water LCA metrics can be reduced with thermal model improvements. In parallel, growth modeling improvements can further validate nutrient assimilation and recycling assumptions, which have major impacts on gray WFs. The feasibility of saline cultivation across the U.S. is another area of future research that will require modifications to the existing process model such as the incorporation of a salinity factor and further validation with experimental saline-strain growth data. The work could also be expanded to include additional conversion pathways to better understand the feasibility of algal biomass as a low-water alternative source of proteins.

In terms of sustainability methods, future work should focus on accounting for green water scarcity impacts. This is particularly relevant in the southeastern U.S. where algal sites rely heavily on green water resources. Moreover, improving the resolution of the nitrogen limits used in gray WFs to a watershed resolution would allow for a more localized understanding of the water pollution impacts of algal farms. Similarly, the assessment could expand to a global resolution as blue-water scarcity characterization factors are available. Future work will focus on a more robust analysis of the interannual variability of rainfall and freshwater availability to better understand the long-term effects and risks to sustainable algal cultivation. Ultimately, the water LCA framework built in this research work can be further expanded to compare water impacts of algal biofuels across different technology pathways and identify optimal cultivation sites across a variety of water LCA metrics.

5.4 Future directions of global sustainability assessment

The global sustainability assessment presented here can be further refined to reduce the uncertainty of TEA and LCA results. TEA improvements must focus on incorporating region-specific discount rates that capture the country-specific risk of investing in technologies with a low technology readiness level such as algal biofuels. In addition, determining the availability and costs of CO₂ is essential for both TEA and LCA metrics and will require extensive geographical information systems modeling. As previously outlined, the LCA lacks marginal environmental impact data, which can be impactful in many of the regions showing promising results. Understanding the marginal impacts of increasing electricity and nutrient demands in regions lacking the infrastructure to support commercial-algal biofuel production must be a primary objective of future work on this research front.

In addition, the current sustainability analysis lacks social sustainability metrics and disregards potential societal effects associated with establishing a mature algal biofuel industry. The addition of social sustainability metrics such as energy independence, environmental justice, resource security and equity would enable a holistic assessment of the sustainability of the system through economic, environmental, and social dimensions. Sustainability modeling could also be expanded to include monetized LCA impacts or estimate damage costs that could enable comparison to TEA metrics within a common scale. By monetizing health and climate impacts, the net costs of algal biofuels under different economic scenarios could also be assessed. Furthermore, stochastic multi-attribute analysis could be integrated for comparison of TRACI impacts across locations. In general, the framework built here allows for the exploration of potential technological improvements and policy scenarios that can further advance the development of sustainable algal biofuels.

REFERENCES

- [1] “Item 4(a) of the provisional agenda Durban Platform for Enhanced Action (decision 1/CP.17) Report of the Ad Hoc Working Group on the Durban Platform for Enhanced Action”, Accessed: Apr. 04, 2023. [Online]. Available: http://unfccc.int/focus/indc_portal/items/9240.php
- [2] “Mitigation of Climate Change Climate Change 2022 Working Group III contribution to the Sixth Assessment Report of the Intergovernmental Panel on Climate Change,” 2022, Accessed: Apr. 04, 2023. [Online]. Available: www.ipcc.ch
- [3] “Net Zero by 2050 – Analysis - IEA.” <https://www.iea.org/reports/net-zero-by-2050> (accessed Apr. 06, 2023).
- [4] “The U.S. National Blueprint for Transportation Decarbonization,” 2050.
- [5] “Global CO2 emissions from transport by subsector, 2000-2030 – Charts – Data & Statistics - IEA.” <https://www.iea.org/data-and-statistics/charts/global-co2-emissions-from-transport-by-subsector-2000-2030> (accessed Jan. 31, 2023).
- [6] “Biofuels – Analysis - IEA.” <https://www.iea.org/reports/biofuels> (accessed Jan. 31, 2023).
- [7] J. McGowen, E. P. Knoshaug, L. M. L. Laurens, and J. Forrester, “Outdoor annual algae productivity improvements at the pre-pilot scale through crop rotation and pond

- operational management strategies,” *Algal Res*, vol. 70, p. 102995, Mar. 2023, doi: 10.1016/J.ALGAL.2023.102995.
- [8] P. J. Lammers *et al.*, “Review of the cultivation program within the National Alliance for Advanced Biofuels and Bioproducts,” *Algal Res*, vol. 22, pp. 166–186, Mar. 2017, doi: 10.1016/J.ALGAL.2016.11.021.
- [9] R. H. Wijffels and M. J. Barbosa, “An Outlook on Microalgal Biofuels,” *Science (1979)*, vol. 329, no. 5993, pp. 796–799, Aug. 2010, doi: 10.1126/SCIENCE.1189003.
- [10] T. Cai, S. Y. Park, and Y. Li, “Nutrient recovery from wastewater streams by microalgae: Status and prospects,” *Renewable and Sustainable Energy Reviews*, vol. 19, pp. 360–369, Mar. 2013, doi: 10.1016/J.RSER.2012.11.030.
- [11] T.-D.-H. Vo *et al.*, “Influence of nitrogen species and biomass retention time on nutrient removal and biomass productivity in a microalgae-based bioreactor,” *Environ Technol Innov*, vol. 28, p. 102880, Nov. 2022, doi: 10.1016/J.ETI.2022.102880.
- [12] A. H. Alami, S. Alasad, M. Ali, and M. Alshamsi, “Investigating algae for CO₂ capture and accumulation and simultaneous production of biomass for biodiesel production,” *Science of The Total Environment*, vol. 759, p. 143529, Mar. 2021, doi: 10.1016/J.SCITOTENV.2020.143529.
- [13] R. Davis and L. Laurens, “Algal Biomass Production via Open Pond Algae Farm Cultivation: 2019 State of Technology and Future Research,” no. April, pp. 1–32, 2020, [Online]. Available: <https://www.nrel.gov/docs/fy20osti/76569.pdf>

- [14] E. P. Knoshaug, E. Wolfrum, L. M. L. Laurens, V. L. Harmon, T. A. Dempster, and J. McGowen, “Unified field studies of the algae testbed public-private partnership as the benchmark for algae agronomics,” *Sci Data*, vol. 5, no. 1, pp. 1–10, Nov. 2018, doi: 10.1038/sdata.2018.267.
- [15] R. L. White and R. A. Ryan, “Long-Term Cultivation of Algae in Open-Raceway Ponds: Lessons from the Field,” *Industrial Biotechnology*, vol. 11, no. 4, pp. 213–220, 2015, doi: 10.1089/ind.2015.0006.
- [16] V. L. Harmon *et al.*, “Reliability metrics and their management implications for open pond algae cultivation,” *Algal Res*, vol. 55, p. 102249, May 2021, doi: 10.1016/J.ALGAL.2021.102249.
- [17] Q. Béchet, A. Shilton, and B. Guieysse, “Maximizing Productivity and Reducing Environmental Impacts of Full-Scale Algal Production through Optimization of Open Pond Depth and Hydraulic Retention Time,” *Environ Sci Technol*, vol. 50, no. 7, pp. 4102–4110, Apr. 2016, doi: 10.1021/acs.est.5b05412.
- [18] R. Davis, J. Markham, C. Kinchin, N. Grundl, E. Tan, and D. Humbird, “Process Design and Economics for the Production of Algal Biomass: Algal Biomass Production in Open Pond Systems and Processing Through Dewatering for Downstream Conversion,” *National Renewable Energy Laboratory*, no. February, p. 128, 2016, [Online]. Available: www.nrel.gov/publications
- [19] S. Jones, Y. Zhu, D. Anderson, R. T. Hallen, and D. C. Elliott, “Process Design and Economics for the Conversion of Algal Biomass to Hydrocarbons : Whole Algae Hydrothermal Liquefaction and Upgrading,” 2014. doi: 10.2172/1126336.

- [20] J. S. Kruger *et al.*, “Enabling Production of Algal Biofuels by Techno-Economic Optimization of Co-Product Suites,” *Frontiers in Chemical Engineering*, vol. 0, p. 83, Jan. 2022, doi: 10.3389/FCENG.2021.803513.
- [21] R. Davis and M. Wiatrowski, “Algal Biomass Conversion to Fuels via Combined Algae Processing (CAP): 2019 State of Technology and Future Research,” 2019, Accessed: Mar. 21, 2022. [Online]. Available: www.nrel.gov/publications.
- [22] J. R. Cruce *et al.*, “Driving toward sustainable algal fuels: A harmonization of techno-economic and life cycle assessments,” *Algal Research*, vol. 54. Elsevier B.V., p. 102169, Apr. 01, 2021. doi: 10.1016/j.algal.2020.102169.
- [23] D. Quiroz, J. M. Greene, J. McGowen, and J. C. Quinn, “Geographical assessment of open pond algal productivity and evaporation losses across the United States,” *Algal Res*, vol. 60, p. 102483, Dec. 2021, doi: 10.1016/J.ALGAL.2021.102483.
- [24] Q. Béchet, A. Shilton, O. B. Fringer, R. Munoz, and B. Guieysse, “Mechanistic modeling of broth temperature in outdoor photobioreactors,” *Environ Sci Technol*, vol. 44, no. 6, pp. 2197–2203, 2010, doi: 10.1021/es903214u.
- [25] J. M. Greene, D. Quiroz, S. Compton, P. J. Lammers, and J. C. Quinn, “A validated thermal and biological model for predicting algal productivity in large scale outdoor cultivation systems,” *Algal Res*, vol. 54, p. 102224, Apr. 2021, doi: 10.1016/j.algal.2021.102224.
- [26] J. Quinn, L. de Winter, and T. Bradley, “Microalgae bulk growth model with application to industrial scale systems,” *Bioresour Technol*, vol. 102, no. 8, pp. 5083–5092, 2011, doi: 10.1016/j.biortech.2011.01.019.

- [27] Q. Béchet, B. Sialve, J. P. Steyer, A. Shilton, and B. Guieysse, “Comparative assessment of evaporation models in algal ponds,” *Algal Res*, vol. 35, no. June, pp. 283–291, 2018, doi: 10.1016/j.algal.2018.08.022.
- [28] C. Quiroz-Arita *et al.*, “A dynamic thermal algal growth model for pilot-scale open-channel raceways,” *Bioresour Technol Rep*, vol. 10, no. February, p. 100405, 2020, doi: 10.1016/j.biteb.2020.100405.
- [29] J. W. Moody, C. M. McGinty, and J. C. Quinn, “Global evaluation of biofuel potential from microalgae,” *Proc Natl Acad Sci U S A*, vol. 111, no. 23, pp. 8691–8696, Jun. 2014, doi: 10.1073/pnas.1321652111.
- [30] Q. Béchet, A. Shilton, and B. Guieysse, “Full-scale validation of a model of algal productivity,” *Environ Sci Technol*, vol. 48, no. 23, pp. 13826–13833, 2014, doi: 10.1021/es503204e.
- [31] Q. Béchet, A. Shilton, J. B. K. Park, R. J. Craggs, and B. Guieysse, “Universal temperature model for shallow algal ponds provides improved accuracy,” *Environ Sci Technol*, vol. 45, no. 8, pp. 3702–3709, 2011, doi: 10.1021/es1040706.
- [32] B. Guieysse, Q. Béchet, and A. Shilton, “Variability and uncertainty in water demand and water footprint assessments of fresh algae cultivation based on case studies from five climatic regions,” *Bioresour Technol*, vol. 128, pp. 317–323, Jan. 2013, doi: 10.1016/j.biortech.2012.10.096.
- [33] L. Batan, J. C. Quinn, and T. H. Bradley, “Analysis of water footprint of a photobioreactor microalgae biofuel production system from blue, green and lifecycle perspectives,” *Algal Res*, vol. 2, no. 3, pp. 196–203, Jul. 2013, doi: 10.1016/J.ALGAL.2013.02.003.

- [34] A. F. Clarens, E. P. Resurreccion, M. A. White, and L. M. Colosi, “Environmental life cycle comparison of algae to other bioenergy feedstocks,” *Environ Sci Technol*, vol. 44, no. 5, pp. 1813–1819, 2010, doi: 10.1021/es902838n.
- [35] P. W. Gerbens-Leenes, L. Xu, G. J. de Vries, and A. Y. Hoekstra, “The blue water footprint and land use of biofuels from algae,” *Water Resour Res*, vol. 50, no. 11, pp. 8549–8563, Nov. 2014, doi: 10.1002/2014WR015710.
- [36] H. Xu, U. Lee, A. M. Coleman, M. S. Wigmosta, and M. Wang, “Assessment of algal biofuel resource potential in the United States with consideration of regional water stress,” *Algal Res*, vol. 37, pp. 30–39, Jan. 2019, doi: 10.1016/J.ALGAL.2018.11.002.
- [37] H. Xu *et al.*, “Balancing Water Sustainability and Productivity Objectives in Microalgae Cultivation: Siting Open Ponds by Considering Seasonal Water-Stress Impact Using AWARE-US,” *Environ Sci Technol*, vol. 54, no. 4, pp. 2091–2102, Feb. 2020, doi: 10.1021/ACS.EST.9B05347/SUPPL_FILE/ES9B05347_SI_001.PDF.
- [38] M. Q. Frank, Edward D., Han, J., Palou-Rivera, I., Elgowainy, A., Wang, “Life-Cycle Analysis of Algal Lipid Fuels with the GREET Model,” 2011.
- [39] Q. Béchet, A. Shilton, and B. Guieysse, “Maximizing Productivity and Reducing Environmental Impacts of Full-Scale Algal Production through Optimization of Open Pond Depth and Hydraulic Retention Time,” *Environ Sci Technol*, vol. 50, no. 7, pp. 4102–4110, Apr. 2016, doi: 10.1021/ACS.EST.5B05412/SUPPL_FILE/ES5B05412_SI_001.PDF.
- [40] J. Roles, J. Yarnold, K. Hussey, and B. Hankamer, “Techno-economic evaluation of microalgae high-density liquid fuel production at 12 international locations,” *Biotechnol*

- Biofuels*, vol. 14, no. 1, pp. 1–19, Dec. 2021, doi: 10.1186/S13068-021-01972-4/FIGURES/4.
- [41] L. Ou *et al.*, “Utilizing high-purity carbon dioxide sources for algae cultivation and biofuel production in the United States: Opportunities and challenges,” *J Clean Prod*, vol. 321, p. 128779, Oct. 2021, doi: 10.1016/J.JCLEPRO.2021.128779.
- [42] E. R. Venteris, R. L. Skaggs, M. S. Wigmosta, and A. M. Coleman, “A national-scale comparison of resource and nutrient demands for algae-based biofuel production by lipid extraction and hydrothermal liquefaction,” *Biomass Bioenergy*, vol. 64, pp. 276–290, May 2014, doi: 10.1016/J.BIOMBIOE.2014.02.001.
- [43] M. S. Wigmosta, A. M. Coleman, R. J. Skaggs, M. H. Huesemann, and L. J. Lane, “National microalgae biofuel production potential and resource demand,” *Water Resour Res*, vol. 47, no. 4, pp. 1–13, 2011, doi: 10.1029/2010WR009966.
- [44] D. Quiroz, J. M. Greene, and J. C. Quinn, “Regionalized Life-Cycle Water Impacts of Microalgal-Based Biofuels in the United States,” *Environ Sci Technol*, Oct. 2022, doi: 10.1021/ACS.EST.2C05552.
- [45] J. C. Quinn, K. B. Catton, S. Johnson, and T. H. Bradley, “Geographical Assessment of Microalgae Biofuels Potential Incorporating Resource Availability,” *Bioenergy Res*, vol. 6, no. 2, pp. 591–600, Jun. 2013, doi: 10.1007/S12155-012-9277-0/TABLES/2.
- [46] J. C. Quinn and R. Davis, “The potentials and challenges of algae based biofuels: A review of the techno-economic, life cycle, and resource assessment modeling,” *Bioresour Technol*, 2015, doi: 10.1016/j.biortech.2014.10.075.

- [47] J. R. Cruce *et al.*, “Driving toward sustainable algal fuels: A harmonization of techno-economic and life cycle assessments,” *Algal Research*, vol. 54. Elsevier B.V., p. 102169, Apr. 01, 2021. doi: 10.1016/j.algal.2020.102169.
- [48] K. Sander and G. S. Murthy, “Life cycle analysis of algae biodiesel,” *International Journal of Life Cycle Assessment*, vol. 15, no. 7, pp. 704–714, Aug. 2010, doi: 10.1007/s11367-010-0194-1.
- [49] J. Yang, M. Xu, X. Zhang, Q. Hu, M. Sommerfeld, and Y. Chen, “Life-cycle analysis on biodiesel production from microalgae: Water footprint and nutrients balance,” *Bioresour Technol*, vol. 102, no. 1, pp. 159–165, Jan. 2011, doi: 10.1016/j.biortech.2010.07.017.
- [50] B. Guieysse, Q. Béchet, and A. Shilton, “Variability and uncertainty in water demand and water footprint assessments of fresh algae cultivation based on case studies from five climatic regions,” *Bioresour Technol*, vol. 128, pp. 317–323, Jan. 2013, doi: 10.1016/j.biortech.2012.10.096.
- [51] M. Q. Frank, Edward D., Han, J., Palou-Rivera, I., Elgowainy, A., Wang, “Life-Cycle Analysis of Algal Lipid Fuels with the GREET Model,” 2011.
- [52] M. S. Wigmosta, A. M. Coleman, R. J. Skaggs, M. H. Huesemann, and L. J. Lane, “National microalgae biofuel production potential and resource demand,” *Water Resour Res*, vol. 47, no. 4, pp. 1–13, 2011, doi: 10.1029/2010WR009966.
- [53] Q. Béchet, B. Sialve, J. P. Steyer, A. Shilton, and B. Guieysse, “Comparative assessment of evaporation models in algal ponds,” *Algal Res*, vol. 35, no. June, pp. 283–291, 2018, doi: 10.1016/j.algal.2018.08.022.

- [54] K. Friedrich *et al.*, “Reservoir evaporation in the Western United States,” *Bull Am Meteorol Soc*, vol. 99, no. 1, pp. 167–187, 2018, doi: 10.1175/BAMS-D-15-00224.1.
- [55] A. F. Clarens, E. P. Resurreccion, M. A. White, and L. M. Colosi, “Environmental life cycle comparison of algae to other bioenergy feedstocks,” *Environ Sci Technol*, vol. 44, no. 5, pp. 1813–1819, 2010, doi: 10.1021/es902838n.
- [56] K. R. Helfrich, E. E. Adams, A. L. Godbey, and D. R. F. Harleman, “Evaluation of Models for Predicting Evaporative Water Loss in Cooling Impoundments,” *Report*, no. March, p. 164, 1982.
- [57] E. Sartori, “A critical review on equations employed for the calculation of the evaporation rate from free water surfaces,” *Solar Energy*, vol. 68, no. 1, pp. 77–89, 2000, doi: 10.1016/S0038-092X(99)00054-7.
- [58] K. D. Ryan, Patrick J, Harleman, Donald R.F., Stolzenbach, “Surface Heat Loss From Cooling Ponds,” *Water Resour Res*, vol. 16, no. 5, 1974.
- [59] E. Sartori, “A critical review on equations employed for the calculation of the evaporation rate from free water surfaces,” *Solar Energy*, vol. 68, no. 1, pp. 77–89, 2000, doi: 10.1016/S0038-092X(99)00054-7.
- [60] E. E. Adams, D. J. Cosler, and K. R. Helfrich, “Evaporation from heated water bodies: Predicting combined forced plus free convection,” *Water Resour Res*, vol. 26, no. 3, pp. 425–435, 1990, doi: 10.1029/WR026i003p00425.
- [61] G. Khawam, P. Waller, S. Gao, S. Edmundson, M. S. Wigmosta, and K. Ogden, “Model of temperature, evaporation, and productivity in elevated experimental algae raceways and

- comparison with commercial raceways,” *Algal Res*, vol. 39, p. 101448, May 2019, doi: 10.1016/j.algal.2019.101448.
- [62] K. Friedrich *et al.*, “Reservoir evaporation in the Western United States,” *Bull Am Meteorol Soc*, vol. 99, no. 1, pp. 167–187, 2018, doi: 10.1175/BAMS-D-15-00224.1.
- [63] S. Wilcox and W. Marion, “Users manual for TMY3 data sets,” *Renew Energy*, 2008, doi: NREL/TP-581-43156.
- [64] T. L. Bergman, A. S. Lavine, F. P. Incropera, and D. P. Dewitt, *Fundamentals of Heat and Mass Transfer*, 7th ed. John Wiley & Sons, Ltd, 2011.
- [65] G. Khawam, P. Waller, S. Gao, S. Edmundson, M. S. Wigmosta, and K. Ogden, “Model of temperature, evaporation, and productivity in elevated experimental algae raceways and comparison with commercial raceways,” *Algal Res*, vol. 39, p. 101448, May 2019, doi: 10.1016/j.algal.2019.101448.
- [66] D. Brunt, “Notes on radiation in the atmosphere. I,” *Quarterly Journal of the Royal Meteorological Society*, vol. 58, no. 247, pp. 389–420, Oct. 1932, doi: 10.1002/qj.49705824704.
- [67] A. Q. Béchet, A. Shilton, J. B. K. Park, R. J. Craggs, and B. Guieysse, “Universal temperature model algal ponds,” 2010.
- [68] J. Lamoureux, T. R. Tiersch, and S. G. Hall, “Pond heat and temperature regulation (PHATR): Modeling temperature and energy balances in earthen outdoor aquaculture ponds,” *Aquac Eng*, vol. 34, no. 2, pp. 103–116, Mar. 2006, doi: 10.1016/j.aquaeng.2005.06.002.

- [69] T. L. Bergman, A. S. Lavine, F. P. Incropera, and D. P. Dewitt, *Fundamentals of Heat and Mass Transfer*, 7th ed. John Wiley & Sons, Ltd, 2011.
- [70] J. Lamoureux, T. R. Tiersch, and S. G. Hall, “Pond heat and temperature regulation (PHATR): Modeling temperature and energy balances in earthen outdoor aquaculture ponds,” *Aquac Eng*, vol. 34, no. 2, pp. 103–116, Mar. 2006, doi: 10.1016/j.aquaeng.2005.06.002.
- [71] J. R. Lloyd and W. R. Moran, “Natural Convection Adjacent To Horizontal Surface of Various Planforms.,” *American Society of Mechanical Engineers (Paper)*, no. 74-WA/HT-66, pp. 443–447, 1974.
- [72] J. R. Lloyd and W. R. Moran, “Natural Convection Adjacent To Horizontal Surface of Various Planforms.,” *American Society of Mechanical Engineers (Paper)*, no. 74-WA/HT-66, pp. 443–447, 1974.
- [73] V. Cepák, P. Příbyl, J. Kvíderová, and J. Lukavský, “Comparative study of zooid and non-zooid forming strains of *Scenedesmus obliquus*. Physiology and cytomorphology,” *Folia Microbiol (Praha)*, vol. 51, no. 4, pp. 349–356, 2006, doi: 10.1007/BF02931829/METRICS.
- [74] J. Liu, C. Yuan, G. Hu, and F. Li, “Effects of light intensity on the growth and lipid accumulation of microalga *Scenedesmus* sp. 11-1 under nitrogen limitation,” *Appl Biochem Biotechnol*, vol. 166, no. 8, pp. 2127–2137, Apr. 2012, doi: 10.1007/S12010-012-9639-2/TABLES/1.
- [75] B. Gris, T. Morosinotto, G. M. Giacometti, A. Bertucco, and E. Sforza, “Cultivation of *Scenedesmus obliquus* in photobioreactors: effects of light intensities and light-dark

- cycles on growth, productivity, and biochemical composition,” *Appl Biochem Biotechnol*, vol. 172, no. 5, pp. 2377–2389, 2014, doi: 10.1007/S12010-013-0679-Z.
- [76] S. J. Edmundson and M. H. Huesemann, “The dark side of algae cultivation: Characterizing night biomass loss in three photosynthetic algae, *Chlorella sorokiniana*, *Nannochloropsis salina* and *Picochlorum* sp.,” *Algal Res*, vol. 12, pp. 470–476, Nov. 2015, doi: 10.1016/J.ALGAL.2015.10.012.
- [77] M. Sengupta, Y. Xie, A. Lopez, A. Habte, G. Maclaurin, and J. Shelby, “The National Solar Radiation Data Base (NSRDB),” *Renewable and Sustainable Energy Reviews*, vol. 89. Elsevier Ltd, pp. 51–60, Jun. 01, 2018. doi: 10.1016/j.rser.2018.03.003.
- [78] S. Wilcox and W. Marion, “Users manual for TMY3 data sets,” *Renew Energy*, 2008, doi: NREL/TP-581-43156.
- [79] J. R. Benemann, R. P. Goebel, J. C. Weissman, and D. C. Augenstein, “Microalgae as a source of liquid fuels. Final technical report. [200 references],” May 1982. doi: 10.2172/6374113.
- [80] J. R. Benemann and W. J. Oswald, “Systems and economic analysis of microalgae ponds for conversion of CO₂ to biomass. Final report,” Pittsburgh, PA, and Morgantown, WV, Mar. 1996. doi: 10.2172/493389.
- [81] T. J. Lundquist, I. Woertz, N. W. T. Quinn, and J. R. Benemann, “A Realistic Technology and Engineering Assessment of Algae Biofuel Production,” 2010.
- [82] R. Davis *et al.*, “Renewable Diesel from Algal Lipids: An Integrated Baseline for Cost, Emissions, and Resource Potential from a Harmonized Model,” 2012.

- [83] J. C. Quinn, K. B. Catton, S. Johnson, and T. H. Bradley, “Geographical Assessment of Microalgae Biofuels Potential Incorporating Resource Availability,” *Bioenergy Res*, vol. 6, no. 2, pp. 591–600, 2013, doi: 10.1007/s12155-012-9277-0.
- [84] R. Davis *et al.*, “Process Design and Economics for the Conversion of Lignocellulosic Biomass to Hydrocarbons: Dilute-Acid and Enzymatic Deconstruction of Biomass to Sugars and Catalytic Conversion of Sugars to Hydrocarbons,” no. March, p. 133, 2015.
- [85] R. Davis *et al.*, “Renewable Diesel from Algal Lipids: An Integrated Baseline for Cost, Emissions, and Resource Potential from a Harmonized Model,” 2012.
- [86] J. McGowen *et al.*, “The Algae Testbed Public-Private Partnership (ATP3) framework; establishment of a national network of testbed sites to support sustainable algae production,” *Algal Res*, vol. 25, pp. 168–177, Jul. 2017, doi: 10.1016/j.algal.2017.05.017.
- [87] L. Rodolfi *et al.*, “Microalgae for oil: Strain selection, induction of lipid synthesis and outdoor mass cultivation in a low-cost photobioreactor,” *Biotechnol Bioeng*, vol. 102, no. 1, pp. 100–112, Jan. 2009, doi: 10.1002/bit.22033.
- [88] E. R. Venteris, R. C. McBride, A. M. Coleman, R. L. Skaggs, and M. S. Wigmosta, “Siting Algae Cultivation Facilities for Biofuel Production in the United States: Trade-Offs between Growth Rate, Site Constructability, Water Availability, and Infrastructure,” 2014, doi: 10.1021/es4045488.
- [89] N. Sun, R. L. Skaggs, M. S. Wigmosta, A. M. Coleman, M. H. Huesemann, and S. J. Edmundson, “Growth modeling to evaluate alternative cultivation strategies to enhance national microalgal biomass production,” *Algal Res*, vol. 49, p. 101939, Aug. 2020, doi: 10.1016/j.algal.2020.101939.

- [90] C. F. Dewes, I. Rangwala, J. J. Barsugli, M. T. Hobbins, and S. Kumar, “Drought risk assessment under climate change is sensitive to methodological choices for the estimation of evaporative demand,” *PLoS One*, vol. 12, no. 3, p. e0174045, Mar. 2017, doi: 10.1371/journal.pone.0174045.
- [91] R. Davis and L. Laurens, “Algal Biomass Production via Open Pond Algae Farm Cultivation: 2019 State of Technology and Future Research,” no. April, pp. 1–32, 2020.
- [92] M. D. Somers and J. C. Quinn, “Sustainability of carbon delivery to an algal biorefinery: A techno-economic and life-cycle assessment,” *Journal of CO2 Utilization*, 2019, doi: 10.1016/j.jcou.2019.01.007.
- [93] R. Davis *et al.*, “Process Design and Economics for the Conversion of Algal Biomass to Biofuels: Algal Biomass Fractionation to Lipid- and Carbohydrate-Derived Fuel Products,” 2013.
- [94] A. P. Williams *et al.*, “Large contribution from anthropogenic warming to an emerging North American megadrought,” *Science (1979)*, vol. 368, no. 6488, pp. 314–318, Apr. 2020, doi: 10.1126/SCIENCE.AAZ9600/SUPPL_FILE/AAZ9600_WILLIAMS_SM.PDF.
- [95] A. Y. Hoekstra, A. K. Chapgain, M. M. Aldaya, and M. M. Mekonnen, *The Water Footprint Assessment Manual*. London: Earthscan, 2011.
- [96] A. M. Boulay *et al.*, “Consensus building on the development of a stress-based indicator for LCA-based impact assessment of water consumption: outcome of the expert workshops,” *International Journal of Life Cycle Assessment*, vol. 20, no. 5, pp. 577–583, May 2015, doi: 10.1007/S11367-015-0869-8/FIGURES/1.

- [97] A. M. Boulay *et al.*, “The WULCA consensus characterization model for water scarcity footprints: assessing impacts of water consumption based on available water remaining (AWARE),” *International Journal of Life Cycle Assessment*, vol. 23, no. 2, pp. 368–378, Feb. 2018, doi: 10.1007/S11367-017-1333-8/FIGURES/2.
- [98] P. W. Gerbens-Leenes, L. Xu, G. J. de Vries, and A. Y. Hoekstra, “The blue water footprint and land use of biofuels from algae,” *Water Resour Res*, vol. 50, no. 11, pp. 8549–8563, Nov. 2014, doi: 10.1002/2014WR015710.
- [99] P. H. Chen and J. C. Quinn, “Microalgae to biofuels through hydrothermal liquefaction: Open-source techno-economic analysis and life cycle assessment,” *Appl Energy*, vol. 289, p. 116613, May 2021, doi: 10.1016/J.APENERGY.2021.116613.
- [100] P. Nguyen *et al.*, “The CHRS Data Portal, an easily accessible public repository for PERSIANN global satellite precipitation data,” *Scientific Data 2019 6:1*, vol. 6, no. 1, pp. 1–10, Jan. 2019, doi: 10.1038/sdata.2018.296.
- [101] B. Zhang and K. Ogden, “Nitrogen balances and impacts on the algae cultivation-extraction-digestion-cultivation process,” *Algal Res*, vol. 39, p. 101434, May 2019, doi: 10.1016/J.ALGAL.2019.101434.
- [102] M. J. Griffiths, R. P. van Hille, and S. T. L. Harrison, “The effect of nitrogen limitation on lipid productivity and cell composition in *Chlorella vulgaris*,” *Appl Microbiol Biotechnol*, vol. 98, no. 5, pp. 2345–2356, Mar. 2014, doi: 10.1007/S00253-013-5442-4/TABLES/2.
- [103] Z. Ikaran, S. Suárez-Alvarez, I. Urreta, and S. Castañón, “The effect of nitrogen limitation on the physiology and metabolism of *Chlorella vulgaris* var L3,” *Algal Res*, vol. 10, pp. 134–144, Jul. 2015, doi: 10.1016/J.ALGAL.2015.04.023.

- [104] K. D. Fagerstone, J. C. Quinn, T. H. Bradley, S. K. de Long, and A. J. Marchese, “Quantitative measurement of direct nitrous oxide emissions from microalgae cultivation,” *Environ Sci Technol*, vol. 45, no. 21, pp. 9449–9456, Nov. 2011, doi: 10.1021/ES202573F/SUPPL_FILE/ES202573F_SI_001.PDF.
- [105] GREET, “GREET Life Cycle Model User Guide,” *Argonne National Laboratory*, pp. 169–232, 2020, [Online]. Available: www.impact-test.co.uk
- [106] U. Lee *et al.*, “Regional and seasonal water stress analysis of United States thermoelectricity,” *J Clean Prod*, vol. 270, p. 122234, Oct. 2020, doi: 10.1016/j.jclepro.2020.122234.
- [107] “THE EMISSIONS & GENERATION RESOURCE INTEGRATED DATABASE eGRID Technical Guide with Year 2019 Data Clean Air Markets Division”.
- [108] U. Lee, H. Xu, J. Daystar, A. Elgowainy, and M. Wang, “AWARE-US: Quantifying water stress impacts of energy systems in the United States,” *Science of the Total Environment*, vol. 648, pp. 1313–1322, Jan. 2019, doi: 10.1016/j.scitotenv.2018.08.250.
- [109] W. Farooq, W. I. Suh, M. S. Park, and J. W. Yang, “Water use and its recycling in microalgae cultivation for biofuel application,” *Bioresour Technol*, vol. 184, pp. 73–81, May 2015, doi: 10.1016/J.BIORTECH.2014.10.140.
- [110] Y. W. Chiu and M. Wu, “Assessing county-level water footprints of different cellulosic-biofuel feedstock pathways,” *Environ Sci Technol*, vol. 46, no. 16, pp. 9155–9162, Aug. 2012, doi: 10.1021/ES3002162/SUPPL_FILE/ES3002162_SI_001.PDF.

- [111] M. Wu, Y. Chiu, and Y. Demissie, “Quantifying the regional water footprint of biofuel production by incorporating hydrologic modeling,” *Water Resour Res*, vol. 48, no. 10, p. 10518, Oct. 2012, doi: 10.1029/2011WR011809.
- [112] “Switchgrass, Perennial Grass-to-Renewable Biodiesel Blend, Biochemical”.
- [113] “Wheat Straw, Wheat Straw-to-Ethanol, Bioelectricity,” 2013.
- [114] Argonne National Laboratory, “Soybean, Soybean-to-Biodiesel,” 2013.
- [115] “Corn Grain-Grain, Fermentation, Dry milling,” *Argonne National Laboratory*, 2013.
- [116] Y. W. Chiu and M. Wu, “Assessing county-level water footprints of different cellulosic-biofuel feedstock pathways,” *Environ Sci Technol*, vol. 46, no. 16, pp. 9155–9162, Aug. 2012, doi: 10.1021/ES3002162/SUPPL_FILE/ES3002162_SI_001.PDF.
- [117] H. Xu and M. Wu, “A First Estimation of County-Based Green Water Availability and Its Implications for Agriculture and Bioenergy Production in the United States,” *Water 2018, Vol. 10, Page 148*, vol. 10, no. 2, p. 148, Feb. 2018, doi: 10.3390/W10020148.
- [118] R. E. Davis *et al.*, “2017 Algae Harmonization Study: Evaluating the Potential for Future Algal Biofuel Costs, Sustainability, and Resource Assessment from Harmonized Modeling,” Golden, CO (United States), Aug. 2018. doi: 10.2172/1468333.
- [119] Q. Tu, M. Eckelman, and J. Zimmerman, “Meta-analysis and Harmonization of Life Cycle Assessment Studies for Algae Biofuels,” *Environ Sci Technol*, vol. 51, no. 17, pp. 9419–9432, Sep. 2017, doi: 10.1021/ACS.EST.7B01049/SUPPL_FILE/ES7B01049_SI_001.PDF.

- [120] B. D. Beckstrom, M. H. Wilson, M. Crocker, and J. C. Quinn, “Bioplastic feedstock production from microalgae with fuel co-products: A techno-economic and life cycle impact assessment,” *Algal Res*, vol. 46, p. 101769, Mar. 2020, doi: 10.1016/j.algal.2019.101769.
- [121] L. M. Wendt *et al.*, “Anaerobic Storage and Conversion of Microalgal Biomass to Manage Seasonal Variation in Cultivation,” *ACS Sustain Chem Eng*, vol. 8, no. 35, pp. 13310–13317, Sep. 2020, doi: 10.1021/ACSSUSCHEMENG.0C03790/ASSET/IMAGES/MEDIUM/SC0C03790_0004.GIF.
- [122] S. Leow, J. R. Witter, D. R. Vardon, B. K. Sharma, J. S. Guest, and T. J. Strathmann, “Prediction of microalgae hydrothermal liquefaction products from feedstock biochemical composition,” *Green Chemistry*, vol. 17, no. 6, pp. 3584–3599, Jun. 2015, doi: 10.1039/C5GC00574D.
- [123] H. Hersbach *et al.*, “The ERA5 global reanalysis,” *Quarterly Journal of the Royal Meteorological Society*, vol. 146, no. 730, pp. 1999–2049, Jul. 2020, doi: 10.1002/QJ.3803.
- [124] “A quick tour of ArcMap—ArcMap | Documentation.” https://desktop.arcgis.com/en/arcmap/latest/map/main/a-quick-tour-of-arcmap.htm#ESRI_SECTION1_37E2CFDB81464043964136A98E8035BC (accessed Mar. 29, 2023).

- [125] J. Bare, “TRACI 2.0: The tool for the reduction and assessment of chemical and other environmental impacts 2.0,” *Clean Technol Environ Policy*, vol. 13, no. 5, pp. 687–696, Jan. 2011, doi: 10.1007/S10098-010-0338-9/METRICS.
- [126] P. Forster *et al.*, “The Earth’s energy budget, climate feedbacks, and climate sensitivity,” 2021.
- [127] G. Wernet, C. Bauer, B. Steubing, J. Reinhard, E. Moreno-Ruiz, and B. Weidema, “The ecoinvent database version 3 (part I): overview and methodology,” *International Journal of Life Cycle Assessment*, vol. 21, no. 9, pp. 1218–1230, Sep. 2016, doi: 10.1007/S11367-016-1087-8/METRICS.
- [128] D. L. Sills, L. G. van Doren, C. Beal, and E. Raynor, “The effect of functional unit and co-product handling methods on life cycle assessment of an algal biorefinery,” *Algal Res*, vol. 46, p. 101770, Mar. 2020, doi: 10.1016/J.ALGAL.2019.101770.
- [129] C. M. Beal *et al.*, “Algal biofuel production for fuels and feed in a 100-ha facility: A comprehensive techno-economic analysis and life cycle assessment,” *Algal Res*, vol. 10, pp. 266–279, Jul. 2015, doi: 10.1016/J.ALGAL.2015.04.017.
- [130] “Argonne GREET Publication : Summary of Expansions and Updates in GREET® 2021.” <https://greet.es.anl.gov/publication-greet-2021-summary> (accessed Jan. 29, 2023).
- [131] H. S. Eggleston, L. Buendia, K. Miwa, T. Ngara, and K. Tanabe, “2006 IPCC guidelines for national greenhouse gas inventories,” 2006.

- [132] A. Dutta *et al.*, “Process Design and Economics for Conversion of Lignocellulosic Biomass to Ethanol: Thermochemical Pathway by Indirect Gasification and Mixed Alcohol Synthesis,” May 2011, doi: 10.2172/1015885.
- [133] D. S. Remer, S. Lin, N. Yu, and K. Hsin, “An update on cost and scale-up factors, international inflation indexes and location factors,” *Int J Prod Econ*, vol. 114, no. 1, pp. 333–346, Jul. 2008, doi: 10.1016/j.ijpe.2008.02.011.
- [134] T. Brown, *Engineering economics and economic design for process engineers*.
- [135] K. Khumphreys, “PROJECT AND COST ENGINEERS’ HANDBOOK, Fourth Edition,” 2005.
- [136] “India’s Organized Manufacturing Sector : U.S. Bureau of Labor Statistics.” <https://www.bls.gov/fls/india.htm#Chart05> (accessed Jan. 29, 2023).
- [137] “Statistics on labour costs - ILOSTAT.” <https://ilostat.ilo.org/topics/labour-costs/#> (accessed Jan. 29, 2023).
- [138] F. Carvalho, J. Portugal-pereira, M. Junginger, and A. Szklo, “Biofuels for maritime transportation: A spatial, techno-economic, and logistic analysis in brazil, europe, south africa, and the usa,” *Energies (Basel)*, vol. 14, no. 16, p. 4980, Aug. 2021, doi: 10.3390/EN14164980/S1.
- [139] C. D. O. Line, “Richardson international construction factors manual,” *Pahrump, NV*, 2008.
- [140] “Table II.1. Statutory corporate income tax rate.” https://stats.oecd.org/index.aspx?DataSetCode=Table_III (accessed Jan. 29, 2023).

- [141] “Sustainable development of algal biofuels in the United States,” *Sustainable Development of Algal Biofuels in the United States*, pp. 1–231, Jan. 2013, doi: 10.17226/13437.
- [142] R. Araújo *et al.*, “Current Status of the Algae Production Industry in Europe: An Emerging Sector of the Blue Bioeconomy,” *Front Mar Sci*, vol. 7, p. 1247, Jan. 2021, doi: 10.3389/FMARS.2020.626389/BIBTEX.
- [143] E. M. Trentacoste, A. M. Martinez, and T. Zenk, “The place of algae in agriculture: Policies for algal biomass production,” *Photosynth Res*, vol. 123, no. 3, pp. 305–315, Mar. 2015, doi: 10.1007/S11120-014-9985-8/FIGURES/4.
- [144] I. J. Okeke, K. Sahoo, N. Kaliyan, and S. Mani, “Life cycle assessment of renewable diesel production via anaerobic digestion and Fischer-Tropsch synthesis from miscanthus grown in strip-mined soils,” *J Clean Prod*, vol. 249, p. 119358, Mar. 2020, doi: 10.1016/J.JCLEPRO.2019.119358.
- [145] “Update of Emission Factors of Greenhouse Gases and Criteria Air Pollutants, and Generation Efficiencies of the U.S. Electricity Generation Sector Energy Systems Division.” [Online]. Available: www.anl.gov.
- [146] M. D. Somers and J. C. Quinn, “Sustainability of carbon delivery to an algal biorefinery: A techno-economic and life-cycle assessment,” *Journal of CO2 Utilization*, vol. 30, pp. 193–204, Mar. 2019, doi: 10.1016/j.jcou.2019.01.007.
- [147] A. A. Adenle, G. E. Haslam, and L. Lee, “Global assessment of research and development for algae biofuel production and its potential role for sustainable development in

- developing countries,” *Energy Policy*, vol. 61, pp. 182–195, Oct. 2013, doi:
10.1016/J.ENPOL.2013.05.088.
- [148] H. Xu, L. Ou, Y. Li, T. R. Hawkins, and M. Wang, “Life Cycle Greenhouse Gas Emissions of Biodiesel and Renewable Diesel Production in the United States,” *Environ Sci Technol*, vol. 56, no. 12, pp. 7512–7521, Jun. 2022, doi:
10.1021/ACS.EST.2C00289/ASSET/IMAGES/LARGE/ES2C00289_0003.JPEG.
- [149] “Africa Electricity Grids Explorer.” <http://africagrid.energydata.info/> (accessed Mar. 17, 2023).
- [150] C. Zhu *et al.*, “Efficient CO₂ capture from the air for high microalgal biomass production by a bicarbonate Pool,” *Journal of CO₂ Utilization*, vol. 37, pp. 320–327, Apr. 2020, doi:
10.1016/J.JCOU.2019.12.023.
- [151] S. Gao *et al.*, “A newly isolated alkaliphilic cyanobacterium for biomass production with direct air CO₂ capture,” *Journal of CO₂ Utilization*, vol. 69, p. 102399, Mar. 2023, doi:
10.1016/J.JCOU.2023.102399.
- [152] J. Hoffman, R. C. Pate, T. Drennen, and J. C. Quinn, “Techno-economic assessment of open microalgae production systems,” *Algal Res*, vol. 23, pp. 51–57, Apr. 2017, doi:
10.1016/J.ALGAL.2017.01.005.
- [153] K. DeRose, C. DeMill, R. W. Davis, and J. C. Quinn, “Integrated techno economic and life cycle assessment of the conversion of high productivity, low lipid algae to renewable fuels,” *Algal Res*, vol. 38, p. 101412, Mar. 2019, doi: 10.1016/J.ALGAL.2019.101412.

- [154] M. L. Bartley, W. J. Boeing, A. A. Corcoran, F. O. Holguin, and T. Schaub, “Effects of salinity on growth and lipid accumulation of biofuel microalga *Nannochloropsis salina* and invading organisms,” *Biomass Bioenergy*, vol. 54, pp. 83–88, Jul. 2013, doi: 10.1016/J.BIOMBIOE.2013.03.026.
- [155] E. R. Venteris, R. L. Skaggs, A. M. Coleman, and M. S. Wigmosta, “A GIS cost model to assess the availability of freshwater, seawater, and saline groundwater for algal biofuel production in the United States,” *Environ Sci Technol*, vol. 47, no. 9, pp. 4840–4849, May 2013, doi: 10.1021/ES304135B/SUPPL_FILE/ES304135B_SI_002.PDF.
- [156] L. F. Lewis, J. van Ryzin, and L. Vega, “Steep Slope Seawater Supply Pipeline,” pp. 2641–2654, Nov. 1989, doi: 10.1061/9780872626874.197.
- [157] H. Ashouri *et al.*, “PERSIANN-CDR: Daily Precipitation Climate Data Record from Multisatellite Observations for Hydrological and Climate Studies,” *Bull Am Meteorol Soc*, vol. 96, no. 1, pp. 69–83, Jan. 2015, doi: 10.1175/BAMS-D-13-00068.1.
- [158] “Water Quality Standards Handbook: Chapter 3: Water... - Google Scholar.”
https://scholar.google.com/scholar?hl=en&as_sdt=0%2C6&q=Water+Quality+Standards+Handbook%3A+Chapter+3%3A+Water+Quality+Criteria&btnG= (accessed Jul. 13, 2022).
- [159] U. Lee, J. Han, A. Elgowainy, and M. Wang, “Regional water consumption for hydro and thermal electricity generation in the United States,” *Appl Energy*, vol. 210, pp. 661–672, Jan. 2018, doi: 10.1016/j.apenergy.2017.05.025.
- [160] “Form EIA-860 detailed data with previous form data (EIA-860A/860B).”
<https://www.eia.gov/electricity/data/eia860/> (accessed Jan. 27, 2022).

- [161] “Power Profiler | US EPA.” <https://www.epa.gov/egrid/power-profiler#/> (accessed Jan. 27, 2022).
- [162] R. M. May *et al.*, “MetPy: A Meteorological Python Library for Data Analysis and Visualization,” *Bull Am Meteorol Soc*, vol. 103, no. 10, pp. E2273–E2284, Oct. 2022, doi: 10.1175/BAMS-D-21-0125.1.
- [163] L. M. Wendt, C. Kinchin, B. D. Wahlen, R. Davis, T. A. Dempster, and H. Gerken, “Assessing the stability and techno-economic implications for wet storage of harvested microalgae to manage seasonal variability,” *Biotechnol Biofuels*, vol. 12, no. 1, pp. 1–14, Apr. 2019, doi: 10.1186/S13068-019-1420-0/TABLES/5.
- [164] “2022 CEPCI updates: December (prelim.) and November (final) - Chemical Engineering.” <https://www.chemengonline.com/2022-cepci-updates-december-prelim-and-november-final/?printmode=1> (accessed Mar. 19, 2023).
- [165] “World Development Indicators | DataBank.” <https://databank.worldbank.org/source/world-development-indicators> (accessed Mar. 20, 2023).
- [166] “ISO - ISO 14044:2006 - Environmental management — Life cycle assessment — Requirements and guidelines.” <https://www.iso.org/standard/38498.html> (accessed Mar. 20, 2023).
- [167] R. M. Handler, R. Shi, and D. R. Shonnard, “Land use change implications for large-scale cultivation of algae feedstocks in the United States Gulf Coast,” *J Clean Prod*, vol. 153, pp. 15–25, Jun. 2017, doi: 10.1016/J.JCLEPRO.2017.03.149.

- [168] M. Gytarsky, W. A. Kurz, S. Ogle, G. Richards, and Z. Somogyi, “Volume 4: Agriculture, Forestry and Other Land Use 1.2 2006 IPCC Guidelines for National Greenhouse Gas Inventories”.
- [169] N. H. Batjes, “IPCC default soil classes derived from the Harmonized World Soil Data Base (Ver. 1.1),” 2010, Accessed: Mar. 20, 2023. [Online]. Available: http://www.isric.org/isric/Webdocs/Docs/ISRIC_Report_2009_02.pdf
- [170] “FAO Map Catalog.”
<https://data.apps.fao.org/map/catalog/srv/eng/catalog.search?id=47105&fname=gez2010.zip&access=private#/metadata/2fb209d0-fd34-4e5e-a3d8-a13c241eb61b> (accessed Mar. 20, 2023).
- [171] A. C. Jennifer Jenkins, H. Daniel Ginzo, S. M. Ogle, L. V Verchot, M. Handa, and A. Tsunekawa, “Volume 4: Agriculture, Forestry and Other Land Use 8.2 2006 IPCC Guidelines for National Greenhouse Gas Inventories”.
- [172] M. Buchhorn *et al.*, “Copernicus Global Land Service: Land Cover 100m: collection 3: epoch 2019: Globe,” Sep. 2020, doi: 10.5281/ZENODO.3939050.
- [173] “Chapter 2: Generic Methodologies Applicable to Multiple Land-Use Categories 2006 IPCC Guidelines for National Greenhouse Gas Inventories 2.1”.
- [174] A. D. Rodel Lasco *et al.*, “Volume 4: Agriculture, Forestry and Other Land Use 5.2 2006 IPCC Guidelines for National Greenhouse Gas Inventories Contributing Authors”.
- [175] A. D. Rodel Lasco *et al.*, “Volume 4: Agriculture, Forestry and Other Land Use 5.2 2006 IPCC Guidelines for National Greenhouse Gas Inventories Contributing Authors.”

- [176] “National Land Cover Database (NLCD) 2019 Products (ver. 2.0, June 2021) - ScienceBase-Catalog.”
<https://www.sciencebase.gov/catalog/item/5f21cef582cef313ed940043> (accessed Mar. 20, 2023).
- [177] A. C. Jennifer Jenkins, H. Daniel Ginzo, S. M. Ogle, L. V Verchot, M. Handa, and A. Tsunekawa, “Volume 4: Agriculture, Forestry and Other Land Use 8.2 2006 IPCC Guidelines for National Greenhouse Gas Inventories.”
- [178] Y. Qian, R. F. Follett, and J. M. Kimble, “Soil Organic Carbon Input from Urban Turfgrasses,” *Soil Science Society of America Journal*, vol. 74, no. 2, pp. 366–371, Mar. 2010, doi: 10.2136/SSSAJ2009.0075.
- [179] T. L. Springer, “Biomass yield from an urban landscape,” *Biomass Bioenergy*, vol. 37, pp. 82–87, Feb. 2012, doi: 10.1016/J.BIOMBIOE.2011.12.029.
- [180] T. Ericsson, K. Blombäck, and A. Neumann, “Demand-driven fertilization. Part I: Nitrogen productivity in four high-maintenance turf grass species,”
<https://doi.org/10.1080/09064710.2012.682735>, vol. 62, no. SUPPL.1, pp. 113–121, May 2012, doi: 10.1080/09064710.2012.682735.
- [181] J. Li *et al.*, “Trends in Renewable Energy Process Design of Microalgae Slurry Pump,” vol. 6, no. 3, pp. 234–244, 2020, doi: 10.17737/tre.2020.6.3.0120.

APPENDIX A

Thermal model

This section describes the additional heat fluxes that are included in the thermal model and the methods used to calculate heat and mass transfer from forced convection. These heat fluxes were adopted directly from Greene et al. MENDELEY CITATION PLACEHOLDER 0.

Direct and diffuse solar radiation

The heat transfer from incoming solar radiation from both direct and diffuse components is modeled using the following equation:

$$Q_{solar} = (1 - f_a) \cdot GHI \cdot \alpha_{culture} \cdot A_s \quad (A1)$$

where $f_a = 0.015$ is the fraction of sunlight converted into chemical energy by the algae during photosynthesis, GHI [W m^{-2}] is the global horizontal irradiance, $\alpha_{culture}$ is the absorptivity of the algae culture set to 0.90, and A_s [m^2] is the pond surface area.

Pond radiation

Radiation emitted by the pond was calculated using the following equation:

$$Q_{reradiation} = -\sigma \cdot \varepsilon_w \cdot T_p^4 \cdot A_s \quad (A2)$$

where ε_w is the emissivity of the culture with a calibrated value of 0.87, T_p is the pond temperature, and σ is the Stefan-Boltzmann constant.

Water Inflow

Heat transfer from incoming water is calculated using the following equation:

$$Q_{inflow} = c_p \cdot m_e \cdot (T_{amb} - T_p) \quad (A3)$$

where c_p is the specific heat of the culture set to 4184 [J kg⁻¹ K⁻¹], and m_e is the water loss from evaporation [kg m⁻² s⁻¹].

Heat transfer by forced convection

Heat transfer from forced convection is calculated using the flat plate correlations described in Bergman et al. MENDELEY CITATION PLACEHOLDER 1:

$$Nu_L = a \cdot (Re_L)^{0.5} (Pr)^{\frac{1}{3}} \quad \text{for } Re_L < (3 \times 10^5) \text{ (Laminar Flow)} \quad (A4)$$

$$Nu_L = b \cdot (Re_L)^{0.8} (Pr)^{\frac{1}{3}} \quad \text{for } Re_L > (5 \times 10^5) \text{ (Turbulent Flow)} \quad (A5)$$

$$Q_{convection} = h_{conv} \cdot (T_{amb} - T_{pond}) \quad (A6)$$

where a and b are empirical coefficients set to 0.75 and 0.015, respectively, h_{conv} [W m⁻² K⁻¹] is the convection coefficient, Re_L is the Reynolds number, and Pr is the Prandtl number.

Thermal validation

Detailed thermal validation data is provided in this section. Meteorological data used for the temperature and evaporation validation included hourly measurements of global horizontal irradiance, ambient temperature, relative humidity, and wind speed. Rainwater was not accounted for in the thermal validation process nor the simulations since the primary focus of this study were calculating the blue water footprint, which is primarily impacted by evaporation losses. In addition, including rainfall events in the incoming water heat flux was found to cause a negligible impact in the temperature error (-0.93 ± 2.72 °C).

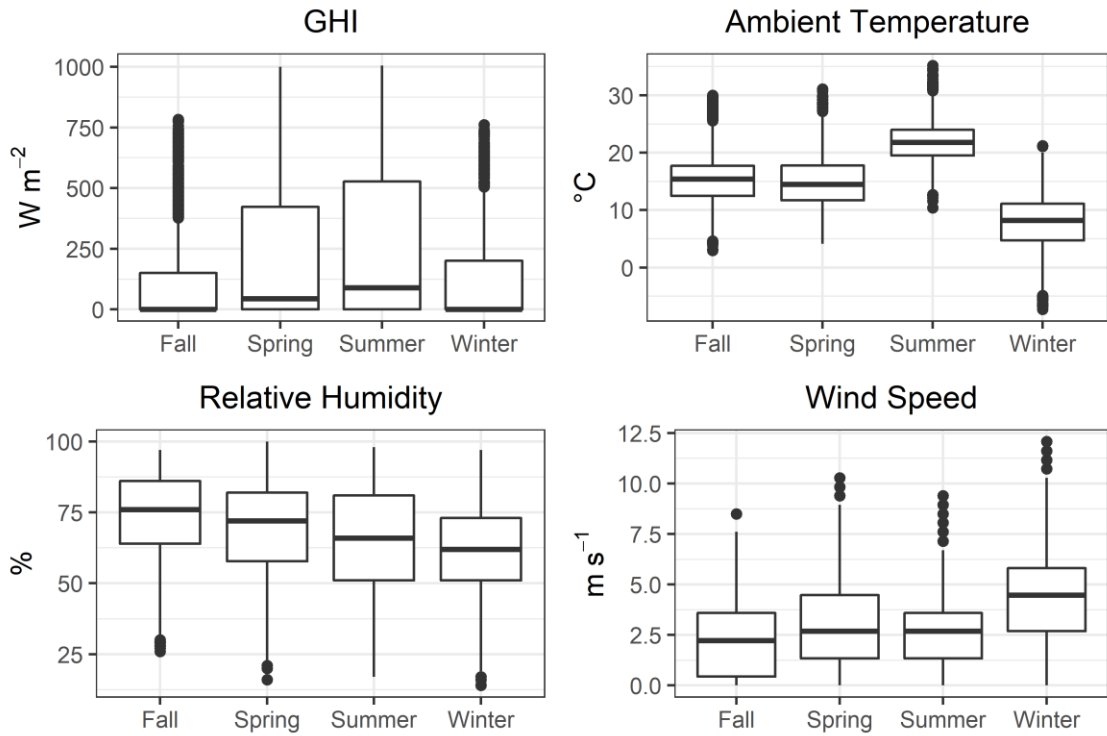


Figure A - 1. Seasonal inputs used in the thermal model validation effort.

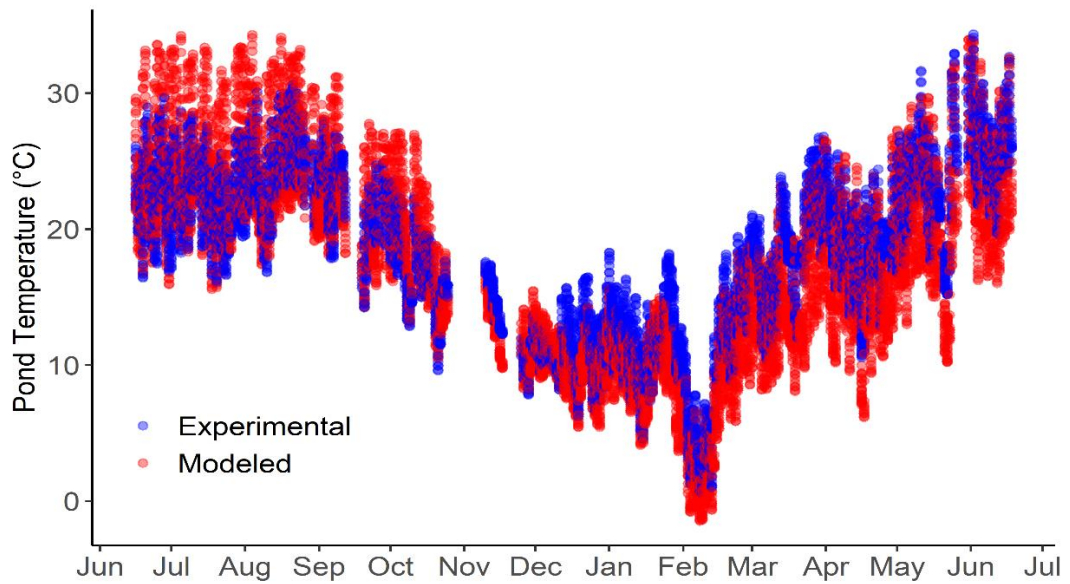


Figure A - 2. Time-series of the modeled and experimental pond temperature.

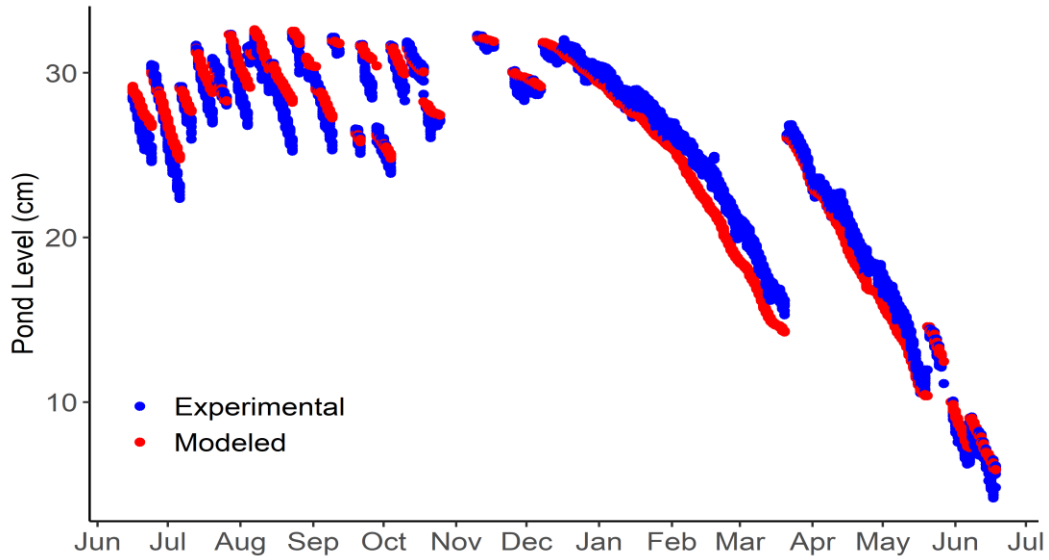


Figure A - 3. Time-series of the modeled and experimental pond depths.

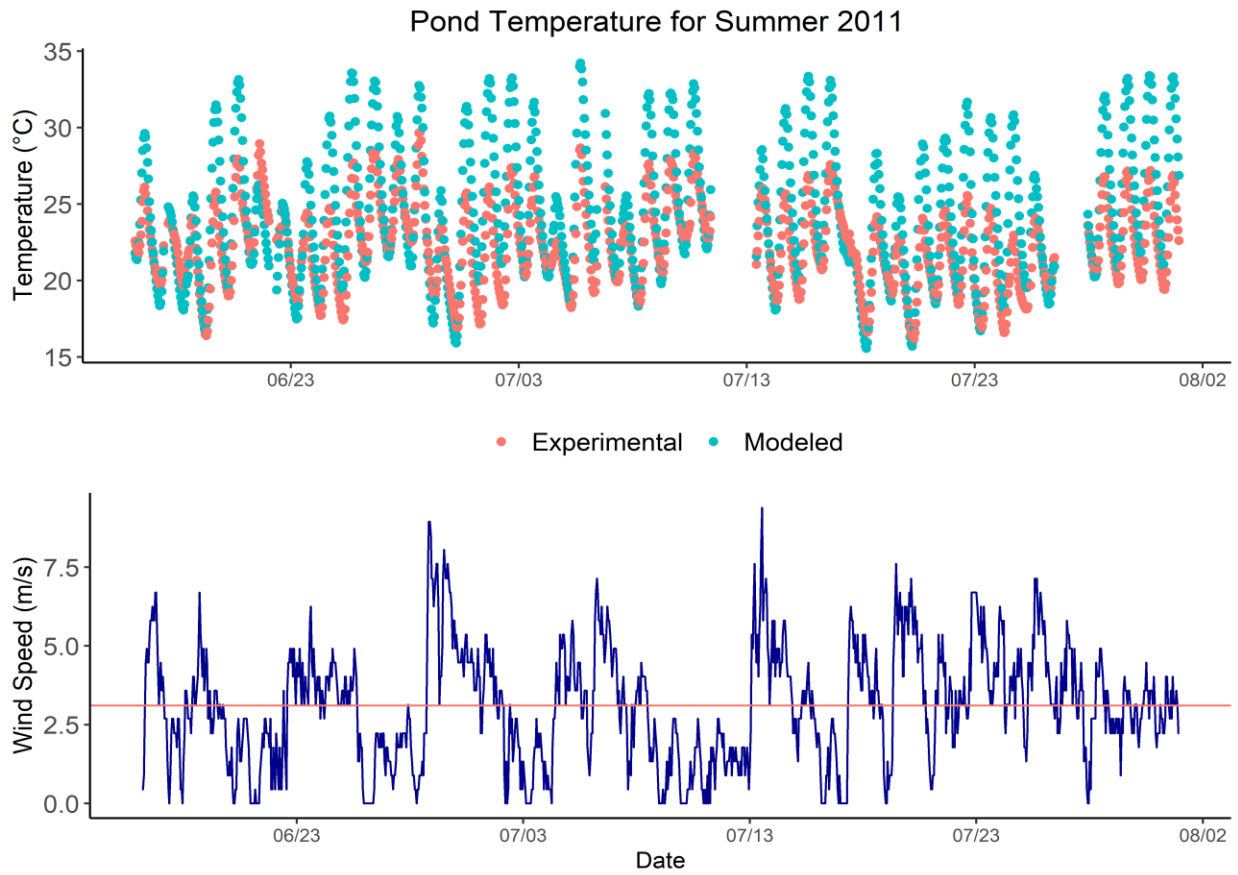


Figure A - 4. Relation between wind speed and pond temperature for Summer 2011. Gaps in the temperature series represent discarded time intervals. The red line denotes the mean wind speed for the period.

Table A1. Seasonal breakdown of the validation error.

SEASON	TEMPERATURE		EVAPORATION	
	ERROR (°C)		ERROR (%)	
	Average	SD	Average	SD
WINTER	-2.19	1.47	5.69	3.71
SPRING	-2.75	2.32	3.18	6.51
SUMMER	1.48	2.41	-3.24	4.7
FALL	0.46	1.85	-1.15	1.97

Growth validation

Table A2. Growth model inputs.

UTEX 393 Strain Parameters			
Parameter	Value	Units	Source
Optimal temperature	32.25	°C	
Maximum temperature	40.9	°C	Empirical adjustment
Minimum temperature	3	°C	Empirical adjustment
Dark loss	3	%	Empirical adjustment
Saturation Light Intensity	480	$\mu mol m^{-2} s^{-1}$	Empirical adjustment
Optical Density Coefficient	0.38	g/L*OD750	AzCATI

Dynamic maps of evaporation losses

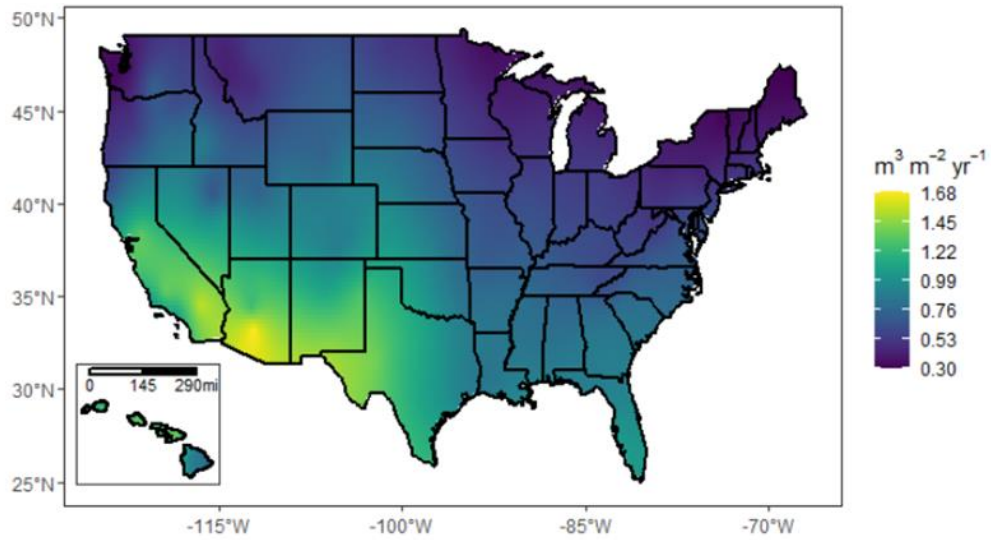


Figure A - 5. Mean annual evaporation losses ($m^3 m^{-2} yr^{-1}$) of a 400-ha farm for the simulated 21 years.

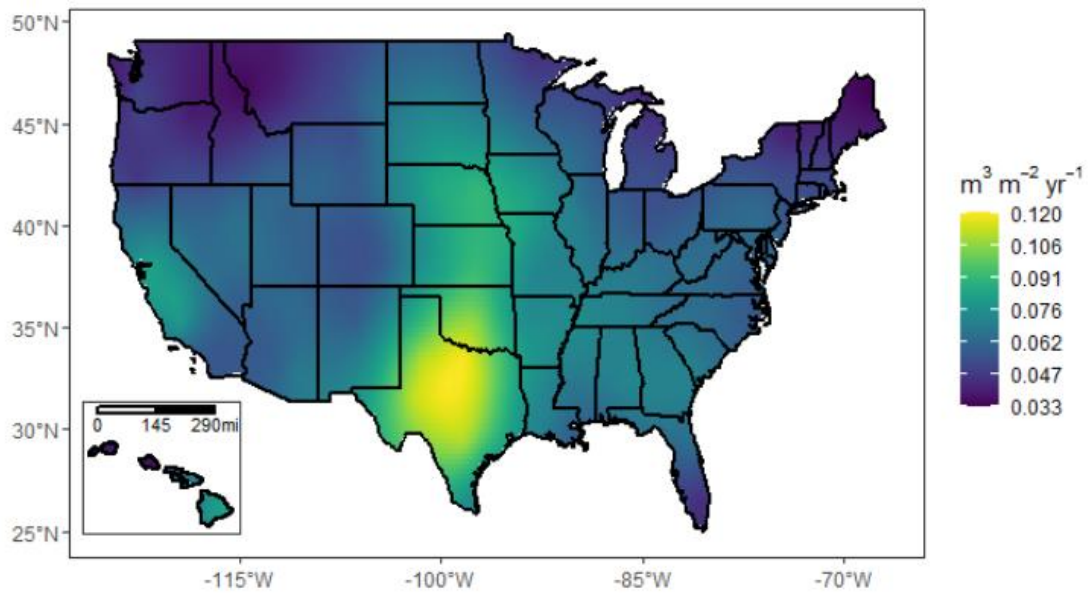


Figure A - 6. Standard deviation of annual evaporation losses ($m^3 m^{-2} yr^{-1}$) of a 400-ha facility for the simulated 21 years.

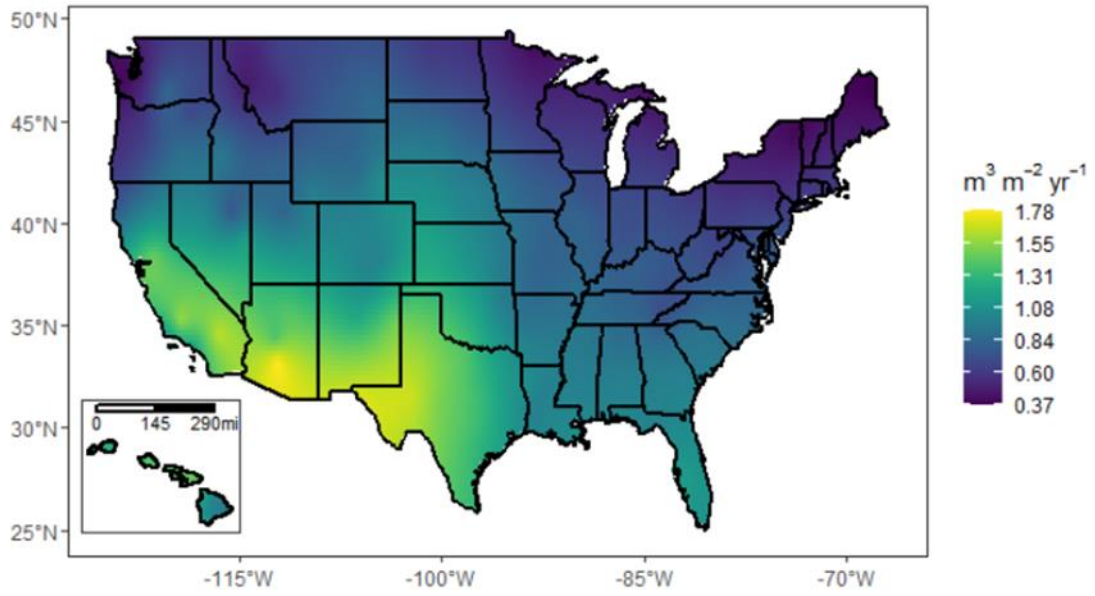


Figure A - 7. Maximum annual evaporation losses ($m^3 m^{-2} yr^{-1}$) of a 400-ha facility for the 21 simulated years.

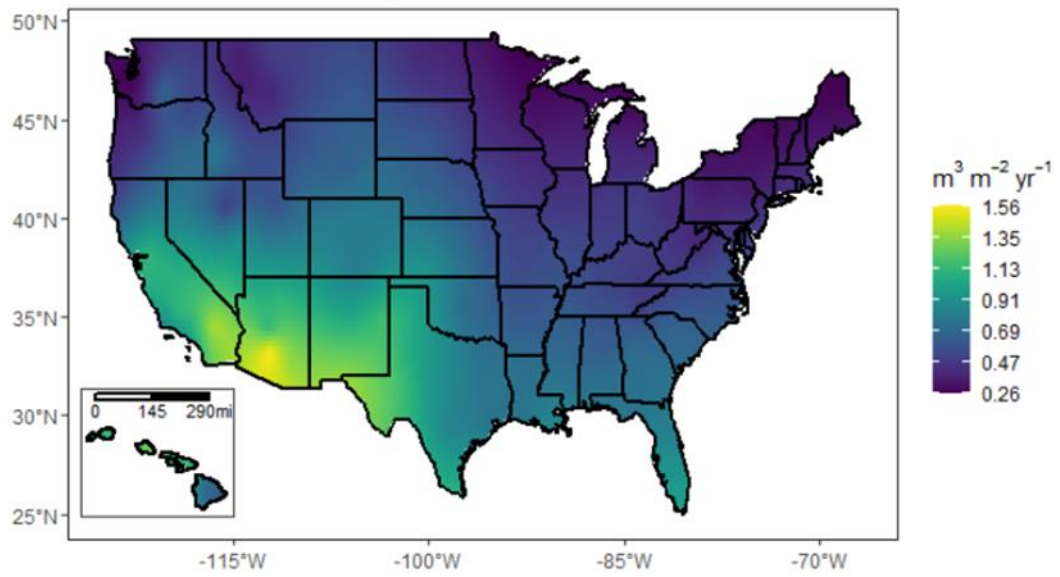


Figure A - 8. Minimum annual evaporation losses ($m^3 m^{-2} yr^{-1}$) of a 400-ha facility for the 21 simulated years.

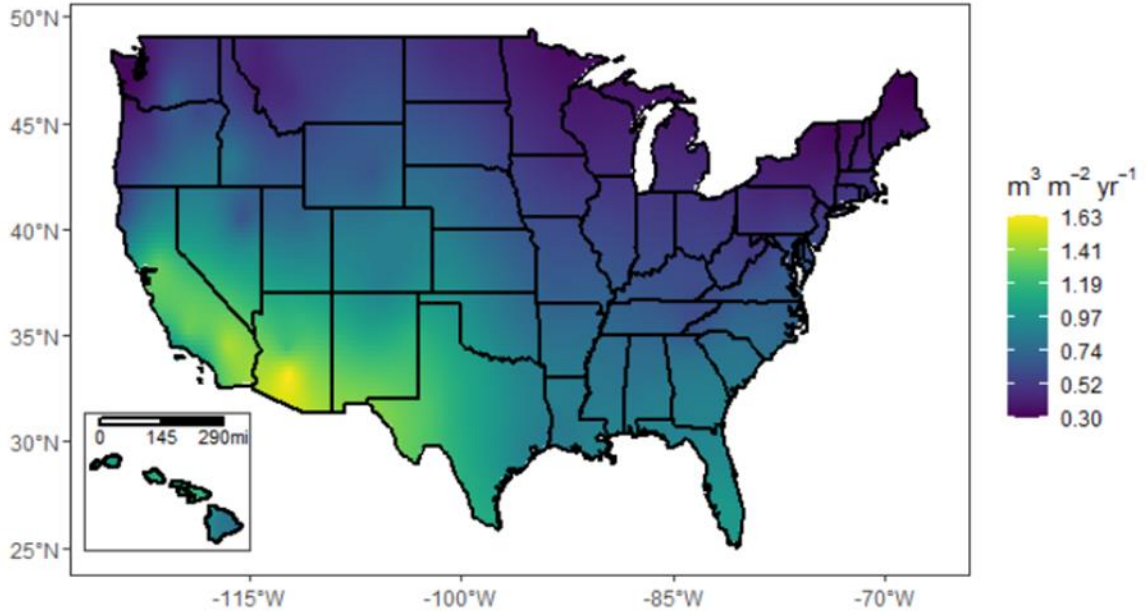


Figure A - 9. Mean annual evaporation losses ($m^3 m^{-2} yr^{-1}$) of a 4000-ha farm for the simulated 21 years.

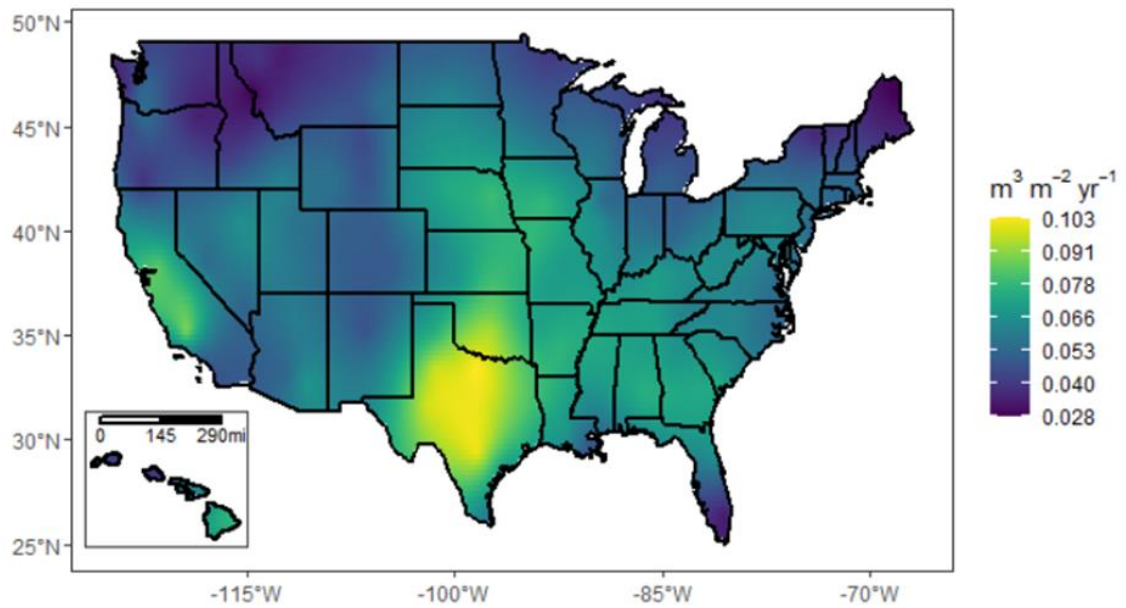


Figure A -10. Standard deviation of annual evaporation losses ($m^3 m^{-2} yr^{-1}$) of a 4000-ha facility for the simulated 21 years.

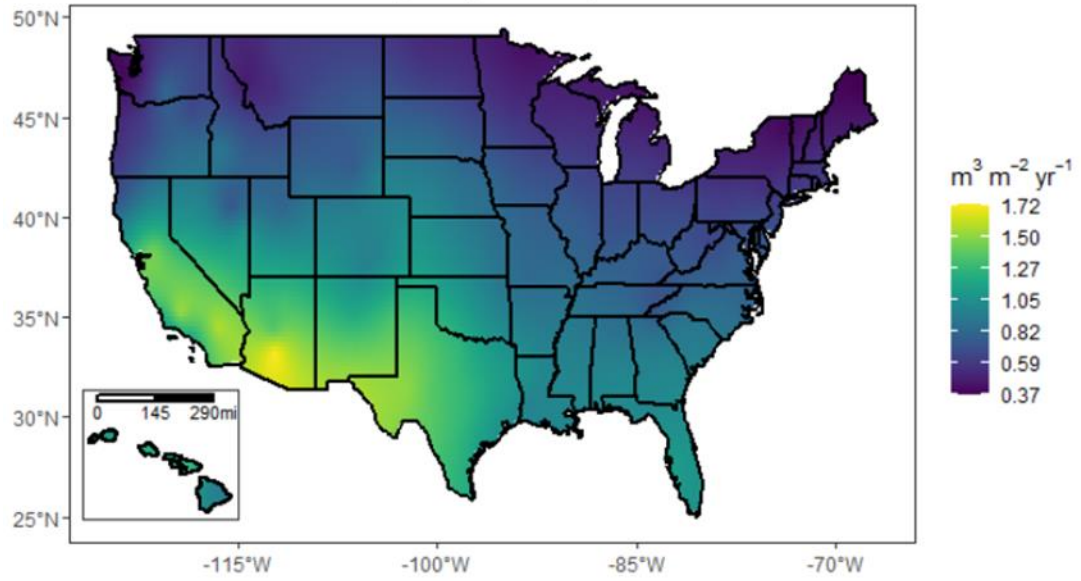


Figure A - 11. Maximum annual evaporation losses ($\text{m}^3 \text{m}^{-2} \text{yr}^{-1}$) of a 4000-ha facility for the 21 simulated years.

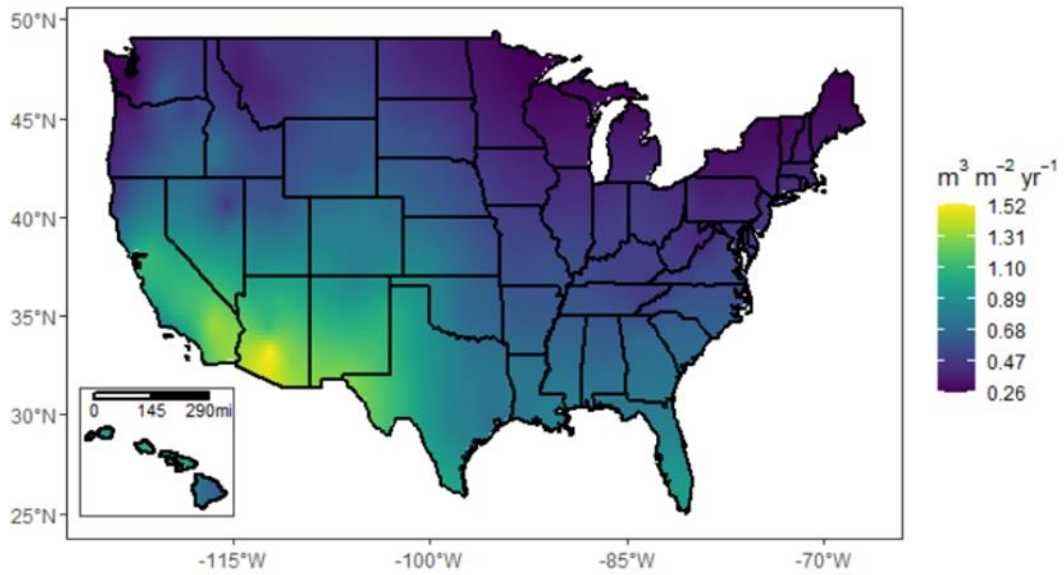


Figure A - 12. Minimum annual evaporation losses ($\text{m}^3 \text{m}^{-2} \text{yr}^{-1}$) of a 4000-ha facility for the 21 simulated years.

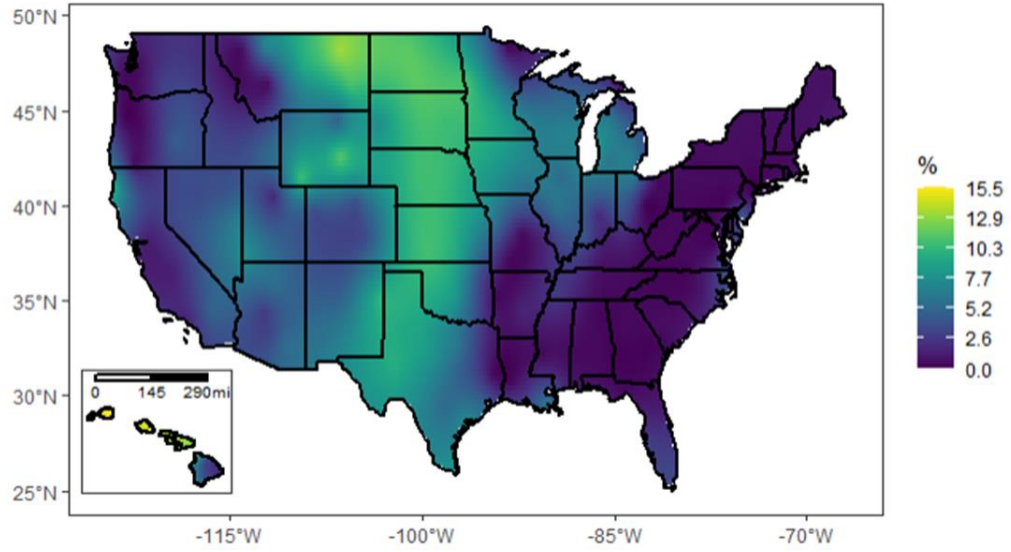


Figure A - 13. Percent difference of the evaporation losses of a 4000-ha to a 400-ha facility generated with weather data from the NSRDB. Results represent the absolute relative difference between annual averages.

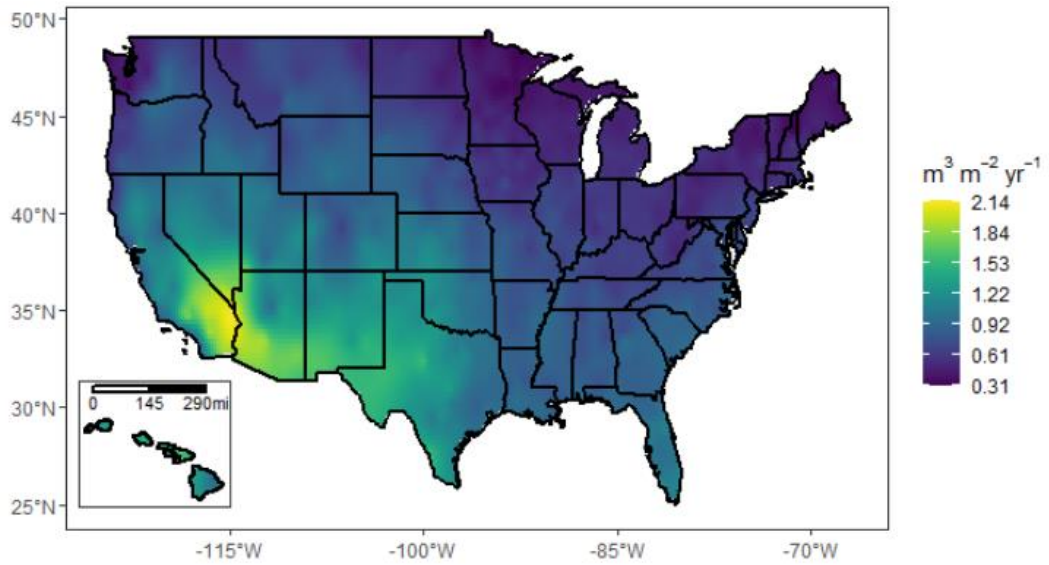


Figure A - 14. Annual evaporation losses of a 400-ha facility estimated with typical meteorological year (TMY3) data.

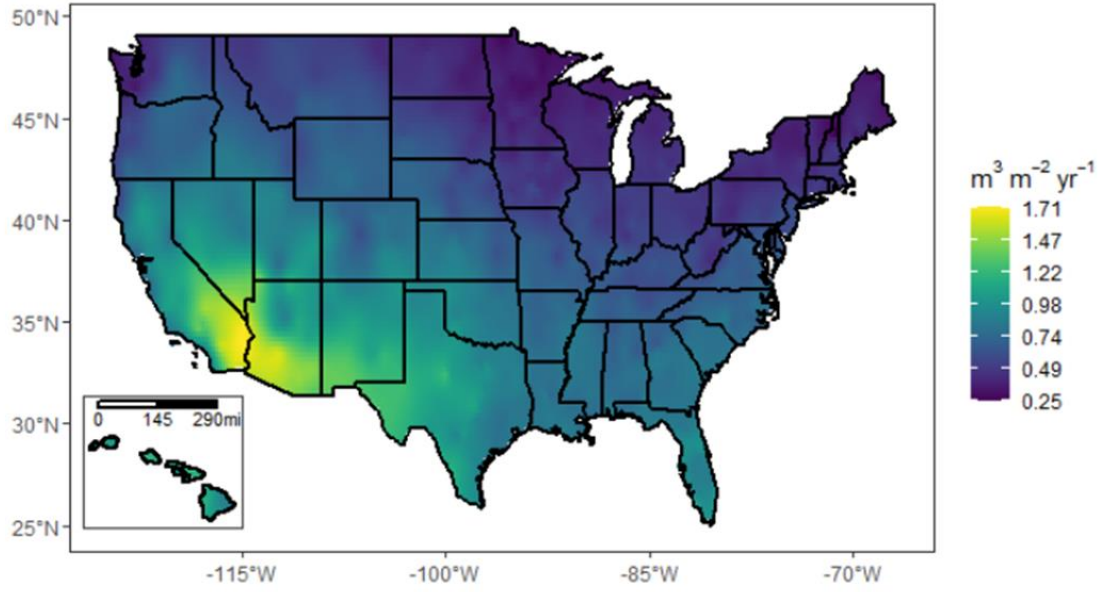


Figure A - 15. Annual evaporation losses of a 400-ha facility estimated with typical meteorological year (TMY3) data.

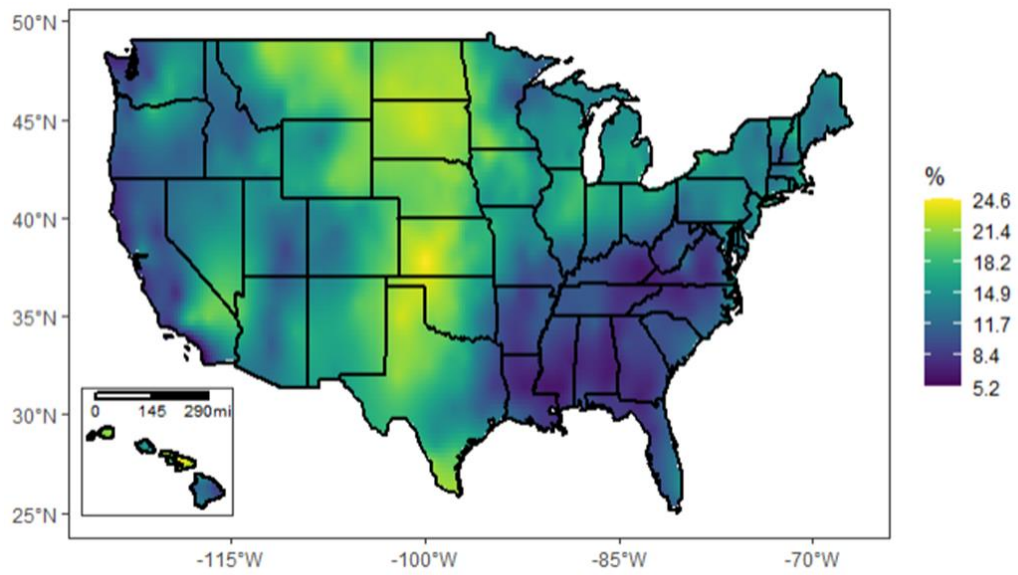


Figure A - 16. Comparison of the evaporation losses of a 4000-ha to a 400-ha facility using TMY weather files.

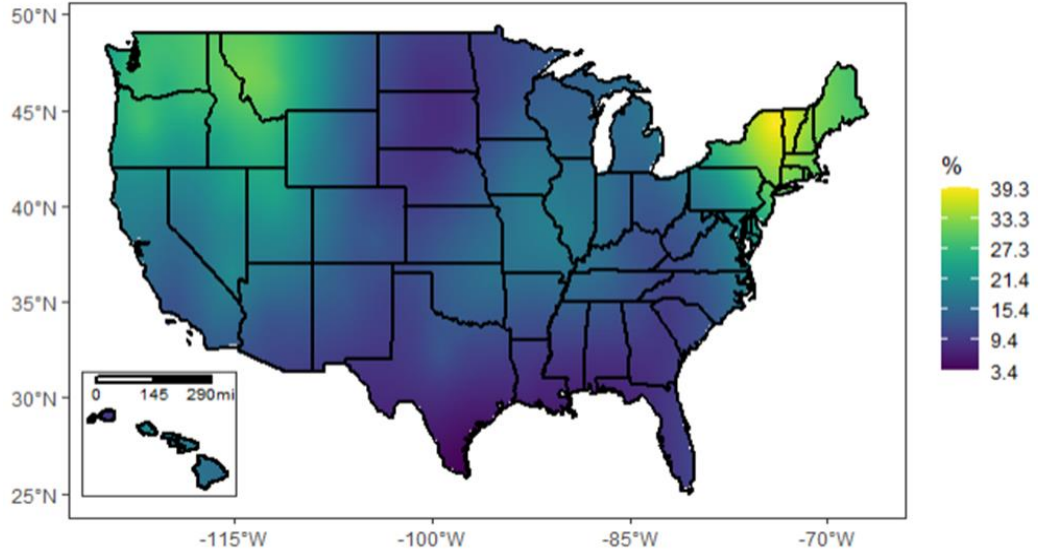


Figure A - 17. Comparison of the evaporation losses generated with TMY3 weather data to results generated with weather data from the NSRDB (annual average 1998-2018). Evaporation losses for a 400-ha facility are illustrated.

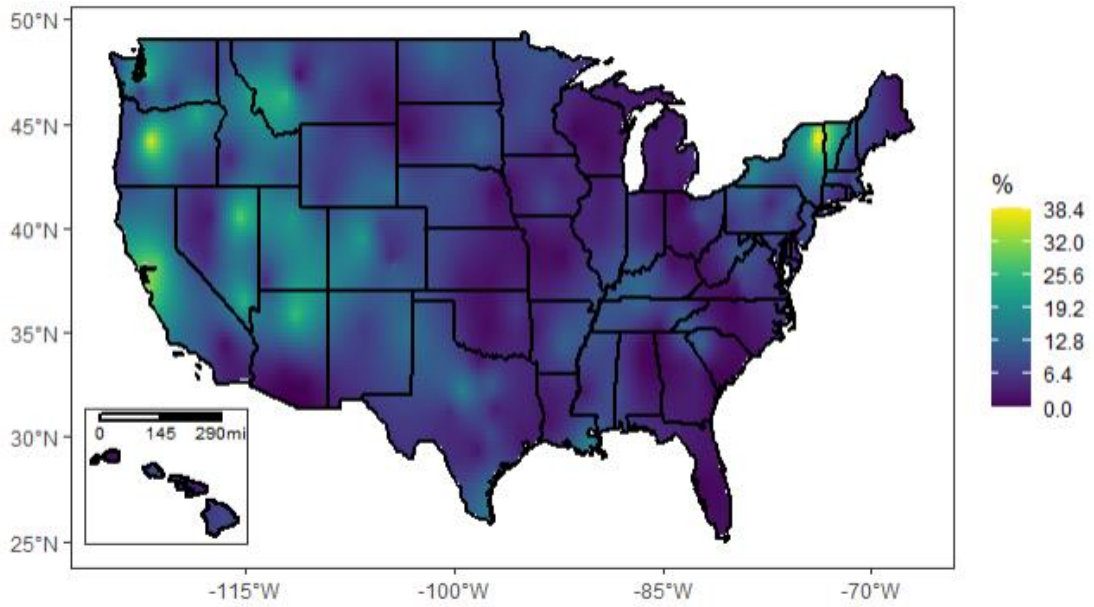


Figure A - 18. Comparison of the evaporation losses generated with TMY3 weather data to results generated with weather data from the NSRDB (annual average 1998-2018). Evaporation losses for a 4000-ha facility are illustrated.

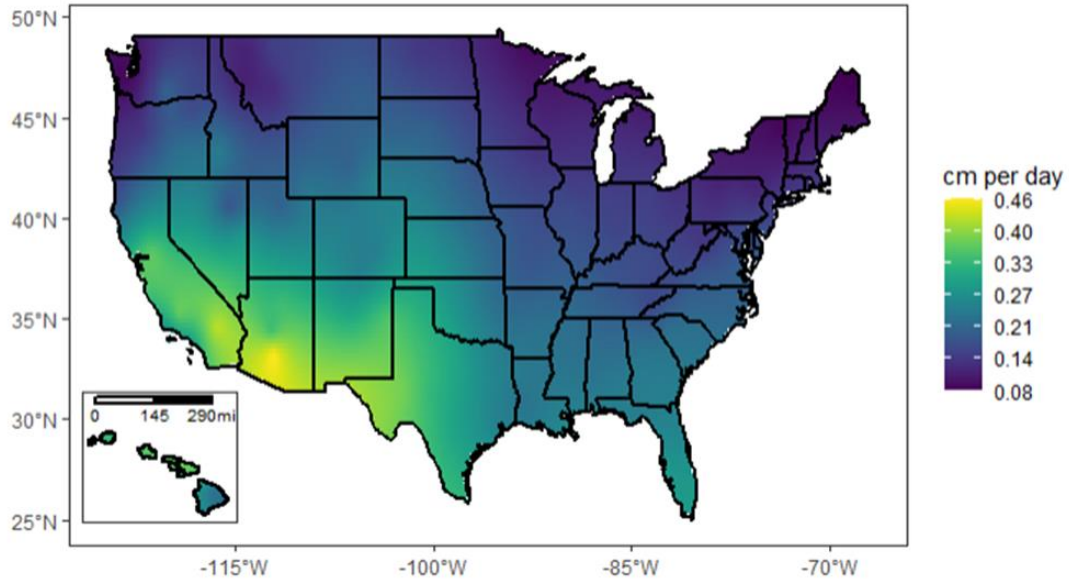


Figure A - 19. Mean annual evaporation rates (cm day^{-1}) for a 400-ha algae farm. Results represent the average of 21 years.

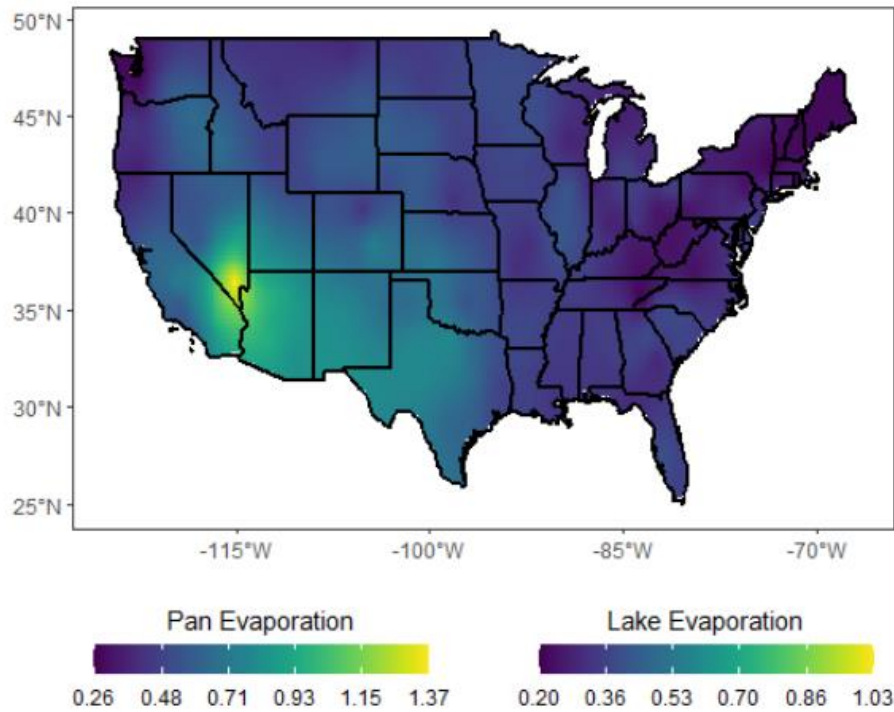


Figure A - 20. Mean annual evaporation rates (cm day^{-1}) from pan evaporation measurements retrieved from Dewes et al. MENDELEY CITATION PLACEHOLDER 3. Lake evaporation or corrected pan evaporation values were calculated by scaling pan measurements by 0.75.

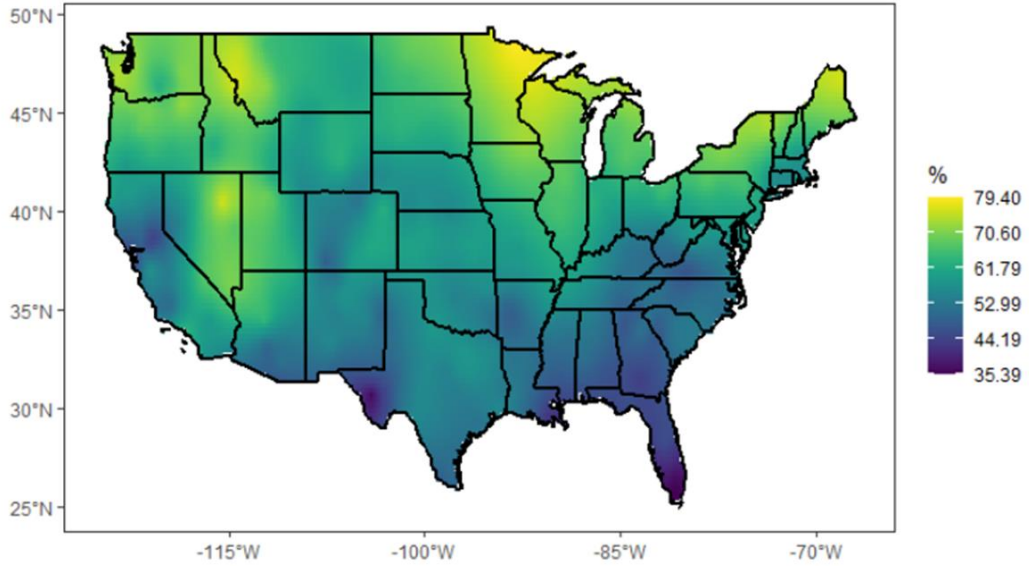


Figure A - 21. Comparison of the evaporation rates from pan evaporation to evaporation rates for an algal facility of 400-ha.

Dynamic maps of pond temperature

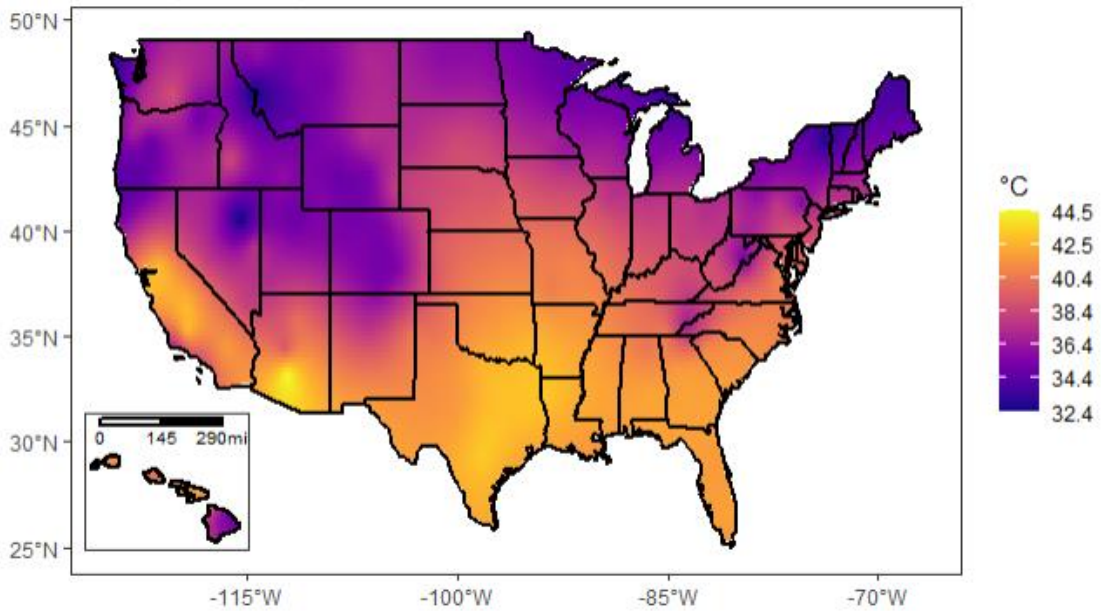


Figure A -22. Mean annual maximum temperatures ($^{\circ}\text{C}$) for a 400-ha facility calculated using historical weather data.

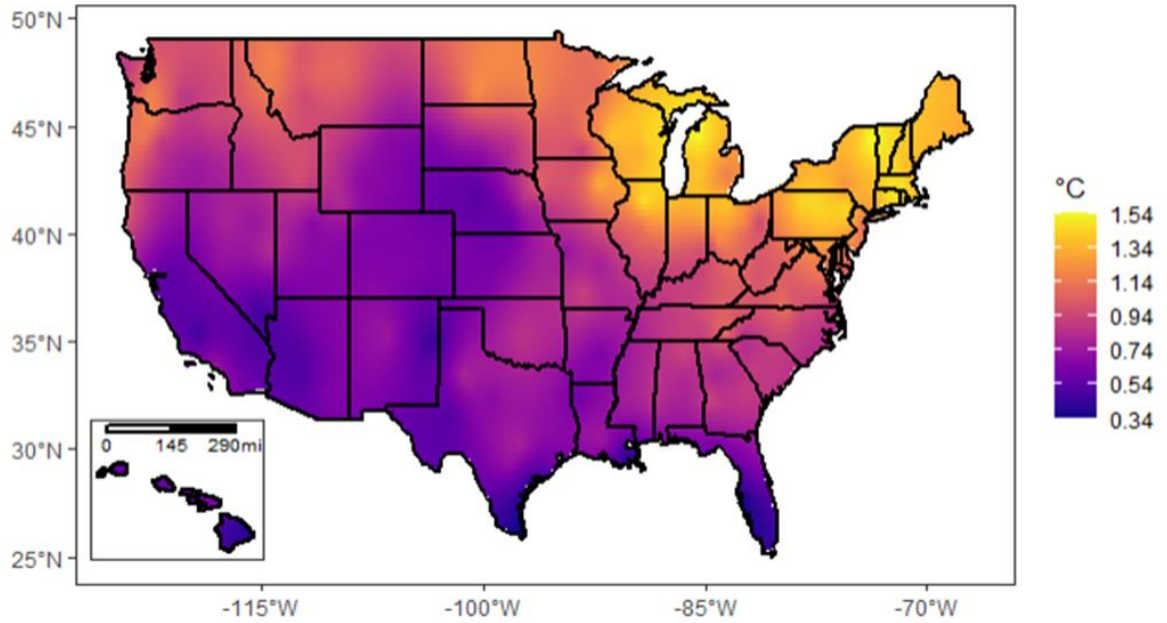


Figure A -23. Standard deviation of annual maximum temperatures (°C) for a 400-ha facility calculated using historical weather data from the NSRDB.

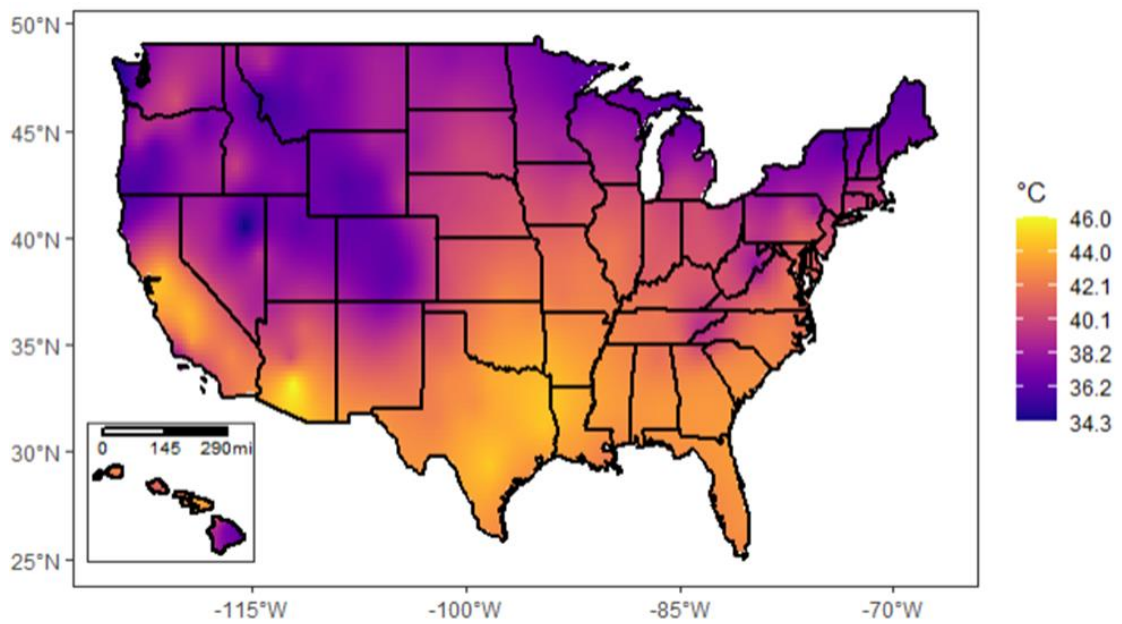


Figure A -24. Maximum of annual maximum temperatures (°C) for a 400-ha facility calculated using historical weather data from the NSRDB.

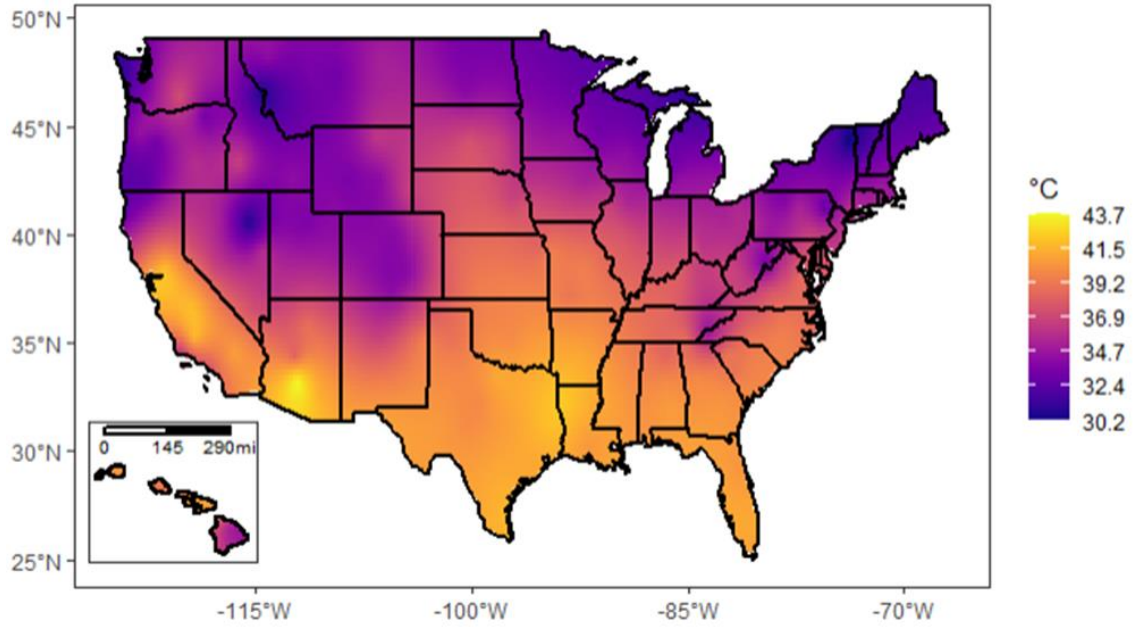


Figure A -25. Minimum of annual maximum temperatures ($^{\circ}\text{C}$) for a 400-ha facility calculated using historical weather data from the NSRDB.

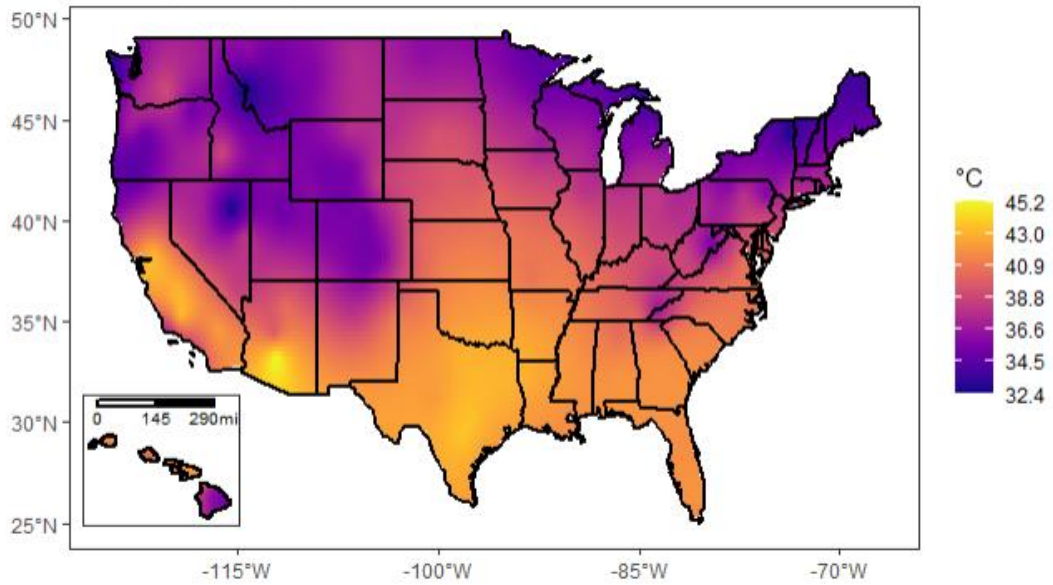


Figure A -26. Mean annual maximum temperatures ($^{\circ}\text{C}$) for a 4000-ha facility calculated using historical weather data.

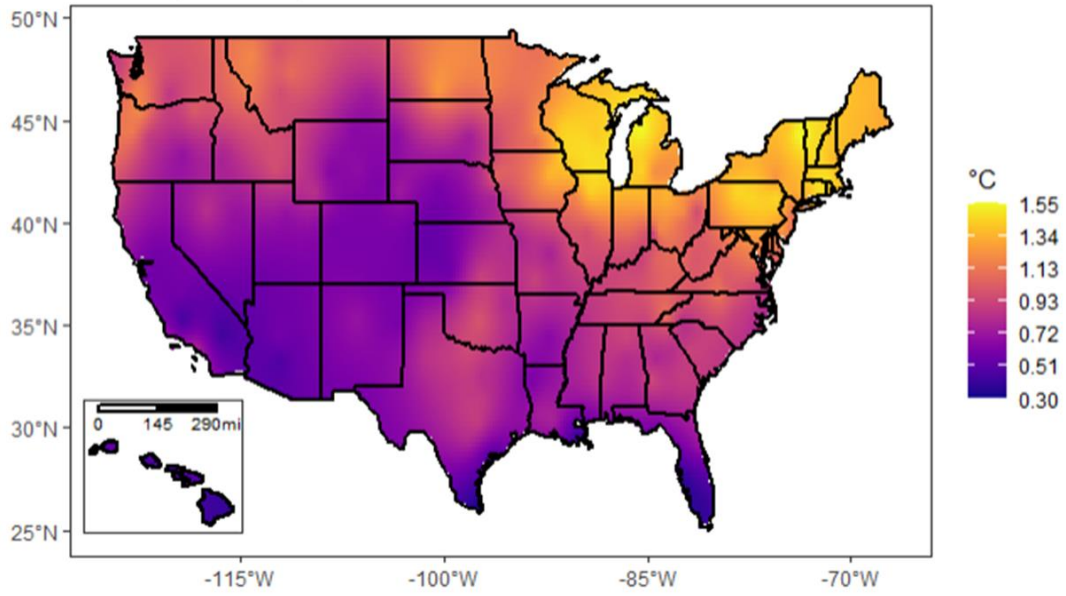


Figure A -27. Standard deviation of annual maximum temperatures ($^{\circ}\text{C}$) for a 4000-ha facility calculated using historical weather data from the NSRDB.

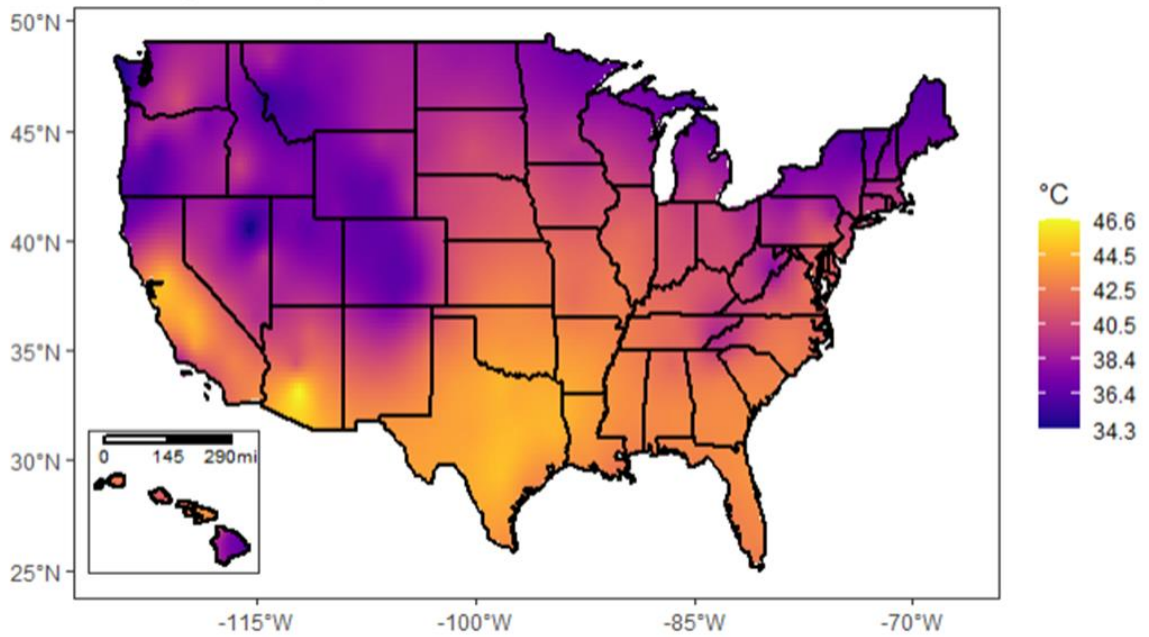


Figure A -28. Maximum of annual maximum temperatures ($^{\circ}\text{C}$) for a 400-ha facility calculated using historical weather data from the NSRDB.

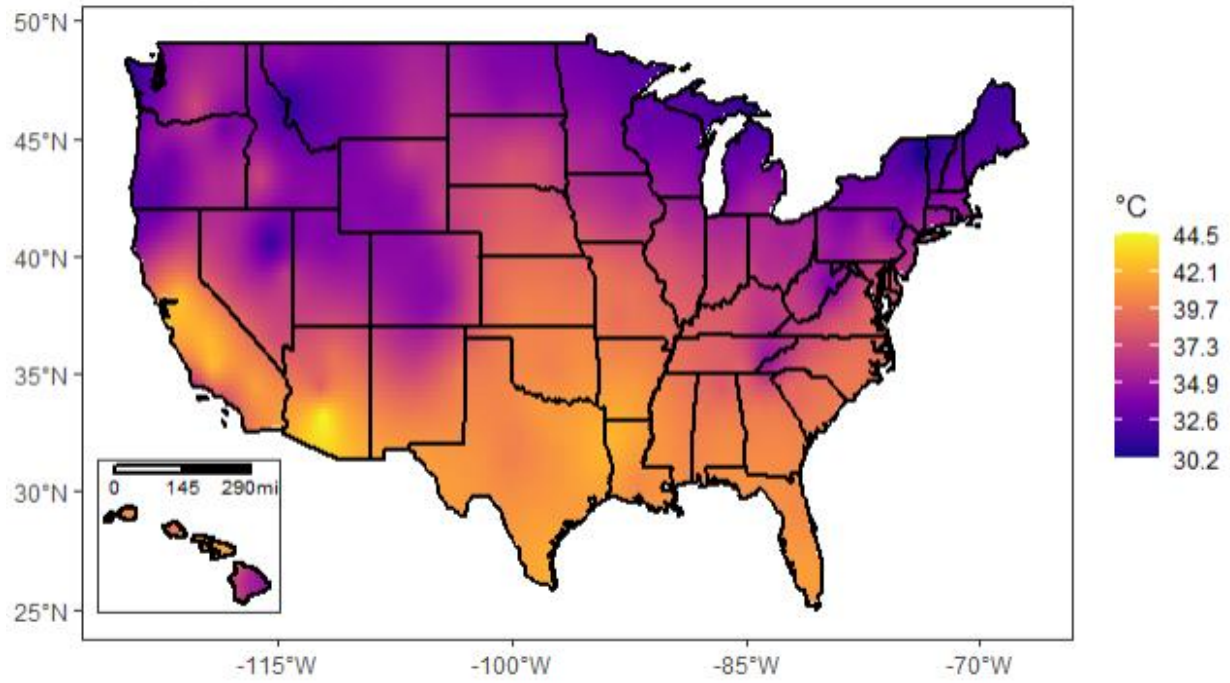


Figure A -29. Minimum of annual maximum temperatures (°C) for a 400-ha facility calculated using historical weather data from the NSRDB.

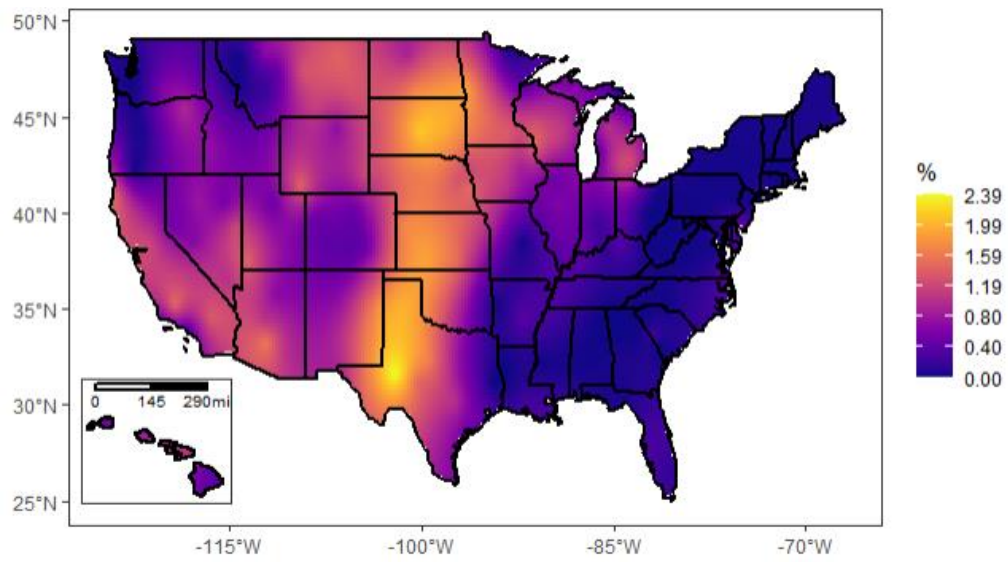


Figure A -30. Mean maximum temperature comparison between a 400-ha and a 4000-ha facility. The mean of the total simulated period (21 years) for each location was compared.

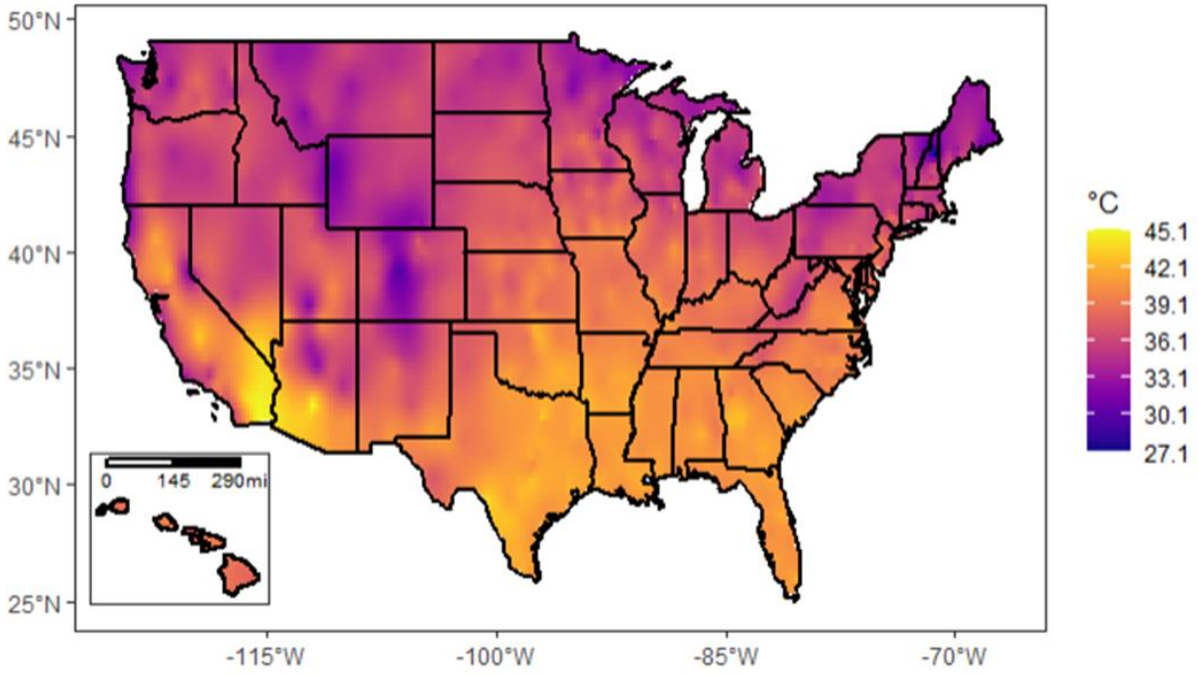


Figure A -31. Maximum temperatures ($^{\circ}\text{C}$) for a 400-ha facility calculated with TMY data.

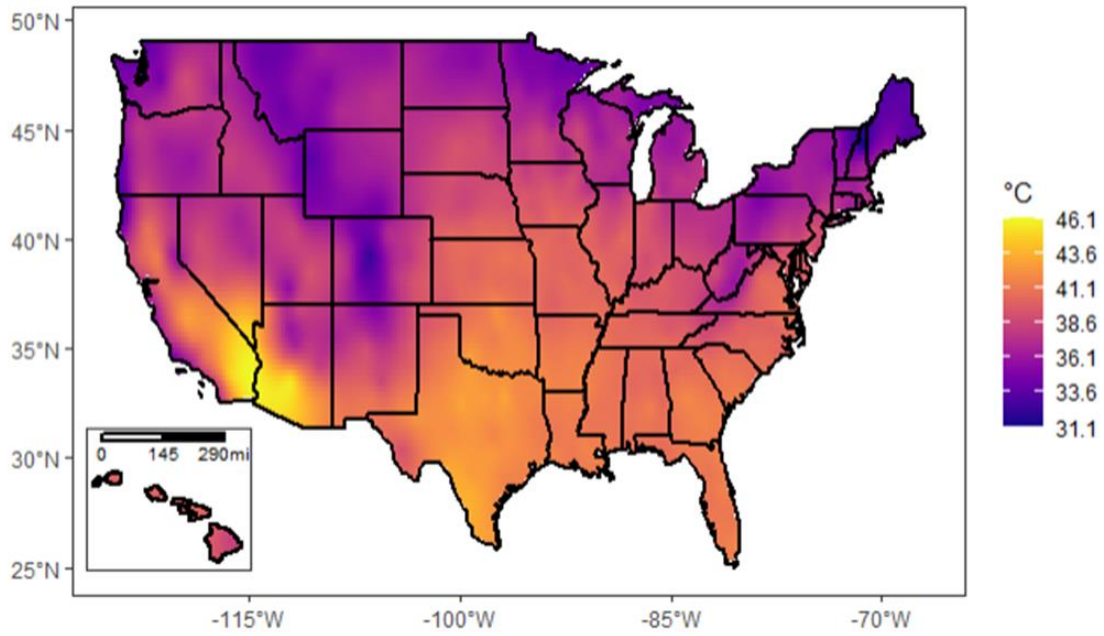


Figure A -32. Maximum temperatures ($^{\circ}\text{C}$) for a 4000-ha facility calculated with TMY data.

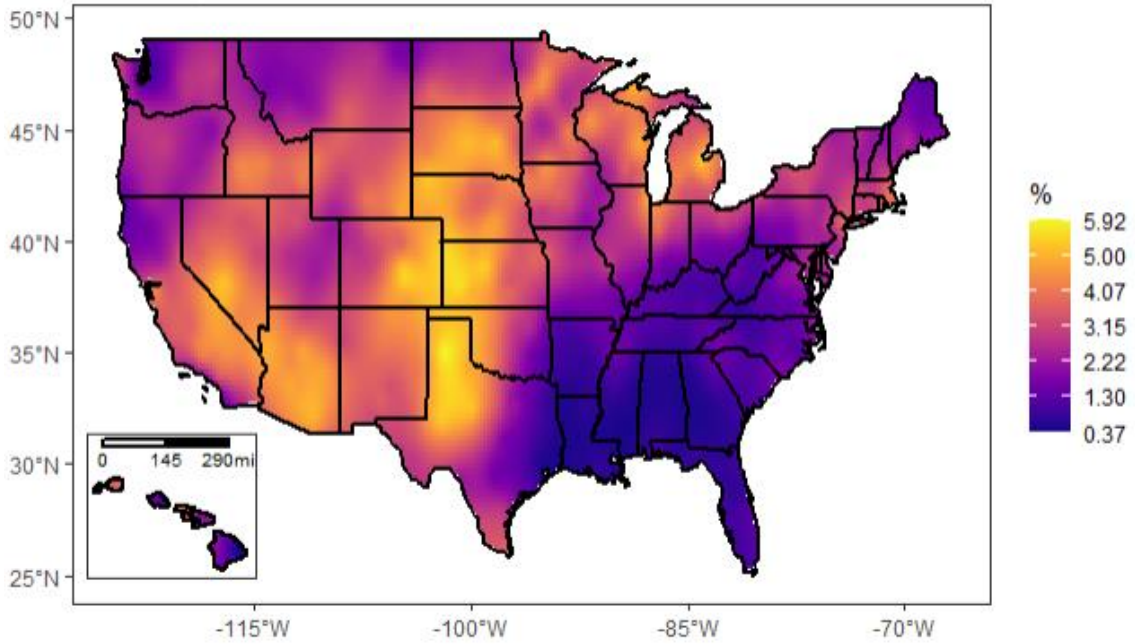


Figure A -33. Comparison of the maximum temperatures reached on a 400-ha and 4000-ha facility using TMY data.

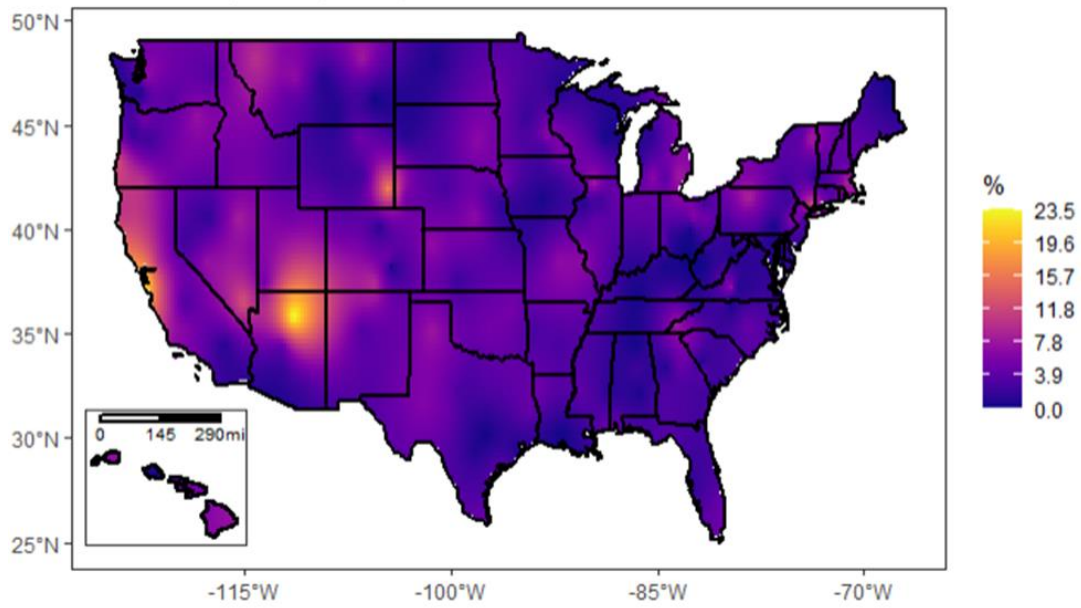


Figure A -34. Comparison of the maximum temperatures calculated with historical weather data and TMY data. Results show temperatures for a 400-ha facility.

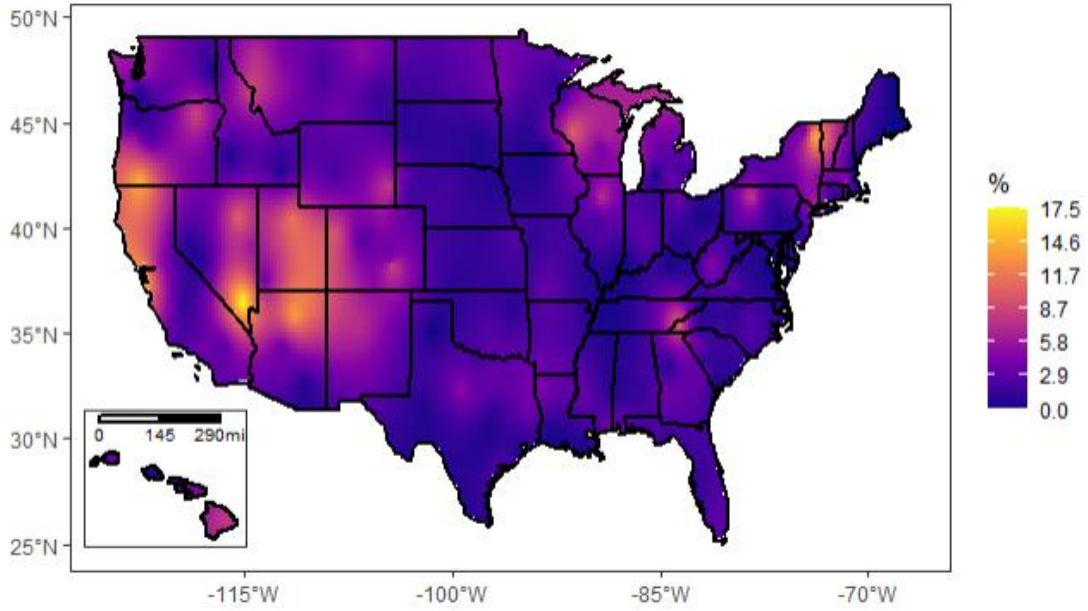


Figure A -35. Comparison of the maximum temperatures calculated with historical weather data and TMY data. Results show temperatures for a 4000-ha facility.

Dynamic maps of relevant weather inputs

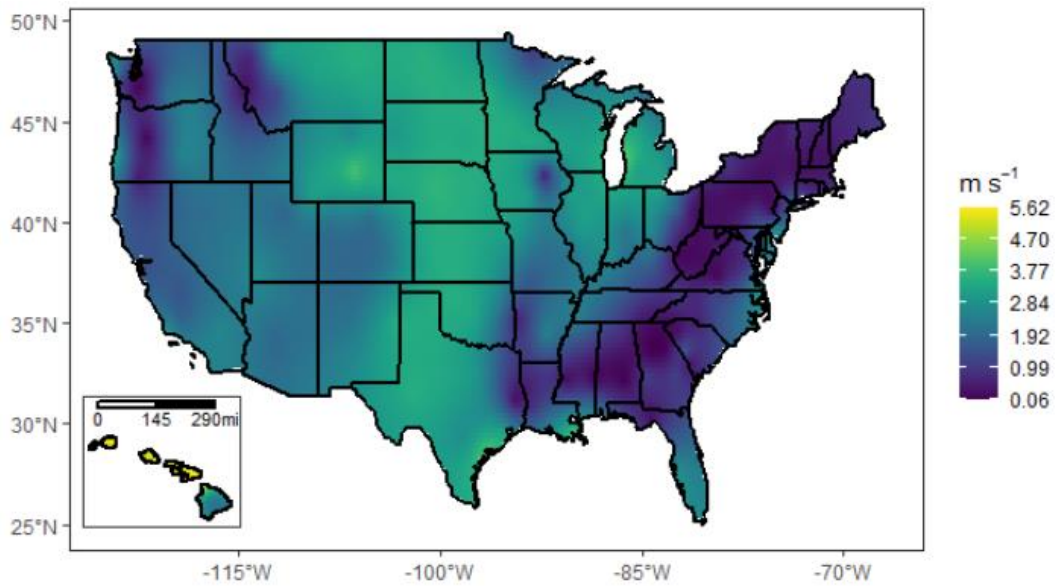


Figure A -36. Average annual wind speed data ($m s^{-1}$) retrieved from the NSRDB. The average of 21 years is shown (1998-2018).

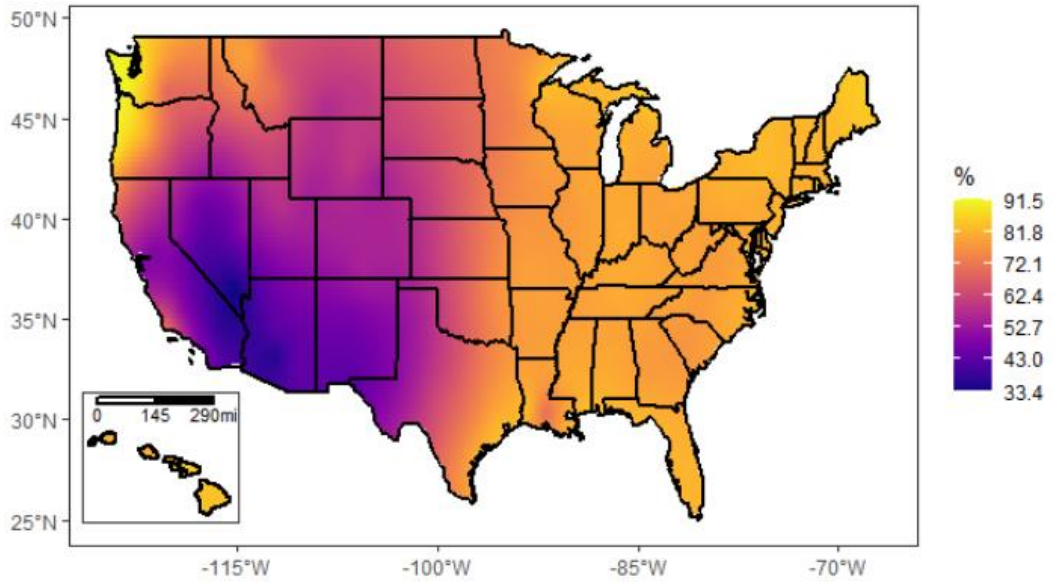


Figure A -37. Average annual relative humidity data (%) retrieved from the NSRDB. The average of 21 years is shown (1998-2018).

APPENDIX B

Facility Design

The algae farm and biorefinery simulated in this study were assumed to be co-located with each other. The wetted area of the algal cultivation process was fixed at 400 hectares, this is assumed to be representative of a commercial-scale system for fuel production and is consistent with previous modeling work [23]. Similarly, the biomass production facility was assumed to be co-located with a direct CO₂ source based on Davis et al. [18]. Determining resource availability was outside the scope of this work and this research assumes that land and CO₂ do not represent a resource constraint for algal cultivation, in any of the modeled sites.

The biomass production process includes the cultivation in open-raceway ponds (ORPs) and biomass dewatering using three different dewatering technologies. The microalgae-to-fuel conversion process was modeled using the open-source hydrothermal liquefaction model developed by Chen et al. [99]. Other facility components such as the inoculum production module were not included in the system boundary since it represents a minimal resource and water consumption in comparison to the cultivation, dewatering, and conversion stages.

Cultivation Model

Open-Raceway Pond Model

The ORPs modeled in this study were assumed to be commercial-scale in-ground ponds such as the ones modeled by Davis et al. [18]. The model used to determine the thermal conditions in the ponds was the previously validated thermal model described in Quiroz et al. [23]. Different from other models in the literature, this model was validated to predict

evaporation rates and temperatures of commercial-scale ponds at a fine timescale [1]. Thermal model inputs include measurements of solar radiation, ambient temperature, relative humidity, and wind speed, as well as the total facility area. Using the pond temperatures calculated with the thermal model, algae growth rates of the strain *Acutodesmus obliquus* (UTEX 393) were modeled using the dynamic growth model developed by Greene et al. [25]. The growth model has been previously validated to predict algae bulk conditions based on light and pond temperatures, reactor design, and strain-specific parameters [25]. For more details on model structure, validation, and strain parameterization in the model, the readers are referred to [23], [25].

Pond Operation

Ponds were operated at a depth of 20 cm with an allowable minimum and maximum depth of 15 and 25 cm, respectively. The ponds were inoculated at 0.1 g L^{-1} and harvested at the first of either achieving a concentration of 0.45 g L^{-1} , after 7 days of system inoculation or when the maximum depth was exceeded. Ponds were harvested by removing 75% of the volume and using the remaining for system inoculation. The ponds were assumed to be turned off during freezing and overheating events and were restarted when no freezing or overheating events were predicted for the next harvesting cycle (7 days). Culture failures due to contamination were not considered in the analysis due to a lack of pond failure data.

Nutrients and CO₂

Microalgae growth in the ORPs was assumed to be supported by the supply of diammonium phosphate (DAP), ammonia, and CO₂. Ammonia and DAP were assumed to be provided with a 20% surplus, while CO₂ was assumed to be delivered via sparging, as described in Davis et al. [18]. The nutrient demand was calculated based on nutrient and biomass

composition as detailed in Greene et al. [25]. The CO₂ demand was calculated after each harvest based on the carbon content of the biomass and CO₂ utilization efficiency [18].

Water Balance

Most water is consumed in the cultivation process; therefore, a detailed water balance of the ponds is needed to ensure the accuracy of the water LCA. The thermal and growth model was implemented in MATLAB© and parameters used in the mass and energy balance were calculated at each time step. The depth of the pond was calculated by tracking the exit and inlet water streams to the ponds, shown in Figure B - 1. Water exiting the system includes the volume that is evaporated or incorporated into the fuel product. Water is added to the ponds either by precipitation, recycling streams (from conversion or dewatering), or directly from the freshwater source. The depth of the ponds is controlled by draining the system when precipitation rates exceed evaporation rates, causing the depth to reach the allowable maximum.

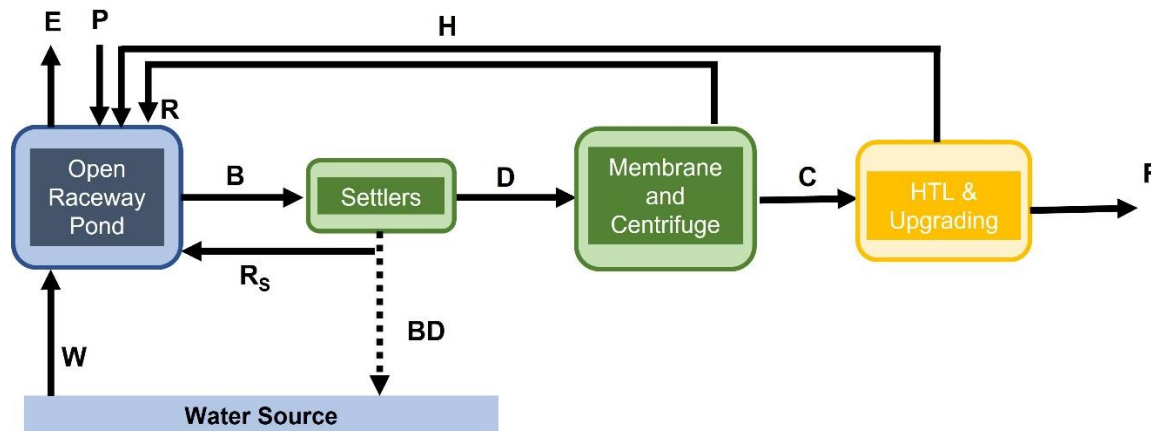


Figure B - 15. Water streams of the algae-to-fuels pathway.

During steady-state conditions, the pond's depth is determined by tracking evaporation and precipitation rates, as defined in the following equation:

$$d^{n+1} = d^n - E^n + P^n \quad (\text{B1})$$

where d is the depth of the pond, E is the evaporated water, P is the rainwater entering the pond, and n is the hourly time-step.

Unsteady state conditions include those in which the ponds are harvested. During harvesting, the water demand is calculated by considering the precipitation that will be available during the next 7 days of pond operation. If enough rainwater to exceed the depth of 25 cm is forecasted, the ponds are drained by routing the recycled water back to the water source (clarified water stream). The net water consumption from the cultivation process is given by the following equation:

$$WD_{cult} = W - C \quad (\text{B2})$$

where W denotes the water withdrawn from the water source and BD is the discharged stream containing clarified water returned to the water source.

The volume of water withdrawn from the water source is a function of the pond depth, recycled stream, and amount of water embedded in the biomass, and it's calculated as follows:

$$W = (d_{fix} - d) + (B - R_S - R) - P_{fut} \quad (\text{B3})$$

where d_{fix} is the fixed depth of the ponds set to 20 cm, d is the volume at harvest, B is the volume of water incorporated in the harvested biomass, R_S is the volume of water recycled from the settlers, R is the water recycled from the membranes and centrifuge stages, and P_{fut} is the volume of rainwater forecasted during the next 7 days. Note that if the volume of water withdrawal is negative, this indicates that no additional water is needed to refill the ponds at 20 cm, and therefore no blue water is physically withdrawn from the water source.

Water discharged is only needed when the ponds are forecasted to reach the maximum depth:

$$C = B - D, \quad R_S = 0 \quad \text{if } (d + P_{fut}) > 25 \text{ cm} \quad (\text{B4})$$

$$C = 0, \quad R_S = B - D \quad \text{if } (d + P_{fut}) < 25 \text{ cm} \quad (\text{B5})$$

where D is the volume of water embedded in the exit stream of the settlers and entering the membrane dewatering process. For the case in which system drainage is required, the volume of water needed to restart the ponds at 15 cm is also accounted for in the water withdrawal calculation.

The water use in the conversion stage was directly computed with the HTL model developed by Chen et al. [99], at an annual resolution for water footprint analysis, and monthly resolution for water scarcity footprint calculations. The aqueous stream recycled from the conversion process was also retrieved from the model, and a nutrient recycling efficiency of 60% was assumed. The water consumed in the conversion process and the aqueous stream represent a minimal water consumption compared to the water usage of the upstream processes and the low temporal resolution of these streams has a negligible impact on the water balance calculations.

Dewatering Module

The performance of the dewatering process has a direct influence on water usage in the biomass production stage. The dewatering technologies modeled in this research were selected based on previous modeling work by Davis et al. [18]. After pond harvesting, the biomass goes through a first dewatering stage in gravity settlers. Most of the recycled water that is returned to the ponds is removed in this process, in which the biomass exits with a concentration of 10 g L^{-1} . The water removed from the biomass stream is assumed to contain negligible biomass, with

biomass blowdown loss set to 0.1% [18]. Additional water is not required to dilute any nutrients remaining in the clarified water stream, which is assumed to contain negligible amounts of DAP and ammonia, based on the stream composition reported in Davis et al. [18].

Following dewatering in settlers, the biomass stream is conducted through a hollow fiber membrane and concentrated to 130 g L^{-1} . The final dewatering process is composed of centrifuges, where the biomass stream exits with a concentration of 200 g L^{-1} . All the recycled water from the last two stages is treated in an ultraviolet light sterilizer before entering the ponds. The energy required to operate the dewatering equipment, ultraviolet sterilizer, and transport biomass between the cultivation and dewatering processes were calculated based on published literature [18], [120].

Saline Cultivation Modeling

To analyze the potential water and energy tradeoffs between freshwater and saline algal cultivation, a saline cultivation scenario was also modeled in two case study locations: Corpus Christi, TX, and Tampa, FL. The saline scenario assumes that seawater with a concentration of 34 g L^{-1} is used for cultivation and a concentration of 45 g L^{-1} is set as the strain salinity tolerance [154]. The system was assumed to be fully restarted once the ponds reached the tolerated salinity. Additionally, seawater was assumed to be transported to the facility through a single pipeline with a pipe diameter of 48 inches and a total pumping head of 64 m (horizontal pumping head of 34 m) [155], [156].

Meteorological Data

The meteorological data used in this analysis includes data retrieved from two different sources. The first dataset consists of historical weather data retrieved from the National Solar

Radiation Data Base (NSRDB) [77]. The NSRDB dataset contains hourly data of solar radiation, wind speed, relative humidity, and ambient temperature measurements from 1998 to 2018 for 220 locations in the continental United States and Hawaii. The second dataset includes daily precipitation data downloaded from the Center for Hydrometeorology and Remote Sensing (CHRS) Data Portal (<https://chrsdata.eng.uci.edu/>) for the years and locations corresponding to the NSRDB files.

The precipitation data was generated using the Precipitation Estimation from Remotely Sensed Information using Artificial Neural Networks–Climate Data Record (PERSIANN-CDR) algorithm to provide long-term rainfall estimates at a fine spatial resolution [157]. The daily measurements were disaggregated to an hourly scale by using a uniform distribution of the daily total:

$$P_h = \frac{P_{daily}}{24} \quad (B6)$$

where P_h is the hourly precipitation and the daily total is denoted by P_{daily} . After curating the precipitation data, the hourly outputs were integrated into the NSRDB files to generate one consolidated dataset.

Gray Water Footprint

The gray water footprint is defined as the virtual water needed to dilute pollutants in waste streams to acceptable pollution standards [95]. In this analysis, the gray water footprint was assumed to be negligible, an assumption supported by nitrogen loading calculations for Tampa, FL. This case study location was selected because of its high volume of discharged water, partly due to intense rainfall, and the results are considered a worst-case scenario relative

to locations with infrequent pond drainage. Nitrogen (N), supplied to the culture by ammonia, was assumed to be the dominant contributor to gray water consumption.

First, outputs from a one-year simulation for the case study location were analyzed to determine the total mass of ammonia consumed by the culture in each harvesting cycle. The initial N concentration in the ponds for harvests where the system was drained, as well as the volume of water discharged by the system, are listed in Table B1. The analysis identified 29 harvests where the culture is partially harvested prior to the complete growth cycle due to rainfall. The average initial nitrogen concentration from the 29 harvests was calculated to be 0.0432 g L^{-1} . The average N concentration in the ponds was then compared to experimental nutrient consumption data to determine the likelihood of complete nutrient assimilation by the culture. According to experimental data reported in the literature [101]–[104] and the calculated average N concentration in the ponds, complete nitrogen assimilation by the culture is usually ensured after retaining the biomass in the ponds for 2 to 3 days [101]–[104]. As shown in Table B1, the lowest biomass retention time in the identified harvests was of 2.6 days, supporting the assumption of complete nutrient assimilation by the biomass.

Table B1. Modeled outputs used in the gray water footprint analysis.

Biomass Retention Time (days per harvest cycle)	Initial Ammonia Concentration in Ponds (g per L)	Volume of Water Discharged per Harvest (m3 per harvest cycle)
4.7	0.0529	596,533
3.9	0.0523	615,754
4.0	0.0519	733,816
5.0	0.0505	627,290
4.1	0.0505	748,466
6.0	0.0499	663,205
3.9	0.0495	846,205
4.1	0.0476	846,044
5.0	0.0469	724,000
4.0	0.0467	787,092
2.6	0.0454	725,637
3.2	0.0450	846,416
3.1	0.0442	903,397
3.1	0.0439	870,561
3.8	0.0434	1,017,853
3.2	0.0433	804,038
4.7	0.0428	869,374
3.9	0.0426	820,967
4.0	0.0418	895,643
5.0	0.0411	918,738
4.1	0.0407	907,116
6.0	0.0404	908,007
3.9	0.0387	895,456
4.1	0.0385	827,456
5.0	0.0384	1,021,768
4.0	0.0381	953,210
2.6	0.0378	822,460
3.2	0.0317	1,076,325
3.1	0.0150	1,071,940

As shown by the results presented in Table B1, the gray water footprints of algal cultivation are a function of nutrient inputs and the retention time in the ponds. The sensitivity of these parameters on the gray water footprints of the system was analyzed and the results are illustrated in Fig. B - 2. The gray water footprints presented in Fig. B - 2 were calculated by quantifying the volume of water needed to reduce the N loading in the discharged water to 1 mg L⁻¹ [158] and by varying the number of harvests with incomplete nutrient assimilation. The results shown in Fig. B - 2 indicate that proper pond management is required to maintain negligible gray water footprints. Specifically, tracking the nutrient loadings in the ponds and the retention time in the ponds is important to ensure that the culture will completely consume the nutrients when pond drainage is required due to rainfall. The analysis indicates that gray water footprints are negligible according to the pond management assumptions used in this study.

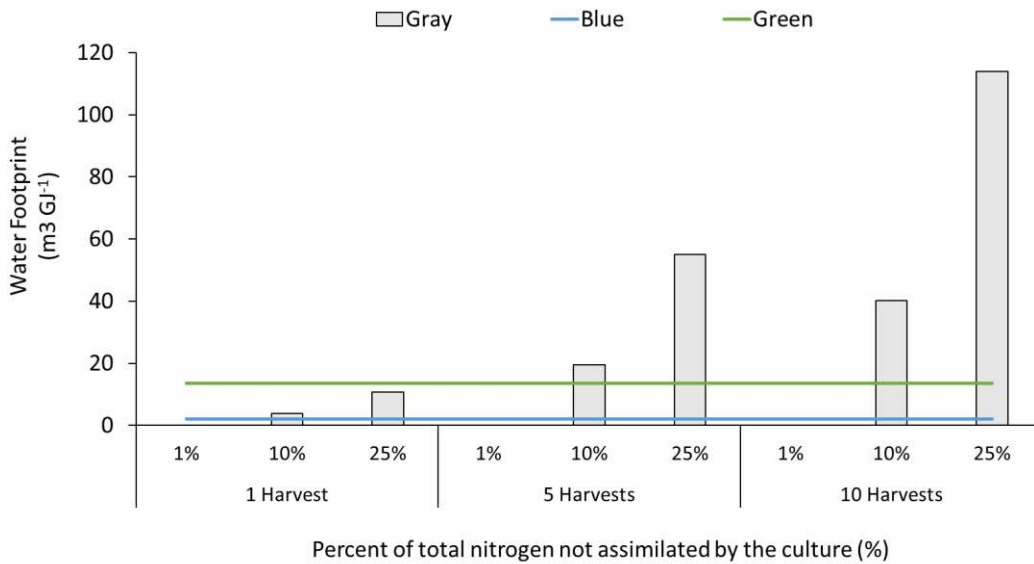


Figure B - 2. Gray water footprint for Tampa, FL as a function of the number of harvests with varying percentage of nitrogen in the discharged water stream.

Indirect Water Footprint Data

The water consumption from upstream processes in the supply chain was estimated using data from different published life cycle assessments and databases. The water footprints for nutrients, hydrogen, and natural gas were retrieved from the GREET 2021 [105] while the water footprint for electricity generation was calculated based on the work from Lee et al. [106], [159]. The water footprint of each of the processes retrieved from the GREET 2021 model is shown in Table B2.

Table B2. Water life cycle inventory.

Process	Water Consumption (m ³)	Normalizing Unit	Source
Diammonium Phosphate	37.0	tonne DAP	GREET 2021
Ammonia	1.728	tonne NH ₃	GREET 2021- Conventional Ammonia Production
Natural Gas	0.640	tonne of natural gas	GREET 2021 - NA NG for use on FT plants
Hydrogen	109.8	tonne of H ₂	GREET 2021 – G.H2 for Steel Production

To capture the regional differences between electricity grids and mixes, the water footprint of electricity generation was calculated at an eGRID subregion [107] level using the water consumption and electricity generation data provided by Lee et al. [106] for thermoelectric power plants and the results from Lee et al. [159] for hydroelectric power plants. The first dataset contains generator-level water consumption and electricity generation measurements for thermoelectric power plants across the US reported by the U.S. Energy Information

Administration (EIA) in 2015 [159]. For hydropower plants, the regional water footprints presented by Lee et al. [159] and electricity generation data retrieved from the eGRID model [107] were used to provide estimates at an eGRID subregion level [107].

The dataset curated by Lee et al. [106] was analyzed and manipulated in the R programming language. First, generators that used saline or reclaimed water for cooling were discarded, and the water consumption and electricity generation of each generator were summed at a power plant level. The adjusted water consumption was used to avoid double counting the water consumption of multitype generators [159]. Once the plant level water consumption and generation were calculated, the coordinates and zip code of each power plant were retrieved from form EIA-860 [160]. The Power Profiler Emissions Tool developed by the Environmental Protection Agency (EPA) [161] was used to determine the eGRID subregion corresponding to each power plant, based on the plant's zip code. The water consumption and electricity generation of power plants that were found to be located in more than one eGRID subregion were averaged between subregions. Finally, water consumption and electricity generation of the 609 thermoelectric power plants in the dataset were added at a subregion level.

For the case of hydroelectricity, two different sources were used to estimate water footprints at a subregional resolution. First, annual net hydroelectricity generation for each subregion was retrieved from the eGRID 2019 model [107]. This data and the water intensities of hydroelectric power reported in Lee et al. [159], for each North American Electric Reliability Corporation (NERC) region, were combined to estimate the total water consumption for each subregion. The reported NERC water intensity was used for each subregion within the corresponding NERC region. For example, the water intensity of subregions in the WECC (NERC region), was given a fixed water intensity of $2.73 \text{ m}^3 \text{ MWh}^{-1}$ [159] and the subregional

resolution was obtained from the differences in annual hydroelectricity generation. Finally, the water consumption and electricity generation for hydroelectric and thermoelectric power plants were added to obtain a subregional water footprint:

$$WF_i = \frac{(WC_{th} + WC_{hyd})_i}{(G_{th} + G_{hyd})_i} \quad (B7)$$

where WF_i is the water footprint of subregion i in $\text{m}^3 \text{MWh}^{-1}$, $(WC_{th} + WC_{hyd})_i$ is the sum of water consumed by thermoelectric and hydroelectric power plants in subregion i , and $(G_{th} + G_{hyd})_i$ is the corresponding electricity generation for thermoelectric and hydroelectric power plants in subregion i . The results of the analysis are shown in Table B3.

Table B3. Water consumption of electricity generation in the United States.

eGRID Subregion	Water Footprint ($\text{m}^3 \text{MWh}^{-1}$)	eGRID Subregion	Water Footprint ($\text{m}^3 \text{MWh}^{-1}$)
CAMX	1.1	RFCE	0.7
ERCT	1.0	RFCM	1.3
FRCC	1.4	RFCW	0.8
HIMS	2.8	RMPA	1.3
HIOA	0.0	SPNO	1.2
MROE	0.0	SPSO	1.3
MROW	1.1	SRMV	1.4
NEWE	1.1	SRMW	1.6
NWPP	0.3	SRSO	1.5
NYCW	2.1	SRTV	1.5
NYLI	0.0	SRVC	1.2
NYUP	0.0	SRVC	1.1

County-Level Interpolation

The monthly water consumption, and biomass and fuel yields for the 220 simulated sites were surface interpolated and averaged at a county level to calculate monthly water scarcity footprints. The outputs from the engineering process model were preprocessed by assigning zero water consumption to facilities meeting certain criteria. First, the facilities having monthly areal productivity lower than $5 \text{ g m}^{-2} \text{ day}^{-1}$ or operating less than 10 days per month were deemed economically unfeasible, therefore, these facilities were assumed to pause operations during the month. This filtered out facilities in locations with harsh winter conditions. A second filter was applied to biorefineries in which the monthly water consumption from cultivation was less than the recycled water from conversion, this was particularly the case for facilities with high biomass yields, high precipitation rates, and low evaporation rates such as algae farms in the Gulf Coast U.S.

After preprocessing, the data was surface interpolated in a 0.1° grid spanning the continental US and Hawaii. Results were interpolated using a kriging method and a county estimate was obtained by averaging the outputs of sites within each county. A cutoff was then applied to facilities with a biomass or fuel yield of fewer than 15 tonnes or 400 GJ per month, respectively. The cutoff was done to improve data visualization and removed less than 1% of the total counties. Subsequently, monthly water scarcity footprints for each county were calculated using AWARE-US characterization factors [108]. Seasonal averages were calculated by averaging the county's water scarcity footprints for the three months of each season. The seasonal outputs were finally illustrated in the form of heatmaps. The R code developed for data manipulation is available for download at the following URL:
<https://github.com/davquirozn/Water-Footprint-Publication>.

Model Outputs

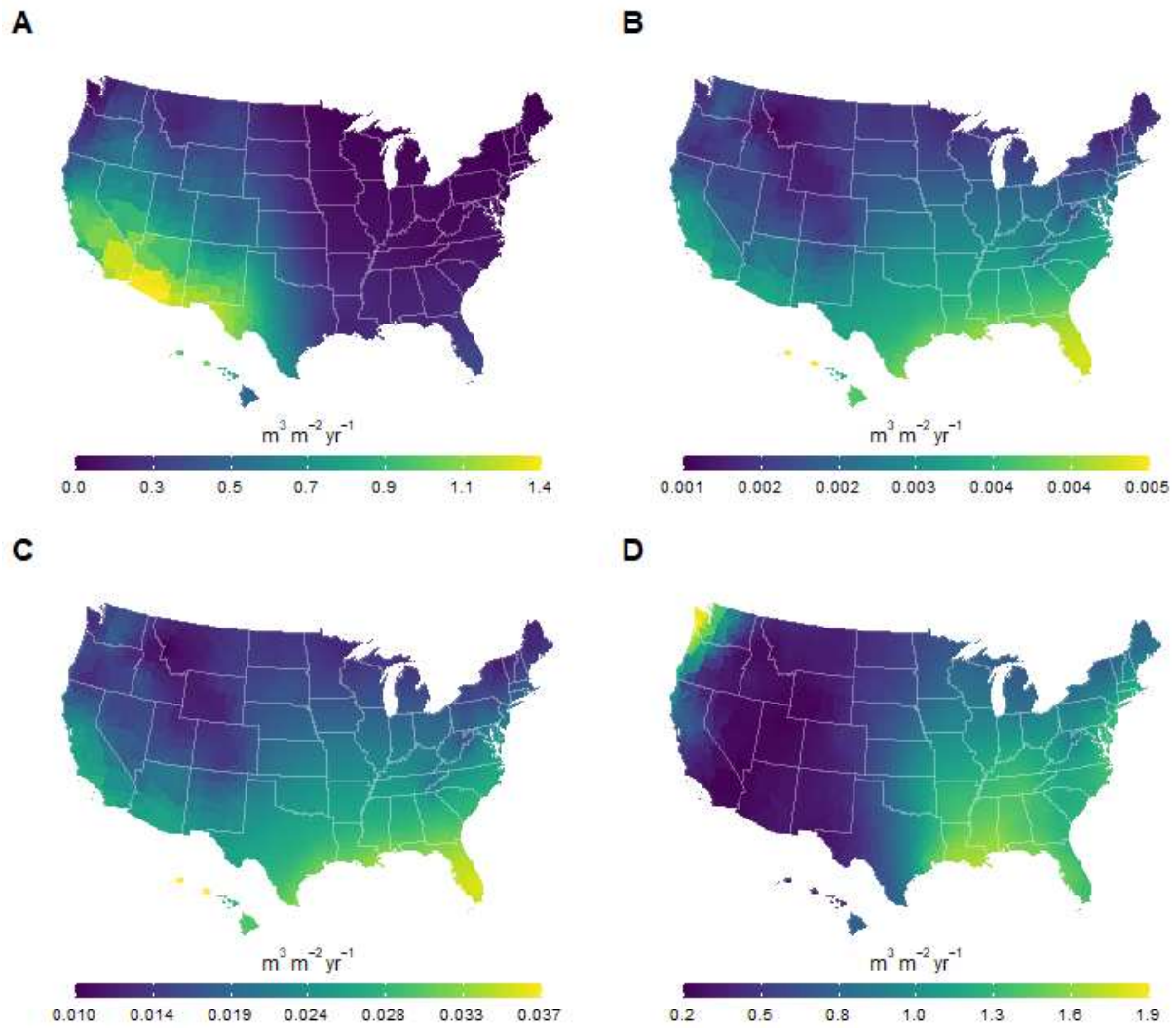


Figure B - 3. Main water streams involved in the production of microalgal fuels: (A) freshwater demand for the cultivation process, (B) freshwater demand for the conversion process, (C) recycled water from the conversion process, (D) rainwater demand for the cultivation process. Values presented here are the annual averages of the 21 simulated years.

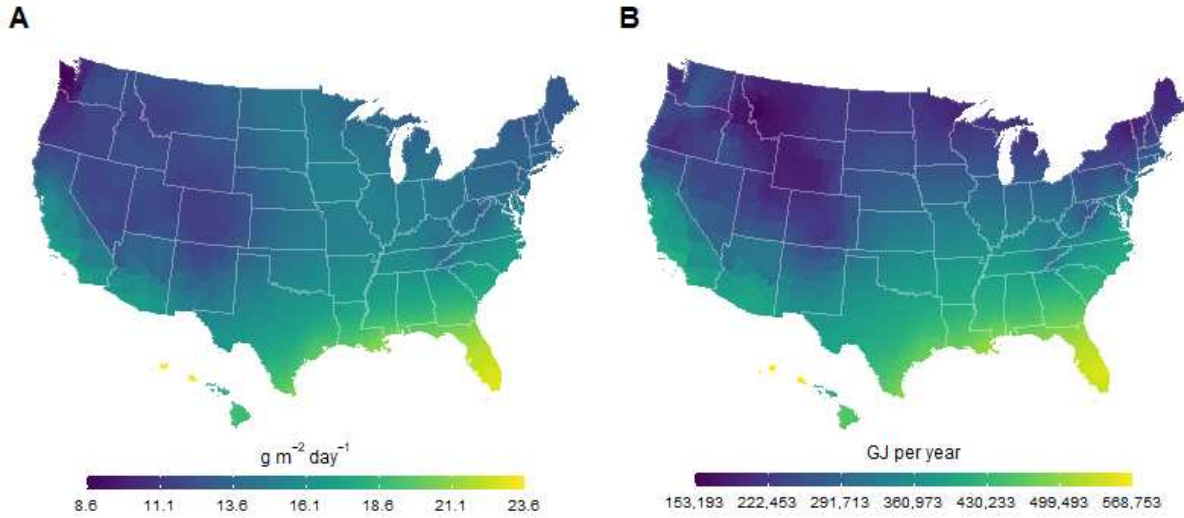


Figure B - 4. Biomass and fuel yields: (A) annual average areal productivity in ash-free dry weight and (B) annual energy output. Values presented here are the annual average of the 21 simulated years.

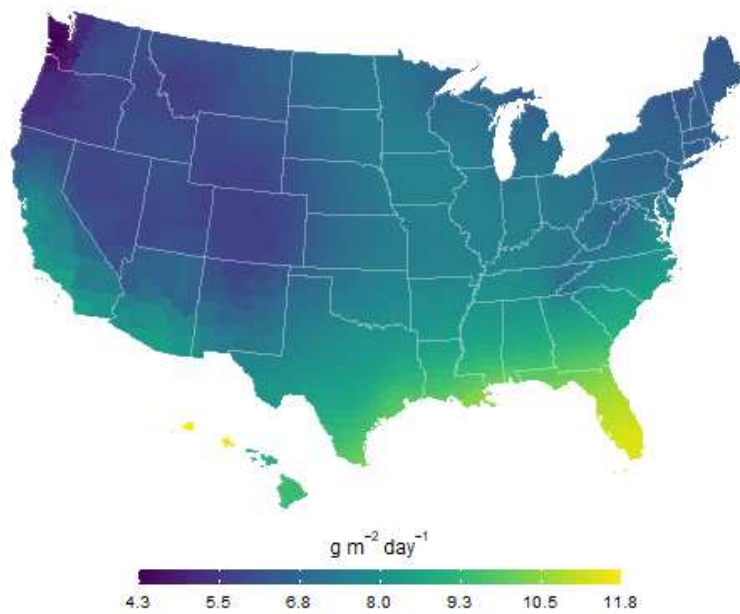


Figure B - 5. Annual average biomass yields with a design safety factor of 0.5, accounting for potential pond contamination and culture failure. Values presented here are the annual average of the 21 simulated years.

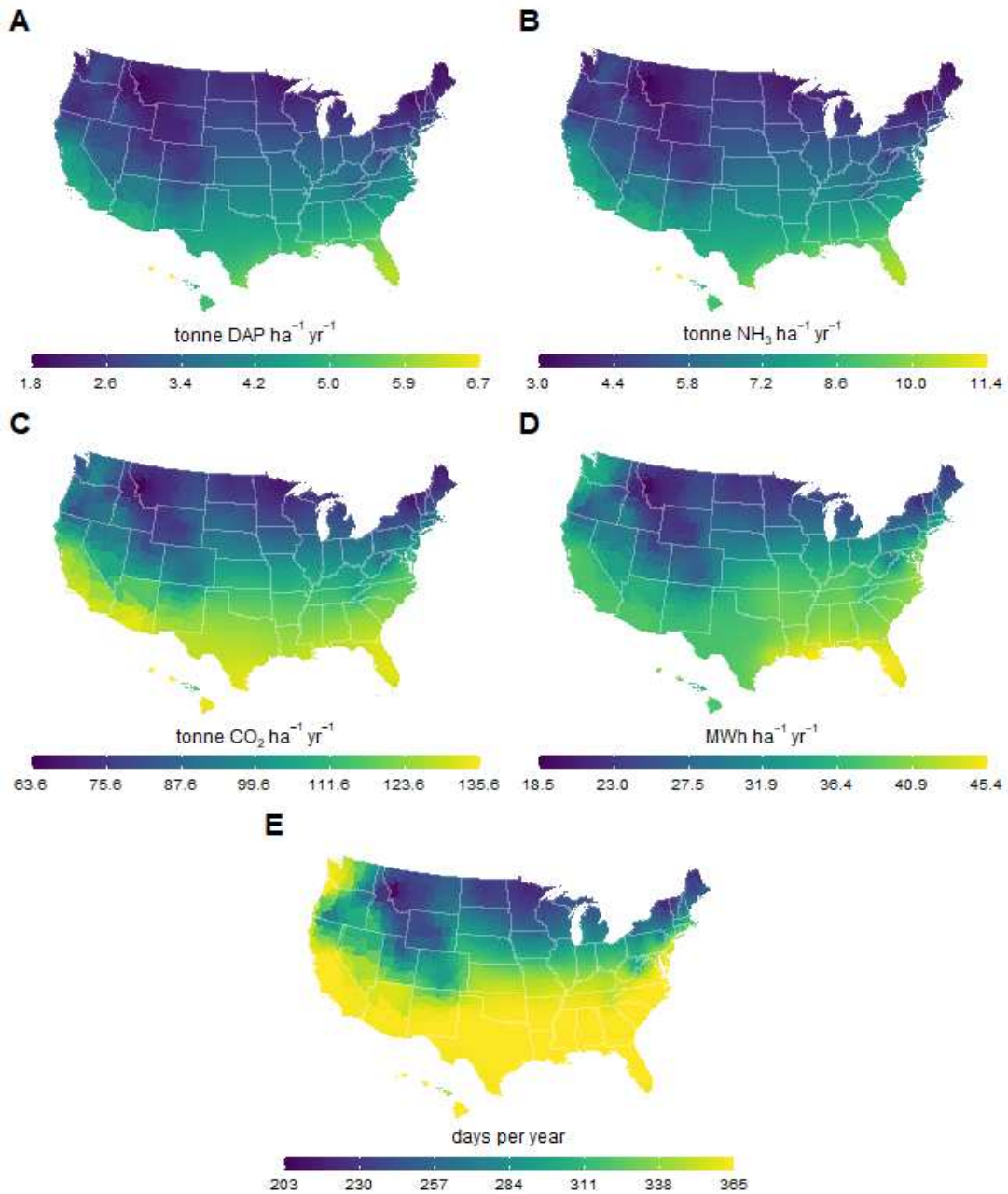


Figure B - 6. Average cultivation model outputs: (A) diammonium phosphate consumption, (B) ammonia consumption, (C) CO₂ consumption, electricity consumption, and (E) operational days for the continental US and Hawaii. Values presented here are the annual averages of the 21 simulated years.

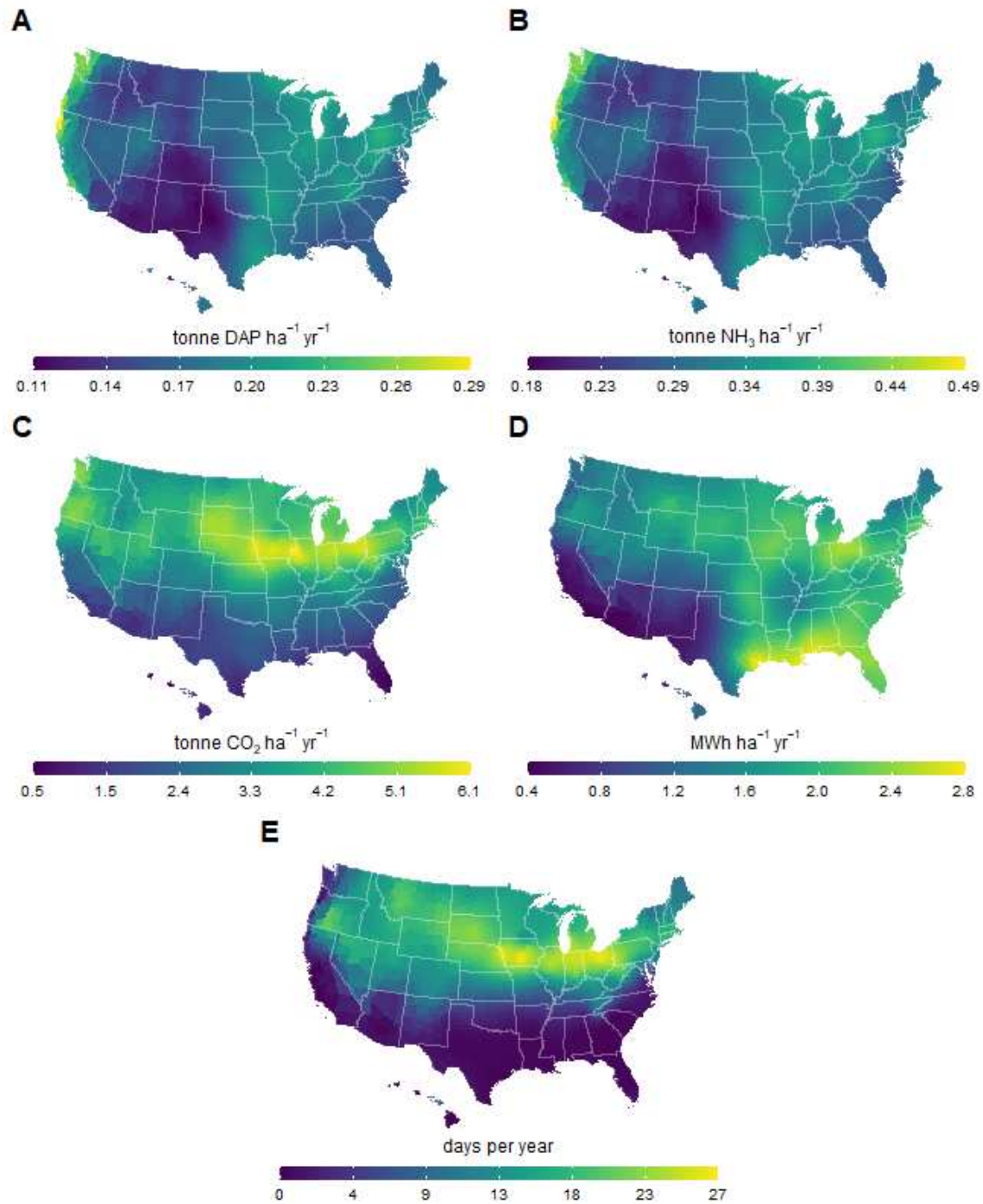


Figure B - 7. Annual standard deviation of cultivation model outputs: (A) diammonium phosphate consumption, (B) ammonia consumption, (C) CO₂ consumption, electricity consumption, and (E) operational days for the continental US and Hawaii. Values presented here are the standard deviation of the annual averages of each simulated year.

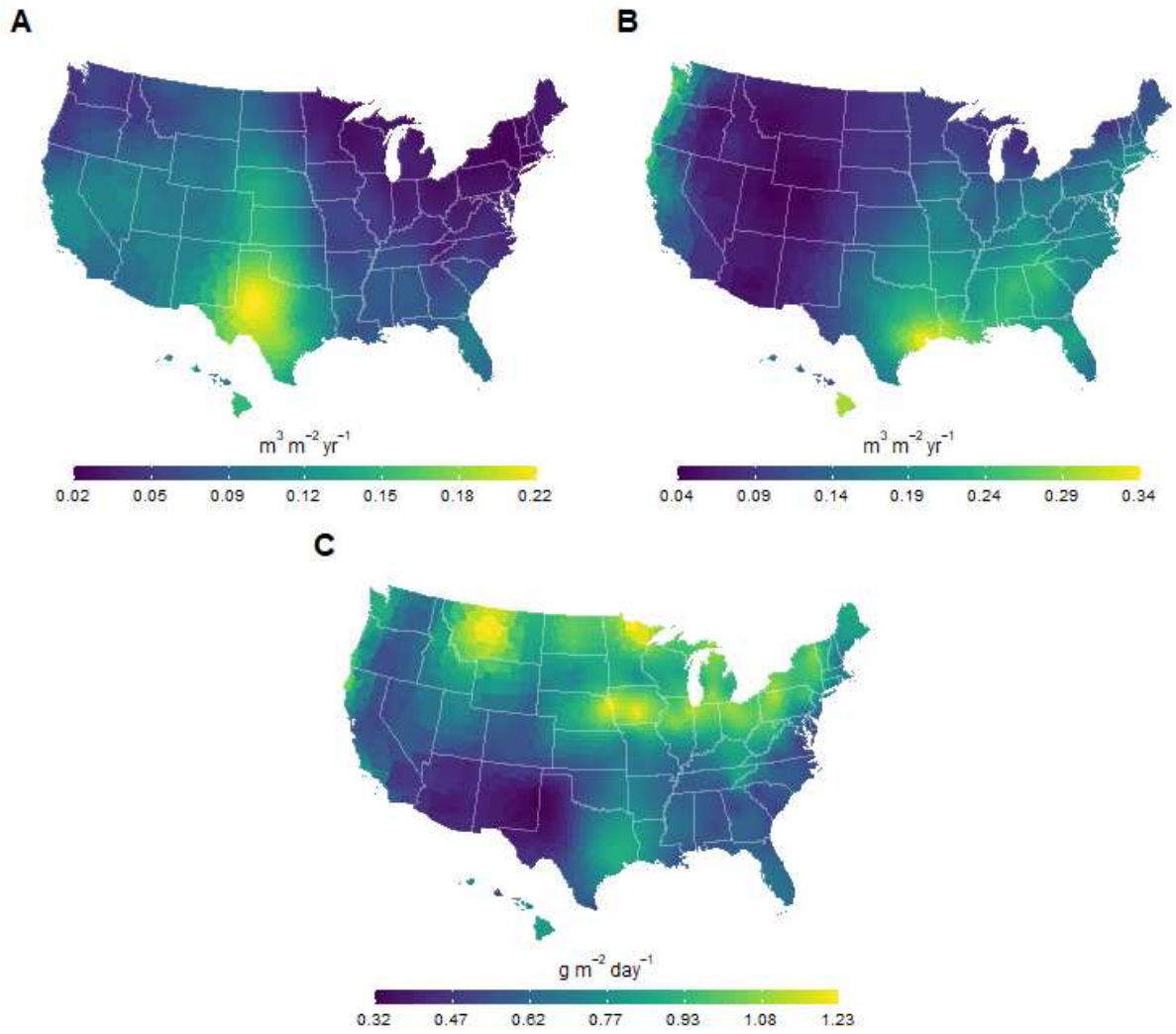


Figure B - 8. Annual standard deviation of cultivation model outputs: (A) freshwater demand, (B) rainwater demand, and (C) areal productivity. Values presented here are the standard deviation of the annual averages of each simulated year.

Water Footprint Results

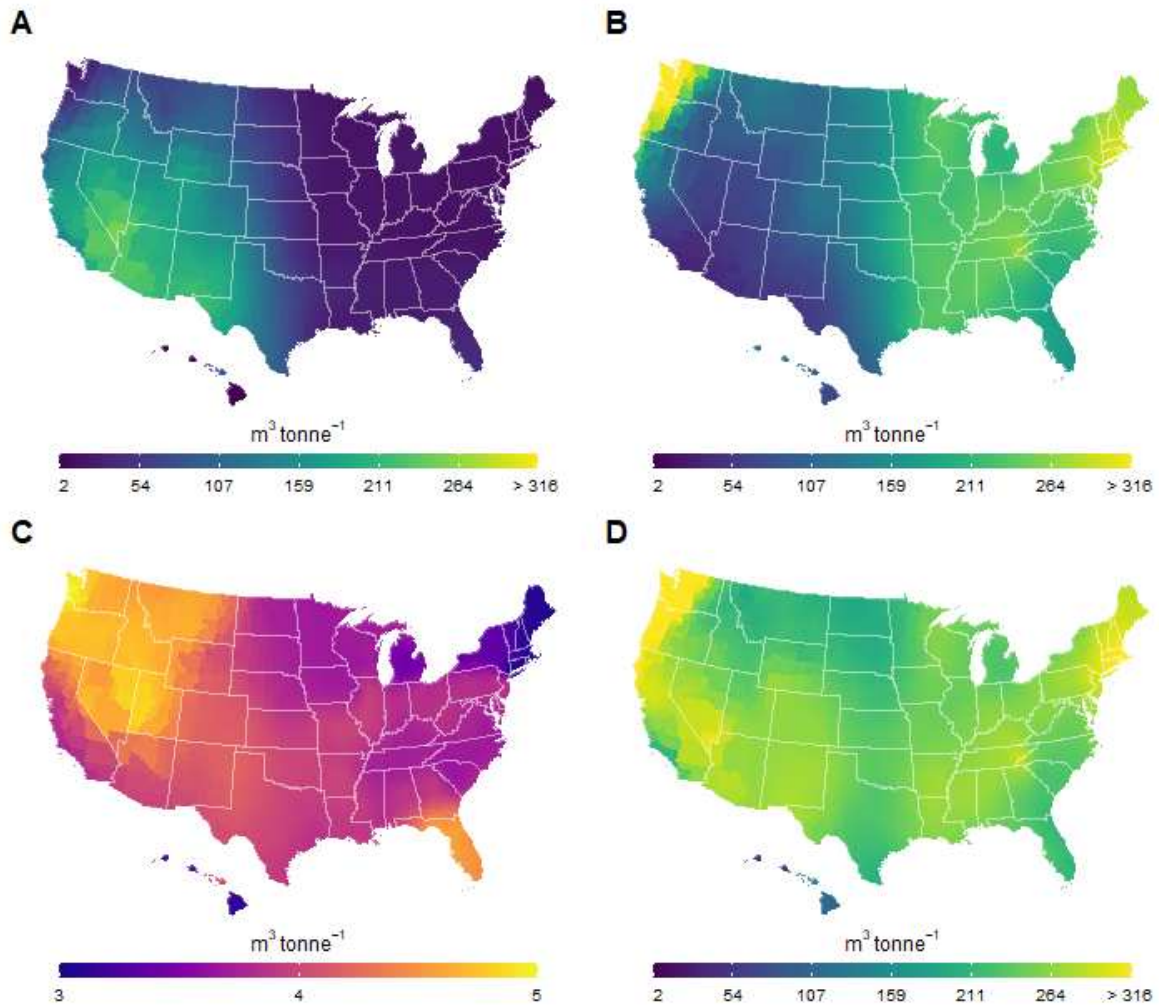


Figure B - 9. Life cycle water footprint breakdown of algal biomass: (A) direct blue water footprint, (B) direct green water footprint, (C) indirect water footprint, and (D) total water footprint.

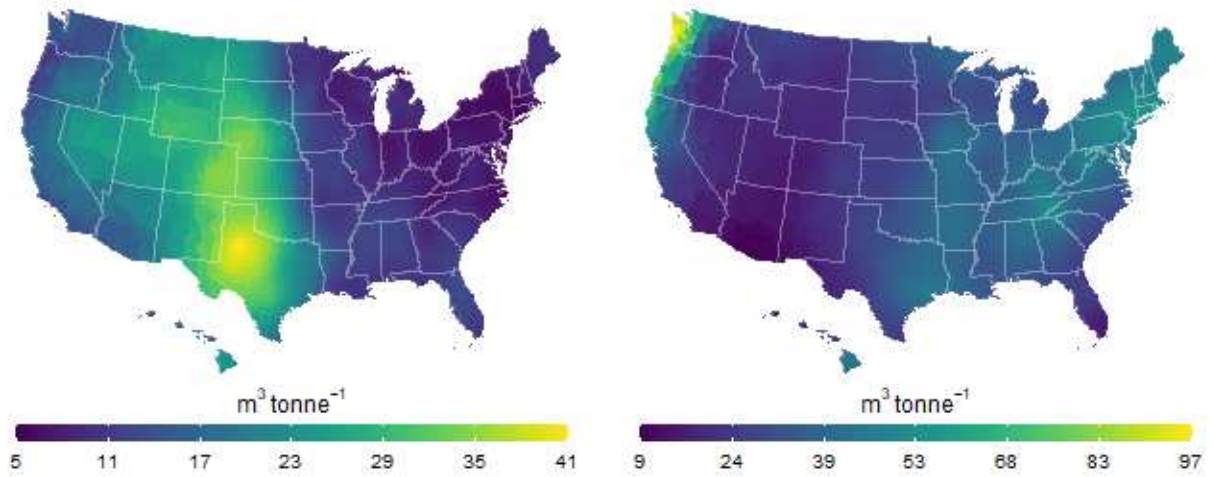


Figure B - 10. Standard deviation of the (A) blue and (B) green water footprint of the biomass system boundary. Results represent the standard deviation of the 21 annual averages calculated from simulation outputs.

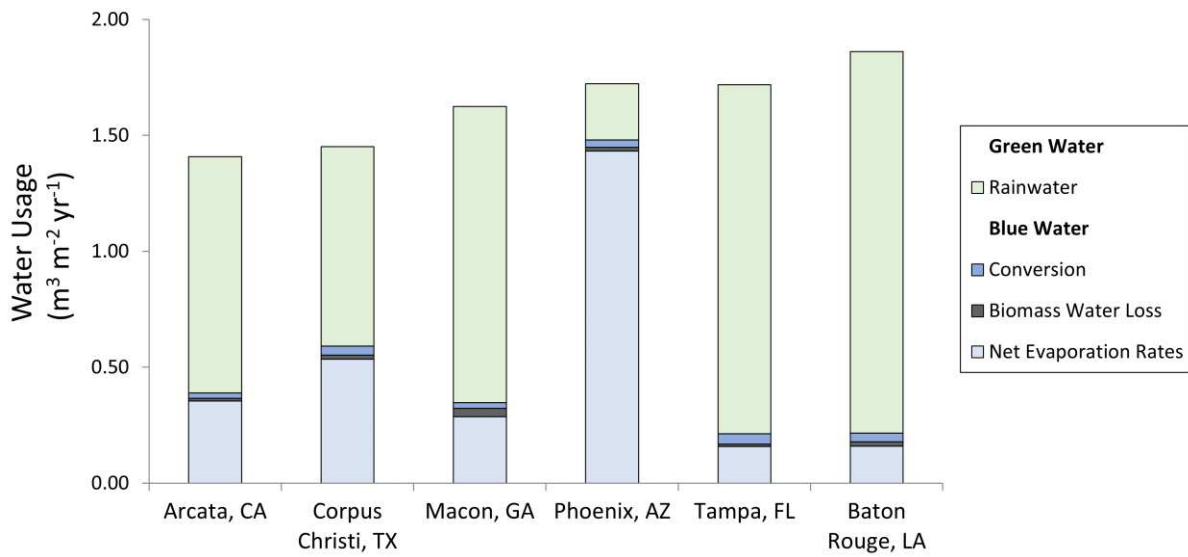


Figure B - 11. Breakdown of direct water consumption for the cultivation of algal biomass and conversion to renewable diesel for six of the 220 locations modeled in the US. Results represent the 21-year average.

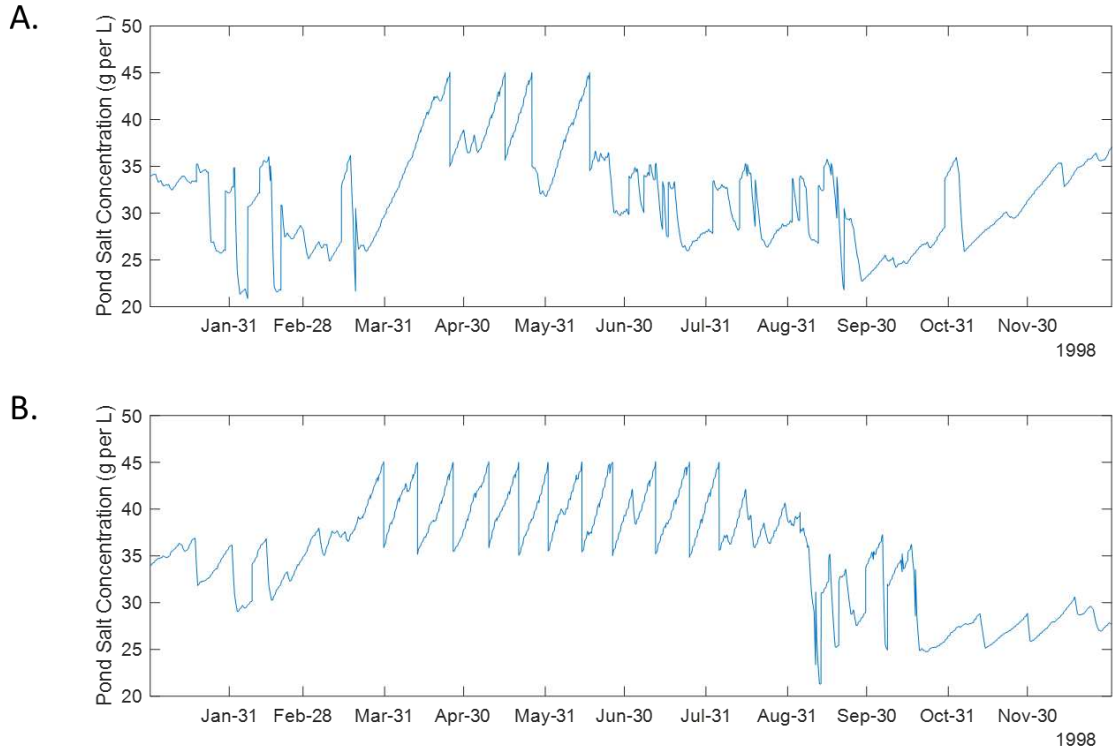


Figure B - 12. Time series of salt concentration in ponds from a simulation run in a) Corpus Christi, TX and Tampa, FL.

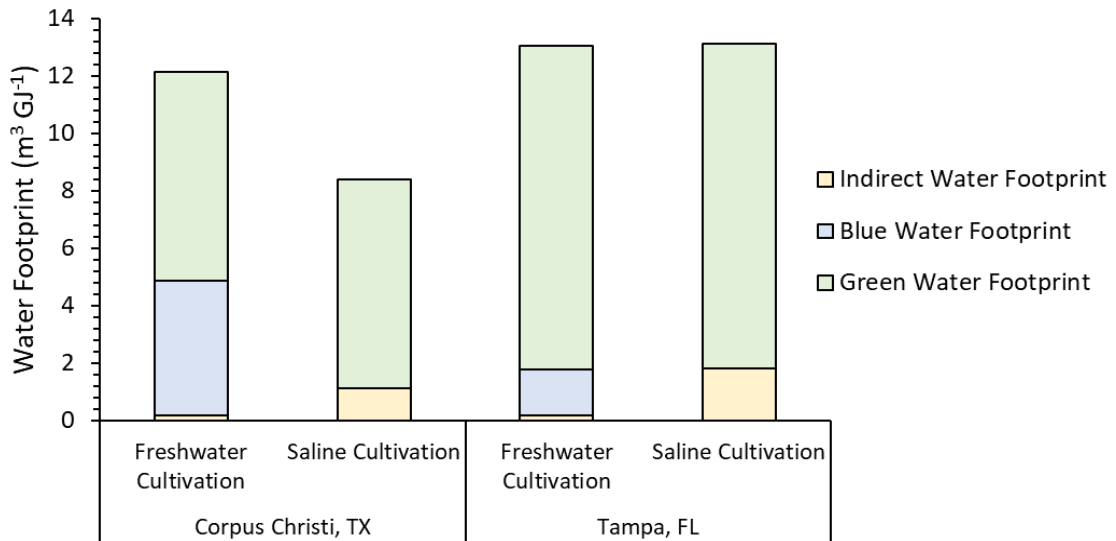


Figure B - 13. Water footprint comparison between saline and freshwater cultivation at two case study locations.

Water Scarcity Footprint Results

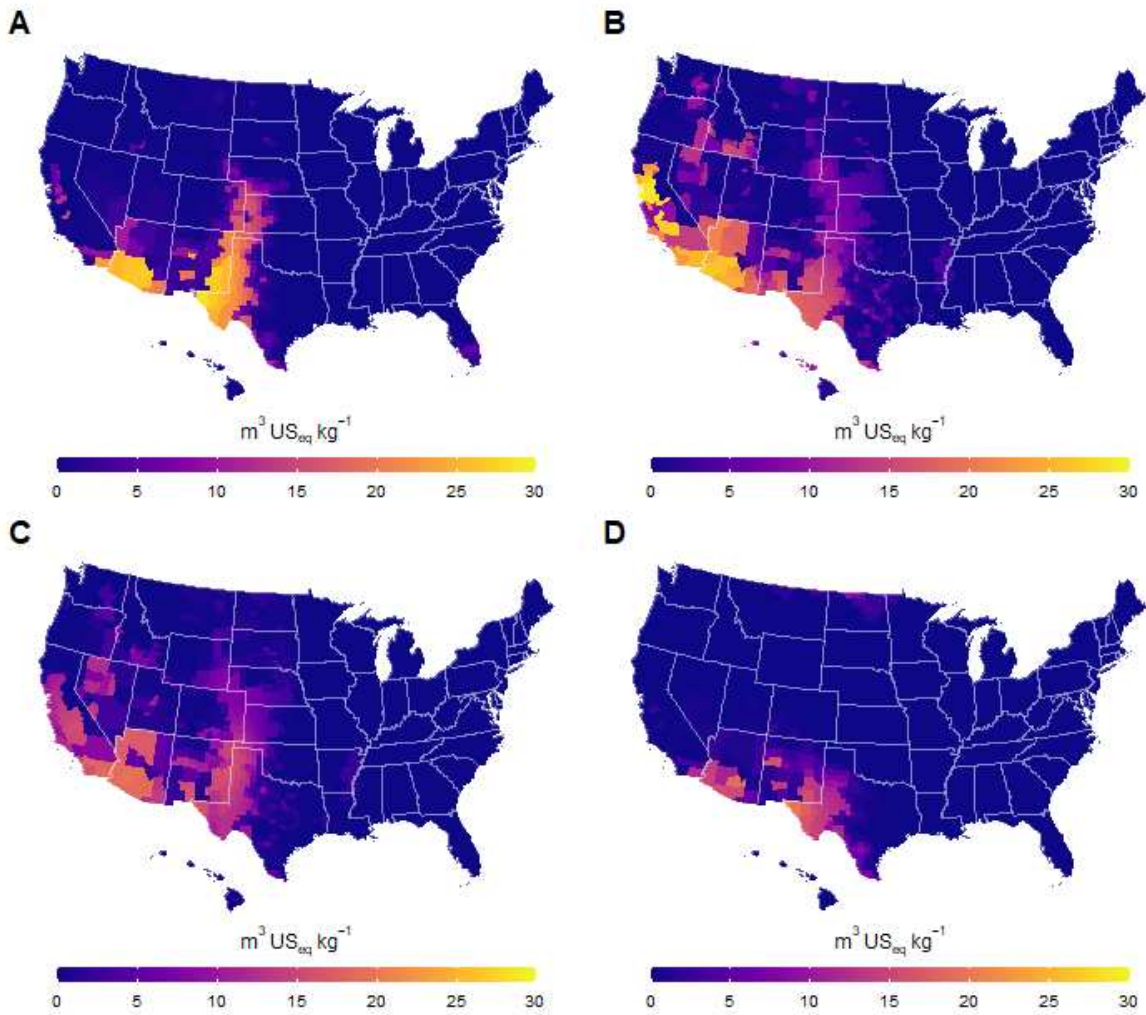


Figure B -14. Seasonal water scarcity footprint of the biomass system boundary: (A) spring, (B) summer, (C) fall, and (D) winter.

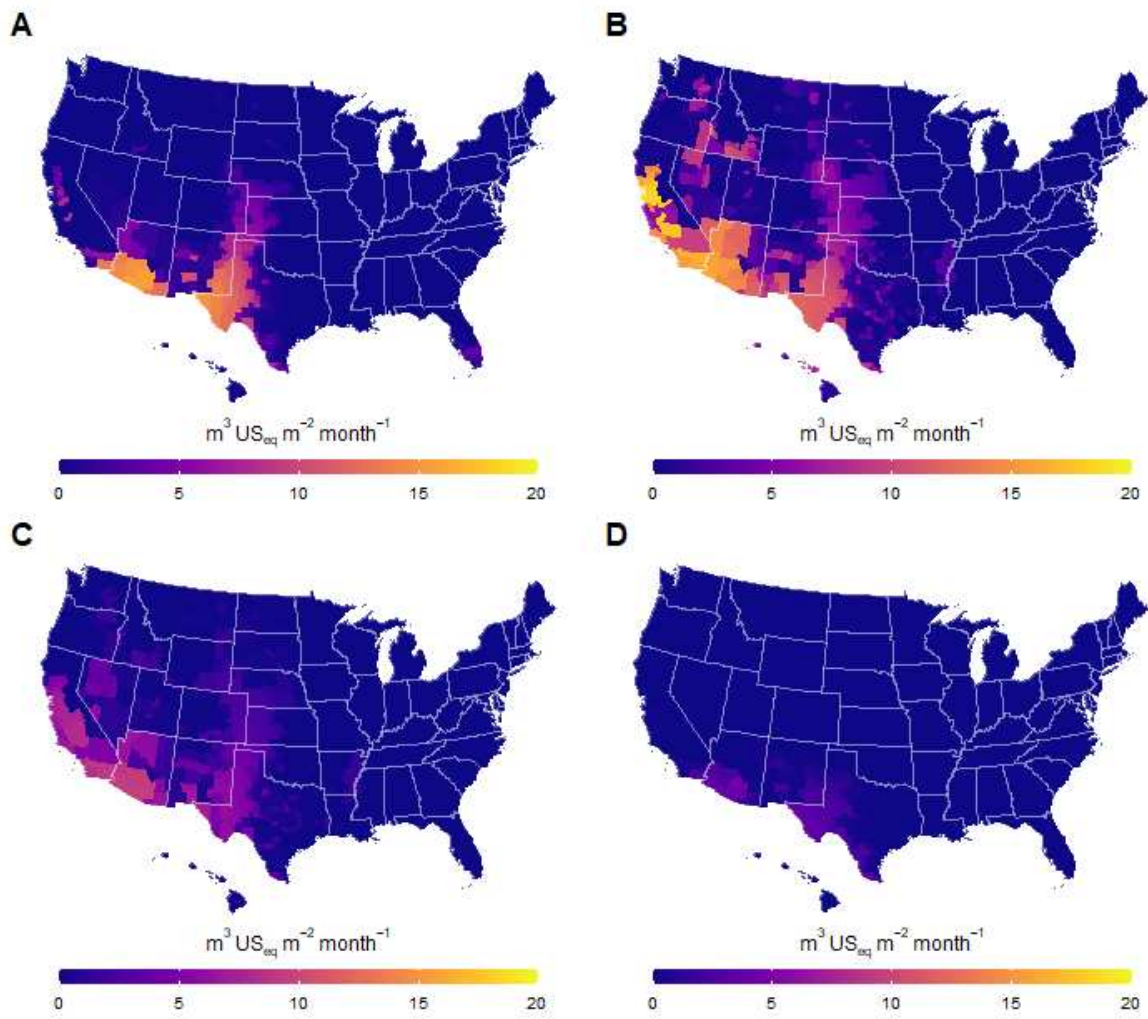


Figure B -15. Seasonal water scarcity footprint of the biomass system boundary: (A) spring, (B) summer, (C) fall, and (D) winter.

Sensitivity Analysis

The sensitivity of the direct blue WF and indirect WF to fundamental input variables was tested for two case study locations. Input variables were decreased and increased independently by 20%, where applicable. Recycling efficiencies, for which the 20% increase yielded values above 100% were set to the allowable maximum, and the days to harvest (baseline value is set to 7 days) were reduced to 3 days and increased to 10 days. The most impactful variables were identified and results for Phoenix, AZ, and Tampa, FL are illustrated in Fig B - 16.

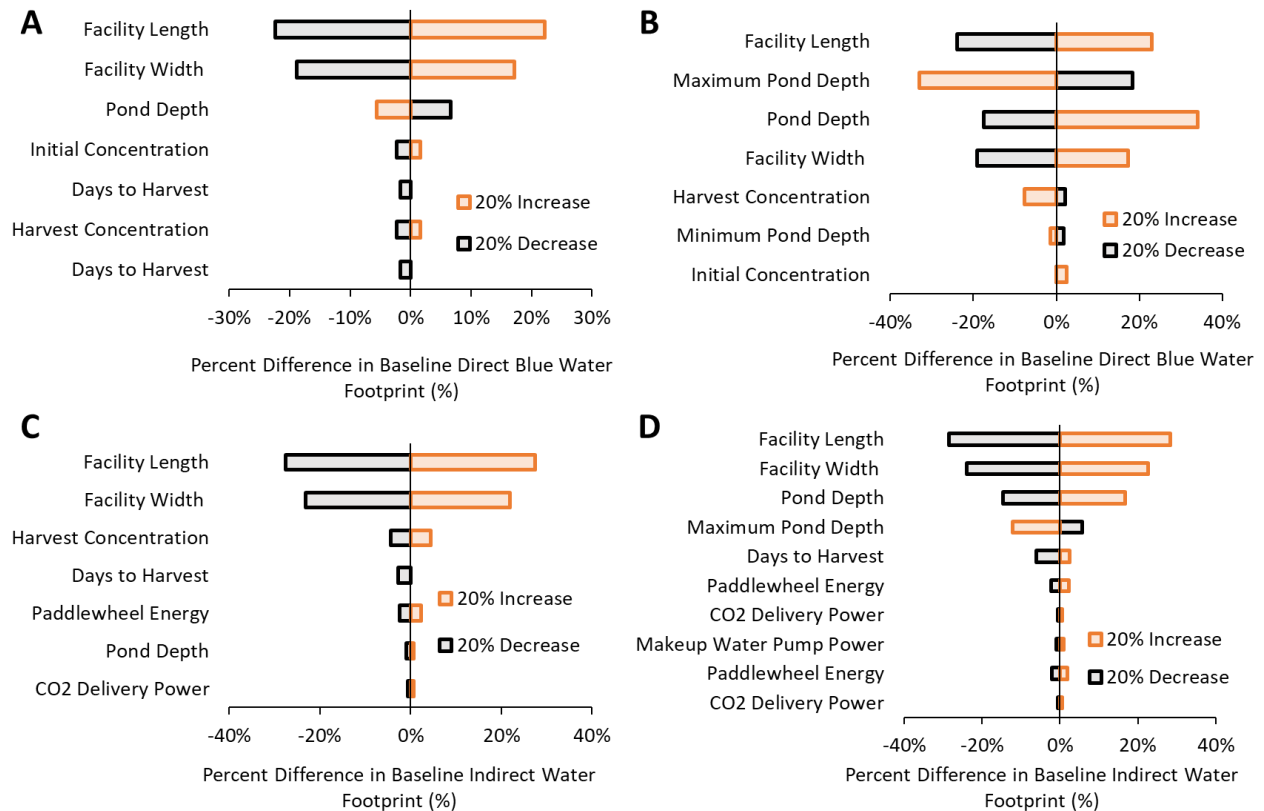


Figure B - 16. Sensitivity analysis for direct blue water footprints in A) Phoenix, AZ, and B) Tampa, FL and for the corresponding indirect water footprints in C) Phoenix, AZ, and D) Tampa, FL.

APPENDIX C

Modeling Architecture. This study leveraged different process models, datasets, and evaluation tools to quantify the global economic viability and environmental impacts of microalgae biofuels. The simulation architecture used in this study is illustrated in Fig. C - 1.

Open Pond Growth Model. Growth modeling calculations were done by using the model validated and developed by Greene et al. [25] along with 6 strain-dependent inputs, photosynthetically active radiation (PAR) data, and pond temperature data. The model accurately calculates the time-resolved bulk algal concentration based on a carbon fixation rate that is dynamically impacted by light and temperature fluctuations [25]. The governing equation differential equation is given by:

$$\frac{dC_x}{dt} = \frac{\phi_L(t)\phi_T(t)PAR(t)\theta_{photon}A}{V} + \frac{D(t)}{V} \quad (C1)$$

where C_x is the biomass concentration, ϕ_L is the time-resolved light efficiency that calculates photoinhibition effects, ϕ_T is the time-resolved temperature efficiency, θ_{photon} is the photon efficiency set to 1.5 g biomass per mol photons, A is the surface area of the pond, $D(t)$ is the respiration decay rate, and V represents the volume of the pond at inoculation [25]. Growth model inputs for the strain *Scenedesmus obliquus* (UTEX 393) were used based on the validation study done by Quiroz et al. [23]. The growth validation leveraged experimental data from the summer 2019 growth trials at the Arizona Center for Algal Technology Innovation in Mesa, Arizona (33.41° N, 111.83° W) [7], [23]. Growth model inputs are provided in Table C1.

Open Pond Thermal Model. Temporally resolved pond temperatures and evaporation rates were calculated using the thermal pond model constructed by Quiroz et al. [23]. The model performs an energy balance on the culture by considering the different heat fluxes acting on the

ponds [23]. Thermal model inputs include the surface area and depth of the pond and measurements of global horizontal irradiance, ambient temperature, relative humidity, and wind speeds [23]. The dynamic pond temperature (T_p) was calculated with the following equation:

$$\rho c_p V \frac{dT_p}{dt} = \sum Q_n \quad (C2)$$

where ρ is the culture density (1000 kg m^{-3}), c_p is the specific heat of the culture ($4184 \text{ J kg}^{-1} \text{ K}^{-1}$), V is the volume of the pond, and Q_n are the heat fluxes including direct and diffuse solar radiation, pond radiation, atmospheric radiation, ground conduction, convection, evaporation, and water inflow [23].

Cultivation Facility. A 5,000-acre facility was modeled based on previous techno-economic assessments of algal biofuels [13], [18], [99]. The facility consists of 50 10-acre ponds operated at an average 20 cm depth, consistent with previous modeling efforts [18], [44]. The ponds were assumed to be operated semi-continuously and harvested every three days or when a concentration of 300 g m^{-3} was reached [7], [14]. Inoculation density was set to 100 g m^{-3} and operations were interrupted if the temperature of the pond reached below 0°C . Ponds were restarted if the temperatures during the next growth trial (3 days) were predicted to be above-freezing conditions. Makeup water to cover evaporation losses was added to the ponds at each harvest or when a minimum depth of 15 cm was reached. Pond contamination was not modeled due to the lack of data [7], [16], however, the costs of an on-site inoculation system were included.

Nutrient-replete conditions were assumed with ammonia and diammonium phosphate as the sources of nitrogen and phosphorus. A 20% nutrient surplus was assumed following previous

modeling exercises [13], [44]. Hourly nutrient demand was calculated based on the biomass composition provided in Table C1 and following the methods used in the literature [18], [23], [44]. Finally, carbon dioxide (CO₂) was treated as an operational expense following the modeling methods detailed in Davis et al. [18]. Co-location to a dilute source of campus, either a coal or natural gas power plant was assumed. The energy needed to concentrate and compress CO₂ was set to 0.542 kWh kg⁻¹ CO₂ based on work by Somers et al. [146]. On-site energy used to transport and sparge CO₂ into the ponds was additionally included [18]. The energy demand of the different pumps, paddlewheel operation, and CO₂ delivery are provided in Table C1.

Meteorological Data. Weather data required for growth and thermal modeling was retrieved from the fifth global reanalysis (ERA5) dataset generated by the European Centre for Medium-Range Weather Forecasts [123]. The dataset includes hourly modeled surface downward irradiance, 2m ambient temperature, 2m dew temperature, and 10m wind speeds for the year 2021 across a 0.25° by 0.25° grid [123]. Data for 6,685 global locations across a 1.5° by 1.5° grid was extracted to reduce the computational time of the calculations. Relative humidity data was calculated from the ambient and dew temperatures using the MetPy Python library [162]. Furthermore, PAR values were calculated using solar irradiance data and following the assumptions presented in Greene et al. [25].

Biomass Dewatering and Storage. Biomass dewatering was modeled following the three-step dewatering process suggested by Davis et al [18]. This includes gravity settlers, membranes, and a centrifuge step to increase the concentration of the biomass to 200 g L⁻¹. System blowdown was done when the concentration of salt in the ponds exceeded 4000 g m⁻³ while the concentration of the makeup water was assumed to be 250 g m⁻³ [44]. Water recycled

from the membrane and centrifuge modules was sterilized through ultraviolet sterilizers following the modeling assumptions in Beckstrom et al. [120]. Moreover, anaerobic storage was modeled to control the seasonal variability of biomass output and provide a constant feed to the biorefinery [163]. The biomass was assumed to be stored in 1,000 m³ belowground storage pits at 20% solids [163]. A 30-day dry matter loss rate of 15% was used based on experimental data from Wendt et al. [163]. Costs for gravity settlers [18] were used as a proxy to estimate the capital expenses of the storage process [163].

Hydrothermal Liquefaction and Upgrading. Conversion to biocrude via hydrothermal liquefaction (HTL) and upgrading to renewable diesel and naphtha via hydrotreating and hydrocracking were modeled using the open-source HTL model developed by Chen and Quinn [99]. The model considers the biochemical composition of the biomass to calculate the solid, gaseous, aqueous, and biocrude yields following the methods in Leow et al. [122]. A 30-minute HTL reactor residence time and 350°C temperature was assumed [99]. Furthermore, 60% of the nutrient-rich aqueous output from HTL was assumed to be recycled to the cultivation ponds. The remaining 40% was assumed to be disposed to a wastewater treatment facility. No revenue value was assigned to the solid biochar to simplify calculations. The gases from HTL and upgrading are assumed to be diverted to the heating utility which reduces natural gas requirements [99]. Accordingly, the combustion of off-gases was modeled using greenhouse gas and air pollutant emission factors for natural gas boilers retrieved from the Greenhouse Gases, Regulated Emissions, and Energy Use in Transportation (GREET) model 2021 [130]. Further conversion inputs are provided in Table C2.

Techno-economic Analysis. Mass and energy outputs of the process model support techno-economic analysis to evaluate the minimum fuel selling price of algal biofuel across the

6,685 simulated locations. A discounted cash flow rate of return calculation was used to determine the net present value (NPV) of the project during its 30-year lifetime. The cash flow uses operational and capital expenses data along with “Nth-of-a-kind” assumptions (Table S3) to solve for a MFSP that yields a NPV of zero. The cost year of the analysis was 2018 and all costs were allocated to the total liquid fuel output on an energy basis by using a liter of gasoline-equivalent (LGE) unit.

The operational and capital expenses from individual processes in the system were estimated from previous modeling efforts in the literature. Capital expenses for the biomass cultivation, dewatering, and storage processes were retrieved from Davis et al. [13] and Beckstrom et al. [120]. For HTL and upgrading, operational and capital expenses were estimated from Chen and Quinn [99]. Costs for baseline equipment size were re-scaled based on the calculated mass and energy flows from the process model with the following equation:

$$New\ Cost = (Base\ cost) \left(\frac{New\ Size}{Base\ Size} \right)^n \quad (C3)$$

in which the scaling exponent n varies across equipment types [18]. Moreover, to capture the differences in construction and installation costs across different geographies, a construction factor (CF) was used. The construction factor measures the capital expenses and costs associated with construction, equipment operation, and purchasing materials at any location relative to the U.S. [133]–[135]. Construction factors for 38 different countries were retrieved from Richardson’s [139] and are shown in Fig. C - 2. The total capital costs are then estimated by:

$$CAPEX_n = (Base\ U.S.\ cost)(CF_n) \quad (C4)$$

where $CAPEX_n$ denotes the capital expenses at the new location, and CF_n is the construction factor of that location. Similarly, variable operational expenses were calculated using the

individual costs of process inputs shown in Table C4. All costs were adjusted to the base cost year by using indices from the Chemical Engineering Plant Index [164] and the following formula [13], [18]:

$$2018 \text{ Cost} = (\text{Base cost}) \left(\frac{2018 \text{ Cost Index}}{\text{Base Year Index}} \right) \quad (\text{C5})$$

Moreover, the U.S.-based labor costs provided by Davis et al. [18] and Chen and Quinn [99] were used to derive location-specific labor expenses by applying a regional labor index (LI). The labor index measures the total hourly labor costs of a location relative to the labor costs of a reference location [134], [135]. Data from the U.S. Bureau of Labor Statistics [136], International Labor Organization [137], and literature [138] were used to calculate country-specific labor costs relative to the U.S. with values provided in Fig. C - 3. The final labor costs for a location n are given by the following equation:

$$\text{Labor Costs}_n = (\text{Base U.S. labor cost})(LI_n) \quad (\text{C6})$$

Finally, the region-specific corporate tax rates illustrated in Fig. C - 4 were used in the discounted cash flow calculations. Corporate tax rates data for 118 were sourced from the Organization for Economic Co-Operation and Development database [140]. Regional averages were used for countries in which no data was available. The regional averages were calculated by following the 23 regional divisions provided by the World Bank Development Indicators [165].

Life Cycle Assessment. A well-to-wheels life cycle assessment (LCA) was conducted following ISO LCA standards and guidelines [166]. The system boundary includes biomass production, dewatering, storage, conversion, transportation, and fuel use processes. In addition, direct land use change emissions were included. The functional unit was set to an energy unit of liquid fuel output (MJ) [44], [99]. Life cycle inventory data for 171 electricity, 9 ammonia, and 4

diammonium phosphate (DAP) markets were retrieved from the EcoInvent 3.91 database [127]. Hydrogen, nutrients, and electricity impacts varied regionally as these are major contributors to the GWP of algal biofuels [99], [128], [129]. Accordingly, life-cycle natural gas impacts from HTL have been found to have a minimal contribution to the overall GWP of the system [99] and were assumed to be constant. Emissions from the end-use phase of the fuel are provided in Table S5. The regional boundaries of the electricity, hydrogen, ammonia, and DAP markets are illustrated in Fig. C – 4 to Fig. C - 7.

Direct Land Use Change Emissions. In addition, The Intergovernmental Panel on Climate Change (IPCC) Tier 1 methodology was used to assess potential emissions resulting from direct land use change (DLUC) assuming the conversion from the native land type (barren land, grassland, forest, etc.) to an algae facility [131]. The IPCC methods and assumptions used in this study closely follow those used by Handler et al. [167]. Both aboveground and belowground biomass and soil organic carbon (SOC) were assumed to contribute to DLUC effects.

IPCC guidelines are published for different tiers of accuracy, based on data availability or depth of modeling assessments for biomass and soil carbon changes [168]. Tier 1 is designed for the simplest use and default parameter values are used. Tier 2 is similar in approach to Tier 1, but with country/region-specific data. Tier 3 is a higher-order method that includes geographically and temporally specific modeling resolution. Tier 1 guidelines are used in this analysis. The default IPCC values for biomass and soil carbon used are based on location-specific soil types, climate regions, and management practices in each location. The soil classes used for this work were assigned based on IPCC default soil classes derived from the Harmonized World Soil Data Base (Version 1.2) created by Niels H. Batjes [169]. IPCC climate zones were assigned using the

Food and Agriculture Organization of the United Nations Global Ecological Zones and Table 4.1 from the 2006 IPCC Guidelines for National Greenhouse Gas Inventories Volume 4: Agriculture, Forestry and Other Land Use [170], [171]. The Copernicus Global Land Service was used to assign each location a native land cover type [172].

To provide a conservative estimate of LUC impacts, all prior biomass (above and belowground) was assumed to be removed and burned during the conversion of the algae facility resulting in 100% of carbon being released as CO₂. In all scenarios conversion from C to CO₂ is based on the ratio of molecular weights (44/12) as specified by IPCC [173]. Both biomass carbon stock changes and SOC changes were assumed to occur over the 30-year lifespan of the algae facility. This assumption was made to average out the impacts of DLUC over the lifetime of fuel production at a facility. The equation used to calculate the net carbon change from pre-LUC to post-LUC is shown in Equation C7:

$$C_{net} = (C_{biomass} + C_{SOC})_{pre} - (C_{biomass} + C_{SOC})_{post} \quad (C7)$$

where C_{net} represents the net carbon change due to LUC effects. A positive C_{net} means that carbon is emitted due to LUC whereas a negative C_{net} means that carbon is sequestered due to LUC effects. $C_{biomass}$ is the combined above and belowground biomass and C_{SOC} is the soil organic carbon both before (pre) and after (post) land use change takes place.

For all land cover types, the default soil organic carbon stocks were provided in Table 2.3 from IPCC and are based on climate region and soil type [173]. Default soil organic carbon values were adjusted for land use and management practices using Equation C8:

$$SOC_{adj} = SOC_{ref} * F_{LU} * F_{MG} * F_I \quad (C8)$$

where SOC_{adj} is the adjusted soil organic carbon value, SOC_{ref} is the default soil organic carbon value, F_{LU} is the stock change factor for land use, F_{MG} is the stock change factor for land management practices, and F_I is the stock change factor for the input of organic matter. The following sections summarize the assumptions used for both biomass and SOC conversions from grassland/shrubland, cropland, forest land, and barren land to algae facilities.

Grassland, Shrubland, Wetland, and Pasture/Hay Land Cover Types

The DLUC emissions for grasslands, shrublands, and pasture/hay land cover types were calculated similarly and will be discussed together in this section. The following sections detail the DLUC emissions from biomass and SOC change. Due to limited guidance by IPCC on wetlands, the above/below-ground biomass and SOC stocks were assumed to be equal to those of grasslands.

Above and Below Ground Biomass

Estimates of biomass carbon lost from the landscape due to clearing of above and belowground biomass come from Table 6.4 of the IPCC guidelines [174]. A carbon ratio of 0.47 tonne C (tonne d.m.)⁻¹ of herbaceous biomass was used, which is the IPCC default value [174]. It should be noted that the total biomass numbers in Table 6.4 align with multiplying the peak biomass values in Table 6.4 by the above to belowground ratios specified in Table 6.1 except for a Cold Temperate, and moist climate. As such, the authors used the value specified in Table 6.4 of 13.6 tonnes d.m. ha⁻¹ and not that calculated by using the above to belowground ratios. Pasture and Hay land cover types were assumed to have the same above and belowground biomass values as grasslands.

Shrublands were considered to be a type of grassland per IPCC guidelines [174]. As such, the same above-ground biomass numbers were used for shrublands, but the shrubland above-ground to below-ground biomass ratio of 0.28 was used from Table 6.1 for all climates [174].

Soil Organic Carbon Factors

All land cover types detailed in this section derived their SOC stock change factors from Table 6.2 in IPCC guidelines [9]. Both grasslands and shrublands were assumed to be native so the default land use and management stock change factors of 1.0 were used [175]. Alternatively, Pasture and Hay land cover types were designated as improved grassland (F_{MG}) per IPCC guidelines and used management stock changes factors of 1.14, 1.17, and 1.16 for Temperate/Boreal, Tropical, and Tropical Montane climates respectively.

Forests

The following sections detail the DLUC emissions from biomass and SOC change associated with forests.

Above and Below Ground Biomass

Above and below-ground biomass emissions were estimated using the IPCC's reference values for above-ground biomass from Table 4.7 and above to belowground biomass ratios from Table 4.4 [171]. Reference values are provided by ecological zone and continent. No values were provided in the IPCC guidelines for Australia. As such, it was assumed that the values for Australia were equal to those provided for continental Asia. Additionally, no values were provided for warmer temperate regions in Europe. In this case, it was assumed that the warm temperate values were equal to the cold temperate values. Lastly, no values were provided for warm temperate moist regions in Africa so these were assumed to be equal to tropical moist

regions. If a range of biomass values was provided, the median value was used. If a range was provided with a recommended value, the recommended value was used. If multiple sub-ecological zones were provided (ex. Temperate oceanic forest, Temperate continental forest, and Temperate Mountain systems), the continental values were used for the entire ecological zone due to limited data availability.

For this work, forest land cover types were classified into Evergreen Forest, Deciduous Forest, and Mixed Forest. The Copernicus Global Land Service further categorizes forests based on if they are open or closed forests, but in this analysis, they were combined into one category due to a lack of information on open/closed forests in IPCC guidelines. In the case of values in Table 4.4 for above to below biomass ratios, conifer values were used for Evergreen Forest, broadleaf was used for Deciduous, and mixed was the mean of the conifer and broadleaf values. If only general forest ratios were provided for a certain ecological zone or forest type, the same ratio was used for all three forest types. A carbon ratio of 0.47 tonne C (tonne d.m.)⁻¹ of woody biomass was used, which is the IPCC default value [171].

Soil Organic Carbon Factors

It was assumed that all forests were native forests and as such the IPCC default value of 1.0 was used for all stock change factors based on IPCC guidance in Table 5.10 [175].

Barren Land

The following sections detail the DLUC emissions from biomass and SOC change associated with barren lands.

Above and Below Ground Biomass

All above and belowground carbon was assumed to be 0 tonnes C ha⁻¹ based off the National Land Cover Database description. Barren land is defined as, “areas of bedrock, desert pavement, scarps, talus, slides, volcanic material, glacial debris, sand dunes, strip mines, gravel pits and other accumulations of earthen material. Generally, vegetation accounts for less than 15% of total cover.” [176].

Soil Organic Carbon Factors

SOC for barren land was assumed to be “native unmanaged land” which is equal to the default IPCC values [175]. Therefore, all stock change factors were set equal to 1.0.

Cultivated Cropland

The following sections detail the DLUC emissions from biomass and SOC change associated with croplands.

Above and Below Ground Biomass

Similar to the methods used by Handler et al. [167], it was assumed that the majority of cropland biomass would be harvested prior to the conversion of cropland to algae facilities. As such, the above-ground biomass on cropland was assumed to be equal to the agricultural Maize residues reported in IPCC Table 2.4 (10.0 tonnes d.m ha⁻¹). It should be noted that Maize has the highest biomass of the residues listed by IPCC, but it was used to provide a conservative estimate of LUC impacts. A carbon ratio of 0.47 tonne C (tonne d.m.)⁻¹ of herbaceous biomass was used, which is the IPCC default value [174]. Default values for below biomass are not

available from IPCC. As such, below-ground carbon stocks are assumed to not change and are set equal to zero [175].

Soil Organic Carbon Factors

Cultivated cropland was assumed to be long-term cultivated (F_{LU}) using full tillage (F_{MG}) and medium soil inputs (F_I) per Table 5.5 from IPCC guidelines [175].

Post-Conversion Carbon Estimates

The algae facilities in this study were assumed to be similar to settlements as defined by IPCC. As such, guidance on the conversion of all land types to settlements was used. The following sections detail the DLUC emissions from biomass and SOC change associated with settlements.

Above and Below Ground Biomass

The default IPCC guidance for conversion to settlements is that all above and belowground carbon is lost to the atmosphere after conversion [177]. However, since not all of an algae facility's footprint is paved over it has been assumed that 8% of the facility footprint is maintained as turfgrass for all land cover types except barren land [82], [167]. Barren land was assumed to not be able to grow turfgrass and was left barren. IPCC does not guide on above or belowground biomass associated with turfgrass. Therefore, we have assumed the above-ground biomass to be equal to 3.45 kg/m² for unirrigated fine fescue from Qian et al. with a moisture content calculated by Springer et al. of 67.6% [178], [179]. The above-ground to below-ground biomass ratio of 40/60 from Ericsson et al. [180] was used. This results in a total biomass carbon value of 13.1 tonne C ha⁻¹ for turfgrass.

Soil Organic Carbon Factors

Per IPCC guidelines, the soil organic carbon in the first 30 cm of soil under paved settlements is assumed to be reduced by 20% from the reference soil values [177]. Therefore, the product of F_{LU} , F_{MG} , and F_I was set equal to 0.8 for the 92% of the algae facility not covered by turfgrass. For the portion of settlement area that is retained as turfgrass, the soil organic carbon values should be comparable to an improved grassland from the IPCC definition, because it would receive periodic management such as fertilization, species management, or irrigation [177]. Therefore, the improved grassland values for management were used for the 8% turfgrass portion of algae facilities using F_{MG} values from IPCC Table 6.2 [171]. F_{LU} and F_I were assumed to be the default values of 1.0.

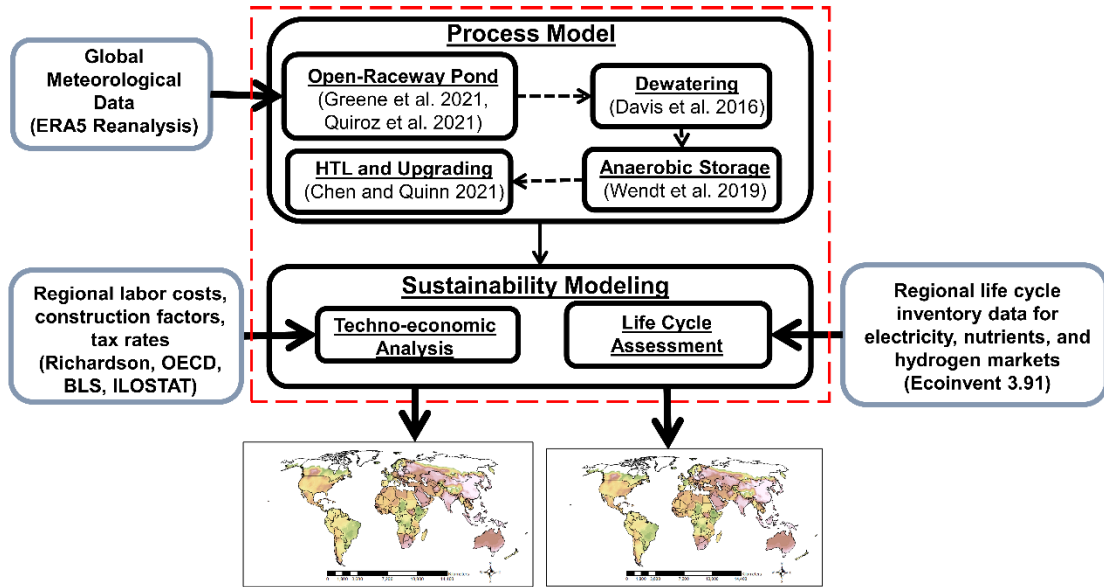


Figure C -1. Modeling architecture showing the integration of process modeling with sustainability assessment. Hourly meteorological data for 6,865 global locations was used to provide spatially temporal modeling outputs while regional economic and life cycle data are leveraged to perform regional sustainability modeling.

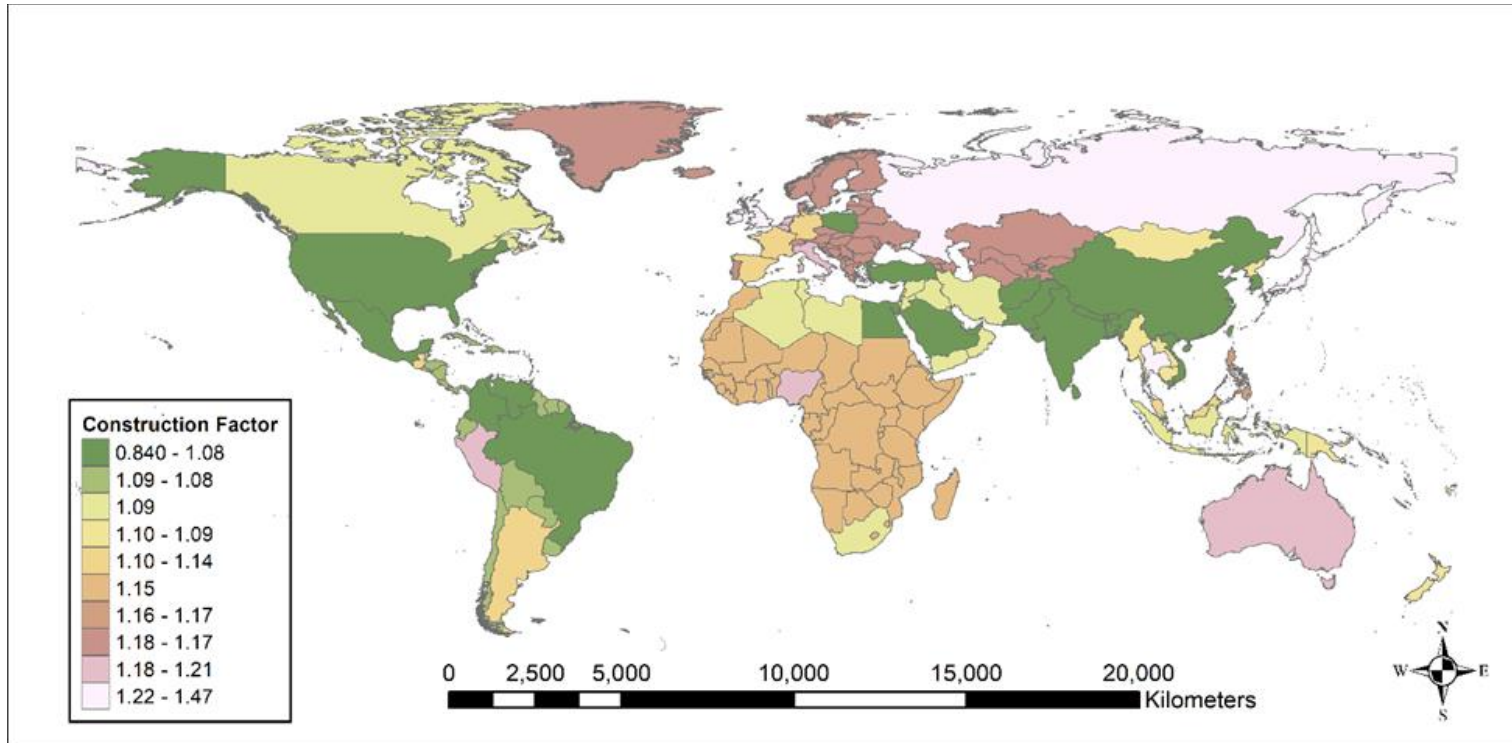


Figure C -2. Regional construction factors used in the techno-economic analysis [139]

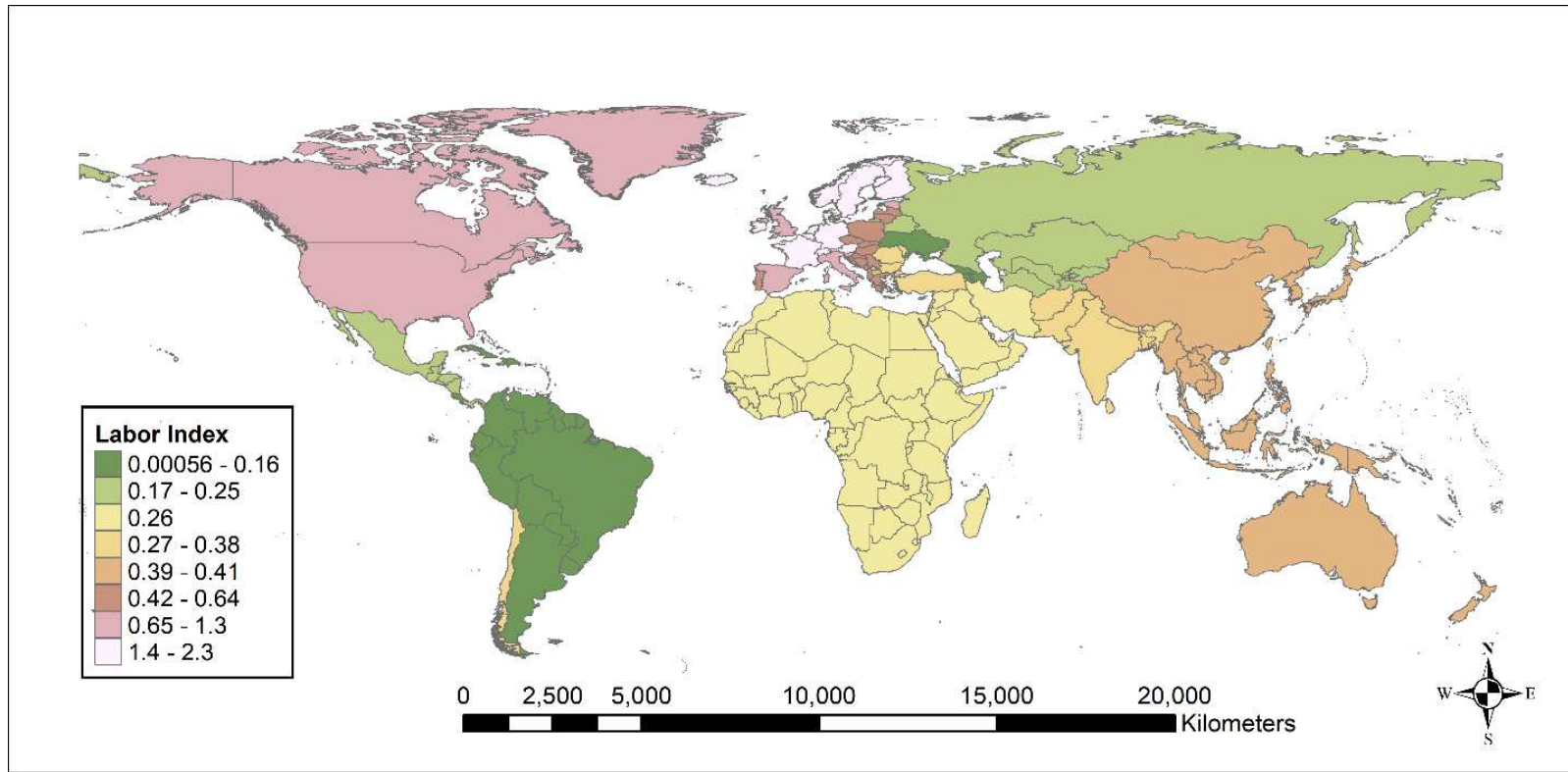


Figure C -3. Regional labor indices used in the techno-economic analysis [136]–[138].

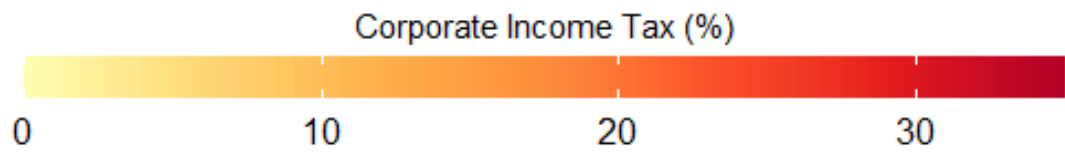
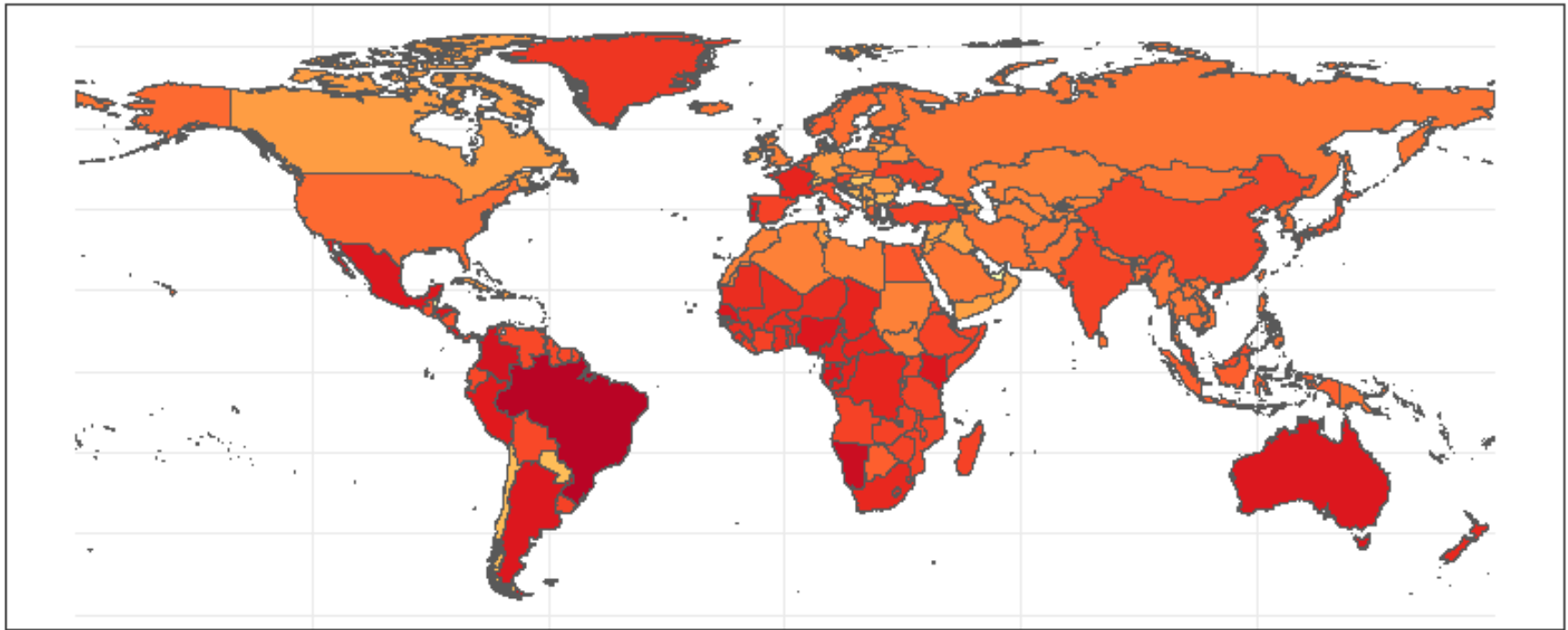


Figure C -4. Corporate tax rate data retrieved from the Economic Co-Operation and Development database [140].

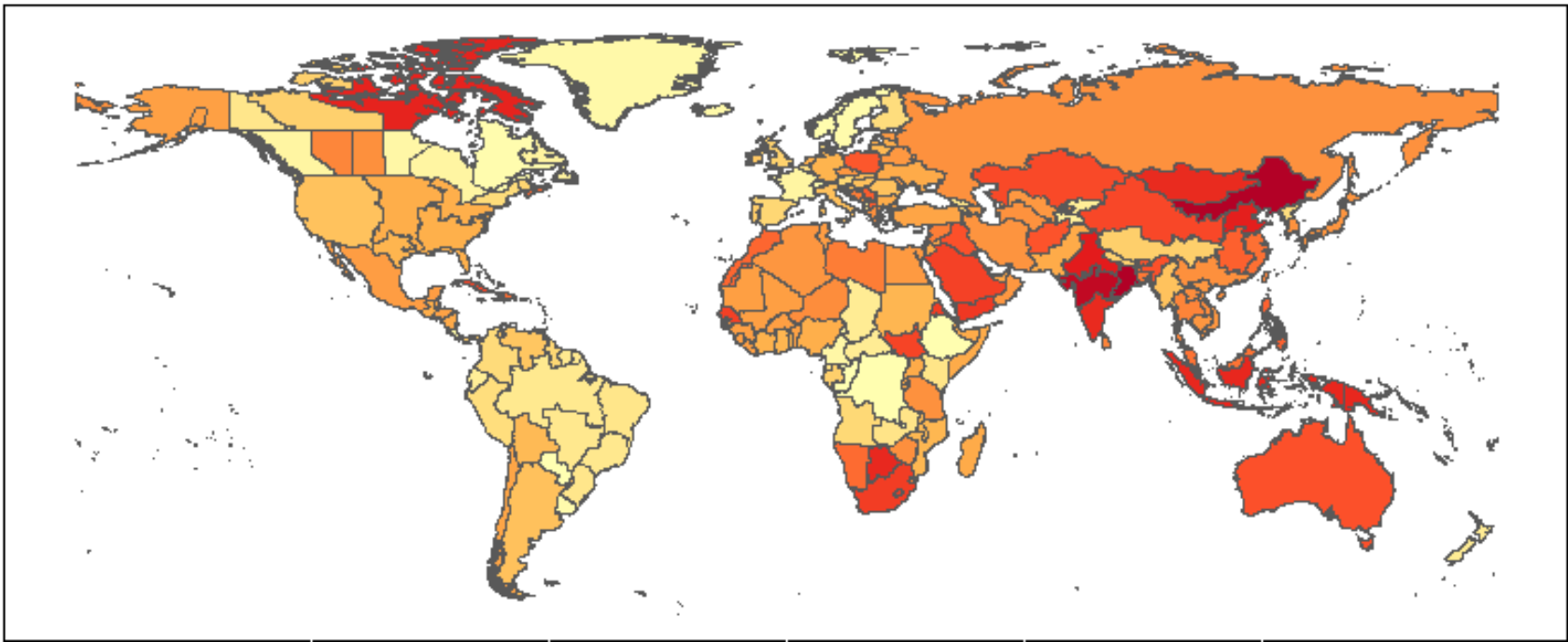


Figure C -5. Geographical resolution of the life cycle impact data for electricity markets [127]. Electricity grids are divided by country boundaries in most cases. Subregional electricity grids are used in the United States, Brazil, Canada, India, and China.

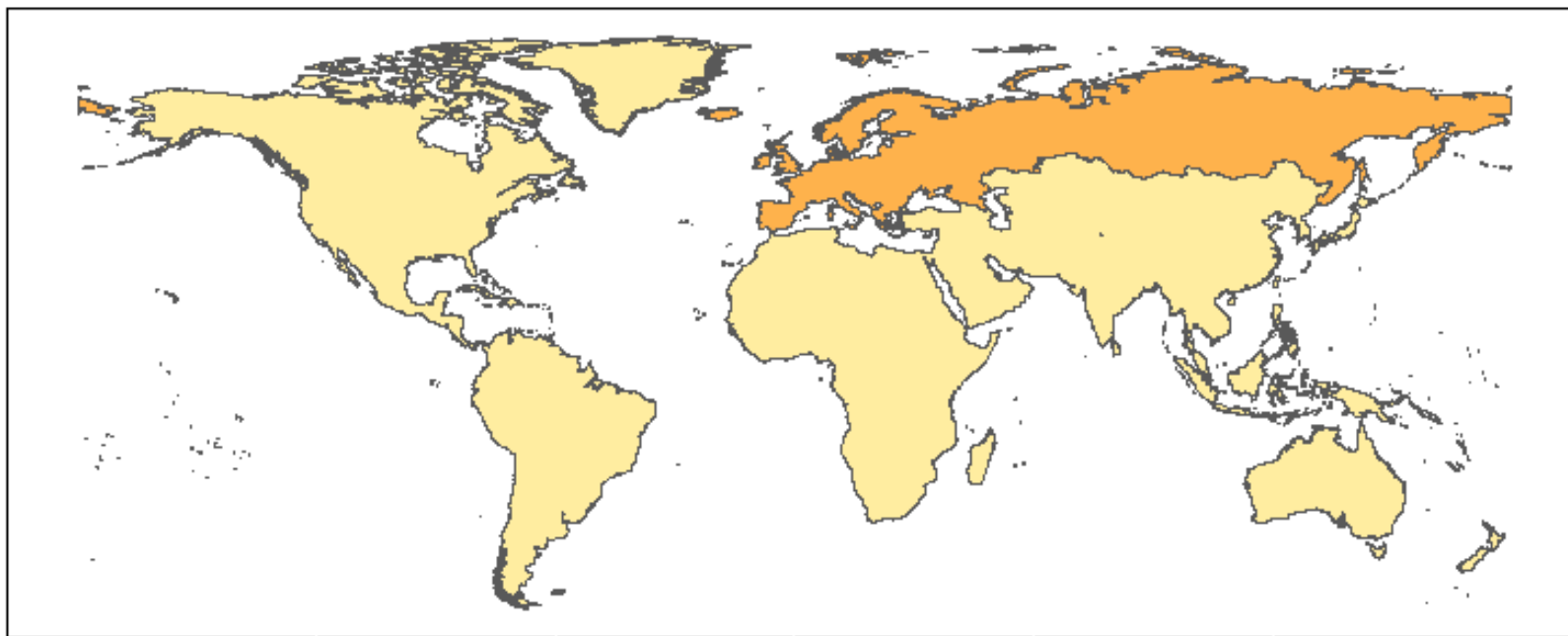


Figure C -6. Geographical resolution of the life cycle impact data for hydrogen markets [127]. Global hydrogen data is divided into a European market and a rest-of-the-world market.

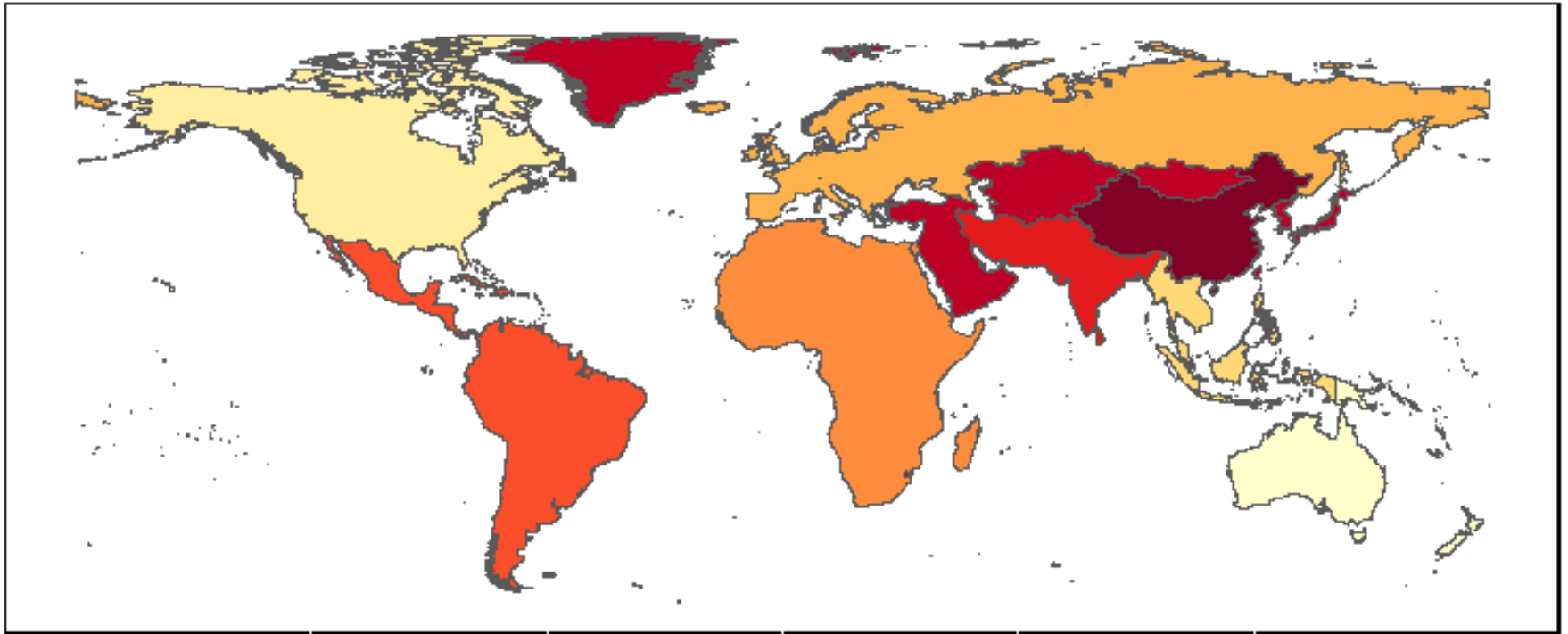


Figure C -7. Geographical resolution of the life cycle impact data for ammonia markets [127]. Global ammonia data is divided into 9 different markets: North America, Latin America, Africa, Europe, China, Southeast Asia, Oceania, South Asia, and a rest-of-the-world market.

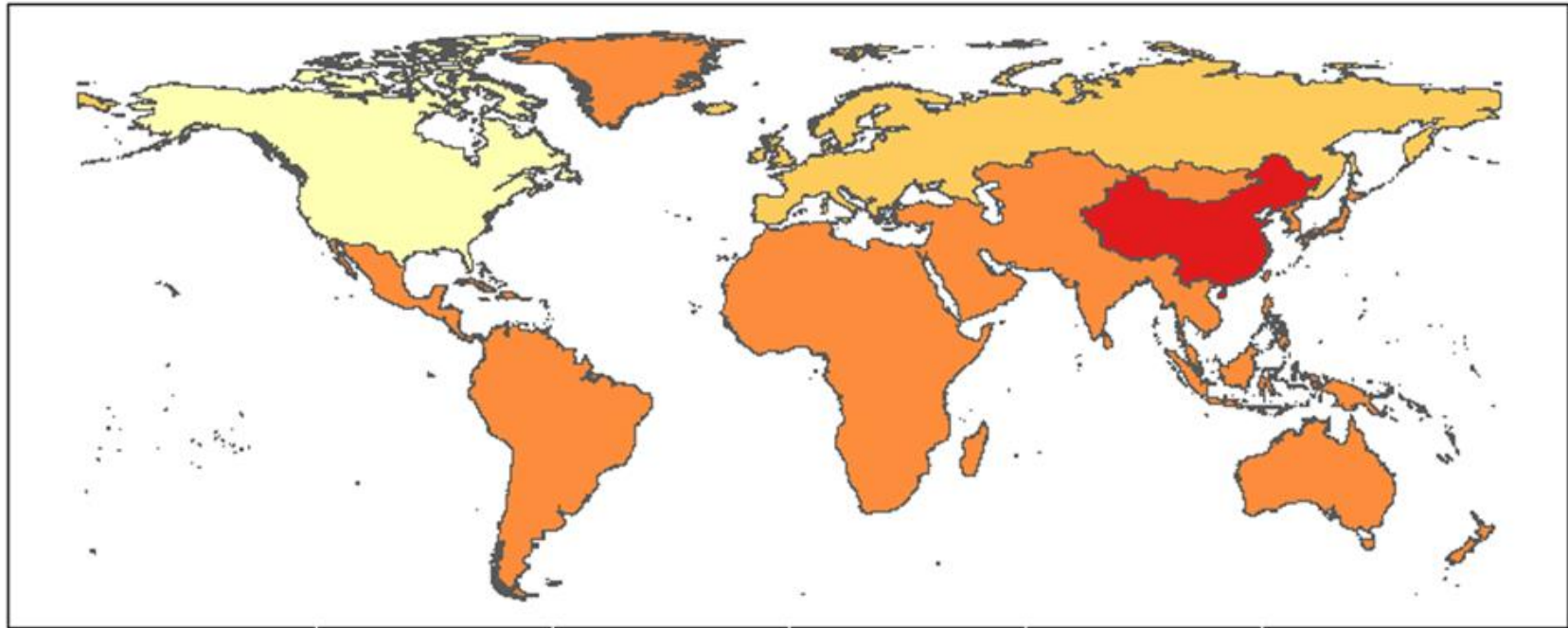


Figure C - 8. Geographical resolution of the life cycle impact data for diammonium phosphate markets [127]. Global diammonium phosphate data is divided into 4 different markets: North America, Europe, China, and the rest-of-the-world market.

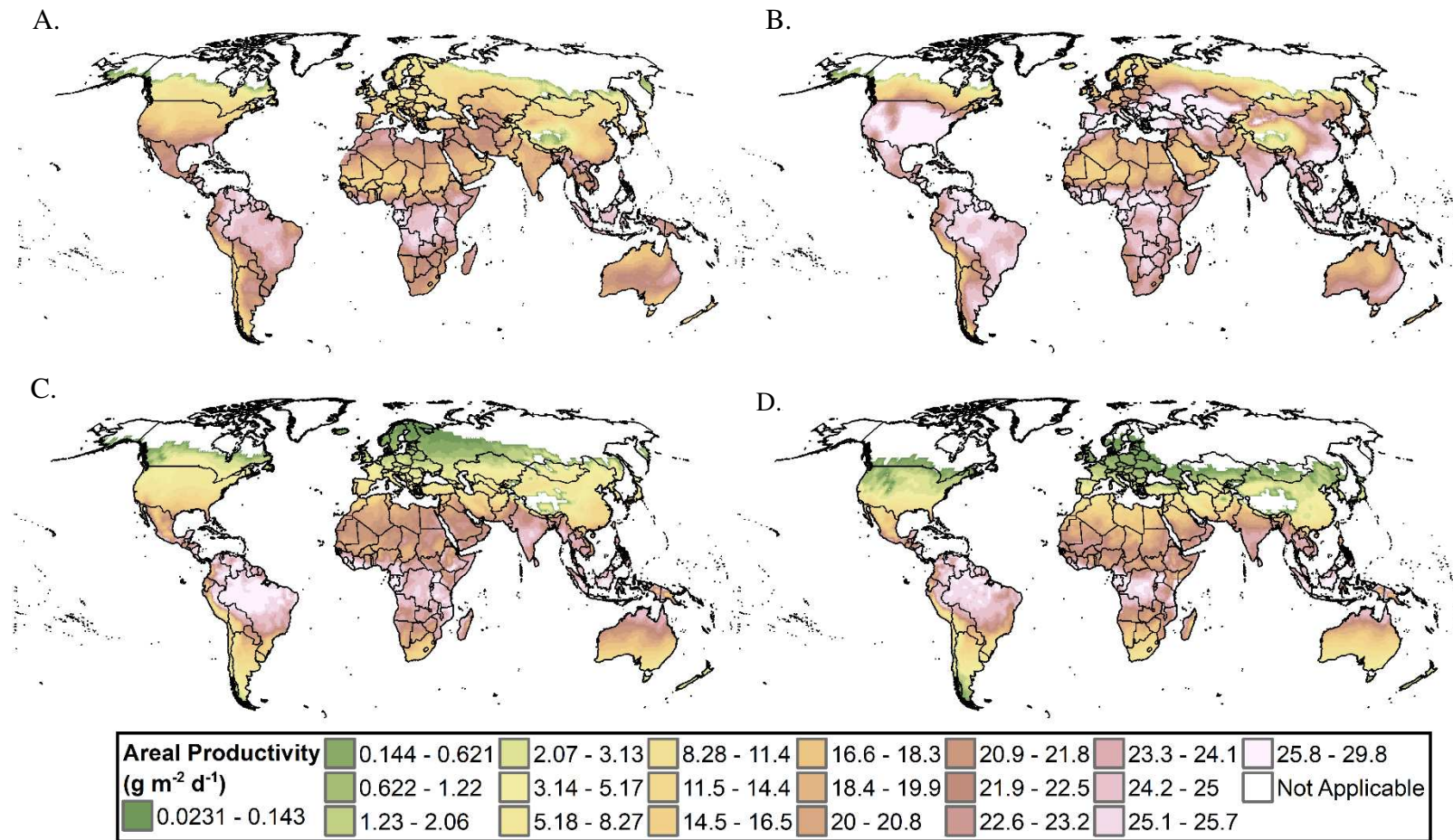


Figure C - 9. Seasonal areal productivity yields for the semi-continuous cultivation of *Scenedesmus obliquus* in open pond systems: A) Spring (March 21 – June 21), B) Summer (June 21-September 21), C) Fall (September 21 – December 21), D) Winter (December 21 – March 21). Results are based on the simulation of 6,865 global locations.

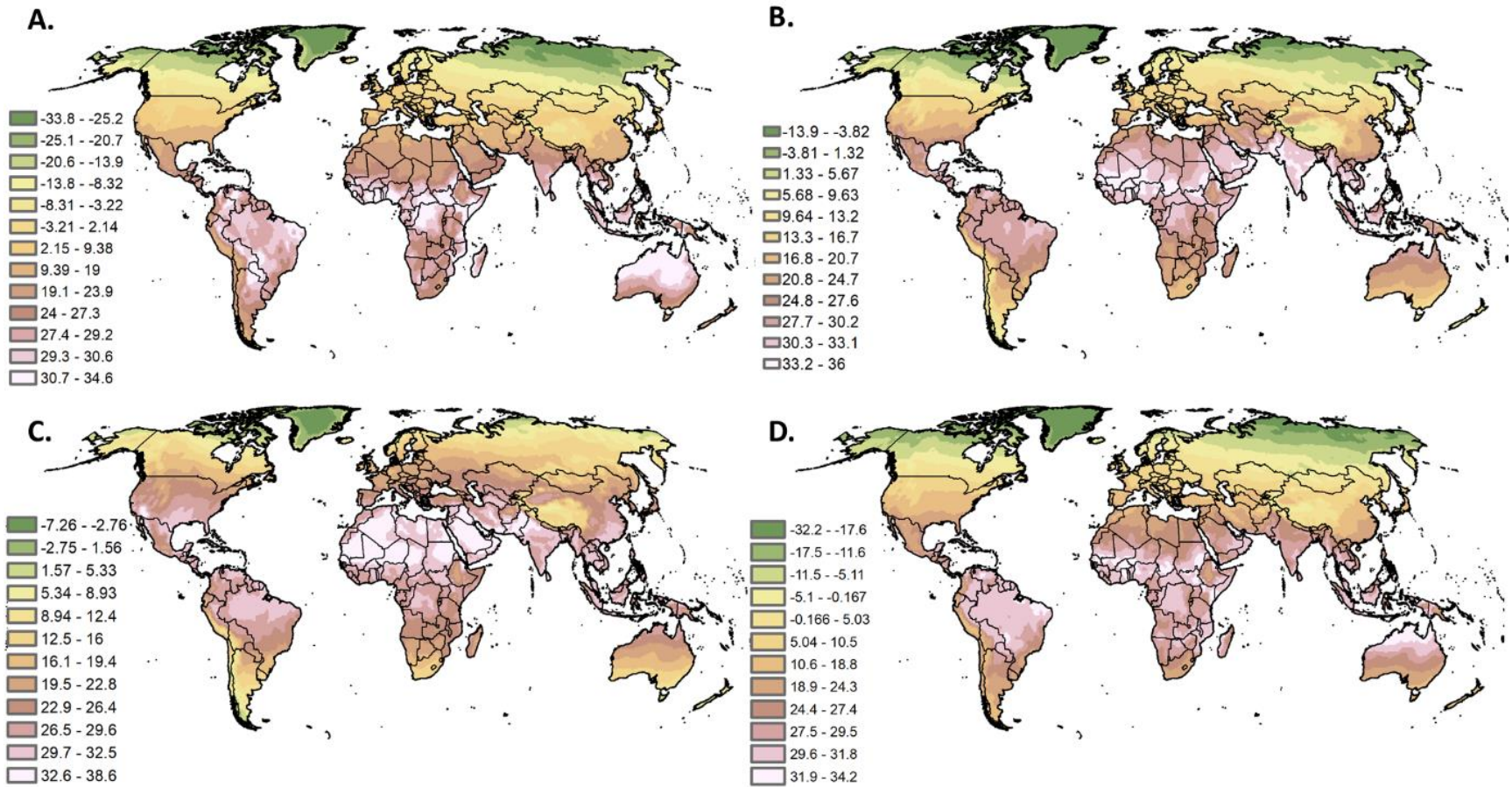


Figure C - 10. Seasonal average pond temperatures ($^{\circ}\text{C}$): A) Spring (March 21 – June 21), B) Summer (June 21-September 21), C) Fall (September 21 – December 21), D) Winter (December 21 – March 21). Results are based on the simulation of 6,865 global locations.

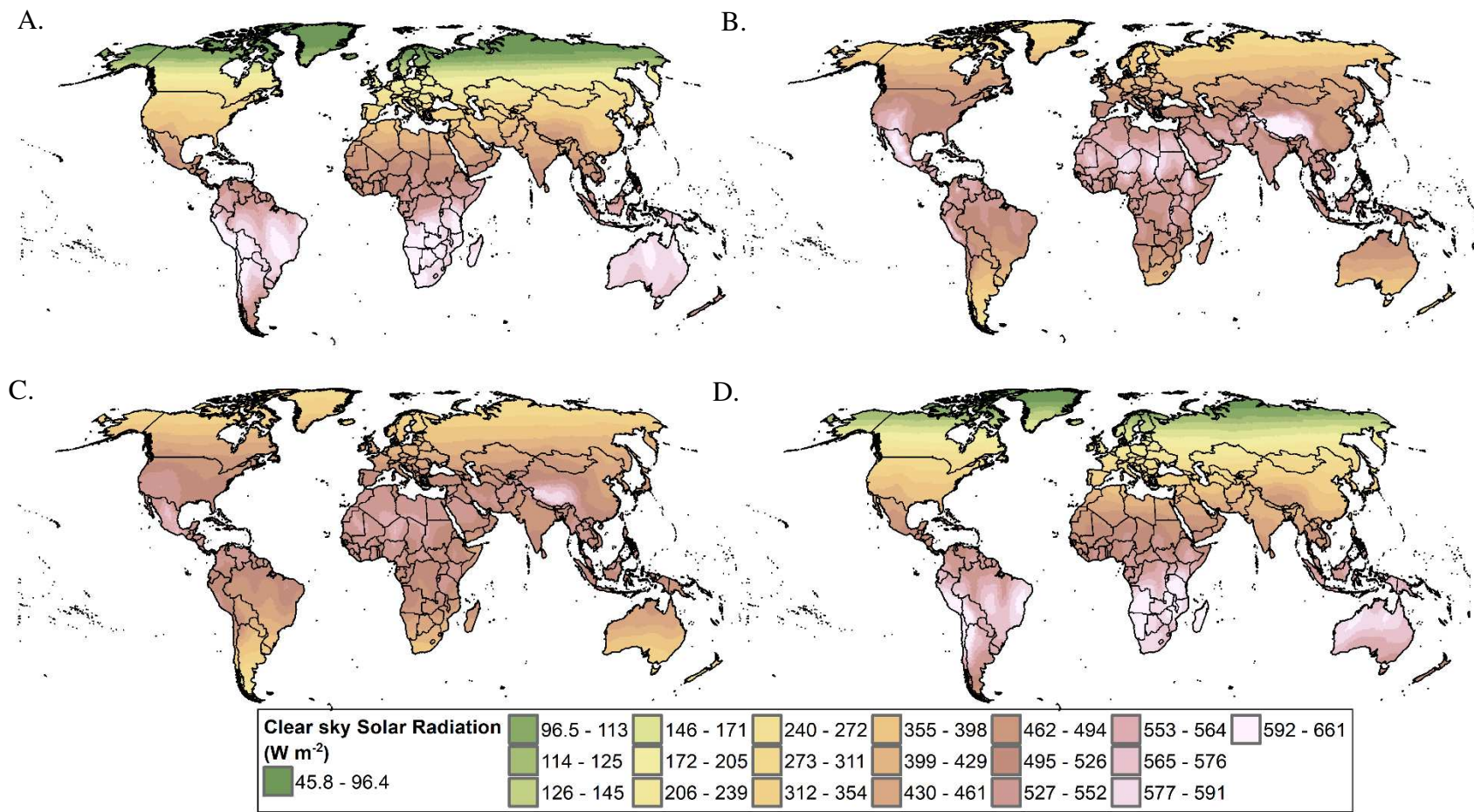


Figure C - 11. Seasonal average clear sky solar radiation: A) Spring (March 21 – June 21), B) Summer (June 21-September 21), C) Fall (September 21 – December 21), D) Winter (December 21 – March 21). Data is representative of the year 2021, retrieved from the fifth global reanalysis (ERA5) dataset generated by the European Centre for Medium-Range Weather Forecasts [123].

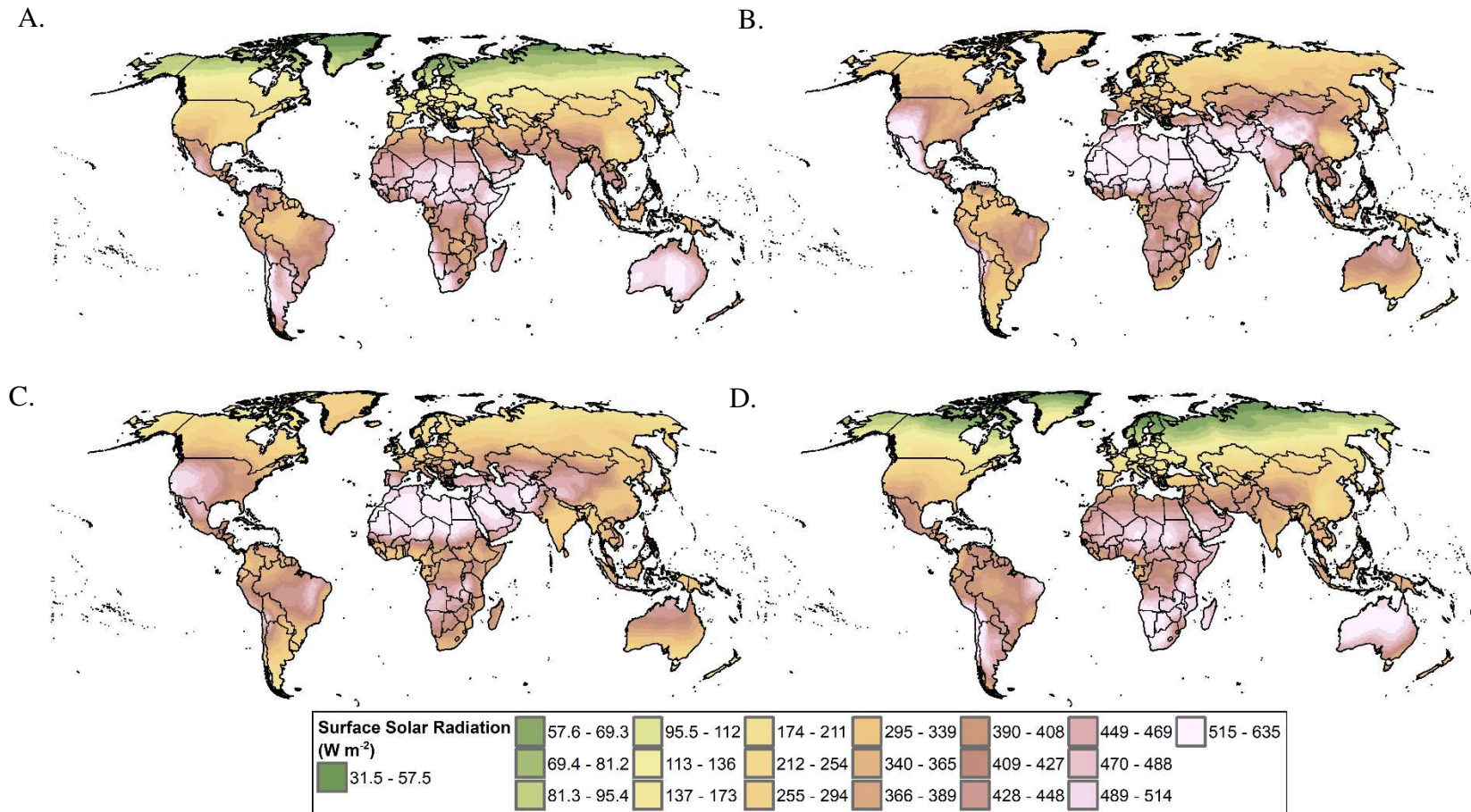


Figure C - 12. Seasonal average solar radiation at surface: A) Spring (March 21 – June 21), B) Summer (June 21-September 21), C) Fall (September 21 – December 21), D) Winter (December 21 – March 21). Data is representative of the year 2021, retrieved from the fifth global reanalysis (ERA5) dataset generated by the European Centre for Medium-Range Weather Forecasts [123].

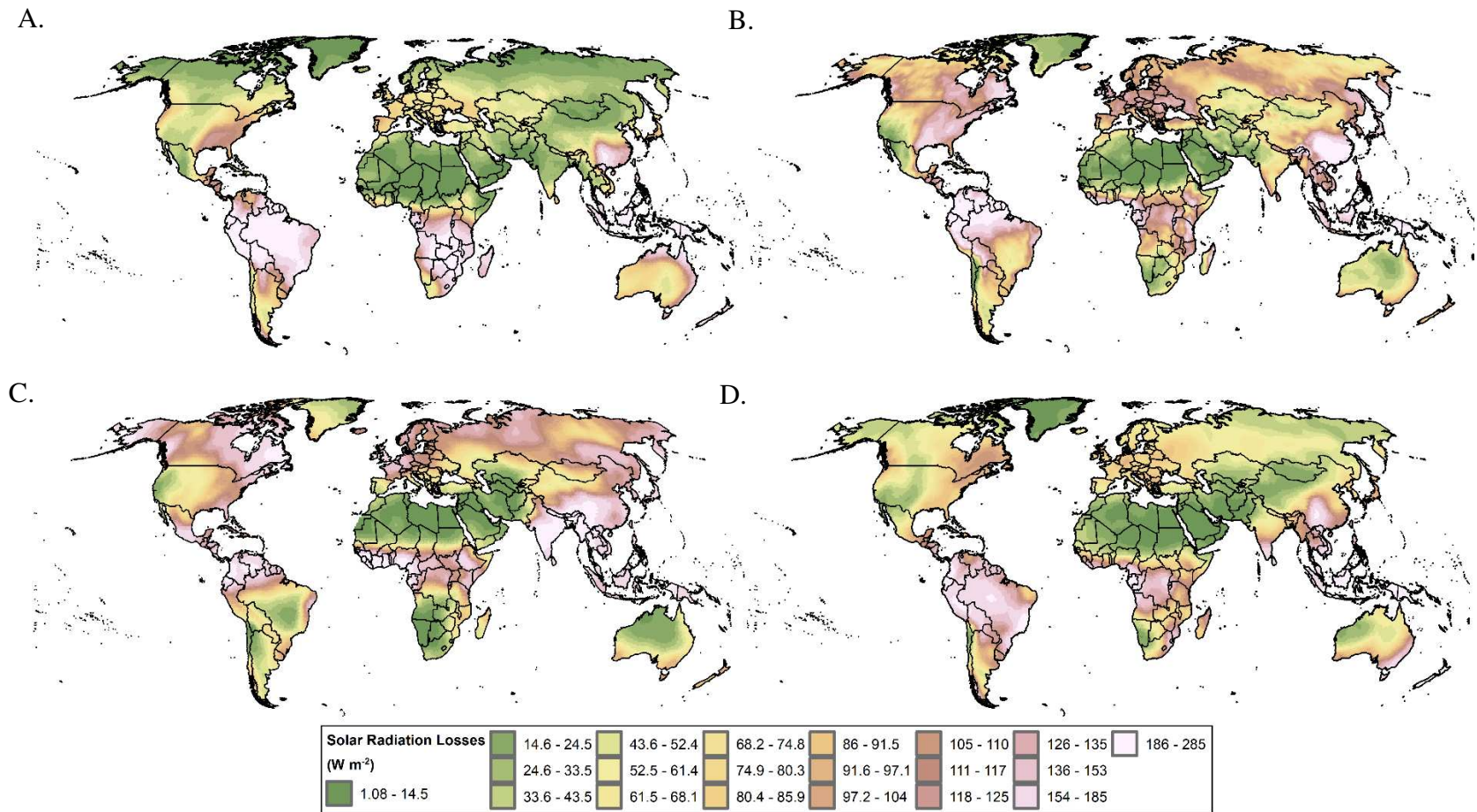


Figure C -13. Seasonal average solar losses: A) Spring (March 21 – June 21), B) Summer (June 21-September 21), C) Fall (September 21 – December 21), D) Winter (December 21 – March 21). Data is representative of the year 2021, solar losses are defined as the difference between clear sky and surface solar radiation [123].

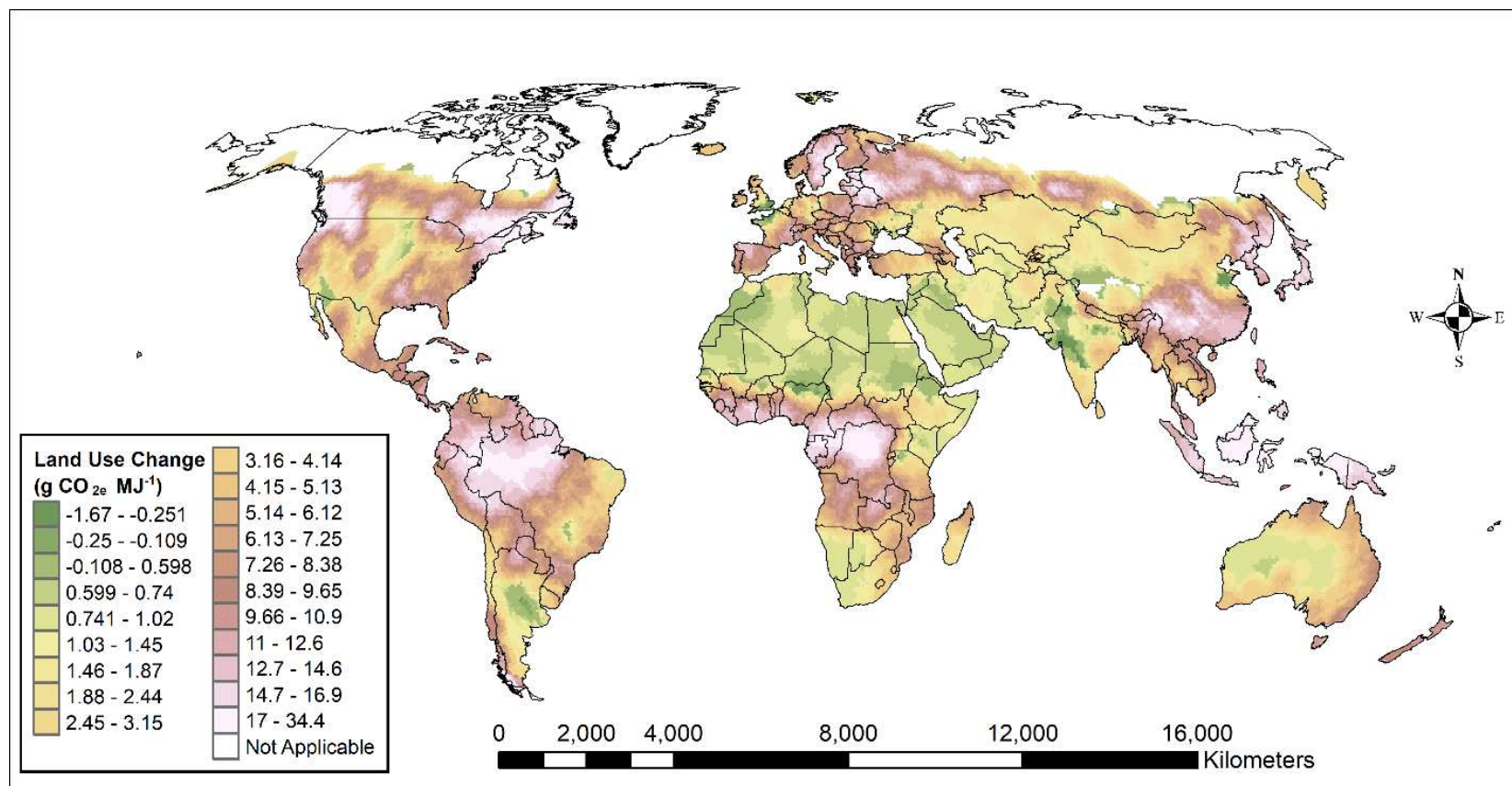


Figure C -14. Global direct land use change emissions.

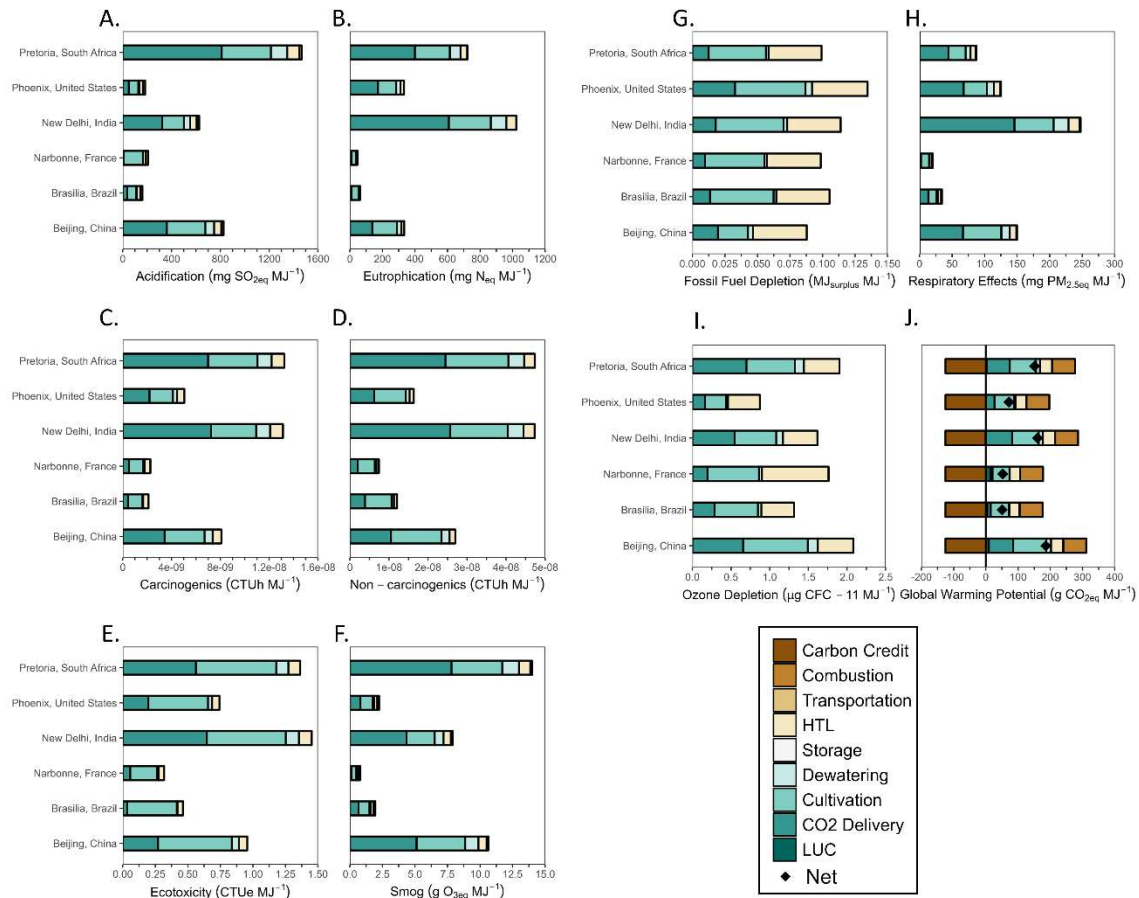


Figure C-15. Well-to-wheels environmental impacts of algal biofuels at five case study locations broken down by process contributions: A) acidification, B) eutrophication, C) carcinogenic, D) non-carcinogenic, E) ecotoxicity, F) smog, G) fossil fuel depletion, H) respiratory effects, I) ozone depletion, and J) global warming potential.

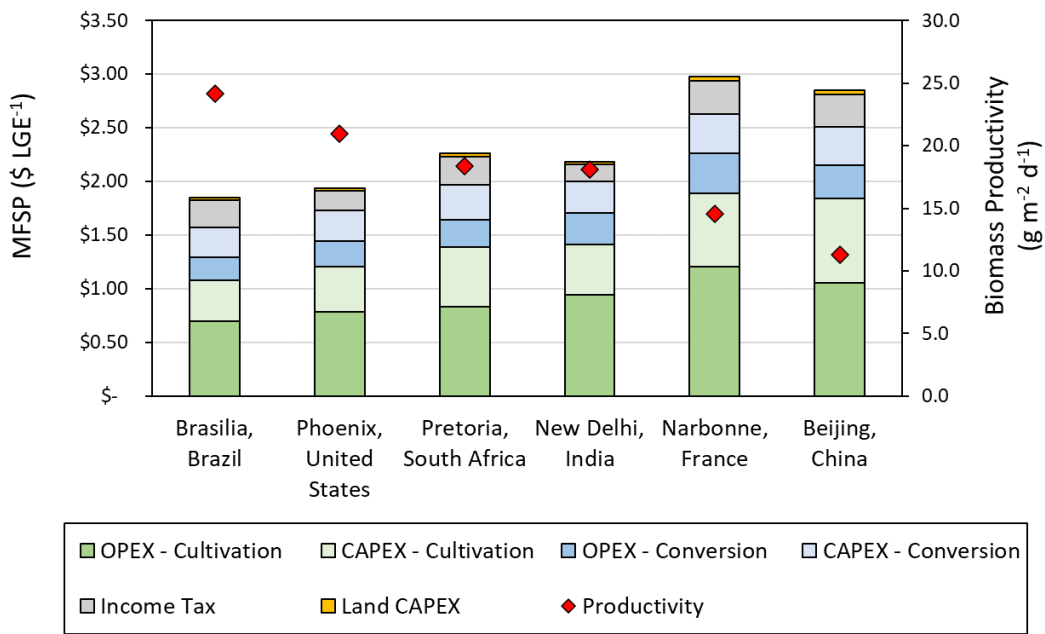


Figure C -16. Fuel prices in liters of gasoline-equivalent (LGE) broken down by operational expenses (OPEX), capital expenses (CAPEX), and annual average areal productivity values for five case study locations. Cultivation includes biomass production, dewatering, and storage processes. Conversion processes include hydrothermal liquefaction and upgrading.

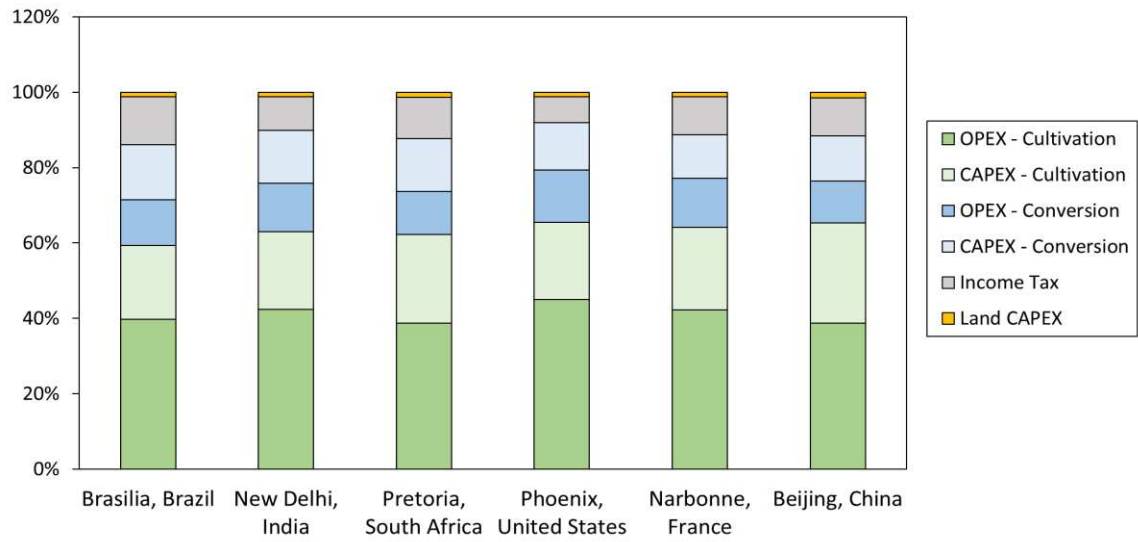


Figure C -17. Fuel selling price of five case study locations broken down by process operational and capital expenses, income tax, and land costs and normalized by percent contribution.

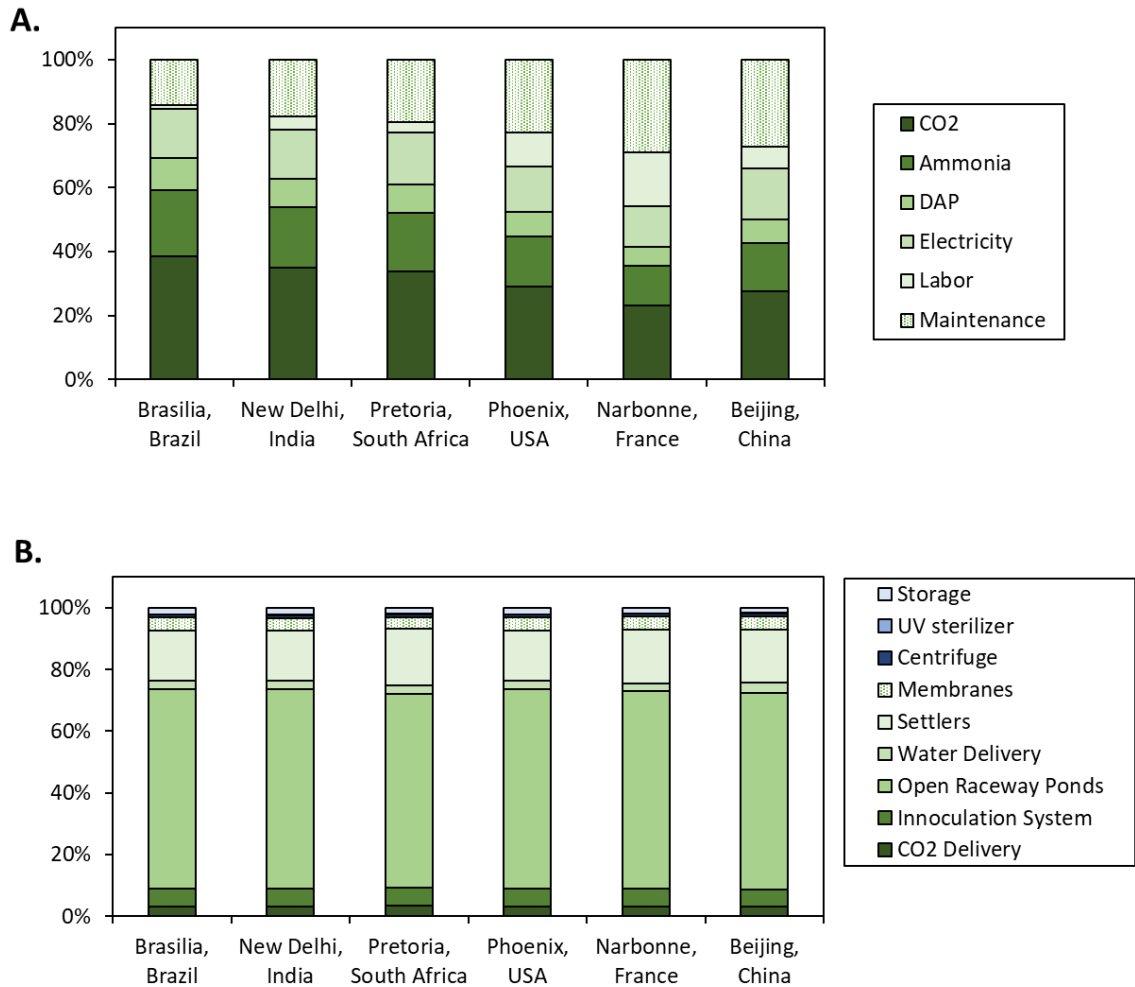


Figure C -18. Cultivation A) operational expenses broken down by source and B) capital expenses broken down by equipment contributions at five case study locations.

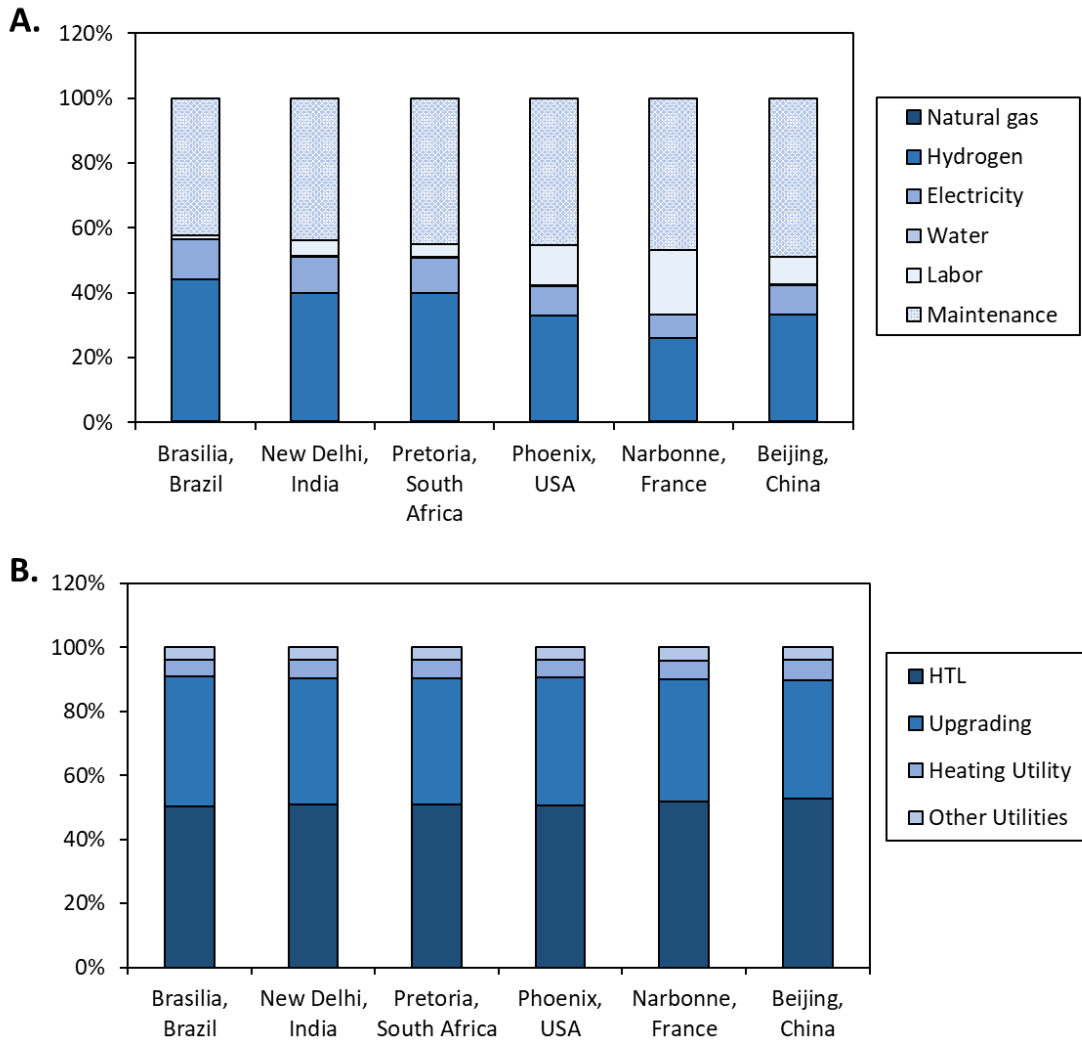


Figure C -19. Conversion A) operational expenses broken down by source and B) capital expenses broken down by equipment contributions at five case study locations.

Table C1. Fundamental cultivation and dewatering inputs.

Strain Parameters [23]	Value	Units
Optimal Temperature	32.3	°C
Minimum Tolerated Temperature	3.1	°C
Maximum Tolerated Temperature	41.0	°C
Optical Density Coefficient	0.38	m ⁻¹
Saturation Light Intensity	480	μmol m ⁻² s ⁻¹
Night Respiration Rate	3	%
Photon Efficiency	1.5	g biomass mol ⁻¹ photon
Biomass Elemental Composition [13]		
Carbon	48.3	% ash-free dry weight
Phosphorus	1.2	% ash-free dry weight
Nitrogen	9.5	% ash-free dry weight
Biomass Component Composition [13]		
Protein	48.09	% dry weight
Carbohydrates	23.30	% dry weight
Lipids	20.21	% dry weight
Ash	8.40	% dry weight
Diammonium Phosphate Composition [18]		
Phosphorous	20	%, weight
Nitrogen	18	%, weight
Ammonia Composition[18]		
Nitrogen	82	%, weight
Dewatering [18]		
Settlers target concentration	10	g L ⁻¹
Settlers separation efficiency	90	%
Membrane target concentration	130	g L ⁻¹
Membrane separation efficiency	99.5	%
Centrifuge target concentration	200	g L ⁻¹
Centrifuge separation efficiency	97	%
Storage [181]		
Inlet and Outlet Pump Head	98.1	m
Pump efficiency	70	%
Energy Inputs		
CO ₂ delivery power [18]	0.0439	kWh kg ⁻¹ CO ₂
Paddlewheel power [18]	55.1	kWh hectare ⁻¹ day ⁻¹
Membrane power [18]	0.04	kWh m ⁻³
Centrifuge power [18]	1.35	kWh m ⁻³
UV sterilizer power [120]	2.71e-03	kWh m ⁻³
Freshwater pump power [18]	0.257	kWh m ⁻³
Ponds to settlers pump power [18]	0.0189	kWh m ⁻³
Settlers recycling pump power [18]	0.0177	kWh m ⁻³
Settlers to membrane pump power [18]	0.129	kWh m ⁻³
Membrane to centrifuge pump power [18]	0.0194	kWh m ⁻³
Recycling stream pump power [18]	0.184	kWh m ⁻³

Table C2. Fundamental hydrothermal liquefaction, hydrotreating, and hydrocracking inputs.

Conversion Inputs [99]	Value	Units
Hydrogen	44.7	kg per tonne biocrude
Natural gas	3.20	kg per tonne biocrude
Process water	1.12	m ³ per tonne biocrude
Grid electricity	0.21	kWh per tonne biocrude
Hydrothermal Liquefaction Yields [130]		
Biocrude	44.7	% weight
Aqueous	25.4	% weight
Solids	8.7	% weight
Gas	12.8	% weight
Ash	8.4	% weight
Fuel Yields [99]		
Diesel	0.657	kg diesel per kg biocrude
Naphtha	0.12	kg diesel per kg biocrude
Boiler Emissions [130]		
CO ₂	59400	g mmBTU ⁻¹ input
CH ₄	1.06	g mmBTU ⁻¹ input
N ₂ O	0.75	g mmBTU ⁻¹ input
VOC	2.54	g mmBTU ⁻¹ input
CO	22.2	g mmBTU ⁻¹ input
NO _x	36.4	g mmBTU ⁻¹ input
PM ₁₀	3.51	g mmBTU ⁻¹ input
PM _{2.5}	3.51	g mmBTU ⁻¹ input
SO _x	0.269	g mmBTU ⁻¹ input

Table C3. Nth-of-a-kind plant assumptions [13], [18], [21], [99].

Input	Value	Units
Internal rate of return	10	%
MACRS depreciation	7	years
On-stream factor	330	days per year
Loan interest rate	8	% annual
Plant financing dept	60	%
Plant equity	40	%
Debt financing terms	10	years
Working capital	5	% fixed capital (excluding land)
Construction period	8	% in year 1
	60	% in year 2
	32	% in year 3
Start-up time	6	Months
Start-up revenue	50	% of total revenue
Start-up costs	75	% of total variable costs
	100	% fixed costs
Indirect capital	60	% of total installed costs